



**UNIVERSITY OF
BIRMINGHAM**

**CFD MODELLING STUDY OF SPRAYS AND
COMBUSTION OF GASOLINE AND DMF IN DIRECT
INJECTION GASOLINE ENGINES**

BY

HAIYING LI

A thesis submitted to the
The University of Birmingham for the degree of
DOCTOR OF PHILOSOPHY

The University of Birmingham
School of Mechanical Engineering
August, 2013

UNIVERSITY OF
BIRMINGHAM

University of Birmingham Research Archive

e-theses repository

This unpublished thesis/dissertation is copyright of the author and/or third parties. The intellectual property rights of the author or third parties in respect of this work are as defined by The Copyright Designs and Patents Act 1988 or as modified by any successor legislation.

Any use made of information contained in this thesis/dissertation must be in accordance with that legislation and must be properly acknowledged. Further distribution or reproduction in any format is prohibited without the permission of the copyright holder.

Abstract

The new biofuel candidate, 2, 5-Dimethylfuran (DMF) has received increasing interest as a potential alternative to fossil fuels, owing to the recent development of its new production technology. However, the effect of DMF properties on the fuel spray and vaporization, subsequent combustion processes and emission formation in the current Gasoline Direct Injection (GDI) engine is still not well understood.

To investigate spray and combustion characteristics of DMF and explore possible applications to the IC engines, a three-dimensional Computational Fluid Dynamics (CFD) model has been developed using the KIVA3V code with improved spray models (nozzle flow model, spray atomization and secondary breakup models) and combustion models. At the same time, the macroscopic and microscopic characteristics of DMF fuel spray were studied through the measurement obtained by using PDPA (Phase Doppler Particle Analyzer) and Shadowgraph techniques and the data are used for validating the spray model. In addition, laminar flame speed was measured by using the Schlieren technique for the development of the combustion model. This CFD model was then applied to study the in-cylinder mixture preparation and combustion characteristics of DMF in a GDI engine.

The mixture preparation analysis shows both insufficient mixing time and significant spray-wall interaction when DMF is used result in relatively poor air/fuel distributions. Compared to the nearly homogeneous mixture with the gasoline fuel spray, a very rich fuel-air mixture of 7.7% and extremely lean mixture of 4.7% of the total charge has been observed in the case of

DMF at the end of compression stroke. The mixing quality of DMF under various injection timing and engine speed conditions has also been investigated and compared with the case of gasoline.

The analysis of combustion characteristics compared with the case of gasoline show that slightly longer combustion duration of DMF results from its lower laminar flame speed. The higher anti-knocking quality of DMF makes more advanced spark timing possible which brings about higher peak pressure and temperature and higher IMEP; however, the higher pressure rise rate and higher temperature result in 187% higher NO_x emissions than for gasoline; in addition, inhomogeneity of the mixture at the stoichiometric air-fuel ratio with DMF considerably compromises its combustion efficiency and fuel economy.

List of Abbreviations

AMD	Arithmetic Mean Diameter
BTL	Biomass-to-Liquids
CAB	Cascade Atomization and drop Breakup
CCD	Charge-Coupled Device
CFD	Computational Fluid Dynamics
CMC	Continuous Multi-Component
CTC	Characteristic Time Combustion
DDB	Dynamic Drop Breakup
DDM	Discrete Droplet Model
DISI	Direct Injection Spark Ignition
DMC	Discrete Multi-Component
DMF	2,5-Dimethylfuran
DNS	Direct Numerical Simulation
EBU	Eddy Break Up
EOI	End of Injection
ER	Equivalence Ratio
ETAB	Enhanced Taylor Analogy Breakup
EV	Electric Vehicles
EVO	Exhaust Valve Opening Time
FMF	Fuel Mass Fraction
GDI	Gasoline Direct Injection
GHG	Greenhouse gas
REET	Greenhouse gases, Regulated Emissions, and Energy use in Transportation
HC	Hydrocarbon
HMF	5-hydroxymethylfurfural
HSP	High Speed Photography
HV	Hydrogen vehicles
IC	Internal Combustion
ILUC	Indirect Land-Use Change
IMEP	Indicated Mean Effective Pressure

IVC	Intake Valve Closing
KH	Kelvin-Helmholtz
LAS	Laser Absorption-Scattering
LES	Larger Eddy Simulation
LHV	Lower Heating Value
LIF	Laser Induced Fluorescence
LSD	Laser Sheet Drop-sizing
MFB	Mass Fraction Burned
MPI	Max Planck Institute
NMHC	Non-methane hydrocarbons
NO _x	Nitrogen oxides
N-S	Navier-Stokes
PDPA	Phase Doppler Particle Analyser
PFI	Port Fuel Injection
PIV	Particle Image Velocimetry
PM	Particulate Matter
RANS	Reynolds Average Navier-Stokes
RNG	Re-Normalisation Group
RT	Rayleigh-Taylor
SI	Spark Ignition
SOI	Start of Injection
SIDI	Spark Ignition Direct Injection
SMD	Sauter Mean Diameter
SR	Swirl Ratio
TAB	Taylor Analogy Breakup
TDC	Top Dead Centre
THC	Total hydrocarbon
TR	Tumble Ratio
TWC	Three-Way Catalyst
VOF	Volume of Fluid
VVA	Variable Valve Actuation

List of Latin Notations

a	Parent drop radius
A_l	Combustion model constant
A_n	Nozzle geometrical constant
B_0, B_1	KH model constants
B_l	Combustion model constant
c_l	Liquid specific heat
c_p	Specific heat
$c_{\varepsilon 1}, c_{\varepsilon 2}, c_{\varepsilon 3}, C_\mu$	Turbulent model constants
C_c	Area contraction coefficient
C_f	Residual gas correction factor for combustion model
C_{m1}, C_{m2}, C_{m3}	Combustion model constant
C_T	Liquid core length model constant
C_θ	Naber-Siebers model constant
d_p	Primary breakup diameter
D	Mass diffusivity
D_c	Diameter at the tip of the liquid core
D_{eff}	Diameter of the initial droplet
D_n	Nozzle hole diameter
D_t	Turbulent diffusion coefficient
E	Activation temperature
f	Droplet probability distribution function
f_t	Delay coefficient
\dot{f}_{bu}	Droplet breakup source term
\dot{f}_{coll}	Droplet collisions source term
\hat{F}	Drop acceleration
FI	Exponential index of fuel concentration
F^s	Momentum rate gained from spray per unit volume
\hat{g}	Specific body force vector
$(\Delta h_f^0)_m$	Formation heat of species m
H, H_0, H_{ln}	Hiroyasu model constants
I	Specific internal energy

I_l	Internal energy of liquid drops
$\hat{\mathbf{J}}$	Heat flux vector
k	Distortion parameter
k_1, k_2, k_3	CAB model constants
K_{bu}	Breakup regime parameter
l_n	Nozzle length
l_t	Turbulent length scale
L	Spray tip penetration
L_c	Liquid core length
$L_{c, grow}$	Liquid core length growth constant
$L(T_d)$	Latent heat of vaporization
$\bar{m}(t)$	Mean mass of the product drop distribution
Nu	Nusselt number
OI	Exponential index of oxygen concentrations
P	Fluid pressure
p_g	Ambient gas pressure
p_{vena}	Pressure in the vena-contracta of the injector nozzle
p_v	Vapor pressure
Pr	Prandtl number
Pr_κ, Pr_ϵ	Turbulent model constants
q_w	Wall heat flux
\dot{Q}^c	Chemical heat release source term
Q_d	Heat conduction rate to the drop
\dot{Q}^s	Spray interaction source term
r	Droplet radii
r_n	Inlet radius in the nozzle hole
r_u	Flame radius
R'	Local residual mass fraction
R_a, R_b	Parameters in local residual mass fraction
Re	Reynolds number
\bar{S}_{ij}	Mean strain tensor
Sc	Schmidt number
Sh	Sherwood number

S_n	Stretched flame speed
S_s	Unstretched flame speed
t	Time
Δt	Numerical time step
t_{bu}	Breakup time
T	Gas temperature
Ta	Taylor parameter
T_d	Drop temperature
T_w	Cylinder wall temperature
\hat{u}	Fluid velocity vector
\hat{u}'	Turbulence velocity
u^*	Friction velocity
u_l	Laminar flame speed
$u_{l,R}$	Laminar burning velocity with dilution correction
u_{rel}	Axial component of the relative speed between the liquid core and surrounding gas
U	Gas velocity at the liquid surface
U_{eff}	Effective velocities of droplets at the nozzle exit
U_{vena}	Velocity in the vena-contracta of the injector nozzle
w	Relative velocity between the spray and gas
W	Molecular weight
We	Weber number
\hat{x}	Droplet position
\dot{y}	Distortion velocity
\ddot{y}	Oscillation velocity
y^+	Dimensionless distance to wall
Y_1	Mass fraction of fuel in the calculating cell
Y_1^*	Mass fraction of fuel on the liquid surface
Y_m	Mass fraction of species m
Y_m^*	Local and instantaneous mass fraction of species m
Z	Ohnesorge number

List of Greek Notations

β_{NO}	NOx model constant
δ	Dirac delta function
ε	Dissipation rate of turbulence kinetic energy
ϕ	Equivalence ratio
η, η_0	Turbulent model constants; ratio of turbulent to mean-strain time scale
k	Turbulence kinetic energy
μ	Liquid viscosity
μ_{air}	Dynamic viscosity of air
μ_t	Turbulent kinematic viscosity
ω_c	Angular velocity
ψ	Thermal diffusivity
θ	Spray cone angle
ρ	Total mass density
ρ_b	Unburned gas density
ρ_m	Mass density of species m
$\dot{\rho}_m^c$	Chemical reaction source term
$\dot{\rho}^s$	Spray evaporation source term
ρ_u	Burned gas density
σ	Liquid surface tension
$\underline{\underline{\sigma}}$	Viscous stress tensor
τ_c	Characteristic time for conversion
τ_l	Laminar-kinetics time
τ_t	Turbulent-mixing time
τ_d	Time from spark to fully turbulent combustion model
ζ	Parameter in turbulent mixing time

List of Subscripts

<i>0</i>	All species exclusive of fuel vapor
<i>1</i>	Stagnation point of nozzle flow; fuel vapor
<i>2</i>	Nozzle exit
<i>bu</i>	Breakup
<i>c</i>	Liquid core
<i>coll</i>	Collision
<i>eff</i>	Effective
<i>g</i>	Gaseous phase
<i>i</i>	Species index
<i>l</i>	Liquid; laminar
<i>n</i>	Nozzle
<i>t</i>	Turbulence
<i>vena</i>	Vena-contracta
<i>w</i>	Cylinder wall

Dedicated to My Parents,
Guohua Li and Baohua Yang

Acknowledgements

Firstly, I would like to express sincere thanks and gratitude to my supervisor Professor Hongming Xu for his guidance and support during the course of this study. I give my deepest thanks to my industrial supervisor Dr Li Cao for his genuine and insightful consulting throughout this research. Also I am grateful to associate supervisor Professor Miroslaw Lech Wyszynski, for his helpful advice.

Additionally, I show my great appreciation to Dr Xiao Ma and Dr Guohong Tian for a wealth of advice and help they have given to me both in research and life.

I am also grateful to Dr Li Xia Wei, Dr Marcin Frackowiak, Professor Akbar Ghafourian, Professor Shijin Shuai, Professor Shaohua Zhong and Dr Asish Sarangi for their valuable suggestions and guidance. Thanks for the technical support by Peter Thornton, Carl Hingley and Lee Guntlett.

Special thanks to my friends and colleagues, Dr Jun Zhang, Dr Yanfei Li, Dr Xuesong Wu, Dr Ritchie Daniel, Dr Nik Rosli Abdullah, Mr Fan Zhang, Mr He Ma, Mr Changzhao Jiang, Mr Chongming Wang, Mr Dai Liu, Mr Po-Wen Tu, Mr Cheng Tan, Mr Jianyi Tian, Mr Daliang Jing and Mr Haichun Ding, for their help and friendship.

TABLE OF CONTENT

ABSTRACT	I
LIST OF ABBREVIATIONS	III
LIST OF LATIN NOTATIONS	V
LIST OF GREEK NOTATIONS.....	VIII
LIST OF SUBSCRIPTS	IX
ACKNOWLEDGEMENTS.....	XI
LIST OF FIGURES	XVII
LIST OF TABLES	XXIV
LIST OF PUBLICATIONS.....	XXV
CHAPTER 1 INTRODUCTION	1
1.1 BACKGROUND	1
1.2 BIOFUELS.....	2
1.2.1 First Generation of Biofuels.....	5
1.2.2 Second Generation of Biofuels.....	6
1.3 2,5-DIMETHYLFURAN(DMF).....	7
1.3.1 Development in DMF Production.....	7
1.3.2 Fuel Properties of DMF.....	10
1.4 CURRENT DEVELOPMENTS AND CHALLENGES FOR THE GDI ENGINE.....	12
1.5 OBJECTIVES	14
1.6 THESIS OUTLINE	15
CHAPTER 2 LITERATURE REVIEW	17

2.1	INTRODUCTION	17
2.2	MODELLING FOR A GDI ENGINE.....	18
2.2.1	Turbulence Modelling	18
2.2.2	Spray Modelling.....	20
2.2.3	Combustion Modelling	36
2.3	OPTICAL TECHNIQUES FOR SPRAY AND COMBUSTION CHARACTERIZATION.....	38
2.4	DEVELOPMENTS IN THE STUDY OF DMF FUEL CHARACTERISTICS	42
2.5	SUMMARY.....	42
CHAPTER 3 NUMERICAL MODELS OF ENGINE SIMULATION..		43
3.1	INTRODUCTION	43
3.2	BASIC CONSERVATION EQUATIONS	43
3.3	TURBULENCE MODEL	46
3.4	HEAT TRANSFER MODEL.....	48
3.5	FUEL SPRAY AND EVAPORATION MODEL	49
3.5.1	Fuel Spray Model.....	49
3.5.2	Drop Evaporation Model	57
3.6	COMBUSTION MODEL FOR SI ENGINES	59
3.6.1	Characteristic Time Combustion (CTC) Model	59
3.6.2	NO _x Model.....	63
3.7	SUMMARY.....	64
CHAPTER 4 SPRAY MODEL VALIDATION AND DMF SPRAY		
CHARACTERISTICS STUDY IN A BOMB.....		66
4.1	INTRODUCTION	66
4.2	EXPERIMENTAL SET-UP AND DATA ANALYSIS.....	67

4.2.1	PDPA Test.....	67
4.2.2	Shadowgraph Test in the Vessel.....	71
4.3	SIMULATION BUILD- UP AND MODEL VALIDATION.....	75
4.3.1	Primary Breakup Model.....	75
4.3.2	Secondary Breakup Model.....	81
4.4	STUDY OF THE DMF SPRAY CHARACTERISTICS.....	90
4.4.1	Effect of Fuel Properties.....	90
4.4.2	Effects of Injection Pressure.....	96
4.4.3	Effects of Ambient Pressure.....	98
4.5	SUMMARY.....	102
CHAPTER 5 SPRAY MODEL VALIDATION IN A SINGLE		
CYLINDER ENGINE.....		104
5.1	INTRODUCTION.....	104
5.2	EXPERIMENTAL SET-UP.....	104
5.3	MODEL VALIDATION.....	105
5.3.1	Numerical 1-D Single Cylinder Engine Model.....	107
5.3.2	Validation with HSP Images from an Optical Engine.....	110
5.4	SUMMARY.....	121
CHAPTER 6 ANALYSIS OF MIXTURE PREPARATION IN A		
STOICHIOMETRIC DIRECT INJECTION DMF ENGINE.....		123
6.1	INTRODUCTION.....	123
6.2	SIMULATION BUILD UP.....	123
6.3	IN-CYLINDER CHARGE MIXING PROCESS.....	125
6.3.1	In-Cylinder Gas Motion.....	125

6.3.2	Effects of Fuel Properties on the Mixing Process	132
6.4	EVALUATION OF MIXING QUALITY.....	144
6.4.1	Effect of Injection Timing	144
6.4.2	Effect of Engine Speed.....	156
6.5	SUMMARY	165
CHAPTER 7 ANALYSIS OF SI COMBUSTION IN A		
STOICHIOMETRIC DI DMF ENGINE WITH CTC MODEL 167		
7.1	INTRODUCTION	167
7.2	EXPERIMENTAL SET-UP AND DATA ANALYSIS.....	167
7.2.1	Experimental Setup	167
7.2.2	Data Processing	169
7.3	LAMINAR COMBUSTION MODEL VALIDATION	172
7.3.1	Numerical Mean Stretched Flame Speed	173
7.3.2	Effect of Laminar Combustion Model Parameters	174
7.4	TURBULENT COMBUSTION MODEL VALIDATION IN PREMIXED CHARGE SPARK IGNITION COMBUSTION	180
7.4.1	Effect of Turbulent Combustion Model Parameters	180
7.5	CTC MODEL VALIDATION IN DIRECT INJECTION SPARK IGNITION COMBUSTION	187
7.5.1	Validation with HSP data.....	188
7.5.2	Comparisons of DMF and Gasoline on the DISI Combustion and Engine Performance.....	191
7.6	SUMMARY.....	198
CHAPTER 8 CONCLUSIONS AND FUTURE WORK 200		

8.1 CONCLUSIONS	200
8.2 RECOMMENDATIONS FOR FUTURE WORK	203
REFERENCES	205

List of Figures

Fig.1.1 World oil production from 1990 to 2035 [1]. (mb/d: million barrels per day)-----	1
Fig.1.2 Global energy use in the transport sector in 2050 [6].-----	3
Fig.1.3 GHG emissions by transportation fuel [9] -----	4
Fig.1.4 Contribution of biofuels to GHG emissions reduction in the transport sector [6]-----	5
Fig.1.5 GHG emissions from direct and ILUC for various energy crops. (35% -initial threshold in EU law; 50%--threshold in 2017) [14] -----	6
Fig.1.6 Predicted transition between first and second generation biofuels from 2005 to 2050 [12]. (Mtoe: million tons of oil equivalent) -----	7
Fig.1.7 Reaction path of 2,5-dimethylfuran converted from sugars [17].-----	8
Fig.1.8 An integrated scheme for producing the DMF from starch [19].-----	8
Fig.1.9 DMF manufacturing process flow chart [23].-----	9
Fig.2.1 Sketch of spray regimes adopted from [62]-----	21
Fig.2.2 Schematic of DDM method [62] -----	22
Fig.2.3 Comparison of three approaches for liquid phase treatment [70]-----	23
Fig.2.4 Blob-injection method of jet atomization [80] -----	24
Fig.2.5 Schematic diagrams showing nozzle flow regimes: a) turbulent flow; b) onset of cavitation; c) super cavitation; d) hydraulic flip; e) partly reattached flow [90] -----	26
Fig.2.6 Illustration of the MPI model (a-nozzle geometry schematic; b-boundary layer and cavitation region) [94]-----	27
Fig.2.7 Schematic of the nozzle flow model developed by Kuensberg [96] -----	28
Fig.2.8 Fitting method adopted by Chaves in the prediction of the spray cone angle [102]. -	30
Fig.2.9 Schematic of different styles of secondary breakup [109]-----	32

Fig.2.10 Schematic of collision regimes [121] -----	34
Fig.2.11 Sketch of the major regimes in the impingement modelling [137] -----	36
Fig.2.12 Schematic of the light path of the Schlieren system [156] -----	39
Fig.2.13 Illustration of light scattering incident on a particle [158] -----	41
Fig.3.1 Illustration of nozzle flow phenomena adopted from [96]-----	50
Fig.3.2 Sketch of MPI primary breakup model adopted from [94]-----	51
Fig.4.1 PDPA experimental schematic [163] -----	68
Fig.4.2 Measuring points on the spray (unit: mm) [163]-----	69
Fig.4.3 Gasoline injection vertical velocity and smoothed data (100 bar injection pressure) at 32 mm axial distance from the nozzle exit [163]-----	70
Fig.4.4 Schematic of the Shadowgraph system-----	72
Fig.4.5 Image processing of Shadowgraph-----	73
Fig.4.6 Determination of spray macroscopic characteristics -----	74
Fig.4.7 Comparison of MPI and original blob-injection CAB models on the penetration ----	76
Fig.4.8 Effect of H_0 on spray tip penetration at EOI with various injection pressures -----	77
Fig.4.9 Effect of H_{ln} on spray tip penetration at EOI under various ambient pressures (at an injection pressure of 50 bar)-----	78
Fig.4.10 Effect of $L_{c,grow}$ on spray tip penetration (at an injection pressure of 50 bar) -----	79
Fig.4.11 Effect of on the spray cone angle (at an injection pressure of 50 bar)-----	81
Fig.4.12 Effect of B_1 in the KH-MPI model on the temporal evolution of axial mean velocity and AMD at different distances away from the nozzle exit (a-32, b-50 and c- 70mm) -----	83
Fig.4.13 Effect of k_1 in the CAB-MPI model on the temporal evolution of axial mean velocity and AMD at different distances away from the nozzle exit -----	84

Fig.4.14 Temporal evolutions of axial mean velocity at various distances downstream from the nozzle exit -----	86
Fig.4.15 Temporal evolutions of AMD at different axial distances away from the nozzle exit -----	87
Fig.4.16 Comparisons of predicted and measured spray development-----	89
Fig.4.17 Comparison of DMF and gasoline on temporal evolution of axial mean velocity at various distances downstream from the nozzle exit -----	91
Fig.4.18 Comparison of DMF and gasoline on temporal evolution of AMD at various distances downstream from the nozzle exit. -----	92
Fig.4.19 Comparisons of DMF and gasoline on spray development -----	94
Fig.4.20 Comparisons of spray tip penetration at EOI and local SMD at the axial distance of 32 mm downstream from the nozzle exit under various injection pressures --	96
Fig.4.21 Spray tip penetration at EOI and spray cone angle under various ambient pressures -----	99
Fig.4.22 Temporal evolution of spray tip penetration under various ambient pressures -----	99
Fig.4.23 Comparison of spray development under various ambient pressures -----	100
Fig.5.1 Schematic of the optical engine [170] -----	105
Fig.5.2 Three-dimensional mesh in the simulation of the optical engine -----	106
Fig.5.3 Schematic of Wave model for the single cylinder optical engine -----	107
Fig.5.4 Comparison of in-cylinder experimental and simulation pressure trace in a motored condition -----	108
Fig.5.5 Cylinder pressure and temperature histories predicted by Wave for the modeling validation-----	109
Fig.5.6 Schematic of Spray Pattern in HSP Imaging-----	110

Fig.5.7 Side view of HSP images and CFD comparisons in an early injection event-----	111
Fig.5.8 Bottom view of HSP images and CFD comparisons in an early injection event-----	113
Fig.5.9 Side view of HSP images and CFD comparisons in a late injection event-----	116
Fig.5.10 Bottom view of HSP images and CFD comparisons in a late injection event-----	118
Fig.6.1 Schematic of spray pattern in the thermal engine-----	124
Fig.6.2 Calculated streamlines at 120° CA ATDC showing the Vortex and coherent structures -----	126
Fig.6.3 Intake flow vectors in the middle of the intake valves-----	127
Fig.6.4 Schematic of the tumble and swirl components-----	128
Fig.6.5 Swirl, tumble and cross tumble ratios in intake and compression strokes-----	128
Fig.6.6 Turbulence kinetic energy during the intake and compression strokes-----	131
Fig.6.7 Turbulent kinematic viscosity during the intake and compression strokes-----	131
Fig.6.8 Comparison of DMF and gasoline in the spray-gas interaction-----	133
Fig.6.9 Evolutions of mass fraction of the liquid fuel impinged on the wall-----	135
Fig.6.10 Comparison of DMF and gasoline in evaporation rate-----	136
Fig.6.11 History of the percentages of three ranges of the equivalence ratio-----	137
Fig.6.12 Calculated distribution of local equivalence ratio in the case of DMF-----	139
Fig.6.13 Calculated distribution of local equivalence ratio in the case of gasoline-----	140
Fig.6.14 Comparison of equivalence ratio distribution near the spark plug at 340 °CA ATDC. (a-DMF, b-gasoline)-----	141
Fig.6.15 Scatters of temperature against ER and ER distribution in the mass density fraction at 340°CA ATDC(a) DMF (Mean= 0.96, COV=0.67) (b) Gasoline (Mean=0.99, COV=0.29)-----	143
Fig.6.16 Effect of injection timing on in-cylinder charge temperature-----	145

Fig.6.17 The spray-gas interaction at 15°CA after SOI-----	147
Fig.6.18 Evolutions of mass fraction of the liquid fuel impinged on the wall for the cases at various injection timings.-----	149
Fig.6.19 Evolutions of fuel vaporization at various injection timings-----	150
Fig.6.20 Evolutions of the percentages of three ranges of the equivalence ratio at various injection timings -----	152
Fig.6.21 Spatial ER distribution at 340°CA ATDC of the early injection cases-----	152
Fig.6.22 Scatters of temperature against ER and ER distribution in the mass density fraction at 340°CA ATDC of the early injection cases-----	153
Fig.6.23 Spatial ER distribution at 340°CA ATDC of the early injection cases-----	154
Fig.6.24 Scatters of temperature against ER and ER distribution in the mass density fraction at 340°CA ATDC of the late injection cases -----	155
Fig.6.25 Evolution of tumble ratio and turbulence kinetic energy under various engine speeds -----	157
Fig.6.26 Comparisons of in-cylinder fuel and air flow under various engine speeds-----	159
Fig.6.27 Evolutions of mass fraction of the liquid fuel impinged on the wall under various engine speeds under various engine speeds-----	161
Fig.6.28 Evolution of fuel vaporization under various engine speeds-----	162
Fig.6.29 Evolution of the percentages of three ranges of the equivalence ratio under various engine speeds -----	163
Fig.6.30 Spatial ER distribution at 340°CA ATDC under various engine speeds-----	164
Fig.6.31 Scatters of temperature against ER and ER distribution in the mass density fraction at 340°CA ATDC under engine speeds of 3000 rpm and 6000 rpm -----	165
Fig.7.1 Schematic of the Schlieren system setup [167] -----	168

Fig.7.2 Illustration of the study range in the Schlieren image [167]-----	169
Fig.7.3 Charts of the calculation method of the laminar burning velocity-----	170
Fig.7.4 Laminar burning velocities of DMF and gasoline at different initial temperatures and equivalence ratios adopted from [167]-----	171
Fig.7.5 Illustration of flame front detection-----	173
Fig.7.6 Effect of E on mean stretched flame speed at different equivalence ratios -----	176
Fig.7.7 Effect of FI on mean stretched flame speed at different equivalence ratios -----	177
Fig.7.8 Effect of OI on mean stretched flame speed at different equivalence ratios -----	178
Fig.7.9 Comparisons of numerical temperature contours and Schlieren images of DMF at ϕ $=1.14$ and 75°C initial temperature-----	179
Fig.7.10 Effect of C_{m1} on the Mass Fraction Burned ($C_{m2}=0.06$) -----	182
Fig.7.11 Effect of C_{m2} on the Mass Fraction Burned ($C_{m1}=1.4$)-----	183
Fig.7.12 Effect of C_{m1} on the pressure trace ($C_{m2}=0.06$)-----	185
Fig.7.13 Effect of C_{m2} on the pressure trace ($C_{m1}=1.4$) -----	185
Fig.7.14 Comparisons of temporal evolutions of pressure and mass fraction burn predicted by the calibrated model and experimental results-----	186
Fig.7.15 Comparisons of numerical combustion process and HSP images in a DISI engine -----	189
Fig.7.16 Temporal evolution of the initial combustion duration (0-10% MFB) at $z=9.03\text{cm}$ -----	192
Fig.7.17 Temporal evolution of the initial combustion duration (10-50% MFB) at $z=9.03\text{cm}$ -----	193
Fig.7.18 Temporal evolution of the initial combustion duration (50-90% MFB) at $z=9.03\text{cm}$ -----	194

Fig.7.19 Comparisons of pressure and MFB profiles during the combustion process ----- 196

Fig.7.20 Comparisons of predicted NOx histories in the DMF and gasoline cases ----- 198

List of Tables

Table 1.1 European emissions regulations for passenger cars, g/km [2]-----	2
Table 1.2 Main fuel properties of DMF, gasoline and ethanol -----	11
Table 1.3 Strategies in a GDI engine-----	13
Table 3.1 Constants for the two κ - ε models-----	48
Table 5.1 Engine specifications and injection parameters -----	105
Table 6.1 Injection parameters -----	123
Table 6.2 Injection timings and charge cooling effect on engine performance -----	143
Table 6.3 Injection parameters under 3000 rpm and 6000 rpm -----	156
Table 7.1 Cases of the effects of C_{m1} and C_{m2} -----	180
Table 7.2 Comparisons of combustion characteristics and engine performance-----	196

List of Publications

SAE conference papers

1. **Haiying Li**, Li Cao, Xiao Ma, Po-Wen Tu, Hongming Xu, Shi-jin Shuai and Akbar Ghafourian, "Numerical Study of DMF and Gasoline Spray and Mixture Preparation in a GDI Engine," SAE Technical Paper 2013-01-1592, 2013.
2. Guohong Tian, **Haiying Li**, Hongming Xu, Yanfei Li and Satish Moham Raj, Spray Characteristics Study of DMF Using Phase Doppler Particle Analyser, SAE technical paper 2010-01-1505, 2010.

Journals

1. Guohong Tian, **Haiying Li**, Hongming Xu, Yanfei Li and Satish Mohan Raj, Spray Characteristics Study of DMF Using Phase Doppler Particle Analyzer. SAE International Journal of Passenger Cars - Mechanical Systems, 2010. 3(1): p. 948-958.
2. Guohong Tian, Ritchie Daniel, **Haiying Li**, Hongming Xu, Shijing Shuai, and Paul Richards. "Laminar Burning Velocities of 2, 5-Dimethylfuran Compared with Ethanol and Gasoline." *Energy & Fuels* 24, no. 7 (2010): 3898-3905.
3. Guohong Tian, Hongming Xu, Ritchie Daniel, **Haiying Li**, and Yanfei Li. "Spray Characteristics and Engine Adaptability of 2,5-Dimethylfuran." *Journal of Automotive Safety and Energy* 2 (2010): 010.
4. Lixia Wei, Laihui Tong, Jia Xu, Zhandong Wang, Hanfeng Jin, Mingfa Yao, Zunging Zheng, **Haiying Li** and Hongming Xu. Primary Combustion Intermediates in Low-pressure Premixed Laminar 2,5-Dimethylfuran/Oxygen/Argon Flames. *Combustion Science and Technology* (GCST-2013-0064). (submitted)

Papers to be submitted

1. **Haiying Li**, Li Cao, Xiao Ma, Po-Wen Tu, Hongming Xu and Shi-jin Shuai.
Multidimensional Modeling of Spray and Mixture Formation in a GDI Engine Fuelled with DMF.

Chapter 1 INTRODUCTION

1.1 Background

The demand for the Internal Combustion (IC) engine has exponentially increased within the 20th century due to its convenience and high energy efficiency. However, owing to the global large-scale exploitation of oil production, as a non-renewable resource, the fossil fuel industry encounters the issue of the depletion of crude oil. As presented in Fig.1.1, the International Energy Agency (IEA) predicts that world crude oil production at the existing fields began to drop after 2009 and the capacity will decrease to 25% by the end of 2035, although the new fields compensate for this decline. Therefore, the vehicle manufacturers have to solve the problems resulting from the increase in oil price stimulated by the oil depletion.

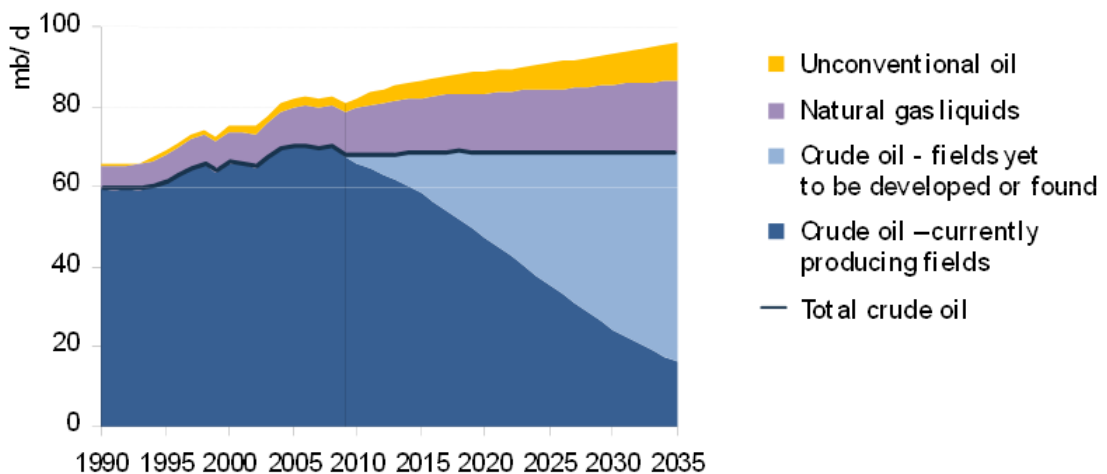


Fig.1.1 World oil production from 1990 to 2035 [1]. (mb/d: million barrels per day)

Meanwhile, vehicle industry is facing the challenge of increasingly stringent emissions standards which are prompted by the worsening air pollution and climate change. As listed in Table 1.1, European emissions regulations prescribe the acceptable limits for emissions, comprising nitrogen oxides (NO_x), total hydrocarbon (THC), non-methane hydrocarbons (NMHC), carbon monoxide (CO), particulate matter (PM) and number of particles (PN).

Table 1.1 European emissions regulations for passenger cars, g/km [2]

Tier	Date	CO	THC	NMHC	NO _x	HC+NO _x	PM	PN*
Euro 1	July 1992	2.72 (3.16)	-	-	-	0.97 (1.13)	-	-
Euro 2	January 1996	2.2	-	-	-	0.5	-	-
Euro 3	January 2000	2.3	0.20	-	0.15	-	-	-
Euro 4	January 2005	1.0	0.10	-	0.08	-	-	-
Euro 5	September 2009	1.0	0.10	0.068	0.06	-	0.005	-
Euro 6 (future)	September 2014	1.0	0.10	0.068	0.06	-	0.0045 ^[3]	6e11 ^[3]

* #/km

1.2 Biofuels

To alleviate the reliance on fossil fuel, alternative energy resources have become the primary strategy in both the national energy security and the development direction of vehicle manufacturers. Hydrogen Vehicles (HV), Electric Vehicles (EV) and biofuels are the optional choices applicable in the transportation sector. For the HV, high capital cost, low well-to-wheel efficiency and problems with compressed hydrogen storage still affect its application at present [4]; with respect to the EV, its current usage range is constrained by the high cost of batteries, problems with battery recharging and low energy storage; while biofuels have the

advantages of higher energy density, cheaper price and are friendly to current engine technology and distribution infrastructure. Therefore, this original resource which fuelled the first engines [5] is brought back to the fuel industry as a replacement for fossil fuels. Fig.1.2 illustrates the use of global energy in the transport sector in 2050, predicted by the IEA [6]. As presented, biofuels share will ultimately reach up to 27% of the total fuel consumed in transportation, which is over twice of the share of electricity and almost four times of that of hydrogen.

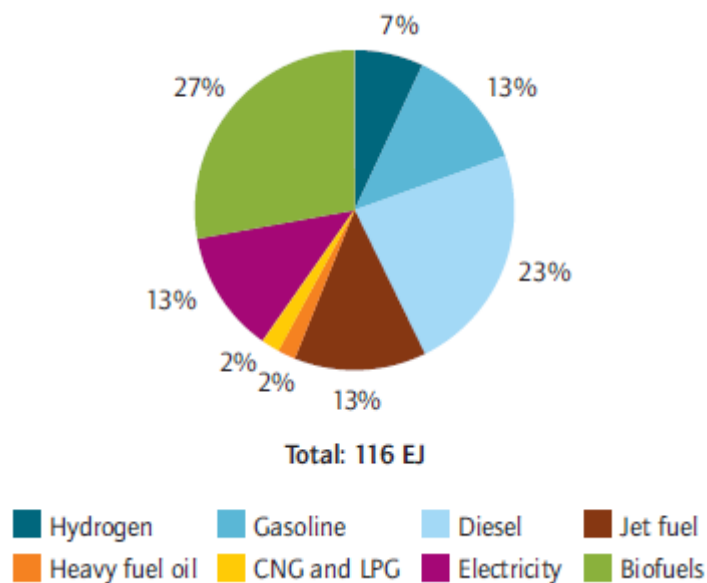


Fig.1.2 Global energy use in the transport sector in 2050 [6].

Additionally, biofuels derived from biomass are beneficial to the saving of the major greenhouse gas (GHG), carbon dioxide (CO₂). In 1996, M. Wang in the Argonne National Laboratory first discovered a methodology named as the Greenhouse gases, Regulated Emissions, and Energy use in Transportation (GREET) model [7], to assess the well-to-wheel life-cycle energy use and GHG emissions. By using the updated GREET model [8], GHG emissions for various kinds of ethanol were predicted and the comparisons against the

replaced gasoline are presented in Fig.1.3. As presented, all the types of ethanol reflect the capacity of CO₂ reduction; cellulosic ethanol achieves 86% reduction of CO₂ emissions, which is better than the other cases of corn ethanol and sugarcane ethanol. Moreover, in order to confine the global warming to below 2.4°C by 2050, the target of 50% CO₂ reduction was agreed by the G8 leaders at the Heiligendamm Summit 2007[10]. For this tough target, a BLUE Map scenario was proposed by the IEA in 2008 [11] as illustrated in Fig.1.4. Within the transportation sector, the use of biofuels contributes to 20% (2.1 gigatonne (Gt) CO₂-equivalent), which is comparable with the contribution from the technology improvements in vehicle efficiency (see Fig.1.4).

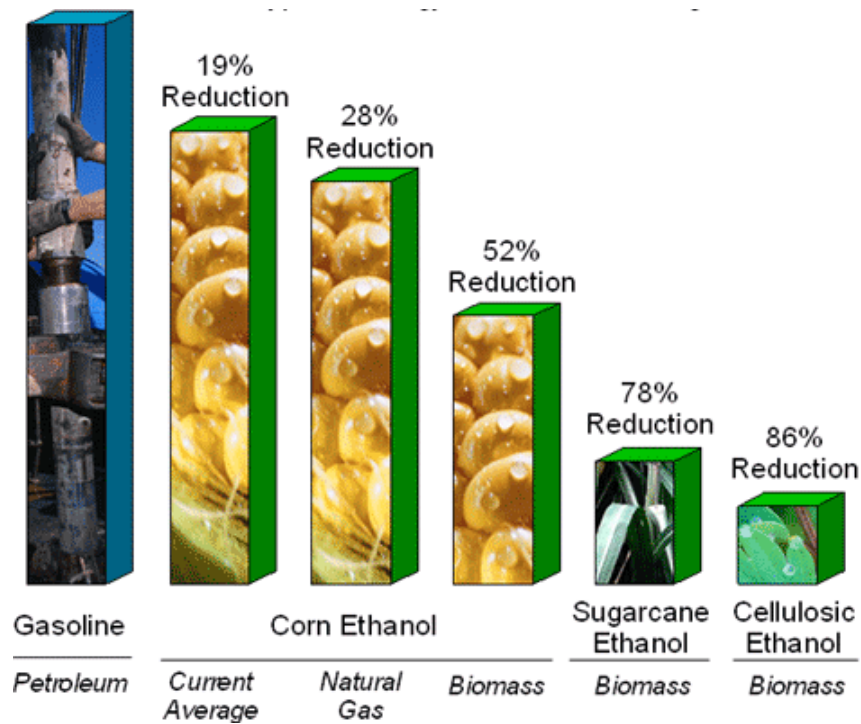


Fig.1.3 GHG emissions by transportation fuel [9]

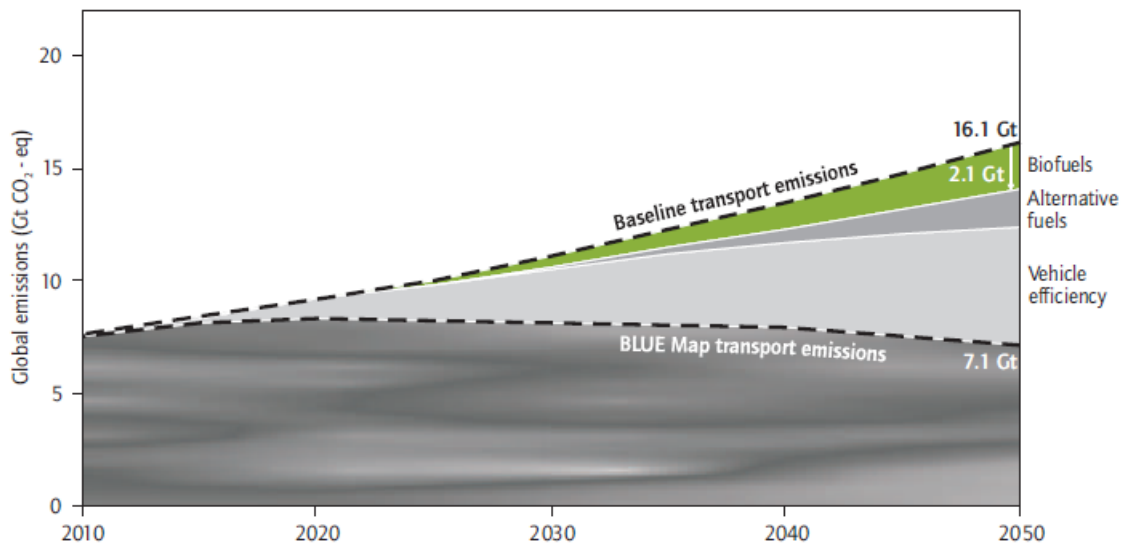


Fig.1.4 Contribution of biofuels to GHG emissions reduction in the transport sector [6]

1.2.1 First Generation of Biofuels

The first generation of biofuels are mainly produced from food crops such as grains, sugar beet and oil seeds [12]. Driven by cheaper prices and support from the policies, a rapid development of commercial markets for their use has taken place during the last decade. However, there are concerns about the sustainability of first generation biofuels' production, due to the direct competition for the natural resources used for food and fibre production [12]. Also the first generation biofuels are further considered as the contributors to the past increases in global prices of food and animal feeds [13].

Additionally, owing to shrinking amounts of land for growing food, the displacement of tropical forest for food production is in place, a phenomenon called Indirect Land-Use Change (ILUC) [14]. As presented in Fig.1.5, the effect of ILUC weakens the benefit of

biofuels on the CO₂ savings. These issues limit the further development of the first generation biofuels.

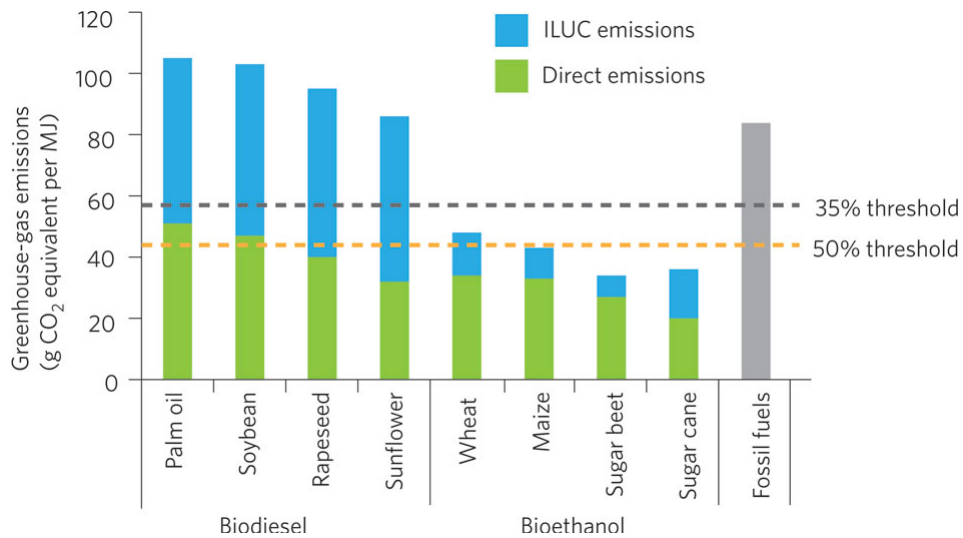


Fig.1.5 GHG emissions from direct and ILUC for various energy crops. (35% -initial threshold in EU law; 50%--threshold in 2017) [14]

1.2.2 Second Generation of Biofuels

To avoid the cumulative environmental and economic impacts, a world-wide interest has been stimulated in promoting second generation biofuels made from non-food biomass [12]. These materials belong to lignocellulosic feedstocks, including agricultural by-products (cereal straw, sugarcane bagasse), forest residues and energy crops [13]. Compared with the first generation biofuels, their high energy contents [12] and the utilization of infertile lands are the main advantages of second generation biofuels. Additionally, second generation biofuels are advantageous for the reduction of GHG emissions as illustrated in Fig.1.3. In order to meet the target of 50% reduction of CO₂ emissions by 2050, as presented in Fig.1.6, the production of the first generation biofuels will be surpassed by the second generation biofuels (Biomass-

To-Liquids (BTL) biodiesel, sugarcane and cellulosic ethanol) in 2020 and be completely replaced in 2050.

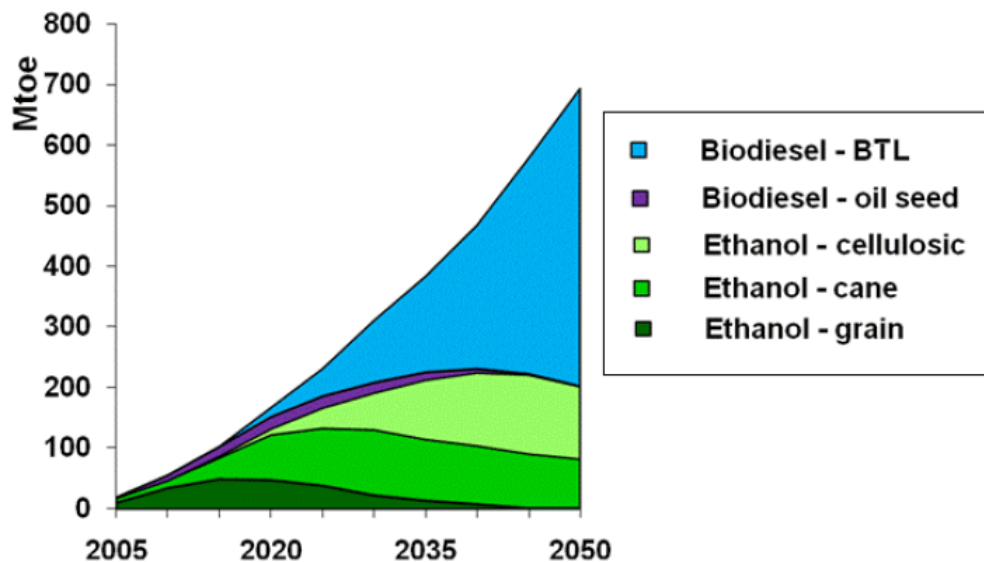


Fig.1.6 Predicted transition between first and second generation biofuels from 2005 to 2050 [12]. (Mtoe: million tons of oil equivalent)

1.3 2,5-Dimethylfuran(DMF)

1.3.1 Development in DMF Production

As reviewed in 1.2.2, lignocellulosic biomass is currently considered as an attractive feedstock for biofuels' production. However, it is a challenge for both researchers and biorefineries to discover how to efficiently produce a potential biofuel from the lignocellulosic resource.

Zhao et. al. [15] and Román-Leshkov et. al. [16] provided an encouraging answer. Both of them discovered catalytic conversion methods for the production of 5-hydroxymethylfurfural

(HMF) from a hexose (e.g. fructose) by dehydration [15-16] and the latter presented a pathway to convert from HMF to 2,5-dimethylfuran (DMF) by hydrogenation and hydrogenolysis (see Fig.1.7).

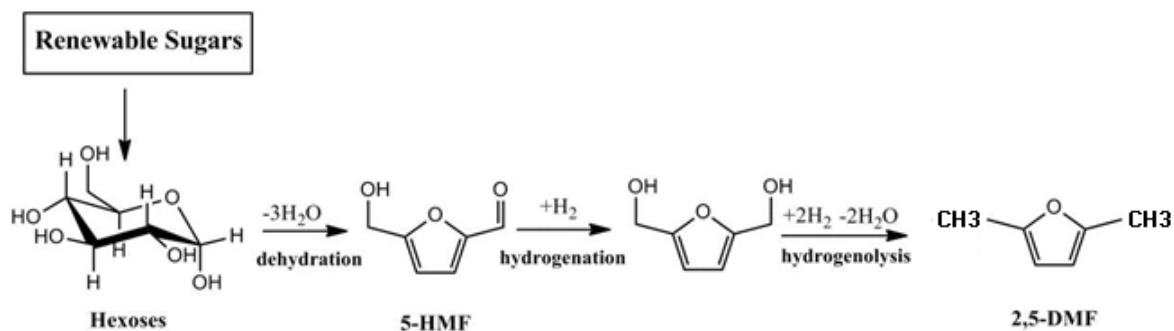


Fig.1.7 Reaction path of 2,5-dimethylfuran converted from sugars [17].

Furthermore, to enable a DMF yield from the lignocellulosic biomass, Binder et. al. [18] used enzymes to depolymerize starch and isomerize glucose to fructose as illustrated in Fig.1.8; researchers [19-20] also made great efforts to increase the conversion efficiency from fructose or glucose to DMF.

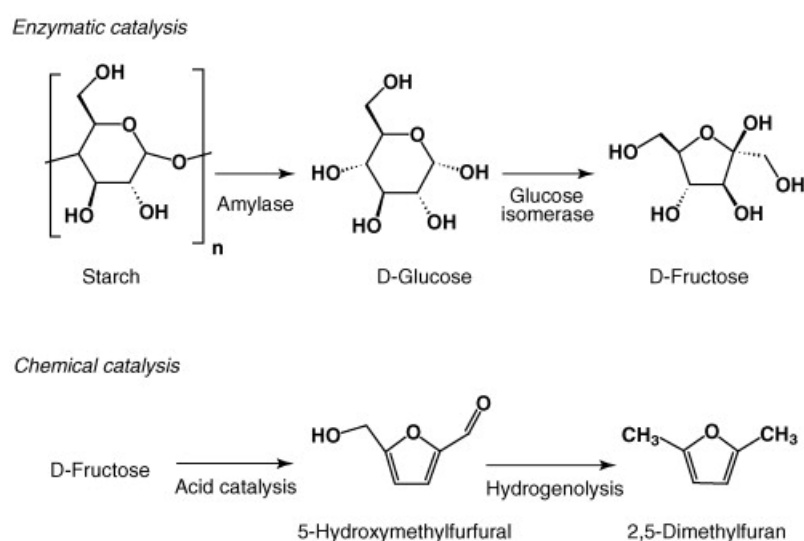


Fig.1.8 An integrated scheme for producing the DMF from starch [19].

In addition, based on the method described in [16, 22], Kazi et.al. [23] analyzed the feasibility on the industrial production of DMF from fructose in terms of economics and technology and a block diagram for DMF production process was also provided (see Fig.1.9).

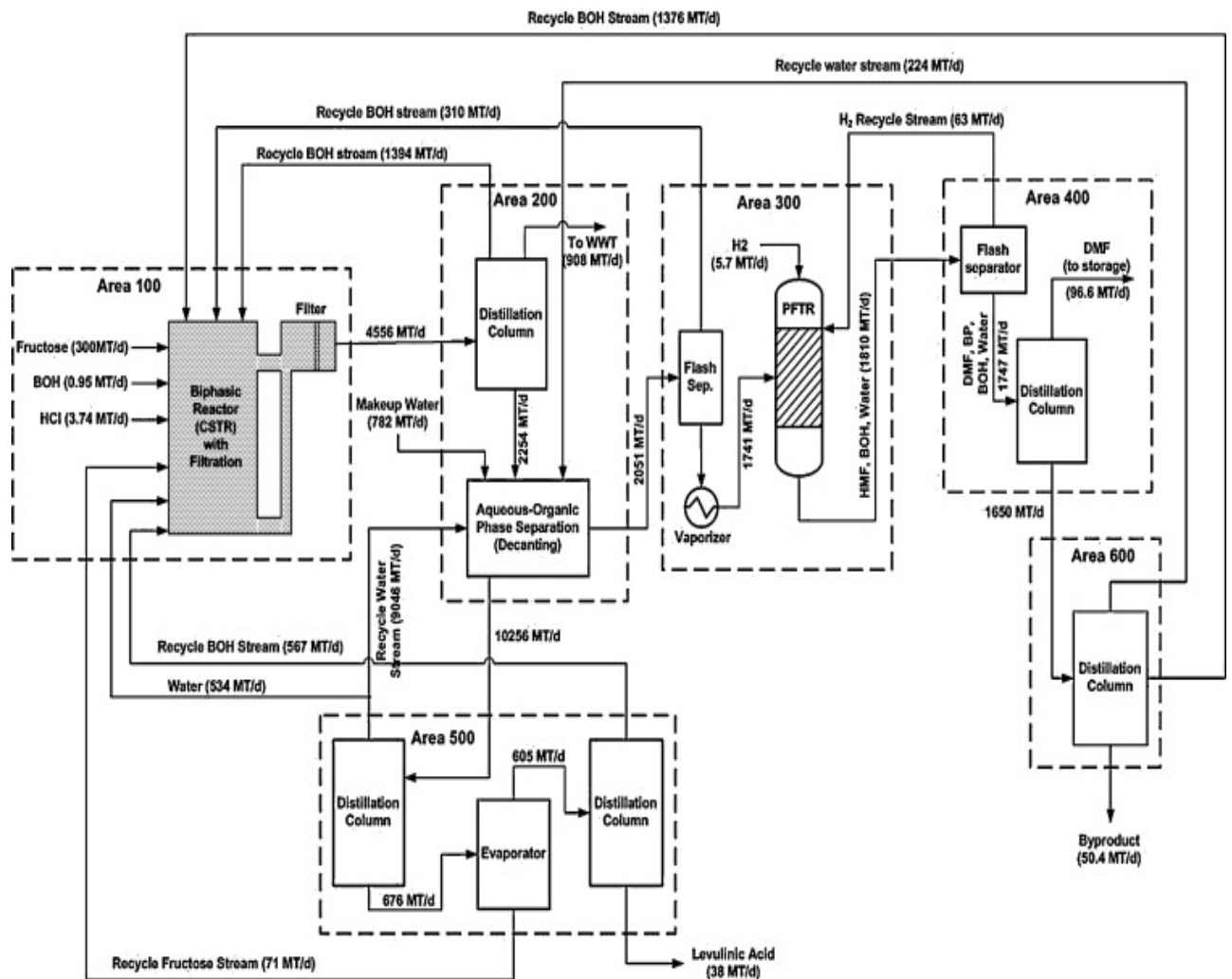


Fig.1.9 DMF manufacturing process flow chart [23].

1.3.2 Fuel Properties of DMF

The fuel properties of DMF are beneficial to its potential as a promising alternative to gasoline as listed in Table 1.2. Through comparing with gasoline and ethanol, its advantages can be summarized as follows:

- High energy content

DMF's volumetric Lower Heating Value (LHV) (comparable with gasoline) is almost 40% higher than ethanol which eliminates the issues of ethanol's limited cruise mileage.

- High octane number

As a fuel appropriate for Spark Ignition (SI) engines, DMF's research octane number is 101, higher than gasoline and a little lower than ethanol, which allows higher compression ratios and consequently, contributes to the improvement in fuel economy and engine performance.

- Low flash point and high auto-ignition temperature

DMF's lower flash point ($-1\text{ }^{\circ}\text{C}$) improves the performance of engine cold-start when fuelled with ethanol ($16.6\text{ }^{\circ}\text{C}$). Its high auto-ignition temperature reduces the chance of pre-ignition; additionally, the value of DMF's auto-ignition temperature ($285.85\text{ }^{\circ}\text{C}$) is more similar to gasoline ($280\text{ }^{\circ}\text{C}$) than ethanol ($363\text{ }^{\circ}\text{C}$), which reflects its similarity with gasoline on the ignition characteristics.

- Low viscosity

DMF has a closer viscosity with gasoline than ethanol, making it easily adoptable with the current injection system designed for gasoline.

- Good water insolubility

DMF's low water insolubility solves the difficulty of ethanol's storage.

Table 1.2 Main fuel properties of DMF, gasoline and ethanol

Name(s)	2,5-Dimethylfuran	Gasoline	Ethanol
Molecular Formula	C_6H_8O	C_2 to C_{14}	C_2H_6O
Molecular Mass	$96.1289 \text{ g mol}^{-1}$ [24]	$100-105 \text{ g mol}^{-1}$ [25]	$46.069 \text{ g mol}^{-1}$ [24]
Initial Boiling Point (1atm) ^[26]	92°C	32.8°C	78.37°C
Latent Heat of Vapor (300K)	372 kJ/kg [27]	316.6 kJ/kg [28]	1030 kJ/kg [28]
Liquid Density (20°C)	895.4 kg m^{-3} [24]	751 kg m^{-3}	789.37 kg m^{-3} [28]
Surface Tension(25°C)	0.02519 N/m [27]	0.01893 N/m [28]	0.02218 N/m [28]
Viscosity(1atm, 20°C)	0.65 cP [27]	$0.4-0.5 \text{ cP}$ [29]	1.145 cP [27]
Stoichiometric Air-Fuel Ratio	10.72	14.46	8.95
Lower Heating Value	32.89 MJ/kg [30]	42.9 MJ/kg [26]	26.9 MJ/kg [26]
Lower Heating Value ^[26]	29.3 MJ/L	31.9 MJ/L	21.3 MJ/L
RON/MON ^[31]	101.3/88.1	96.8/85.7	107/89
Reid Vapor Pressure (310.9 K)	13.4 kPa [32]	70.6 kPa	15.9 kPa [32]
Flash Point	-1°C [33]	-43°C [34]	16.6°C [34]
Auto-Igniton Temperature	285.85°C [33]	280°C [34]	363°C [34]

Water Solubility ^[32]	1.47 g/L	0 g/L	>1000 g/L
----------------------------------	----------	-------	-----------

However, great debates about the prospect of DMF applied into vehicles were concentrated on its toxicology in the neurotoxicity of hexane in humans [35]. Although DMF is hazardous, the risk levels for humans dealing with DMF are almost the same as those for dealing with gasoline [33].

1.4 Current Developments and Challenges for the GDI Engine

Driven by the consideration of GHG emissions' reduction, downsizing/downspeeding becomes one of the mainstream technologies in commercial engine production [36]. A high specific low end torque is the essential factor for the transient driving performance of downsizing. Compared to the Port Fuel Injection (PFI) system, this prerequisite can be realized by the Gasoline Direct Injection (GDI) system because of its enhanced accuracy of dynamic air/fuel ratio with the aid of the Variable Valve Actuation (VVA) and turbocharging techniques [37].

For the GDI engine, a Three-Way Catalyst (TWC) is effective to convert exhaust CO, HC and NO_x into CO₂, water and nitrogen near the stoichiometric point [38]. In this case, compared to a diesel engine, the PM emissions are usually negligible due to the homogeneous combustion in a GDI engine. However, a new emission target for particulate number (6e11particles/km) has been legislated in Euro 6. To meet this standard, minimization of the

particulate formation in the combustion chamber is the only solution without exhaust aftertreatment.

It is known that rich fuel-air ratio and high temperature (1500-2200K) [39] contribute to the particulate formation. Additionally, the main sources of particulate formation lie in wall-wetting such as spray impingement on the piston, cylinder wall and combustion chamber roof [40]. Therefore, effective organization of homogeneous fuel-air mixture and reduction of wall-wetting is crucial to the control of engine output emissions. The main strategies in a GDI engine are summarized in Table 1.3 in terms of air delivery, fuel delivery and combustion performance.

Table 1.3 Strategies in a GDI engine

Terms	Targets
Air Delivery	Sufficient fresh air
	Optimization of intake and exhaust valve overlap
	Residual gas fraction control
Fuel Delivery	Global air/fuel ratio control
	Enhanced spray atomization
	Spray pattern optimization
	Multiple injection strategy
	Minimize wall wetting
Combustion Performance	Charge motion optimization
	Sufficient air/fuel mixing
	Spark timing optimization

1.5 Objectives

The aim of this study is to investigate the spray and combustion characteristic of DMF in a GDI engine compared with gasoline in order to provide the support for the optimization of the injection strategy and injection system update. The objectives can be described as follows:

1. To study the spray behaviours and laminar combustion characteristics of DMF through optical diagnostic techniques in a constant volume vessel.
2. To develop a spray atomization model to reproduce DMF spray behaviours, involving the build-up of DMF fuel library, implementation of the primary breakup model and selection of the secondary breakup models.
3. To develop a combustion model for describing the combustion propagation and heat transfer process, including the validation of the laminar and turbulence combustion models.
4. To investigate the influence of fuel properties, injection timing and engine speed on the fuel-air mixing quality and spray impingement in a GDI engine with the validated spray model.
5. To study the differences of DMF and gasoline in the combustion characteristics and engine performance in a GDI engine using the validated combustion model.

1.6 Thesis Outline

The thesis is divided into eight chapters. A brief summary of each chapter is given below.

In Chapter 2, a review of literature relating to the numerical modelling of a GDI engine is presented, especially the spray and combustion simulation, providing the foundation for the model selection in Chapter 3. Next, optical diagnostic techniques and current progress in the DMF fuel studies are discussed.

Chapter 3 describes the details of the sub-models used or implemented in the thesis. The models include a turbulence model, a modified heat transfer model, a quasi-global reaction combustion model and an emission model for NO_x. The primary breakup model accounting for cavitation, three secondary breakup models and empirical models of liquid core length and spray cone angle are introduced as well.

In Chapter 4, after a description of the experimental setup and analysis of the data measured in an open air and in a constant volume vessel, the spray model is adjusted according to the experimental results. Then the comparison on the spray characteristics of DMF and gasoline is discussed under variable injection pressures and ambient pressures.

Chapter 5 begins with the engine specifications and mesh generated and then introduces briefly a 1-D engine simulation tool, providing the initial and boundary conditions for the 3-D simulation. Finally, the validation of the spray model in the GDI engine is presented.

The mixture preparation in a stoichiometric direct injection DMF engine is discussed in Chapter 6 by using the validated spray model. Following an introduction of the characteristics of in-cylinder gas motion in a Spark Ignition Direct Injection (SIDI) engine, effects of fuel properties, injection timing and engine speed on the mixing quality are discussed.

In Chapter 7, laminar flame characteristics of DMF are investigated using an optical technique, comparing with gasoline and ethanol. Based on the data from this test and the thermal engine performance, the combustion model constants are adjusted. Subsequently the validation of this combustion model using a high speed photographic technique is presented. Finally, by using this combustion model, analyses of combustion phase, heat release and pollutant emissions are investigated and compared with gasoline.

Chapter 8 contains the conclusions drawn by the results gained in Chapters 4 to 7 and recommendations for future work.

Chapter 2 LITERATURE REVIEW

2.1 Introduction

As described in section 1.4, to meet the demands of the forthcoming emission standards, downsizing technology is crucial to every GDI engine manufacturer. The core problems of this technology are the control strategies in terms of air delivery, fuel delivery and the combustion process. It is known that compressible transient flows (e.g. in-cylinder aerodynamics, spray, fuel-air mixing and combustion) exist in the scenario of a GDI engine. In particular, as the major in-cylinder flow—turbulence, its wide range of length scale and the randomised character of small-scale vortices are the main difficulties for analyzing of fuel-air mixing quality and combustion performance. To better understand the in-cylinder complicated physical phenomenon, Computational Fluid Dynamics (CFD) in conjunction with optical methods, has attracted increasingly popular attention in the vehicle industry.

In this chapter, the main developments in the modelling for GDI engines will be reviewed, including turbulence models, spray and combustion simulations, and also relevant optical techniques and current achievements in the area of DMF fuel research will be discussed.

2.2 Modelling for a GDI Engine

2.2.1 Turbulence Modelling

Turbulence is a flow characterized by diffusion, chaos, rotationality, dissipation and a high Reynolds number [41]. In a engine cylinder, turbulence diffusion rates of mass and momentum are several orders of magnitude larger than those of molecular diffusion [42], which is essential to the homogeneity of charge motion; the varieties of turbulence in spatial and temporal distributions are the main source of cycle-to-cycle variations in Spark Ignition (SI) engines, which contributes to 50 % of the flame growth rate fluctuations when the engine is run without fuel or residual gas fluctuations [43]. Therefore, it is a worthwhile effort for researchers to study the effects of turbulent flow in GDI engines.

In the CFD approach, the fundamental basis is the numerical solution of Navier-Stokes (N-S) equations with complex closure models to provide a valid description of the turbulent flow field. In particular, a variety of time and length scales for turbulent flows are the primary difficulties in its modelling.

Firstly, an approach named Reynolds Average Navier-Stokes (RANS) was proposed by Reynolds in 1895 [44], which provided an approximate time-averaged solution method to the N-S equations. However the nonlinear term of Reynolds stresses requires additional models to close the solution. To resolve this issue, a linear eddy viscosity theory was proposed by Boussinesq [45]. In this method, the Reynolds stresses were solved by an algebraic equation with the turbulent viscosity.

The subsequent zero-equation model (Cebeci-Smith model) [46], one-equation model (Prandtl's mixing length model) [47] and two-equation model (standard k- ϵ model) [48] are all derived from this method. The standard k- ϵ turbulence model is widely applied in IC engine research, because of its computational robustness and good accuracy for high Reynolds number turbulent flows, with combination of suitable boundary restrictions [49]. The dominant drawback of the standard k- ϵ model is the difficulty of simulating low Reynolds number flows, especially in the prediction of the near-wall turbulence characteristics, resulting from the assumption of isotropic flow [50]. To account for the small-scale flow, through applying a mathematical Re-Normalisation Group (RNG) method to the standard k- ϵ model, a new turbulent model namely RNG k- ϵ model was addressed by Yakhot et al [51]. In this approach, an additional term was introduced to the ϵ equation to account for the effect of mean strain rate, which was attributed to a better prediction of flow in the high shear stresses area such as separation and reattaching near the wall [52].

To incorporate the effects of the near-wall stress anisotropy, low Reynolds number or nonlinear eddy viscosity models such as k- ζ -f model [53-55] were proposed; however, the extremely fine mesh close to the wall limits its industrial usage. In addition, to reflect the directional effect of Reynolds stress fields, an approach named as Reynolds stresses model (RSM) was discovered by Launder to directly solve the transport equations of the Reynolds stresses [56]. This approach needs additional transport equations to calculate the Reynolds stresses and hence it is computationally expensive and less stable [57].

With the rapid increase of computer capacity, another approach named Larger Eddy Simulation (LES) arouses wide attention. Unlike the RANS models, this approach can solve

both large eddies and small eddies instead of the ensemble averaging turbulence field, by using a subgrid-scale model derived from the Kolmogorov's (1941) theory of self similarity [58]. Conventional LES models are dependent on fine grids to gain high accuracy. Rutland [59] reviewed the recent developments of LES models, especially in the decrease in CPU time and the improvements in low Reynolds number scenarios. Rutland pointed out that LES results are less model dependent and appropriate for cyclic variations and combustion instabilities [59]. A solution similar to LES was named as Direct Numerical Simulation (DNS) [60], where N-S equations were solved without any turbulence model; but the computational grids in DNS were necessary to contain all the scales of the turbulence field, which made it impracticable to simulate complex physical phenomenon in engines.

In summary, although LES has great potential in engine application, the RNG k- ϵ model balances the calculation accuracy and CPU cost and is the current most applicable choice in the spray and combustion modeling of a new fuel.

2.2.2 Spray Modelling

For GDI engines, the organization of fuel-air mixture is of great importance in the subsequent combustion process and emission formation. With the increasing concern of the environmental aspects, novel fuels and updated injection systems require deep understanding of spray characteristics. The accuracy of spray modelling directly influences the performance of spray strategies and injection system improvements. Thus, the significance of spray modelling is increasingly highlighted and an intensive development has been achieved in the last few decades.

However, sprays are characterized by a broad range of size and time scales; the interaction between sprays and the surrounding gas is a complex two-phase flow. These make spray numerical simulation a challenging task. An applicable method is to introduce sub-models to describe the sub-grid scale physical phenomenon related to the spray process. In the IC engine simulation, spray sub-models generally include atomization, drop drag and deformation, drop breakup and evaporation, drop collision/coalescence, and spray/wall interaction [61]. Developments in these sub-models will be discussed in the following content.

Firstly, it is necessary to describe the spray regimes. As presented in Fig.2.1, a dense region exists near the nozzle exit, where spray atomization, drop collisions and coalescence are the dominant forms of the two-phase dynamics. Far from the nozzle, a dilute region can be seen where spray drops become wide-spaced and their masses and volumes can be neglected compared to those of the surrounding gas. Between the two regions is an intermediate region, where the drop/gas interactions such as drop wake disturbances and deformation become significant [61]. Additionally, the whole atomization process can be classified into primary and secondary breakup as illustrated in Fig.2.1.

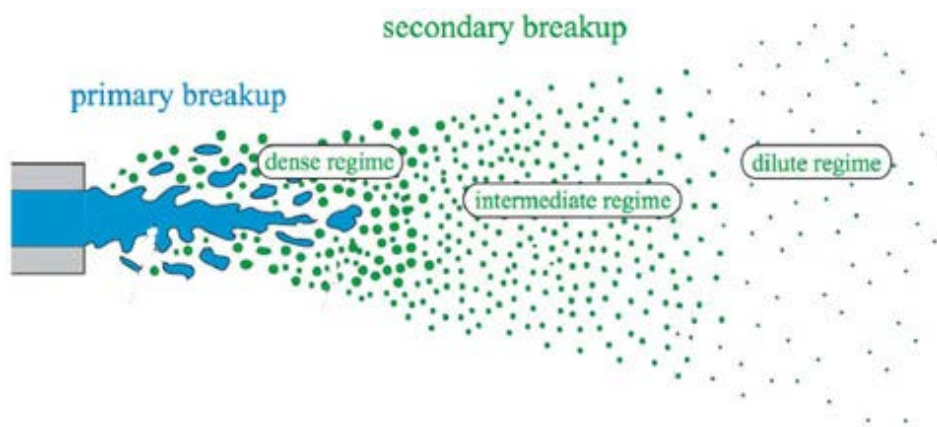


Fig 2.1 Sketch of spray regimes adopted from [62].

To describe the two-phase flow in the atomization process, the Volume of Fluid (VOF) method [63], Eulerian multi-fluid treatment [64] and Discrete Droplet Model (DDM) [65] Lagrangian method [66] are currently the three major approaches. Using the VOF method which is an interface tracking approach, an accurate evolution of the gas-liquid interfaces and the shapes and sizes of all the particles can be obtained, but very grids are required to track every interface, which limits its application in IC engines [67]. In the Eulerian multi-fluid approach, the liquid-gas phases are treated as continuous phases and are solved using the Eulerian description of an ensemble averaging method [68]. However, to fully capture the droplet size distribution, an enormous number of grids are necessary to denote each size group and thus this method becomes computationally expensive [69]. The Lagrangian method is a particle tracking approach, in which the gas phase is solved using an Eulerian scheme and the parcels of droplets are tracked in a Lagrangian framework [69]. By using the DDM, the coherent liquid core can be efficiently discretized into groups of equally sized droplets as illustrated in Fig.2.2 and the numerical diffusion in the liquid phase solution is greatly enhanced. Due to its simplicity and steadiness, it is widely used in current spray simulations. The three approaches compared against the experimental image are illustrated in Fig.2.3.



Fig.2.2 Schematic of DDM method [62]

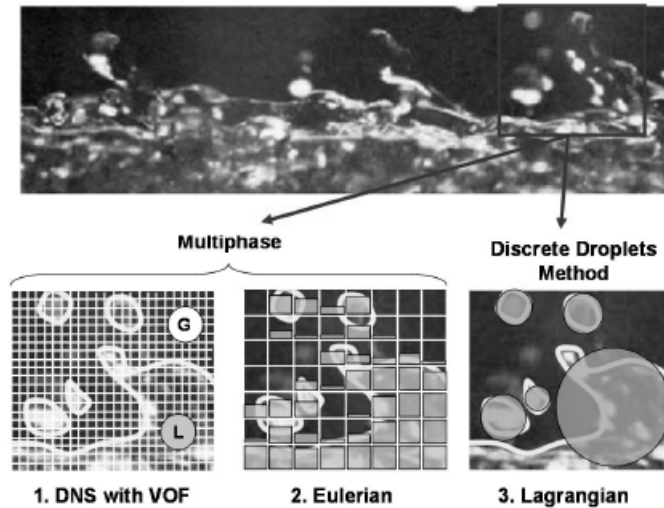


Fig.2.3 Comparison of three approaches for liquid phase treatment [70]

2.2.2.1 PRIMARY BREAKUP MODELS

To employ the DDM Lagrangian model, the initial conditions such as the drop size and velocity distributions at the nozzle exit are essential to the accuracy of spray simulation [67]. These conditions are provided by the primary breakup model. For high-speed atomizing sprays, the liquid column is disintegrated into drops and ligaments with the combination of inertia force, surface tension and aerodynamics shear [67, 71]. Gosman [71] summarized that the five major theories about the mechanism of the jet atomization included the disturbance of aerodynamic shear stresses (Kelvin-Helmholtz instabilities) [72], the inner liquid turbulence [73-76], the velocity profile relaxation [77], the bulk liquid oscillation [78] and the cavitation-induced disturbance [79]. Thus, spray atomization models were established by the single theory or hybrid theories as mentioned above.

Among the atomization models based on the hypothesis of the disturbance of the aerodynamic forces, the Kelvin-Helmholtz (KH) model [80] and the Taylor Analogy Breakup (TAB) model

[81] are widely used in research and industry. The former model, proposed by Reitz, was derived from the Kelvin-Helmholtz instabilities. This model assumed that the jet disintegration was caused by the surface disturbance growth [80]. While in the TAB model proposed by O'Rourke et al., it was assumed that jet atomization was considered as an analogy to the spring-mass system, which was determined by the comprehensive effects of aerodynamic forces, liquid surface tension and viscosity [81].

A concept of “blobs” injection was the basis of these models, which was introduced by Reitz and Diwakar [82]. For the blob-injection method, the intact liquid was represented by a train of spherical blobs with the same size of the nozzle hole diameter at the nozzle exit and the liquid was injected as large discrete parcels within the intact core region near the nozzle exit as presented in Fig.2.4. Additionally, it was assumed to be indistinguishable for the liquid jet atomization and the subsequent drop breakup process [67]. However, without consideration of effects of nozzle flow on the drop size distribution, the initial diameter of these blobs was under adjustment by reference to experimental data [71].

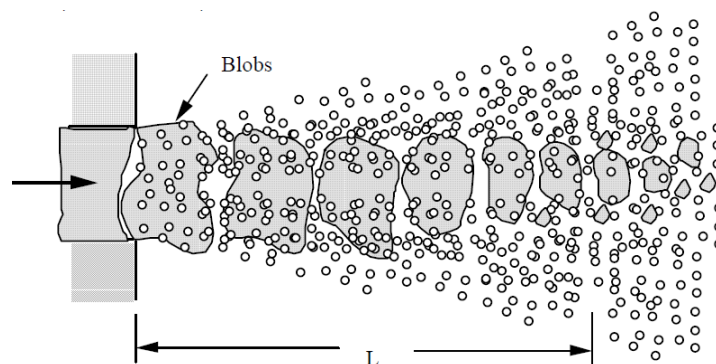


Fig.2.4 Blob-injection method of jet atomization [80]

Huh et al. [83] developed a phenomenological model to account for the influences of the nozzle-generated turbulence on the jet atomization on the basis of the KH model. The turbulence length and decay time scale were chosen to denote the turbulent flow field in the nozzle hole. They were assumed to be functions of the average turbulence kinetic energy and its dissipation rate at the nozzle exit [83]. However, as the core character of the nozzle flow, discharge coefficient was under correction and was greatly related to the characteristics of cavitating nozzle flow.

Cavitation in the nozzle is known as the formation and the implosion of vapor cavities, which are formed in the areas where the liquid static pressure is lower than the liquid vapor pressure, caused by the vena contracta. Researchers have made great efforts on the investigation of effects of cavitation in the nozzle flow and subsequent primary breakup experimentally and numerically.

In the experimental analysis of cavitation, Hiroyasu et al. studied the geometrical factors of the inlet nozzle orifice and the injection velocity on the characteristics of cavitating flow, and discovered the super-cavitation behaviour [84-85]. Kim [86] and Arcoumanis [87] reported the third origin of cavitation—the nozzle sac volume--using the transparent injector models. Dumouchel [88] reviewed the development of experimental investigations of cavitation in the nozzle flow and summarized the influence of cavitation on the liquid primary breakup as: increasing the effective velocity at the nozzle exit and promoting the turbulence intensity attributed by the vapor cavities bursting and collapsing. However, Dumouchel pointed out these effects varied from one investigation to another, due to the various nozzle internal designs and flow structures.

In the theoretical analysis of cavitation, a criterion named choking flow was proposed by Nuick [89] to identify the cavitation inception and the discharge coefficient was described as a function of the area contraction coefficient and cavitation number. Based on the experimental investigations and the choking flow theory, five regimes of cavitation in the nozzle flow were summarized by Kuensberg [90], including turbulent flow, onset of cavitation, super cavitation, hydraulic flip and partly reattached flow, as presented in Fig.2.5.

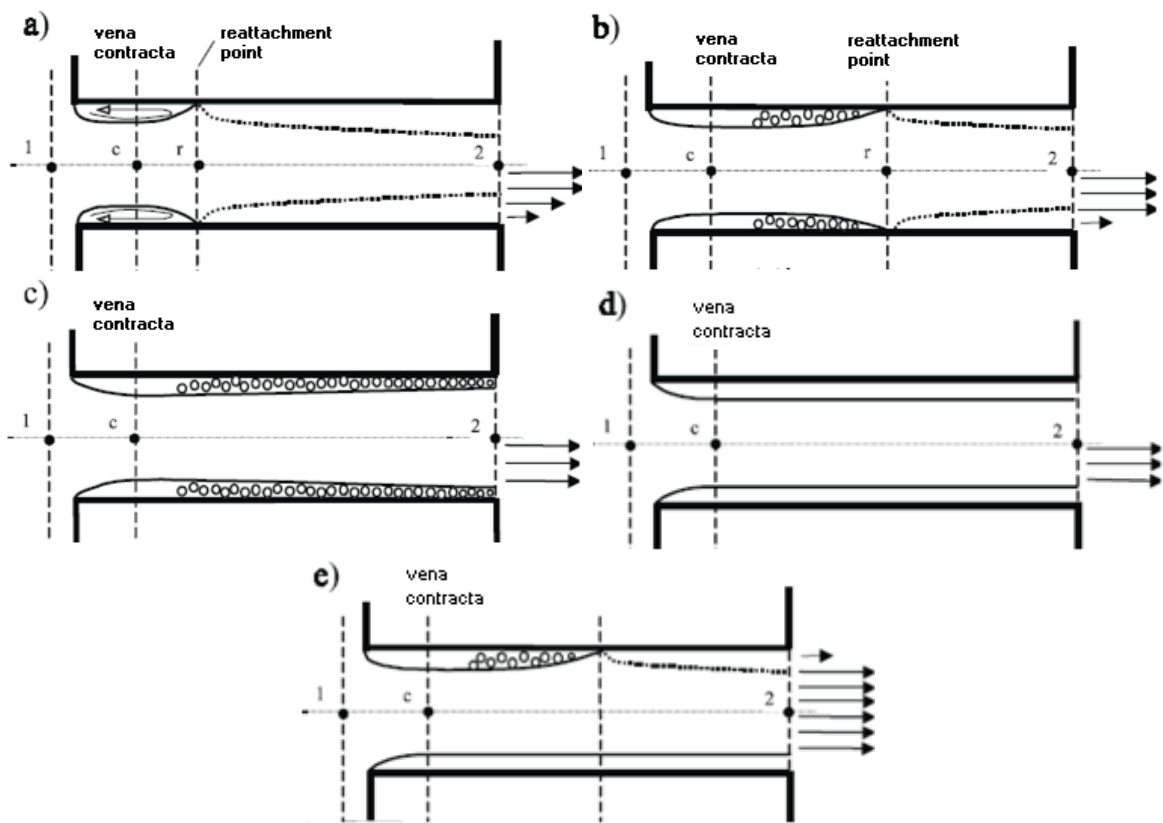


Fig.2.5 Schematic diagrams showing nozzle flow regimes: a) turbulent flow; b) onset of cavitation; c) super cavitation; d) hydraulic flip; e) partly reattached flow [90]

Obermeier and Chaves at the Max Planck Institute (MPI) [91-93] developed a cavitation model based on the boundary layer analysis. A separation/cavitation region was created in this

model as presented in Fig.2.6a. The region downstream from the position of x_0 was artificially separated into the turbulent boundary layer and cavitation region. According to the pressure in the cylinder p_{ch} and the length of the cavitation region, regimes characterized as non-cavitating, cavitating flow and cavitating flow with reattachment were discussed, respectively. However, the critical pressure and intermediate parameters were determined by the iterative calculation and the method was complicated as an ad-hoc manner.

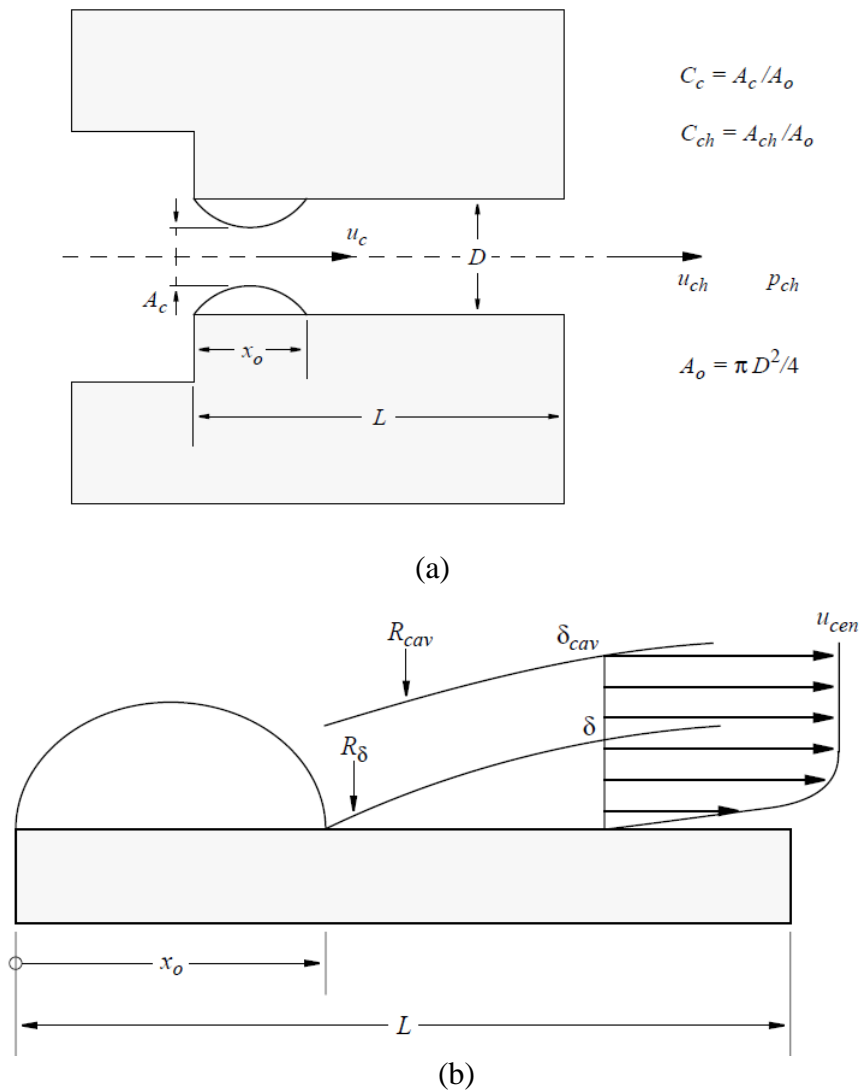


Fig.2.6 Illustration of the MPI model (a-nozzle geometry schematic; b-boundary layer and cavitation region) [94]

the vital link between the primary breakup and secondary breakup, respectively. Due to their importance, various models concerning these two parameters are proposed.

The model for the spray cone angle can be divided into two groups, turbulence based and aerodynamic-based approaches. The former approach was generally derived from the Huh [83] model and the spray cone angle was defined as a function of the atomization length scale, the breakup time scale and the effective velocity at the nozzle exit; its accuracy was greatly dependent on the nozzle flow simulation. The latter approach was based on the empirical equations and widely used in both research and engineering applications.

A well-known relation for the spray cone angle θ was given by Reitz and Bracco [101]:

$$\theta = 2 \tan^{-1} \left[\frac{4\pi}{A_n} \sqrt{\frac{\rho_g}{\rho_l}} f(Ta) \right] \quad (\text{Equation 2.1})$$

where ρ_g and ρ_l are the gas and liquid densities, respectively; A_n is a nozzle geometrical constant and is approximated by a function of the ratio of the nozzle length to the nozzle diameter; $f(Ta)$ is a Taylor function of Weber and Reynolds numbers, related to the gas density and the liquid viscosity [101]. For the high speed injection, $f(Ta)$ becomes asymptotically equal to $3^{0.5}/6$ [96] and hence the spray cone angle is underestimated [90]. Additionally, the spray cone angle is over-predicted by this relation in the low pressure injection cases [90]. To solve these issues, Chaves [102] adopted a linear segmentation fitting to the experimental data, as presented in Fig.2.8.

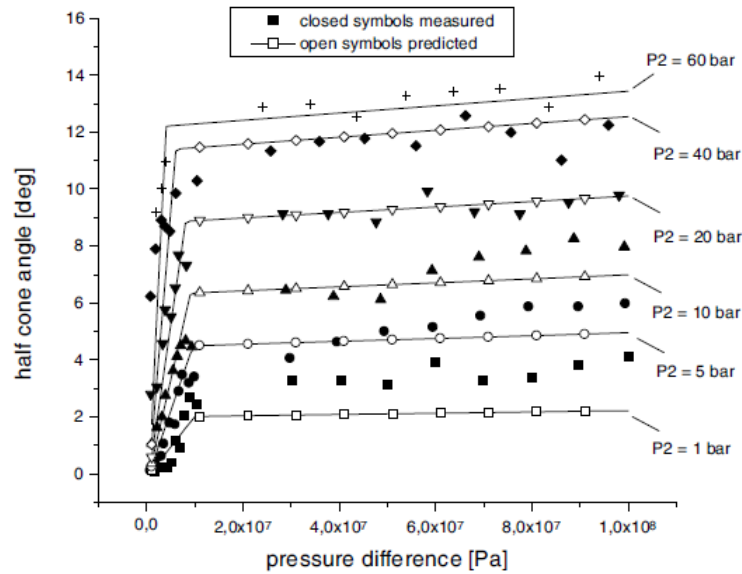


Fig.2.8 Fitting method adopted by Chaves in the prediction of the spray cone angle [102].

The effects on the spray cone angle such as the gas/liquid density ratio and the nozzle length/diameter ratio, as represented in this model above, frequently reappear in the other models. For instance, the Naber-Siebers model [103] was a power function of the gas/liquid density ratio with a different power exponent; the model proposed by Hiroyasu [104] was also a function of the gas/liquid density ratio, the nozzle length/diameter ratio and the ratio of the nozzle hole diameter to the sac chamber diameter; the Sovani model [105] was a linear combination of the atomized gas/liquid mass ratio, the injection pressure and the quartic polynomial of the gas density. These empirical models were calibrated based on the diesel injectors and hence, the Naber-Siebers model was more applicable to a GDI injector than the others, due to its simplicity and flexibility.

Similar with the spray cone angle, the classical relation for the liquid core length L_c was given by Taylor [106]:

$$L_c = C_T D_n \sqrt{\frac{\rho_l}{\rho_g}} \frac{1}{f(Ta)} \quad (\text{Equation 2.2})$$

where D_n is the nozzle hole diameter and C_T is the constant. As discussed previously, the term $1/f(Ta)$ is nearly constant in the high pressure injection conditions. Thus, determination of the value of C_T is a key issue: a value of 4.04 was recommended by Cheroudi and Bracco [107] for typical diesel injectors and in the modified MPI model, this constant was changed into 2.31 by Obermeier [92]; further, C_T was in a range of 1.73 to 6.35 as reviewed by Baumgarten [96]. This means some other effects should be considered, except for the liquid/gas density ratio. Through a series of visualization tests in the spray structure inside the injector, Hiroyasu and Arai [104] provided a more detailed relation to consider the influence of the ambient pressure, the nozzle length/diameter ratio and the nozzle inlet configuration.

2.2.2.2 SECONDARY BREAKUP MODELS

The drops detached from the continuous liquid jet undergo the secondary breakup process and are further disintegrated into even smaller drops. Ohnesorge number and Weber number (We) are widely used for the criteria of the secondary breakup mechanism. Ohnesorge number is a dimensionless number that relates the viscous forces to inertial and surface tension forces. For the general liquid, the Ohnesorge number is below one. Under this circumstance, according to the Weber number, three main mechanisms were proposed by Liu [108]: bag breakup ($6 \leq We < 80$), stripping breakup ($80 \leq We < 350$) and catastrophic breakup ($We > 350$), as presented in Fig.2.9.

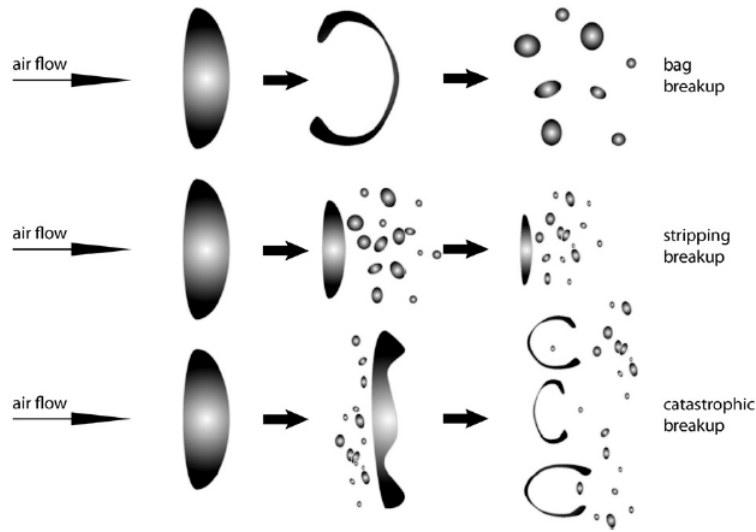


Fig.2.9 Schematic of different styles of secondary breakup [109]

Various models have been developed to describe the secondary breakup process. Except for the most commonly used TAB and KH models, there are several extra secondary models such as ETAB/CAB [110-111], DDB [112] and RT [113].

Based on the TAB model, an Enhanced TAB (ETAB) model was addressed by Tanner [110]. In the ETAB model, according to the specific breakup mechanism (bag or stripping breakup), the droplets experienced a cascade breakup by an exponential law until the product droplets reached a stable condition. Thus, the spectrum of droplet size was extended compared to the TAB model [114]. For a better prediction in the average velocity of the product droplets, the radial component of the product droplet was determined by the energy conservation. Further, the Cascade Atomization and drop Breakup (CAB) model was proposed by Tanner [111] for extending the applicable range to the catastrophic breakup mechanism. In addition, with the introduction of continuity between different regimes, the number of model constants reduced [111].

The Dynamic Drop Breakup (DDB) model was proposed by Ibrahim et. al. [112] and considered as a nonlinear formation of the TAB model. In the DDB model, the droplet breakup resulted from its excessive elliptic deformation. In contrast with the TAB model, the deformation was defined as the motion of the mass centre of the half-drop instead of the droplet equator [112]. However, the strong grid dependency of this model limited its application [115].

The Rayleigh-Taylor (RT) model was addressed by Su et al. [113] on the basis of the RT instability theory. The disintegration of the droplet was a catastrophic breakup due to the deceleration of the droplets caused by the aerodynamic force [116]. The KH-RT hybrid model [117-118] was a combination of the KH and RT models, where the KH model alone was used for the primary breakup simulation and the both models were used for the secondary breakup simulation. This model was widely used for diesel sprays.

2.2.2.3 OTHER SPRAY SUB-MODELS

Drop Drag and Deformation

Given by the relative velocity between the drop and surrounding gas, the drops are decelerated and distorted by the aerodynamic drag force [96]. Amsden et al. proposed a relation of the Reynolds number to calculate the drop drag coefficient, where the drop was assumed to be a rigid sphere [119]. According to the TAB model, the relation was corrected by Liu et al. [108] to consider the effects of the drop deformation from the spherical shape.

Drop Collisions and Coalescence

As previously mentioned, drop collisions and coalescence become dominant in the dense spray region. Three dimensionless parameters are introduced to describe the collision characteristics, including the drop Weber number, the impact number and the drop diameter ratio [120]. Based on the former two parameters, the outcomes of collisions were classified into five regimes: bouncing, coalescence, reflexive separation, stretching separation, and shattering [121].

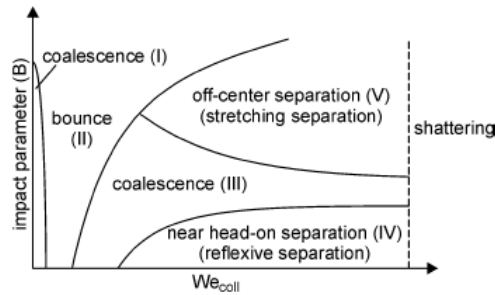


Fig.2.10 Schematic of collision regimes [121]

A famous stochastic collision model was proposed by O'Rourke [122], where the two regimes were regarded: coalescence or grazing collision (stretching separation) [123], according to the theory of the coalescence efficiency [124]. A considerable development in the collision models has been achieved recently. The models for extra collision regimes were proposed successively: reflexive separation model (Tennison et al. [125]), shattering collisions model (Georjon and Reitz [126]) and bouncing model (Estrade et al. [127]). To provide a practicable solution to cover different collision regimes, a composite collision model was developed by Post et al. [128]. The fragmentation from the colliding drops was taken into account via a separation volume coefficient addressed by Ko [129] and finally utilized in a model of

Munnannur [120] to account for all collision regimes. The grid dependency of the Munnannur model was reduced by Nishad using an approach namely Clover Leaf Artefact instead of the control volume method [130].

Drop Vaporization

As the link between the spray breakup and the mixture preparation, the drop vaporisation is crucial to the combustion and pollutant formation processes [96]. The basic drop vaporization model is a d^2 -law (the linear reduction of the square of the drop diameter with time) model [131], which is widely used because of its simplicity. However, in the standard d^2 -law model, the gas phase was supposed to be quasi-steady and there was no temperature variation on the drop surface [132]. Ramos reported the drop internal temperature was not uniform if the gas-to-liquid thermal capacity ratio was smaller than 0.3 [133]. To extend its applicability, the influences on the drop vaporization rate, especially the liquid phase heat transfer, were taken into account to various degrees. The temporal variation on the liquid surface was allowed in the rapid-mixing model [134]; the radial heat and mass transfer within the drop was considered in the effective diffusivity model proposed by Jin and Borman [135].

In addition, a multi-component model is given increasing attention by researchers. It can be divided into two styles: the Continuous Multi-Component (CMC) model and the Discrete Multi-Component (DMC) model. In the former method, the fuel composition is treated as a continuous distribution function according to a thermodynamic parameter and thus it is efficient in the vaporization simulation but not suitable for the combustion simulation coupled with chemistry; conversely, individual component tracking is the key characteristic of the

DMC method and hence the computational expense increases due to vast additional transport calculations [136].

Spray-Wall Impingement

The regimes for the impingement modelling are stick, rebound, spread and splash [137], as illustrated in Fig.2.11. The criteria for the phenomenon above varies from one model to another, mainly according to the drop Weber number and the impact number (a function of Ohnesorge and Reynolds number) [138]. The first impingement model was developed by Naber and Reitz [139] and influences of wall conditions were considered in the subsequent models: such as the roughness (Senda et al. [140]), the wetness (Bai and Gosman [141]) and the thickness of the wall (O'Rourke and Amsden [142]).

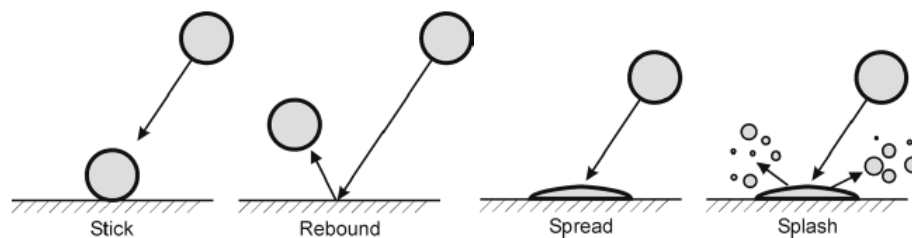


Fig.2.11 Sketch of the major regimes in the impingement modelling [137].

2.2.3 Combustion Modelling

In a GDI engine, the combustion process is characterized as premixed flame propagation, involving flame initiation, laminar burning and turbulent burning. The fuel consumption rate, as the essential parameter in the combustion, is influenced by the comprehensive interactions of molecular and turbulent diffusion and chemical kinetics [143].

Spalding [144] proposed the well-known Eddy Break Up (EBU) model to solve this problem. For the premixed combustion, the turbulent mixing time scale is some orders of magnitude larger than the chemical time scale and hence the model assumed that the combustion process was dominated by the turbulent mixing rate. Thus, in the EBU model, the mean chemical production rate was considered to be inversely proportional to the turbulent eddy turn over time [144].

However, the EBU model is theoretically only applicable to the turbulent combustion at a high-Reynolds number, and unsuitable for the processes which are controlled by the chemical kinetics such as high fuel-lean burn and low temperature combustion. To include the chemical kinetics-controlled processes, the Characteristic Time Combustion (CTC) model was proposed by Abraham et al. [145-146], derived from the EBU model. In the CTC model, the time when each species approaches its equilibrium is the sum of the chemical-kinetics time and the turbulent-mixing time, where the chemical-kinetics time is determined by an Arrhenius-formed equation. Because of its good balance between the computational expense and accuracy, this model is widely used in the prediction of the engine performance, especially the heat release and in-cylinder pressure.

Another group of combustion models are based on the geometric description of the turbulent flame—flamelet models. The premise of these models is that, a turbulent flame is a nonreacting turbulent flow surrounded with thin layers of reactive laminar flame [147]. Thus, the turbulence flow can be decoupled from the combustion process. As representatives among

these models, the Coherent Flame Model [148] and G-Equation model [149] are currently fluently used for combustion modelling coupled with chemistry.

Ignition, as the initial stage of the combustion process, is of importance on the combustion duration, phasing and cycle variation [150]. However, due to the very small domain of the ignition occurrence, a sub-grid scale model is chosen for the ignition modelling. An approach of time-dependent energy deposition in the specified ignition regions was adopted in KIVA-3 [151]. Fan et al. [152] proposed a discrete particle ignition kernel model to reduce the grid dependency, where the flame kernel was described in the framework of Lagrangian. Based on this model, an arc and kernel tracking ignition model [153] and a spark channel ignition monitoring model [154] were developed to account for effects of the flame kernel expansion and turbulent mixture fluctuations, respectively.

2.3 Optical Techniques for Spray and Combustion

Characterization

Optical diagnostics are frequently chosen for the investigation of spray and combustion characteristics. The commonly used techniques include direct imaging, Schlieren photography, Mie scattering, laser induced fluorescence (LIF), particle image velocimetry (PIV), phase Doppler particle analyser (PDPA), laser sheet drop-sizing (LSD) and laser absorption-scattering (LAS).

Direct imaging is the simplest one among these techniques and the most widely used technique to measure the macroscopic spray and combustion characteristics such as spray

structure, wall impingement and flame propagation. In detail, this technique is utilized by a photographic film or Charge-Coupled Device (CCD) camera to continuously record the events during the spray and combustion process. For different purposes, the major light sources of the direct imaging include a mercury vapor/xenon lamp, flashlight and laser sheet [155].

Schlieren photography is a visualization of the flow of liquid or gaseous fluid using the density gradient. As shown in Fig.2.12, the light source is collimated by a condenser lens and a knife-edge located at the focal point is used for the light cut-off. In IC engines, this technique is widely used in the research of the in-cylinder flow field, fuel-air mixing and flame structure, occasionally adopted to decouple the spray from the turbulent flow [156].

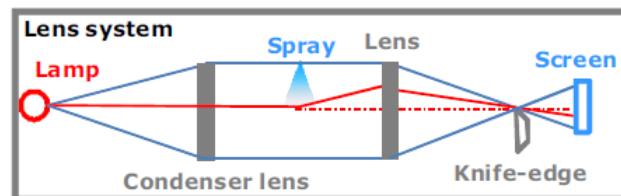


Fig. 2.12 Schematic of the light path of the Schlieren system [156]

Mie-scattering is an elastic scattering of light, when the particle size is bigger than the wavelength of the incident light. Two-dimensional Mie scattering is used for the detection of the envelope of the liquid phase.

LIF is utilized with the excitation by a laser beam. Two processes are included, the electronic absorption of a molecular and the red-shifted light emission from the molecular or atoms disassociated from the molecular. The signal intensity of LIF is proportional to the molecular

density and hence LIF is applied to measure concentration. Additionally, due to the remarkable difference between the signal intensities from the liquid and gaseous phase, LIF is capable of investigating the concentrations of the liquid and fuel vapor simultaneously. However, the quantitative LIF test is difficult to carry out due to the quenching effects at high pressures [157].

PIV is a spatially-resolved flow visualization technique which traces the motion of the seeding particles within a known time interval to visualize the transient full velocity field. The main difficulty is implementation: twin lasers have to be split in time and converged into a coincident plane. Two dimensional PIV is widely used for measuring the in-cylinder flow field and applicable to investigate the fuel spray flow. However, it is unsuitable for dense sprays due to the difficulty of implementation [157].

PDPA is a non-intrusive microscopic technique utilizing a laser Doppler effect to capture the information of individual particles. The PDPA system generally contains a laser-based optical transmitter, an optical receiver and a signal processor. Particle velocities and sizes are obtained by calculating the Doppler frequency difference between the illuminating beam and scattered beam and the phase shift between the first and second refracted beams (see fig.2.13) from different detectors within the receiver, respectively. Because of its highly spatial and temporal resolution, PDPA is advantageous for an accurate statistical analysis of the spray flow. However, this technique is unsuitable for high dense sprays, given that no more than one droplet is required in a probe volume [159].

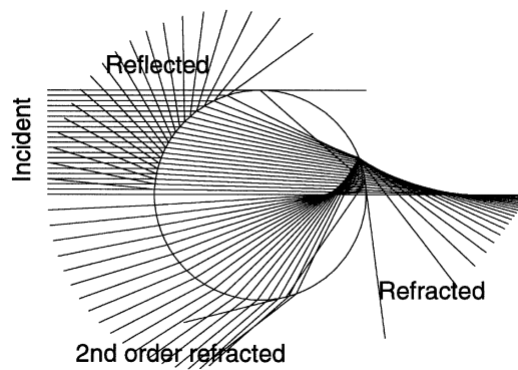


Fig.2.13 Illustration of light scattering incident on a particle [158]

LSD is a two-dimensional imaging technique that provides instantaneous or time-averaged Sauter Mean Diameter (SMD) of fuel sprays. This technique is utilized by the combination of LIF and Mie scattering. In detail, the LSD signal is the ratio of the LIF signal to the Mie scattering signal. Compared with the PDPA technique, this technique is advantageous to measure the dense spray characterization and is highly efficient for the qualitative analysis. However, these measuring results require calibration with known drop sizes [160].

The LAS technique is used for the quantitative analysis of the liquid and vapor fuel. Compared with the LIF technique, the temperature dependency reduces and the signal-to-noise ratio increases in this technique. However, due to that fact that the LAS measurement is on the basis of the light absorption and scattering of drops, it is difficult to avoid the overlap of the absorption wavelength for multi-component sprays [161].

2.4 Developments in the Study of DMF Fuel Characteristics

The author's group was the first to research DMF as an engine fuel [26, 162]. As to its spray characteristics, the spray behaviour of DMF was studied by a PDPA under various injection pressures [163] and will be discussed in Chapter 4. A concept of dual injection with DMF and gasoline in a GDI engine was also studied [164]. As to its combustion characteristics, the progress in the research related to the laminar burning velocity of DMF have been published [165-169]; flame behaviour of DMF in an optical engine was investigated by using high speed filming [170]; regulated emissions of DMF was measured and compared with gasoline and ethanol in a DISI engine [171].

2.5 Summary

In this chapter, a literature review of the CFD modelling in GDI engines has been carried out in terms of turbulent modelling, spray modelling and combustion modelling. In particular, the relevant spray sub-models are discussed, including primary breakup, secondary breakup, drop deformation, drop collisions and coalescence, drop vaporization and spray/wall impingement. Then the frequently used optical techniques for spray and combustion characterization are introduced, including Schlieren photography, Mie scattering, LIF, PIV, PDPA, LSD and LAS. Finally, the recent developments in the investigation of DMF characteristics have been reviewed.

Chapter 3 NUMERICAL MODELS OF ENGINE SIMULATION

3.1 Introduction

The computational programme applied in this research is the mature version of KIVA (KIVA3V release2 [172, 173]). This chapter presents the basic models in this numerical study. Firstly, the governing equations for mass, momentum and energy and the spray equation employed are discussed. Then the sub-models used or implemented to account for the turbulence, gas/wall heat transfer, fuel spray, fuel evaporation, SI combustion and NO_x emissions models are introduced.

3.2 Basic Conservation Equations

For a gas flow coupled with liquid droplets, the basic equations in the gas phase contain conservation equations of mass, momentum and energy with the consideration of the effect of turbulence. The spray-gas interaction is represented by using an exchange function. The following equations are used in the KIVA code [174, 123] and have been averaged by using mass-weighted (Favre) average.

In a multi-component gas mixture system, the mass conservation for species m is

$$\frac{\partial \rho_m}{\partial t} + \nabla \cdot (\rho_m \hat{u}) = \nabla \cdot \left[\rho D_t \left(\frac{\rho_m}{\rho} \right) \right] + \dot{\rho}_m^c + \dot{\rho}^s \delta_{m1} \quad (\text{Equation 3.1})$$

where t is time, ρ_m is the density for species m , ρ is the total density, \hat{u} is the velocity vector, ∇ is defined as $\nabla = \frac{\partial}{\partial x} \hat{i} + \frac{\partial}{\partial y} \hat{j} + \frac{\partial}{\partial z} \hat{k}$, D_t is the turbulent diffusion coefficient. $\dot{\rho}_m^c$

and $\dot{\rho}^s \delta_{m1}$ are the chemical reaction and spray vaporization source terms, respectively.

Subscript 1 denotes the fuel and δ is the Dirac delta function.

The momentum equation is

$$\frac{\partial \rho \hat{u}}{\partial t} + \nabla \cdot (\rho \hat{u} \hat{u}) = -\nabla p - \nabla \cdot \left(\frac{2}{3} \rho \kappa \right) + \nabla \cdot \overline{\overline{\sigma}} + F^s + \rho \cdot \hat{g} \quad (\text{Equation 3.2})$$

where p is the pressure, κ is the turbulence kinetic energy, $\overline{\overline{\sigma}}$ is the viscous stress tensor, F^s is the momentum rate per unit volume from the spray, and \hat{g} is the specific body force vector.

The internal energy conservation equation is

$$\frac{\partial \rho I}{\partial t} + \nabla \cdot (\rho \hat{u} I) = -p \nabla \cdot \hat{u} - \nabla \cdot \hat{J} + \rho \varepsilon + \dot{Q}^c + \dot{Q}^s \quad (\text{Equation 3.3})$$

where I is the specific internal energy except the chemical energy, \hat{J} is the heat flux vector and ε is the dissipation rate of turbulence kinetic energy. \dot{Q}^c and \dot{Q}^s are the chemical heat release and spray interaction source terms, respectively.

The KIVA3V code employs a spray equation formulation to account for the distribution of drop sizes, velocities \hat{v} and temperatures T_d in the liquid phase. In this formulation, a droplet probability distribution function f is given as

$$f(\hat{x}, \hat{v}, r, T_d, y, \dot{y}, t) \cdot d\hat{v}drdT_d dyd\dot{y}$$

is the probable number of droplets per unit volume at position \hat{x} and time t with a radius interval $(r, r + dr)$, temperature interval $(T_d, T_d + dT_d)$, velocity interval $(\hat{v}, \hat{v} + d\hat{v})$ and displacement intervals $(y, y + dy)$ and $(\dot{y}, \dot{y} + d\dot{y})$. The temporal evolution of f is solved by the following spray equation,

$$\frac{\partial f}{\partial t} + \nabla_x \cdot (f \cdot \hat{v}) + \nabla_v \cdot (f \cdot \hat{F}) + \frac{\partial}{\partial r} (f \cdot \dot{r}) + \frac{\partial}{\partial T_d} (f \cdot \dot{T}_d) + \frac{\partial}{\partial y} (f \cdot \dot{y}) + \frac{\partial}{\partial \dot{y}} (f \cdot \ddot{y}) = \dot{f}_{coll} + \dot{f}_{bu}$$

(Equation 3.4)

where \hat{F} is the acceleration of a drop, and T_d , \dot{r} , \dot{y} and \ddot{y} are the change rates of a drop temperature, radius, distortion and oscillation velocity, respectively. Furthermore, \dot{f}_{bu} and \dot{f}_{coll} are the droplet breakup and collisions source terms, respectively [81]. The spray equation above is based on a Lagrangian droplet evolution (i.e., one that travels with the

droplets) and “parcels” of droplets with identical characteristics are considered. This approach is used since it is not computationally feasible to track each spray droplet separately.

In this equation, the exchange functions $\dot{\rho}_s$, F^s and Q^s can be obtained for the use in Eqs. 3.1, 3.2 and 3.3. They are integrated by the change rate of mass, momentum, and energy of all droplets at time t and position \hat{x} .

$$\dot{\rho}_s = -\int f \rho_d 4\pi r^2 \cdot \dot{r} \cdot d\hat{v} dr dT_d dy d\dot{y} \quad (\text{Equation 3.5})$$

$$F^s = -\int f \rho_d \left(\frac{4}{3} \pi r^3 \hat{F}' + 4\pi r^2 \cdot \dot{r} \hat{v} \right) \cdot d\hat{v} dr dT_d dy d\dot{y} \quad (\text{Equation 3.6})$$

$$Q^s = -\int f \rho_d \left\{ 4\pi r^2 \cdot \dot{r} \left[I_l + \frac{1}{2} (\hat{v} - \hat{u})^2 \right] + \frac{4}{3} \pi r^3 \left[c_l \dot{T}_d + \hat{F}' \cdot (\hat{v} - \hat{u} - \hat{u}') \right] \right\} \cdot d\hat{v} dr dT_d dy d\dot{y} \quad (\text{Equation 3.7})$$

where $\hat{F}' = \hat{F} - \hat{g}$, \hat{u}' is the turbulence velocity, generally fluctuated with a variance of $\frac{2}{3} \kappa$.

Also, c_l and I_l are the droplet specific heat and internal energy, respectively. Through those exchange functions, the spray-gas interaction is then presented.

3.3 Turbulence Model

The turbulence model is used to incorporate the effects of small-scale turbulence. The so-called standard κ - ϵ model [48] is selected in the original KIVA3V code.

$$\frac{\partial \rho \kappa}{\partial t} + \nabla \cdot (\rho \hat{u} \kappa) = -\frac{2}{3} \rho \kappa \nabla \cdot \hat{u} + \overline{\overline{\sigma}} : \nabla \hat{u} + \nabla \cdot \left[\left(\frac{\mu}{Pr_\kappa} \right) \nabla \kappa \right] - \rho \varepsilon \quad (\text{Equation 3.8})$$

$$\frac{\partial \rho \varepsilon}{\partial t} + \nabla \cdot (\rho \hat{u} \varepsilon) = -\left(\frac{2}{3} c_{\varepsilon 1} - c_{\varepsilon 3} \right) \rho \varepsilon \nabla \cdot \hat{u} + \nabla \cdot \left[\left(\frac{\mu}{Pr_\varepsilon} \right) \nabla \varepsilon \right] + \frac{\varepsilon}{\kappa} \left[c_{\varepsilon 1} \overline{\overline{\sigma}} : \nabla \hat{u} - c_{\varepsilon 2} \rho \varepsilon \right] \quad (\text{Equation 3.9})$$

where Pr_κ , Pr_ε , $c_{\varepsilon 1}$, $c_{\varepsilon 2}$ and $c_{\varepsilon 3}$ are turbulent model constants and are presented in Table 3.1.

The current study utilizes the RNG κ - ε model [51] to account for the small-scale turbulent flows. Briefly, there is no change for the κ equation in the RNG κ - ε model, compared with the standard κ - ε model; however, instead of using an ‘‘ad-hoc’’ equation with empirical constants; the ε equation in the RNG model derived from rigorous mathematical theory [52] is given by,

$$\frac{\partial \rho \varepsilon}{\partial t} + \nabla \cdot (\rho \hat{u} \varepsilon) = -\left(\frac{2}{3} c_{\varepsilon 1} - c_{\varepsilon 3} \right) \rho \varepsilon \nabla \cdot \hat{u} + \nabla \cdot \left[\left(\frac{\mu}{Pr_\varepsilon} \right) \nabla \varepsilon \right] + \frac{\varepsilon}{\kappa} \left[c_{\varepsilon 1} \overline{\overline{\sigma}} : \nabla \hat{u} - c_{\varepsilon 2} \rho \varepsilon \right] - \rho R \quad (\text{Equation 3.10})$$

where the R is defined as:

$$R = \frac{c_\mu \eta^3 (1 - \eta / \eta_0)}{1 + \beta_1 \eta^3} \cdot \frac{\varepsilon^2}{\kappa} \quad (\text{Equation 3.11})$$

where $\eta = S \kappa / \varepsilon$, $S = \left(2 S_{ij} S_{ij} \right)^{1/2}$ is the magnitude of the mean strain $\overline{\overline{S}}_{ij} = \frac{1}{2} \left(\frac{\partial u_i}{\partial x_j} + \frac{\partial u_j}{\partial x_i} \right)$.

The following equation was added by Han [175], to account for the compressibility effects:

$$c_{\varepsilon 3} = \frac{-1 + 2c_{\varepsilon 1} - 3m_1(n_1 - 1) + (-1)^\delta \sqrt{6}c_\mu c_\eta \eta}{3} \quad (\text{Equation 3.12})$$

where $m_1 = 0.5, n_1 = 1.4$ for an ideal gas, $c_\eta = \frac{c_\mu \eta^3 (1 - \eta / \eta_0)}{1 + \beta \eta^3}$, and $\delta = 1$, if $\nabla \cdot \hat{u} < 0$; or otherwise, $\delta = 0$.

Table 3.1 Constants for the two κ - ε models.

	c_μ	$c_{\varepsilon 1}$	$c_{\varepsilon 2}$	$c_{\varepsilon 3}$	$1 / \text{Pr}_\kappa$	$1 / \text{Pr}_\varepsilon$	η_0	β_t
RNG κ - ε	0.0845	1.42	1.68	Eq.3.12	1.39	1.39	4.38	0.012
Std. κ - ε	0.09	1.44	1.92	-1.0	1.0	0.769		

By comparing the ε equation in the two models, it is shown that the RNG κ - ε model has one extra R term. According to Yahot and Orzag [52], this term accounts for non-isotropic turbulence. Papageorgakis and Assanis [176] applied this model to simulate the gas jet experiments. Their results indicated that the RNG-based model achieved a better agreement with experimental results than the standard κ - ε model.

3.4 Heat Transfer Model

A temperature wall function model developed by Han and Reitz [177], to account for the convective heat transfer between the gas and the wall, which is applicable to a relatively coarse mesh for the cells close to the cylinder wall with the same accuracy in the prediction of heat transfer. Within the boundary layer, the gas density becomes inhomogeneous and the

turbulent Prandtl number enhances. With the consideration of these effects, the wall heat flux is calculated by using a one-dimensional energy conservation equation, expressed as:

$$q_w = \frac{\rho c_p u^* T \ln(T/T_w)}{2.1 \ln(y^+) + 2.5} \quad (\text{Equation 3.13})$$

where q_w is wall heat flux, c_p is specific heat, T and T_w are gas temperature next to wall and cylinder wall temperature, respectively. u^* is friction velocity, y^+ is dimensionless distance to wall.

3.5 Fuel Spray and Evaporation Model

3.5.1 Fuel Spray Model

3.5.1.1 CAVITATION SUB-MODEL

An initial survey of different primary breakup models resulted in the selection of the Max Planck Institute (MPI) model [91-93], due to its strength on the prediction of the initial conditions such as the droplet size and velocity distributions at the nozzle exit. A schematic diagram of nozzle flow phenomena and occurrence of cavitation is presented in Fig.3.1. The effective velocities of droplets at the nozzle exit, U_{eff} , and the diameter of the initial droplet, D_{eff} , are determined by the following relations [90].

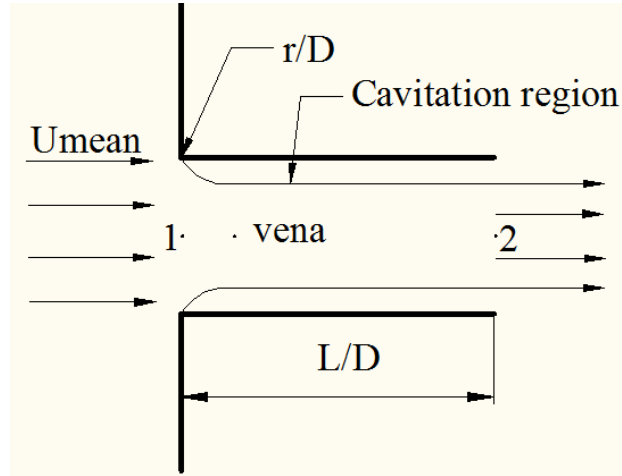


Fig.3.1 Illustration of nozzle flow phenomena adopted from [96]

$$U_{eff} = U_{vena} - \frac{P_2 - P_{vapor}}{\rho_l \cdot U_{mean}}, \quad D_{eff} = D \sqrt{\frac{U_{mean}}{U_{eff}}} \quad (\text{Equation 3.14})$$

U_{vena} is the velocity in the vena-contracta and is determined by:

$$U_{vena} = \frac{U_{mean}}{C_c} \quad (\text{Equation 3.15})$$

where C_c is the contraction coefficient related with nozzle geometrical configuration and specially, it equals to 0.62 for sharp-edged orifices given by Nurick [89].

The pressure in the vena-contracta is determined by

$$P_{vena} = p_1 - \frac{\rho_l}{2} U_{vena}^2 \quad (\text{Equation 3.16})$$

If the pressure in the vena-contracta is below the fuel vapor pressure, the initial conditions will be assigned for spray calculation in Eq.3.14.

3.5.1.2 MPI PRIMARY BREAK-UP MODEL

MPI model assumes that primary droplets are stripped off from the liquid core which is divided into several segments with diameters D_{seg} , as shown in Fig.3.2,

$$D_{seg} = D_{eff} - (D_{eff} - D_c) L_c \quad (\text{Equation 3.17})$$

where L_c is the liquid core length; D_c is the diameter at the tip of the core, with the same size of the primary drops formed there.

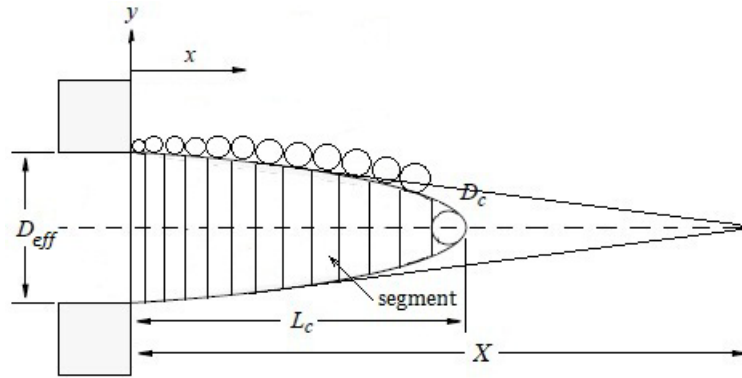


Fig.3.2 Sketch of MPI primary breakup model adopted from [94]

The quantity X is defined in Fig. 3.2, and is given by

$$X = \frac{D_{eff}}{D_{eff} - D_c} L_c \quad (\text{Equation 3.18})$$

The axial component of the relative speed between the liquid core and surrounding gas, u_{rel} , and its gradient normal to the injection direction are approximated by

$$u_{rel} = \frac{U_{eff}}{2} \left(1 - \frac{3x}{4X} \right) \quad (\text{Equation 3.19})$$

$$\frac{du}{dy} = \frac{2u_{rel}}{1.2D_{eff} - D_{seg}} \quad (\text{Equation 3.20})$$

Primary breakup diameter d_p is calculated from the presumed equilibrium of the lift force and the surface tension force by the following relation:

$$d_p = \sqrt{\frac{52.34 \frac{\sigma}{\rho_g u_{rel} \frac{du}{dy}}}{}} \quad (\text{Equation 3.21})$$

3.5.1.3 KELVIN-HELMHOLTZ (KH) SECONDARY BREAKUP MODEL

The KH model assumes that the growth of Kelvin-Helmholtz instabilities are the reason for the droplet disintegration from the continuous liquid jet [80]. The change rates of the parent and child droplet sizes are dependent on the wavelength (Λ) and frequency (Ω) of the fastest growing surface wave, given as below:

$$\Omega \left(\frac{\rho_l a^3}{\sigma} \right)^{0.5} = \frac{0.34 + 0.38 We_g^{1.5}}{(1+Z)(1+1.4T^{0.6})},$$

$$\frac{\Lambda}{a} = 9.02 \frac{(1+0.45Z^{0.5})(1+0.4T^{0.7})}{(1+0.87We_g^{1.67})^{0.6}}$$

(Equation 3.22)

where a represents the parent drop or blob radius. The Weber numbers for the gaseous and liquid phases are $We_g = \rho_g U^2 a / \sigma$ and $We_l = \rho_l U^2 a / \sigma$ respectively. U is the gas velocity at the interface, Ohnesorge number for the drop is $Z = We_l^{0.5} / Re_l$ with Reynolds number $Re_l = \rho_l U a / \mu_l$. $Ta = Z We_g^{0.5}$ is the Taylor parameter. The new drops are assumed to be created (with droplet radius r) from a parent drop (with radius $a = d/2$) with

$$r = B_0 \Lambda \text{ where } (B_0 \Lambda \leq a), \text{ or}$$

$$r = \min \left[\left(3\pi a^2 U / 2\Omega \right)^{1/3}, \left(3a^2 \Lambda / 4 \right)^{1/3} \right] \text{ where } (B_0 \Lambda > a, \text{ only one time})$$

(Equation 3.23)

where B_0 is the breakup size constant. The mass of child drops is derived from the parent drop. The change rate of a parent drop radius is supposed to follow the relation, given as below:

$$\frac{da}{dt} = -\frac{a-r}{\tau} \text{ with } (r \leq a), \text{ in which } \tau \text{ is the breakup time } \tau = 3.788 B_1 \frac{a}{\Lambda \Omega}$$

(Equation 3.24)

where B_1 is the breakup time constant related to the injector configuration.

3.5.1.4 TAYLOR ANALOGY BREAKUP (TAB) SECONDARY BREAKUP MODEL

The TAB model [81] uses an analogy of a spring-mass system for the droplet breakup and assumes the droplet is detached from the liquid surface by the droplet oscillation and deformation. In this model, the aerodynamic force, the liquid surface tension force, and the liquid viscous stress are analogous, respectively, to the external force acting on a mass, the restoring force of a spring, and the damping force. The distortion parameter k is given as below:

$$\ddot{k} = \frac{2}{3} \frac{\rho_g}{\rho_l} \frac{w^2}{r^2} - \frac{8\sigma}{\rho_l r^3} k - \frac{5\mu_l}{\rho_l r^2} \dot{k} \quad (\text{Equation 3.25})$$

where ρ_g and ρ_l are the gas and liquid densities, respectively; μ and σ are the liquid viscosity and surface tension, respectively; and w is the relative velocity between spray and the gas. When the value of k exceeds unity, the new droplets with a smaller size will be generated from the parent droplet and the new droplet radius follows the given distributions [81].

3.5.1.5 CASCADE ATOMIZATION BREAKUP (CAB) SECONDARY BREAKUP MODEL

Based on the standard TAB model, the CAB model assumes that the number of product droplets is proportional to the number of the parent droplets [110]. Thus, derived from the

mass conservation between the parent and product droplets, the rule of CAB is basically given as

$$\frac{d}{dt} \bar{m}(t) = -3K_{bu} \bar{m}(t) \quad (\text{Equation 3.26})$$

where $\bar{m}(t)$ represents the average mass of the product droplets and the parameter K_{bu} is related to the regimes of the drop breakup. According to the gas Weber number, the breakup regimes are classified into the bag, stripping and catastrophic breakup regime, respectively.

In detail, the K_{bu} can be expressed as [111]

$$K_{bu} = \begin{cases} k_1 \omega & \text{if } 6 < We \leq 80 \\ k_2 \omega \sqrt{We} & \text{if } 80 < We \leq 350 \\ k_3 \omega We^{0.75} & \text{if } 350 < We \end{cases} \quad (\text{Equation 3.27})$$

where the constant k_1 needs to be determined (in Chapter 4), while the constants k_2 and k_3 are calculated based on the continuity of K_{bu} at the transition of various breakup regimes [111].

Further, the distribution of product droplets is assumed to be equally sized [110], and hence

Eq.3.26 changes to

$$\frac{r}{a} = e^{-K_{bu} t_{bu}} \quad (\text{Equation 3.28})$$

where a are the parent droplets radii, r are the product droplets radii, and t_{bu} is the breakup time.

Besides, the radial component of the velocity of product droplets (perpendicular to the trajectory of the parent droplet) is calculated by the energy conservation between parent and product droplets. And the initial drop distortion rate $\dot{\gamma}$ is obtained by the critical deformation condition such that the initial breakup time is considerably delayed according to the experimental jet breakup length [110].

3.5.1.6 OTHER SUB-MODELS

Except for the breakup model, liquid core length and spray cone angle are two important characteristic parameters of spray. In particular, liquid core length is the key value in the primary breakup calculation and is also taken as a switch of its deactivation.

The Hiroyasu/Arai model [104] is used for liquid core length calculation considering the factor of ambient gas pressure. Steady state liquid core length $L_{c,steady}$ is given by

$$L_{c,steady} = HD_{eff} \left(1 + 0.4 \frac{r_n}{D_n} \right) \left(\frac{P_g}{\rho_l U_{eff}^2} \right)^{0.05} \left(\frac{l_n}{D_n} \right)^{0.13} \sqrt{\frac{\rho_l}{\rho_g}} \quad (\text{Equation 3.29})$$

where r_n is the radius of a round inlet in the nozzle hole, l_n is the nozzle length, p_g is ambient gas pressure and H is the coefficient, defined by $H = H_0 + H_{ln} \ln \left(\frac{P_g}{1atm} \right)$, where H_0 and H_{ln} are constants.

Hiroyasu presumed that liquid core length grows linearly, whose growth rate is defined by

$$\frac{dL_c}{dt} = L_{c,grow} U_{eff} \quad (\text{Equation 3.30})$$

where $L_{c,grow}$ is the liquid core length growth constant.

In terms of the spray cone angle, the Naber-Siebers [103] model accounts for the effect of gas density, in which the spray cone angle θ is defined as

$$\theta = 2 \tan^{-1} \left[C_\theta \left(\frac{\rho_g}{\rho_l} \right)^{0.19} \right] \quad (\text{Equation 3.31})$$

where C_θ is the constant.

3.5.2 Drop Evaporation Model

Given by the Frossling correlation [178] derived from the d^2 -law model [131], the drop radius change rate due to evaporation is obtained as the following function,

$$\frac{dr}{dt} = - \frac{\rho D}{2\rho_1 r} \frac{Y_1^* - Y_1}{1 - Y_1^*} Sh \quad (\text{Equation 3.32})$$

where D is the mass diffusivity of fuel vapor in air; Y_1 and Y_1^* are the mass fraction of fuel in the calculating cell and on the liquid surface, respectively, where $Y_1 = \rho_1 / \rho$ and the species 1 denotes to the fuel vapor. The Sherwood number Sh is given by

$$Sh = (2.0 + 0.6 \text{Re}_d^{1/2} Sc^{1/3}) \frac{\ln(1 + \frac{Y_1^* - Y_1}{1 - Y_1^*})}{\frac{Y_1^* - Y_1}{1 - Y_1^*}} \quad (\text{Equation 3.33})$$

where $Sc = \mu_{\text{air}}/\rho D$ is the Schmidt number of the air, where μ_{air} is the dynamic viscosity of air. If the partial pressure of fuel vapor is assumed to be the vapor pressure $p_v(T_d)$ at the drop temperature, then the mass fraction of fuel on the liquid surface is given by

$$Y_1^*(T_d) = \frac{W_1}{W_1 + W_0 \left(\frac{p}{p_v(T_d)} - 1 \right)} \quad (\text{Equation 3.34})$$

where, W_1 is the fuel molecular weight and W_0 is the mean molecular weight of all species exclusive of fuel vapor.

With the consideration of the latent heat and the heat conduction from the gas on the energy conservation, the change in the drop temperature can be obtained based on Eq.3.4 and Eq.3.7,

$$\rho_l \frac{4}{3} \pi r^3 c_l \dot{T}_d - \rho_l 4\pi r^2 \frac{dr}{dt} L(T_d) = 4\pi r^2 Q_d \quad (\text{Equation 3.35})$$

where $L(T_d)$ is the latent heat of evaporation, c_l is the liquid specific heat, and, Q_d , the heat conduction rate to the droplet, is obtained on the basis of the Ranz-Marshall correlation

$$Q_d = \frac{\psi(T - T_d)}{2r} Nu \quad (\text{Equation 3.36})$$

where ψ is the thermal diffusivity and Nu is the Nusselt number

$$Nu = (2.0 + 0.6 Re_d^{1/2} Pr^{1/3}) \frac{\ln(1 + \frac{Y_1^* - Y_1}{1 - Y_1^*})}{\frac{Y_1^* - Y_1}{1 - Y_1^*}} \quad (\text{Equation 3.37})$$

where Pr is the air Prandtl number $\mu_{\text{air}}/\rho\psi$.

3.6 Combustion Model for SI Engines

3.6.1 Characteristic Time Combustion (CTC) Model

The CTC model was originally developed by Abraham et al. [145]. In this study, when the local temperature is beyond 1000K, the combustion propagation is initiated and the turbulent combustion model becomes activated. The model achieves an acceptable accuracy in the combustion performance for SI engines [146].

The change rate of the partial density for species m is calculated by [146]:

$$\frac{dY_m}{dt} = -\frac{1}{\tau_c}(Y_m - Y_m^*) \quad (\text{Equation 3.38})$$

where Y_m is the mass fraction for species m , Y_m^* is the local and transient mass fraction at equilibrium, and τ_c is characterized as the time to attain the equilibrium. Seven species, including fuel, oxygen, nitrogen, water, carbon dioxide, carbon monoxide and hydrogen are considered in the current model.

The characteristic time, τ_c , is obtained by summing up the laminar-kinetics time (τ_l) and the turbulent-mixing time (τ_t), given by:

$$\tau_c = \tau_l + f_t \tau_t \quad (\text{Equation 3.39})$$

where f_t , namely the delay coefficient, indicates the influence of the turbulent mixing on the

combustion process, calculated by $f_t = \frac{(1 - e^{-R})}{0.632}$ [146]. The time (τ_d) from spark to fully

turbulent combustion model is described as $\tau_d = C_{ml} l_t / u_l$, where l_t and u_l are turbulent length scale and laminar flame speed, respectively. C_{ml} is the model constant.

Derived from the laminar flame speed correlation, the laminar-kinetics time (τ_l) is given as below,

$$\tau_l = A_l \cdot T \cdot p^{-(1+2\beta)} \cdot \exp\left[E \frac{g(\phi)}{T}\right] \frac{1}{C_f^2} \quad (\text{Equation 3.40})$$

where $\beta = 0.22\phi - 0.38$, $g(\phi) = B_l |1.15 - \phi| + 1$. ϕ is the mixture equivalence ratio. $E=15098$ K, is usually a fixed value related to the apparent activation energy and whereas A_l and B_l can be tuned according to the laminar combustion characteristics of fuel. In the case of isooctane, $A_l=3.09 \times 10^{-12}$ atm·s/K and $B_l=-0.08$ as provided in [146]. Additionally, the laminar-kinetics time is also influenced by the residual gas remained in-cylinder. A parameter C_f used for the correction of the residual ratio, is given as:

$$C_f = R_a \cdot (1 - R_b \cdot R') \quad (\text{Equation 3.41})$$

where R' is the mass fraction of the local residual gas. R_a and R_b are model constants, where R_b can be obtained from the analysis of the influence of the residual ratio on the laminar burning velocity and R_a is the correction factor of C_f to ensure $C_f = 1$ at a residual mass fraction of 10 %. For the isooctane case, $R_a = 1.27$ and $R_b = 2.1$ given in [146].

Global reaction of DMF oxidation is given by:



Thus, derived from the one-step reaction rate correlation, another method was introduced to the calculation of the laminar-kinetics time (τ_l) as follows [179]:

$$\tau_t = A_t \cdot [Fuel]^{FI} \cdot [O_2]^{OI} \cdot \exp(E/T) / C_f^2 \quad (\text{Equation 3.43})$$

where FI and OI are the exponential indexes of fuel and oxygen concentrations, respectively. This function directly indicates the laminar combustion characteristics of fuel in a chemical sense.

According to the EBU theory, τ_t can be defined as a relation of turbulence kinetic energy and its dissipation rate:

$$\tau_t = C_{m2} \zeta \kappa / \varepsilon \quad (\text{Equation 3.44})$$

where, C_{m2} is the model constant and the parameter ζ is defined as

$$\zeta = \begin{cases} 1 & h \geq 1 \\ 1/h & h < 1 \end{cases}, \text{ where } h = \frac{C_{m2}}{C_{m3}} \frac{Y_p - Y_{ps}}{Y_F - Y_F^* + Y_{O_2} - Y_{O_2}^*}. \quad (\text{Equation 3.45})$$

where, $C_{m3}=0.097$ as given in [146]. The subscript p denotes a sum over all of the products (CO, CO₂, H₂, H₂O), and the subscript ps denotes the product sum at the time of the spark.

The source terms due to the chemical reaction, $\dot{\rho}_m^c$ and \dot{Q}^c in Eq.3.1 and Eq.3.3, respectively, can be solved by this model. A first-order accurate stiffly stable numerical scheme is employed to calculate both the change in species density and the heat release due to chemical reaction,

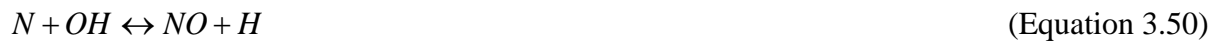
$$\Delta\rho_m = -\rho(Y_m - Y_m^*) \cdot (1 - e^{-\Delta t/\tau_c}) \quad (\text{Equation 3.46})$$

$$\Delta Q = -\sum_m \frac{\Delta\rho_m}{W_m} \cdot (\Delta h_f^0)_m \quad (\text{Equation 3.47})$$

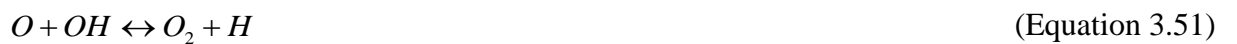
where Δt is the numerical time step, $(\Delta h_f^0)_m$ is the formation heat of species m . Thus, the equivalent source terms are $\dot{\rho}_m^c = \Delta\rho_m / \Delta t$ and $\dot{Q}^c = \Delta Q / \Delta t$.

3.6.2 NO_x Model

The extended Zel'dovich model is chosen to predict the NO_x production. Three reactions as below are solved in this theory [180].



As assumed to be a steady-state population of N , the reaction as below reaches equilibrium, given by:



The change rate of NO in the model is followed by

$$\frac{d[NO]}{dt} = \frac{2R_1 \left\{ 1 - \left([NO] / [NO]_Q \right)^2 \right\}}{1 + \left([NO] / [NO]_Q \right) \cdot R_1 / (R_2 + R_3)} \beta_{NO} \quad (\text{Equation 3.52})$$

where $[]_Q$ indicates the state in equilibrium and $[]$ represents the steady state. R_1 , R_2 and R_3 are coefficients of the reaction rate as presented in the reference [181]. β_{NO} is a model constant, allowing the model to meet the EPA NO₂-based standard.

3.7 Summary

The basic models in the numerical study by using the KIVA code are presented in this chapter. From the turbulence flow simulation, RNG κ - ϵ is selected as the substitute of the standard κ - ϵ model; the heat transfer model between the gas and the wall surface is improved with a temperature correction function to consider the influence of the varying gas density within the boundary layers; the extended Zel'dovich mechanism is chosen for the prediction of the NO_x formation. In addition, a CTC model has been chosen to predict the SI combustion to account for the influence of laminar kinetics and turbulence mixing.

As for the spray breakup model, several models are implemented in the KIVA code:

- MPI--selected as the primary breakup model with the consideration of the effect of cavitation;

- CAB--chosen as the optional secondary breakup model together with the other two widely-used models KH and TAB;
- Hiroyasu/Arai—used for the liquid core length calculation;
- Naber-Siebers—applied to the prediction of the spray cone angle.

Chapter 4 SPRAY MODEL VALIDATION AND DMF

SPRAY CHARACTERISTICS STUDY IN A BOMB

4.1 Introduction

In modern high pressure GDI injectors, cavitation is prompted by the high speed fluid flow in the nozzle. As reviewed in subsection 2.2.2.1, with the effect of cavitating flow, available flow area reduces and effective liquid velocity increases at the nozzle exit; additionally, the vapor cavities explosion and collapsing enhance the turbulence disturbance and surface wave instability. Further, the subsequent liquid jet atomization--primary breakup--is promoted by their comprehensive effects. Therefore, a cavitation induced primary breakup model is necessary for the spray modelling in this scenario.

However, cavitation is characterized as a complex two-phase flow. Detailed multi-dimensional simulation of nozzle internal flow is computationally expensive for the purpose of in-cylinder spray study. Thus, a phenomenological cavitation model called MPI is used to account for the effect of nozzle geometrical features on the cavitation.

The MPI model is implemented into KIVA, where the constants in the liquid core length and spray cone angle models are validated against the visualization data obtained from the Shadowgraph. As to the secondary breakup, three models (KH, TAB and CAB) are evaluated in terms of spray tip penetration, droplet axial velocity and size distribution through using the PDPA and backlit imaging experimental data. The spray model constants are also adjusted for

gasoline as a reference fuel. At the end of this chapter, effects of injection pressure and ambient pressure on the characteristics of DMF spray are investigated.

4.2 Experimental Set-up and Data Analysis

Comparing with other techniques such as LSD and PIV, the PDPA technique is advantageous in a high spatial and temporal resolution of measuring the droplet size and velocity distribution. Therefore, this technique becomes the first choice for the validation of spray breakup models.

4.2.1 PDPA Test

The experimental spray system schematic of PDPA is presented in Fig. 4.1. The injector used in this test was a 6-hole gasoline direct injection injector. The positions of the holes are optimized for the combustion chamber and hence they are not symmetric. All of the 6 holes were chosen for the experimental setup but an arbitrary one was used for all the tests. The fuel is delivered from a fuel accumulator which is pressurized by a compressed nitrogen bottle. Injection pressure can be adjusted by the regulator of the nitrogen bottle. The injection duration is controlled by a computer with a National Instruments timer and counter card (PCI-6602).

Spray pattern images were taken by a high resolution, low speed CCD camera from LaVision. Each image was captured from the injection with a specific time delay. The spray was

illuminated by a Xenon stroboscope flash light from Polytech with an intensity of 2.16J/flash and frequency of 100Hz (highest possible settings).

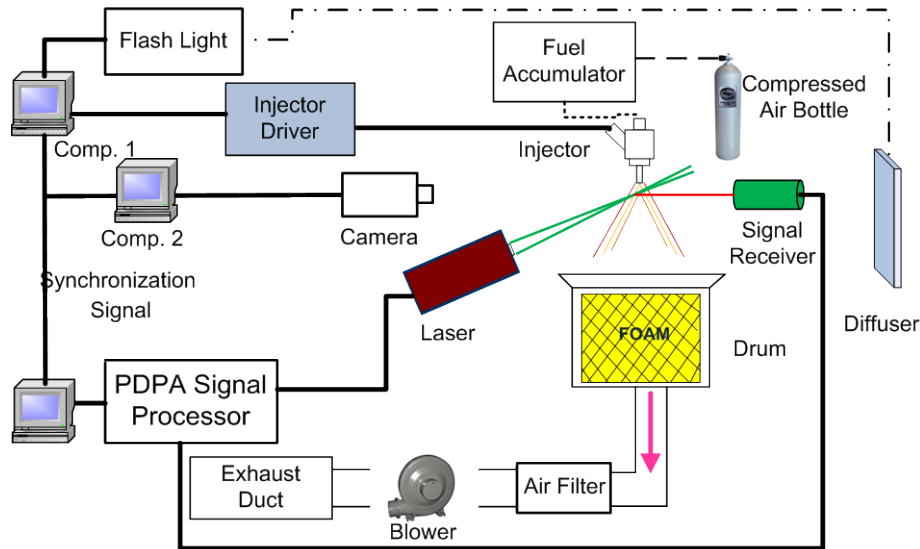


Fig.4.1 PDPA experimental schematic [163]

The TSI 2-D PDPA system uses a 4W Ar⁺ laser to generate two different groups of laser beams with wavelengths of 514.5 and 488nm. The laser beams are transferred to the transmitter by optical fibres. The focal lengths of the optical transmitter and receiver are 250 and 500mm respectively. A 150 μm slit was used before the photo detector in the receiver to limit the scattering light. A 3-D traverse was used so that the measurement position was precisely controlled (resolution of 60 steps per mm). Three computers which control the fuel injection, flash light, camera and PDPA were finely synchronized between each other so that all the results were on the same time base.

In order to eliminate the fire risk hazard and environmental pollution, the injected fuel was collected and filtered. A piece of foam, normally used in racing car tanks, was inserted into a

drum. This drum was connected with an activated carbon filter and eventually to the exhaust duct through a centrifugal blower. The sponge-like foam is used for collecting the liquid fuel. The activated carbon filter from Camfil allows a 0.15s contact time with a flow rate of 300 m³/hr; suitable for removing fumes associated with fuel droplets. The blower is able to deliver a flow rate up to 300l/m, which gives an air/fuel ratio of more than 300:1, under the maximum fuel injection ratio. This ratio is far beyond the ignition point, which eliminates any risk of explosion.

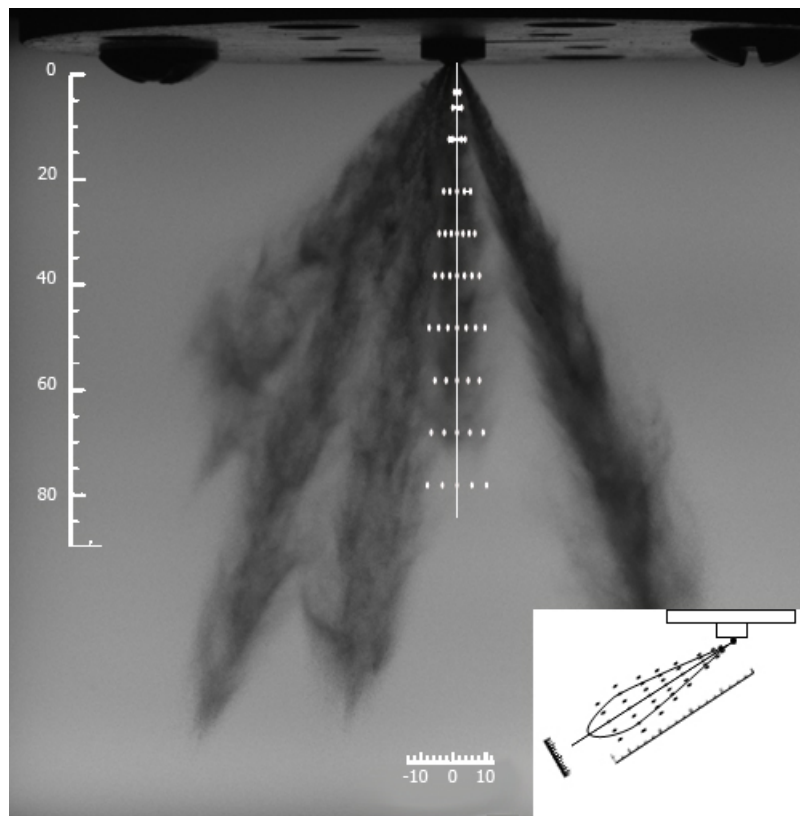


Fig.4.2. Measuring points on the spray (unit: mm) [163]

As presented in Fig.4.2, one of the 6 axisymmetric spray plumes was studied. The sketch at the bottom right hand corner illustrates the view of the measured spray from the right. The axis of the spray was on the vertical plane and perpendicular to the PDPA receiver. The angle

between the spray axis and the vertical axis was 50° . Two sets of points on the two perpendicular planes, which intersect at the spray axis, were measured. Each set contained 52 points with the axial distances in the range of 5-81mm from the nozzle exit. For the PDPA tests, each droplet which flew through the measurement volume was recorded as one sample each time. An enormous number of samples were required for statistical analysis. In this test, at each measurement point, 20,000 validated samples were attempted.

The fuel was injected into an open environment (atmospheric pressure and 20°C room temperature), which is similar to the conditions of a GDI engine with early injection. The 100 bar injection pressure was chosen with 2ms injection duration, which corresponds to around 3bar Indicated Mean Effective Pressure (IMEP) engine load condition.

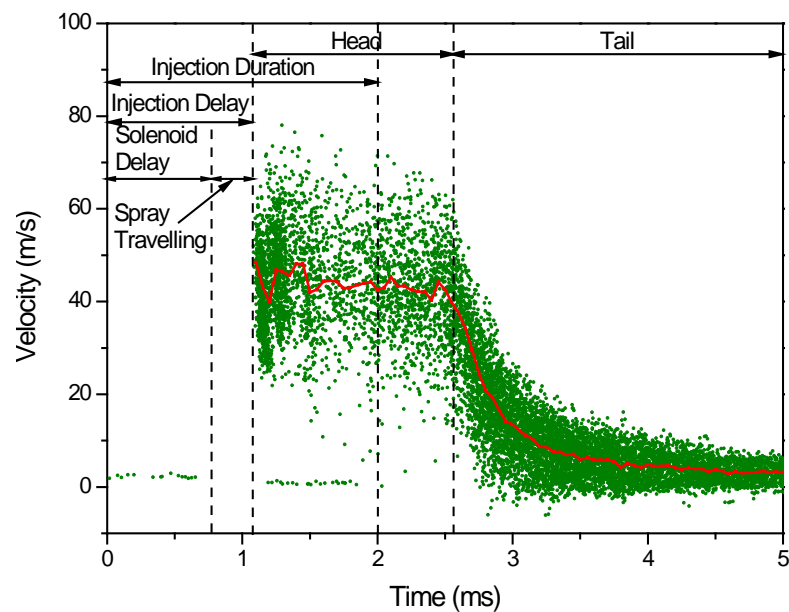


Fig.4.3. Gasoline injection vertical velocity and smoothed data (100 bar injection pressure) at 32 mm axial distance from the nozzle exit [163]

The description of a spray is shown in Fig.4.3 by measuring pure gasoline droplet velocities with time, 32mm from the nozzle, under an injection pressure of 100bar. The profile of the spray velocity is artificially separated into two parts: “main spray (head)” and “spray tail” [163], as shown in Fig.4.3. In the main spray, an obvious plateau can be seen with a high level of velocity; while in the spray tail, the droplet velocity exponentially drops down to a low level.

As presented in Fig.4.3, a delay of 1.1 ms in the essence of available data can be seen, including the delay from the system of 0.7 ms and the time for spray attaining the measuring point. Additionally, intense vibrations in the magnitude of velocity occur during the main spray and the maximum difference reaches nearly 60 m/s, which indicates a dominant breakup process takes place. With respect to the duration of the spray tail, a certain amount of negative velocities can be found, which is resulted from the wake created by the droplets at the front of spray with the effect of aerodynamic drag force. Also a small amount of samples with an extremely low magnitude of velocity can be observed before the main spray arriving and during the main spray, which is a noise caused by residual sprays in the previous cycles. In order to provide a clear evolution of spray characteristics, it is necessary to smooth the scatters to obtain the trend of the spray development.

4.2.2 Shadowgraph Test in the Vessel

To achieve the special combustion style such as lean burn, late injection (near combustion Top Dead Centre (TDC)) is necessary to form a stratified fuel-air mixture. Unlike the early injection, for the late injection, the injection process is under the high in-cylinder pressure and

high temperature. Thus, an analogous experiment in a constant volume vessel was applied to study the effects of in-cylinder pressure on DMF spray characteristics. The ambient pressure was adjusted by the pressure gauge. DMF and gasoline spray development under ambient pressures of 1 bar, 3 bar and 6 bar respectively can be captured with a CCD camera. The injection pressure and duration were set at 50 bar and 2 ms respectively.

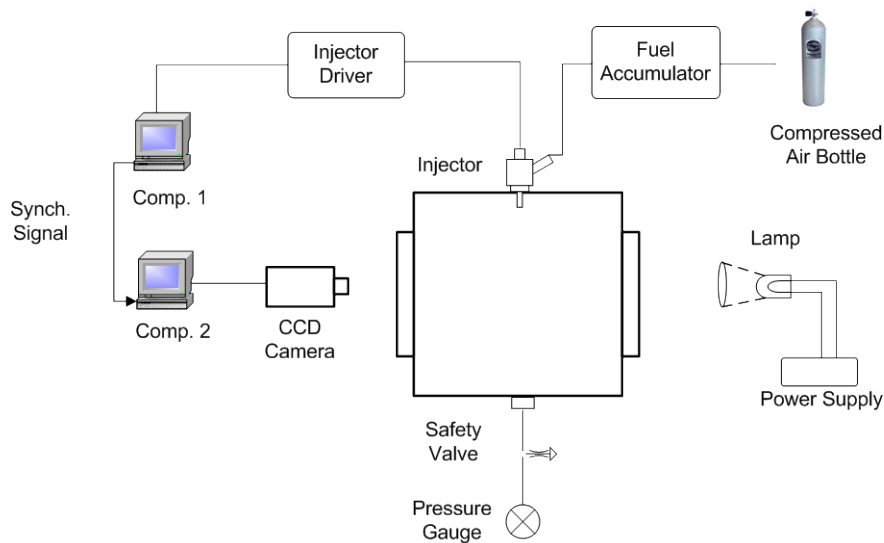


Fig.4.4 Schematic of the Shadowgraph system

The macroscopic structure of the spray jet is captured by the Shadowgraph system (see Fig.4.4). Afterwards, the image is processed by the procedure calculated by MatlabTM software. In detail, as illustrated in Fig.4.5, firstly the original image is subtracted from the background image, and then converted into a binary image through calculating the global threshold of gray scale. Finally the binary image is inverted to be ready for modeling validation.

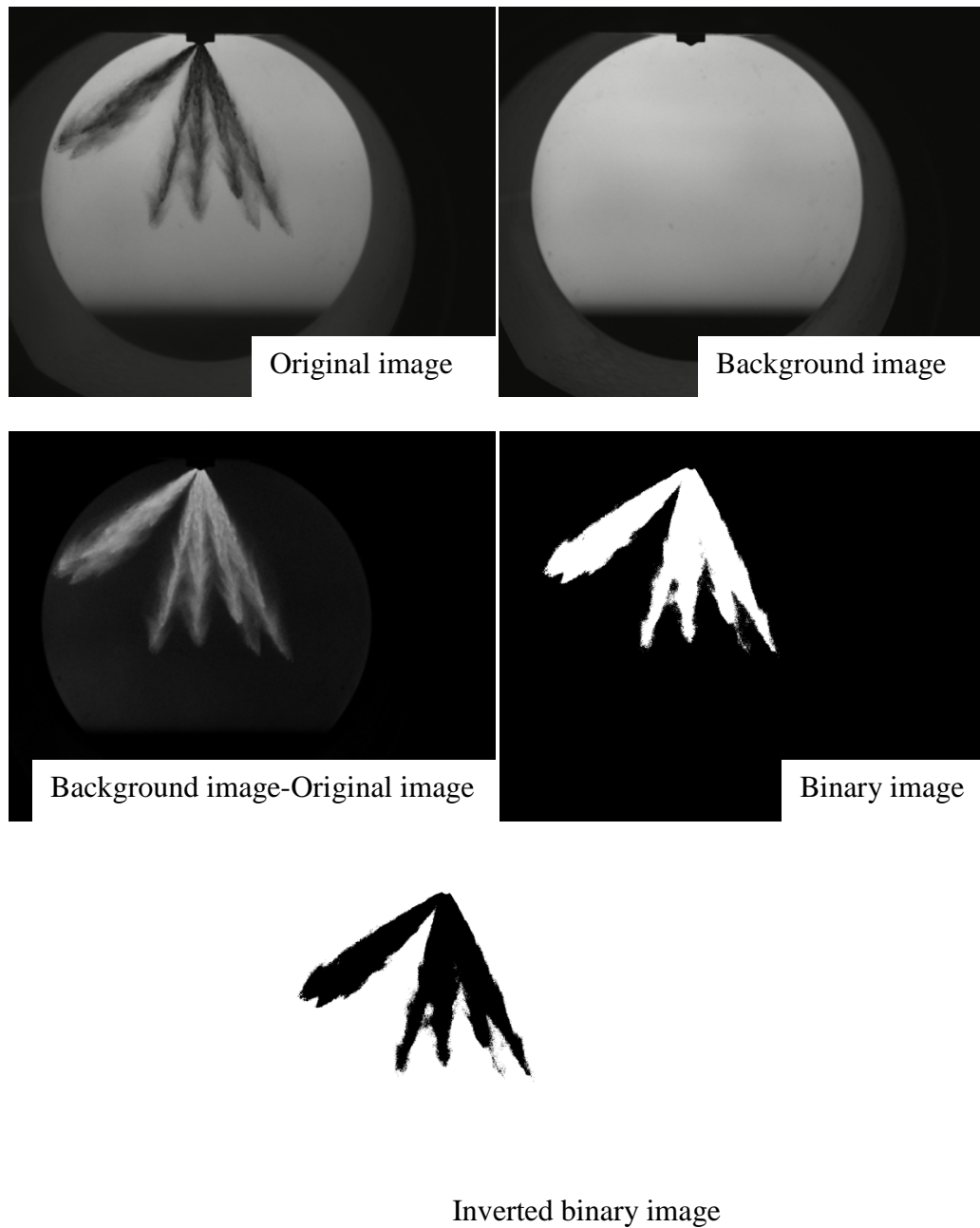


Fig.4.5 Image processing of Shadowgraph

Fig.4.6 illustrates the determination of the spray tip penetration and spray cone angle. The real spray tip penetration L and cone angle θ and their projections L' and θ' are shown in Fig.4.6a.

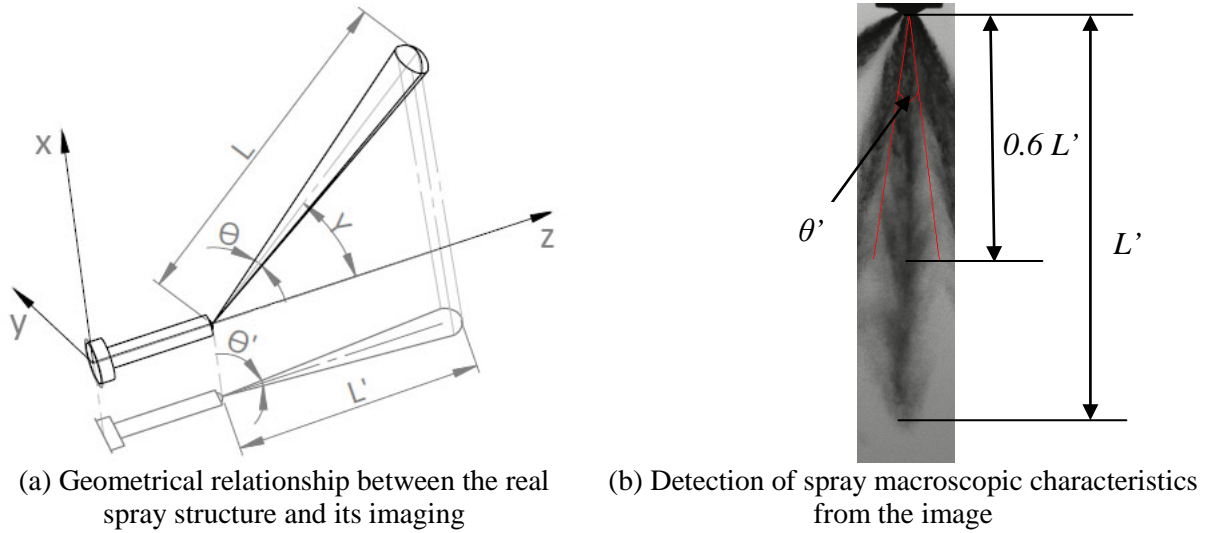


Fig.4.6 Determination of spray macroscopic characteristics

The relations between the real spray macroscopic characteristics and their projections are given as,

$$\theta = 2 \arctan \left[\tan \left(\frac{\theta'}{2} \right) \cos \gamma \right] \quad (\text{Equation 4.1})$$

$$L = L' / \cos \gamma \quad (\text{Equation 4.2})$$

where γ is the spray inclination angle.

In addition, as presented in Fig.4.6b, spray tip penetration in the image L' is defined as the axial distance from the nozzle exit to the farthest position of the spray plume. The red lines encompassing the plume start from the nozzle tip to the position whose axial distance is $0.6 L'$. Hence, spray cone angle in the image θ' is defined as the angle between these two red lines. Then the real spray tip penetration and cone angle are obtained by Eq.4.1 and Eq.4.2, respectively.

4.3 Simulation Build- up and Model Validation

Numerical simulation on DMF fuel and gasoline sprays were undertaken in the constant volume cylindrical chamber with the size of 40 mm in diameter and 200 mm in depth. The injector is located at the top centre of the cylinder. The numerical grid used for analysis is 40,000 computational cells (radial x circumferential x axial cells = 20x20x100). To avoid repetition, the following sub-sections are focused on the case of DMF fuel spray.

4.3.1 Primary Breakup Model

As reviewed in subsection 2.2.2.1, in the conventional blob method, the diameter at the nozzle exit is taken to be the same size of the nozzle hole diameter without the consideration of the influence of the nozzle internal flow on the diameter correction. This subsection discusses the process of primary breakup model validation in terms of spray tip penetration and spray cone angle compared with data captured from the Shadowgraph test.

4.3.1.1 SPRAY TIP PENETRATION

Spray tip penetration as an important macroscopic indicator of spray characteristics is chosen for this comparison. Fig.4.7 presents the temporal evolution of spray tip penetration by using the CAB combined with the MPI primary breakup (CAB-MPI) and original blob-injection CAB (CAB-blob) models at an injection pressure of 100 bar in an open air. As shown in Fig.4.7, CAB-MPI was shown to achieve a better agreement with the measurement. In the initial linear penetration growth stage, both models match the measurement, which indicates

the nozzle exit velocities are reproduced by both models. After 1.2ms, the penetration tip length predicted by the CAB-Blob model starts to depart from the measurement. This discrepancy can be explained by the larger initial droplet size predicted by the blob-injection model, leading to a longer liquid penetration, owing to the reduction of the drag force.

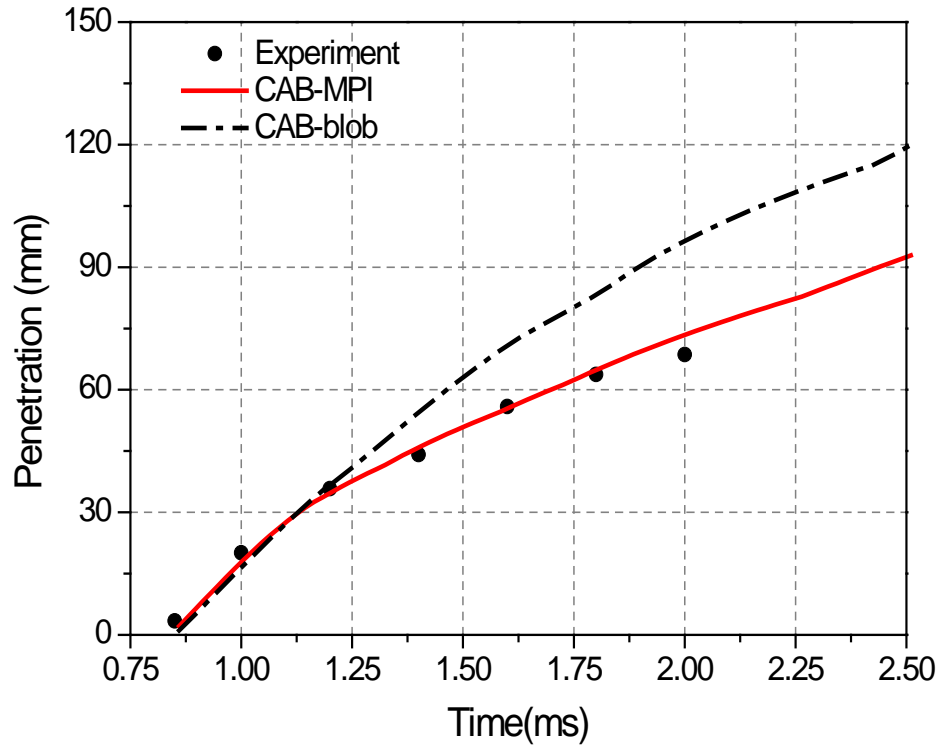


Fig.4.7 Comparison of MPI and original blob-injection CAB models on the penetration

In the MPI primary breakup model, except for the effect of cavitation, liquid core length is an important factor on the spray tip penetration. Additionally, the liquid core length is the vital link between the primary breakup and secondary breakup. According to Eq.3.29 and Eq.3.30, three constants are available for the adjustment of the liquid core length, H_0 , H_{ln} and $L_{c,grow}$. The standard values of these three constants are 7.0, 0.0 and 1.0, respectively [104]. In addition, the first two constants determine the end of linear liquid penetration growth and the last one is available to adjust the gradient of liquid spray penetration.

Fig.4.8 presents the effect of H_0 on spray tip penetration at the End of Injection (EOI) with various injection pressures. It is remarkable that penetration is more sensitive to H_0 under the injection pressure of 50 bar. Especially for the case of $H_0=7$ (default value), the predicted penetration is almost 7 mm longer than the experimental and the relative error is up to 11%. Remarkably, the standard value is determined by the diesel spray test, whereas DMF, similar to gasoline, whose surface tension and viscosity is much smaller than that of diesel, is easy to strip off the primary breakup droplet under the same condition as compared to diesel. Therefore, it is reasonable to reduce the value of H_0 . Generally, when $H_0=3$, simulated penetrations achieve a good agreement with measured penetrations.

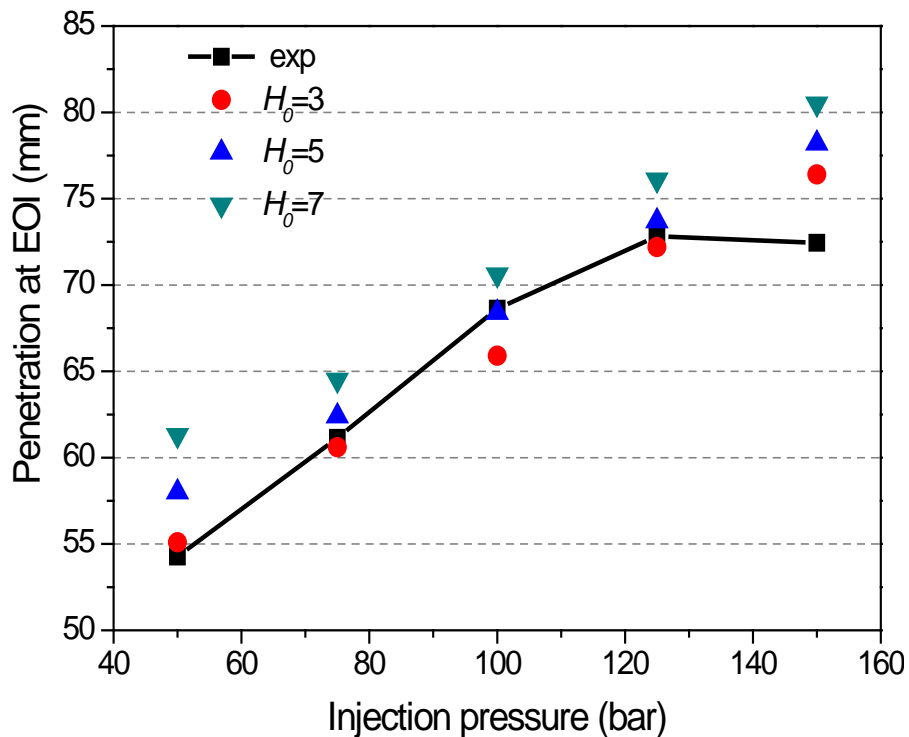


Fig.4.8 Effect of H_0 on spray tip penetration at EOI with various injection pressures

According to Eq.3.29, H_{ln} represents the factor of ambient gas pressure on the liquid core length. As shown in Fig.4.9, with an injection pressure of 50 bar, the penetration is greatly dependent on the value of H_{ln} under the high ambient gas pressure. As expressed in Eq.3.29,

the effect of ambient gas pressure on the spray tip penetration reflects a trend of a natural logarithm. The prediction with the standard value becomes worse as the ambient pressure increases. Especially under the ambient pressure of 6 bar, the predicted penetration with $H_{ln}=0$ is only 23.6 mm, almost the half of the measured penetration. With the value of H_{ln} increasing, the difference between prediction and measurement becomes gradually smaller. It is obvious that $H_{ln}=8$ is the optimal value.

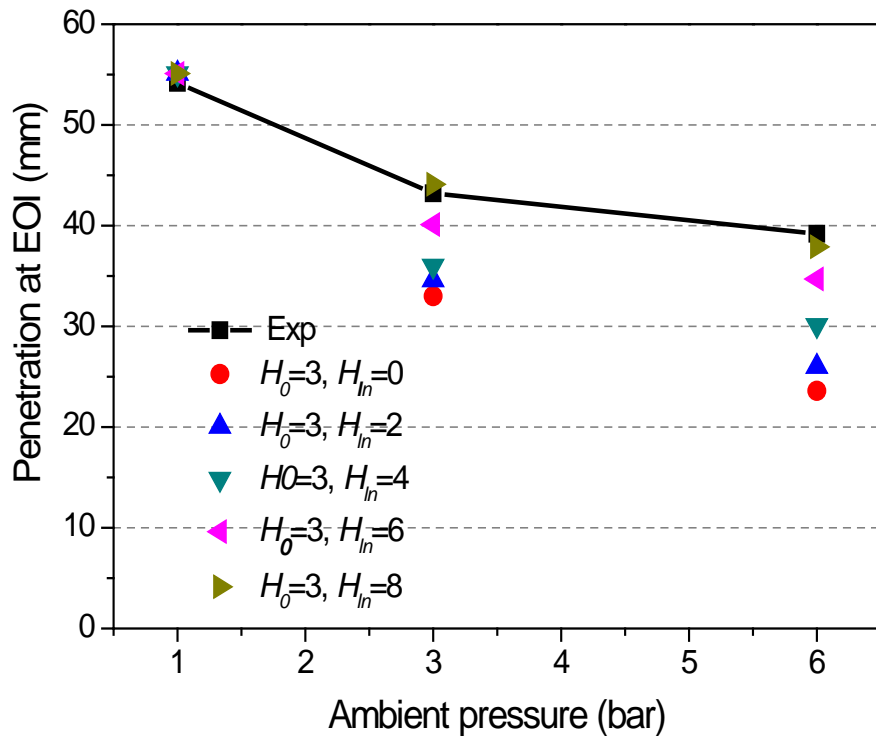
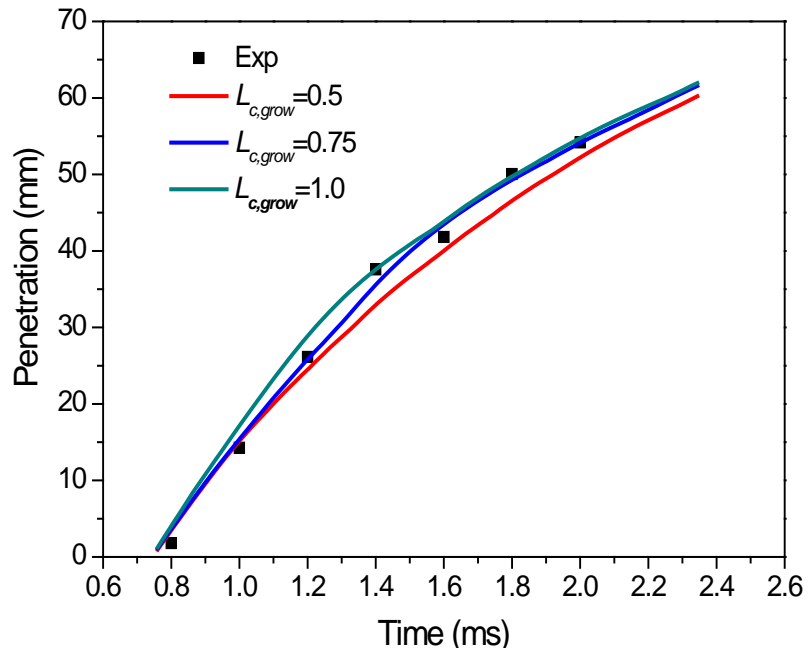


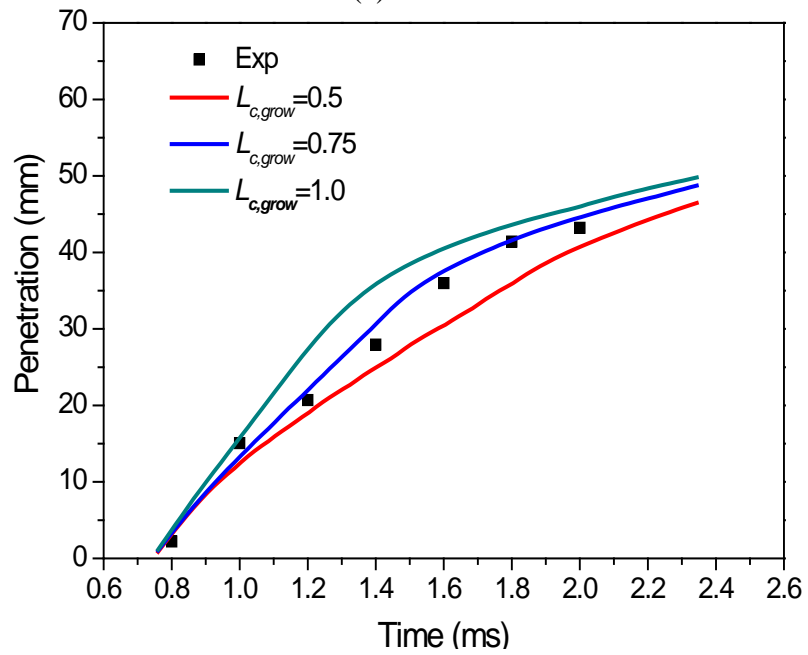
Fig.4.9 Effect of H_{ln} on spray tip penetration at EOI under various ambient pressures (at an injection pressure of 50 bar)

After adjustment of H_0 and H_{ln} , the spray tip penetration at the end of injection is determined, but its temporal evolution is to be adjusted by $L_{c,grow}$. Fig.4.10 illustrates the factor of $L_{c,grow}$ on spray tip penetration under different ambient pressures of 1 bar, 3 bar and 6 bar. As $L_{c,grow}$ increases, the initial gradient of spray tip penetration becomes large and the difference among individual simulation cases narrows at the end of injection. It is remarkable that the history of spray tip penetration becomes more sensitive to $L_{c,grow}$, when ambient pressure becomes

higher. For example, as seen in Fig.4.10a, under an ambient pressure of 1 bar, the maximum difference of simulated penetration at 1.4 ms is less than 5 mm; while as seen in Fig.4.10c, under an ambient pressure of 6 bar, the difference at 1.4 ms is more than 10 mm, equivalently almost 25% of the penetration at EOI. Compared with the measurement, the case of $L_{c,grow}=0.75$ achieves the best agreement.



(a) 1 bar



(b) 3 bar

Fig.4.10 Effect of $L_{c,grow}$ on spray tip penetration (at an injection pressure of 50 bar)

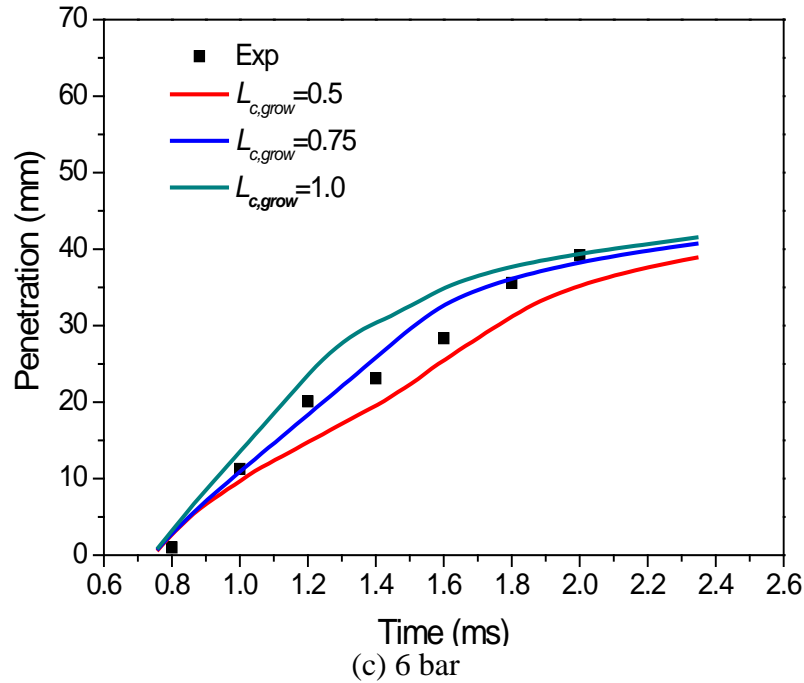


Fig.4.10 Effect of $L_{c,grow}$ on spray tip penetration (cont.)

4.3.1.2 SPRAY CONE ANGLE

The value of spray cone angle determines the radial distribution of spray droplets. As an indicator of the effect of air entrainment [182], spray cone angle is important for the mixture preparation. The wider the spray cone angle is, the more sufficient the mixing. As a result, a wider spray cone angle encourages a more homogeneous mixture formation.

According to Eq.3.31, C_θ is the factor of the ambient gas density on the spray cone angle, whose standard value is 0.3. Fig.4.11 presents its influence on the spray cone angle under various ambient pressures. As the C_θ increases, the spray cone angle enlarges linearly. The predicted spray cone angles with $C_\theta = 0.5$ are closest to those measured ones.

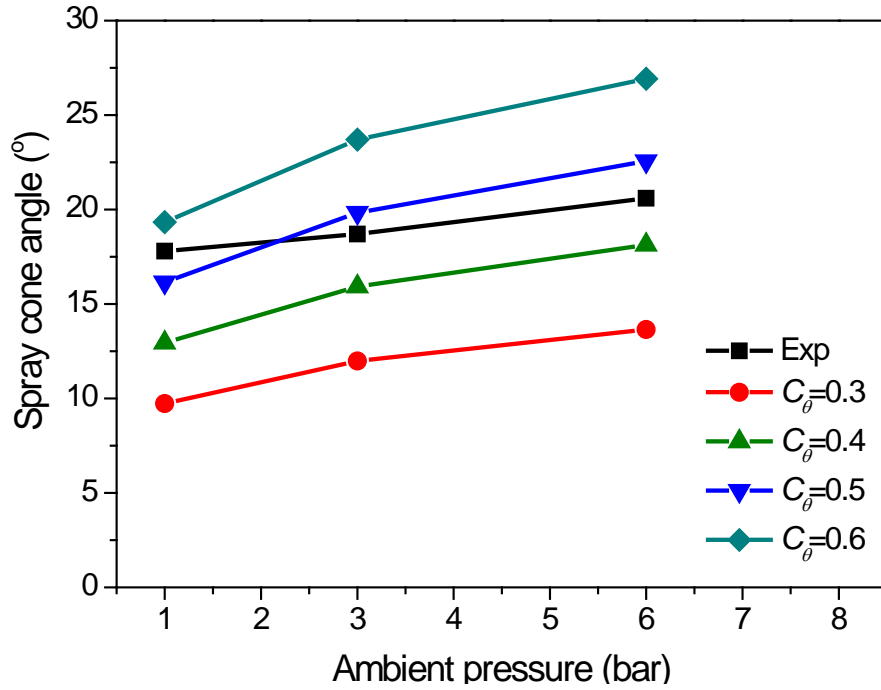


Fig.4.11 Effect of C_θ on the spray cone angle (at an injection pressure of 50 bar)

4.3.2 Secondary Breakup Model

The droplet breakup process is simulated by an aerodynamically induced breakup model. In this subsection, three secondary breakup models, namely KH-MPI, TAB-MPI and CAB-MPI breakup models are used to compare with the PDPA measurement data with an injection pressure of 100 bar.

4.3.2.1 EFFECT OF SECONDARY BREAKUP MODEL PARAMETERS

For the TAB-MPI model, the default value is selected. Figs.4.12 and 4.13 present the effect of main parameters in the KH-MPI and CAB-MPI models on the temporal evolution of axial

velocity and Arithmetic Mean Diameter (AMD) at the axial distance of 32, 50 and 70mm downstream from the nozzle tip, respectively.

It is observed that B_1 in the KH-MPI model and k_1 in the CAB-MPI model represent similar effects on AMD as illustrated in Figs.4.12 and 4.13. For the KH model, according to Eq.3.24, B_1 is the breakup time constant which affects the change rate of the radius of parent droplets; smaller B_1 accelerates the droplet breakup and results in smaller child droplets, as is evident from Fig.4.12. On the other hand, according to Eq.3.27 and 3.28, k_1 in the CAB model determines the radii ratio of product to parent drops; smaller k_1 slows down the droplet breakup, as seen in Fig.4.13. In the term of axial mean velocity, B_1 makes almost no effect and k_1 plays a dominant role, as is evident from Fig.4.12 and 4.13, respectively. In the KH model, as described in Eq.3.23, drops are continuously detached from the parent drops during their lifetimes [61]. Reversely, in the CAB model, drop breakup takes place only when the drop distortion exceeds the specified value (normally one) and also the radii ratio of parent to product droplets contributes to the radial component of the product droplets [111].

As to the optimal value, it can be seen that except in the initial stage, the computed AMDs are found to be similar when $B_1=10$ and $B_1=5$, that is, AMD is insensitive to further accelerations in the secondary breakup; this is because the number of droplets increase with accelerating the secondary breakup and consequently, the chance of drop collision and coalescences increases, neutralizing the effect of the size reduction due to the secondary breakup [61]. Besides, the regular range of B_1 is from 10 to 60 [183]. Thus, it is reasonable to select $B_1=10$ as the tuned value for the KH-MPI model. For the CAB-MPI model, it is clear that when $k_1=0.06$, the

predicted results achieve overall the best agreement in terms of axial mean velocity and AMD.

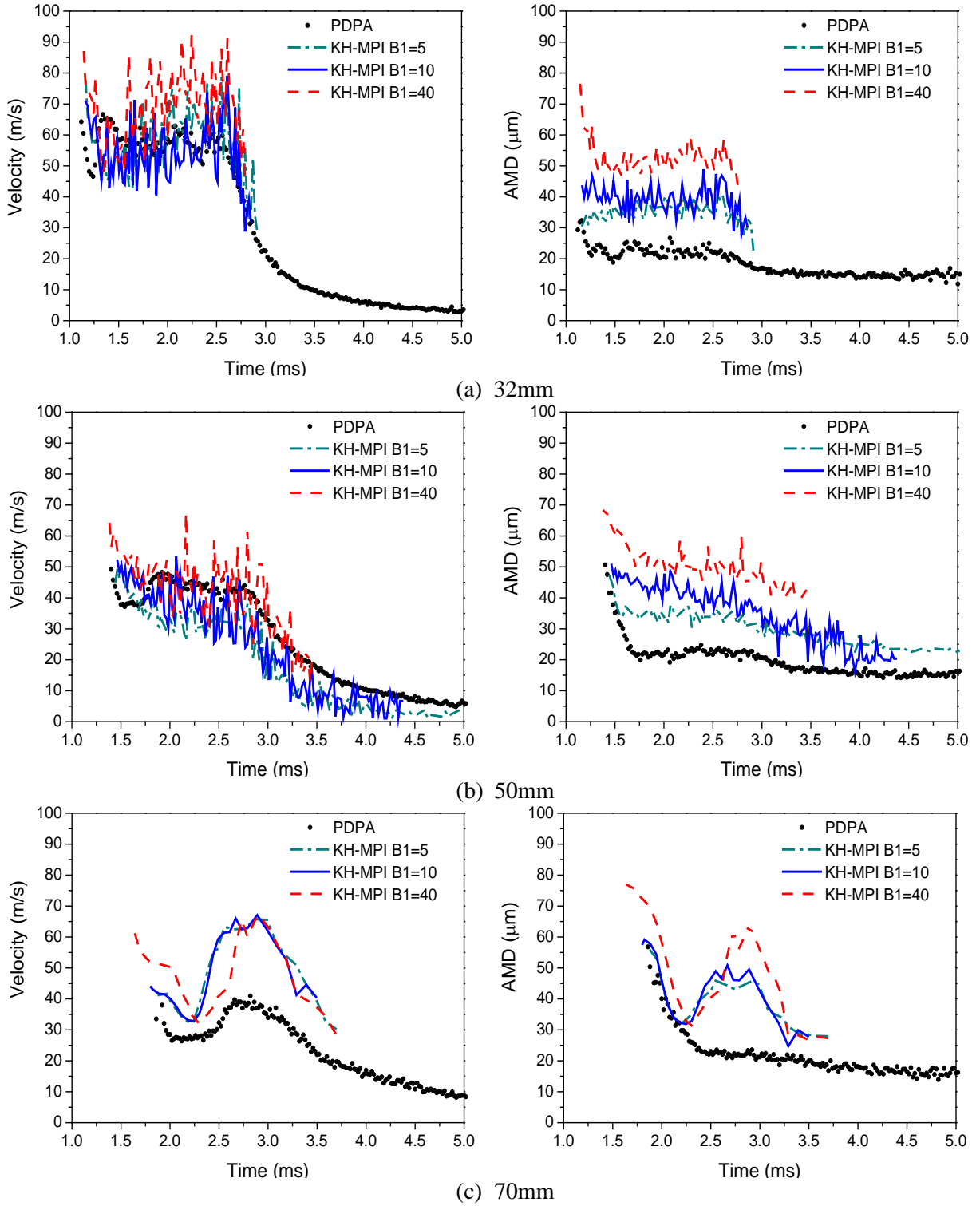
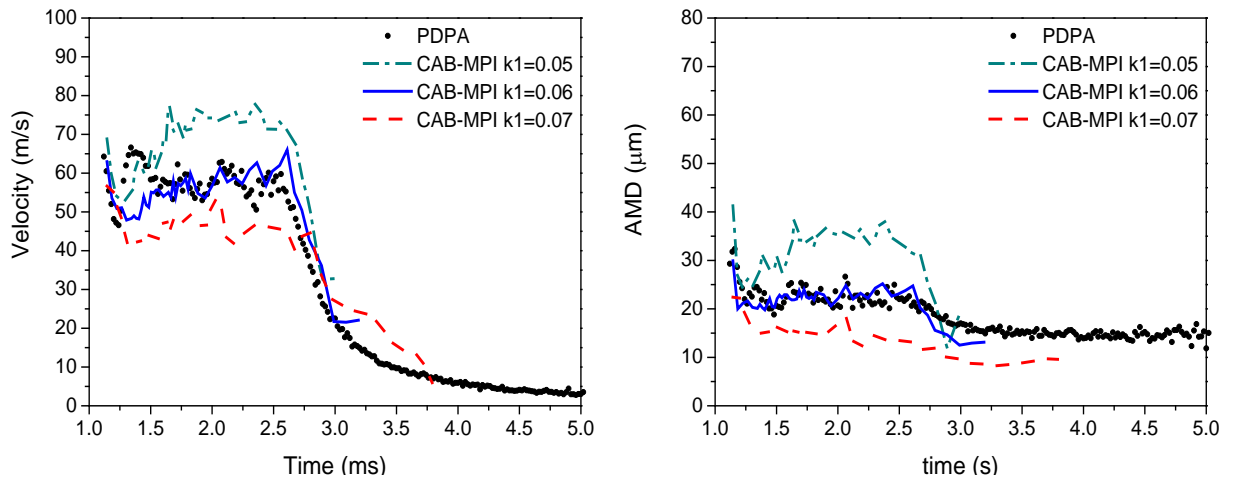
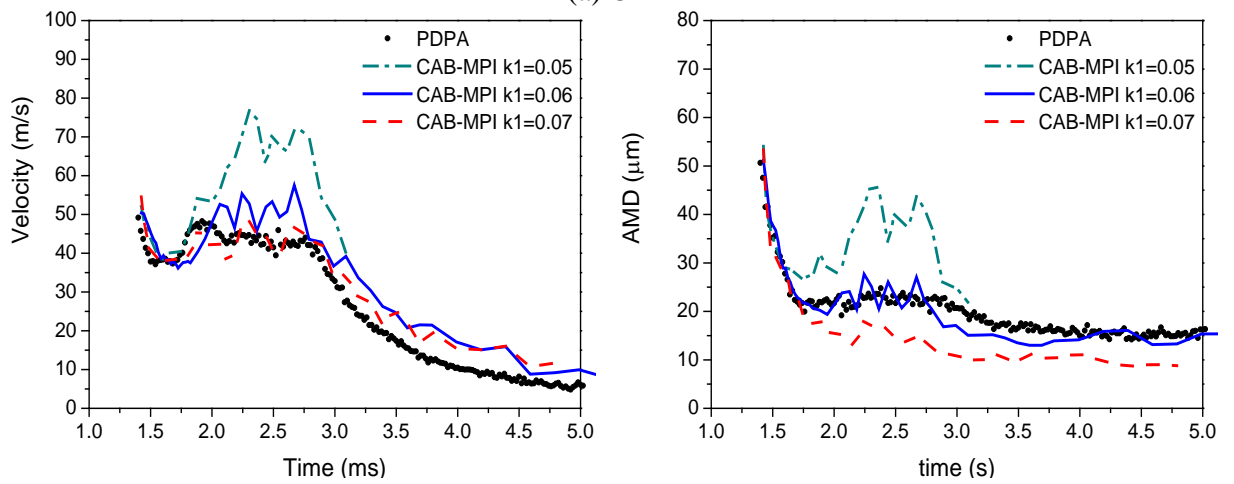


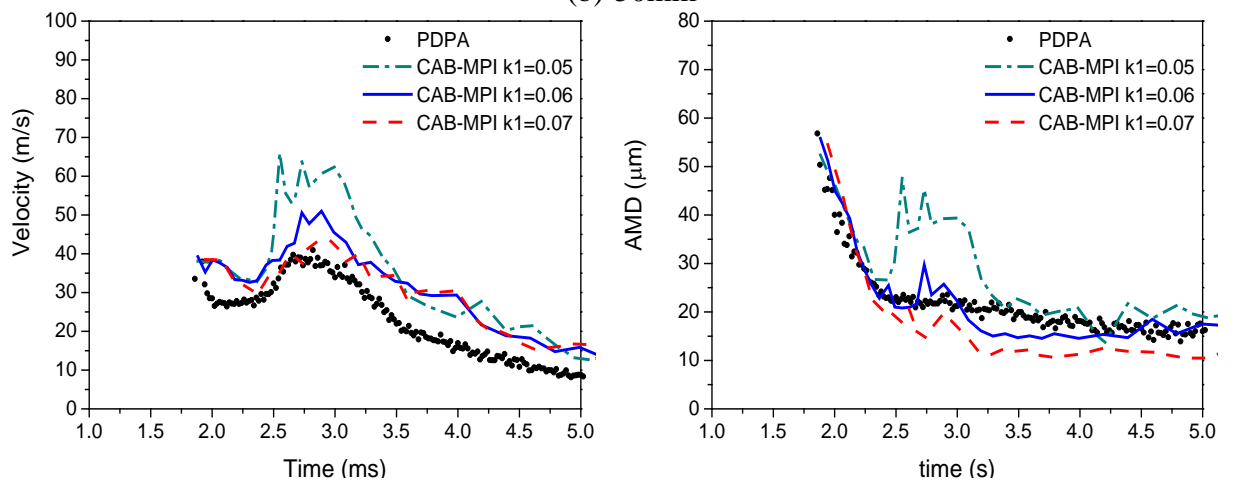
Fig.4.12 Effect of B_1 in the KH-MPI model on the temporal evolution of axial mean velocity and AMD at different distances away from the nozzle exit (a-32, b-50 and c-70mm).



(a) 32mm



(b) 50mm



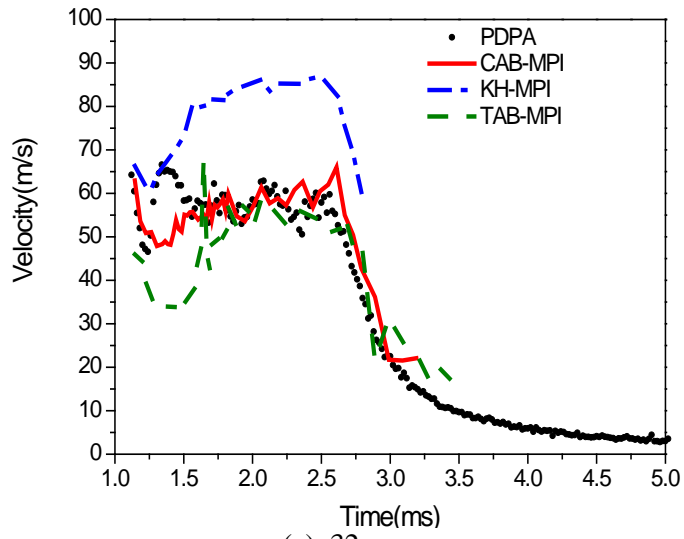
(c) 70mm

Fig.4.13 Effect of k_1 in the CAB-MPI model on the temporal evolution of axial mean velocity and AMD at different distances away from the nozzle exit.

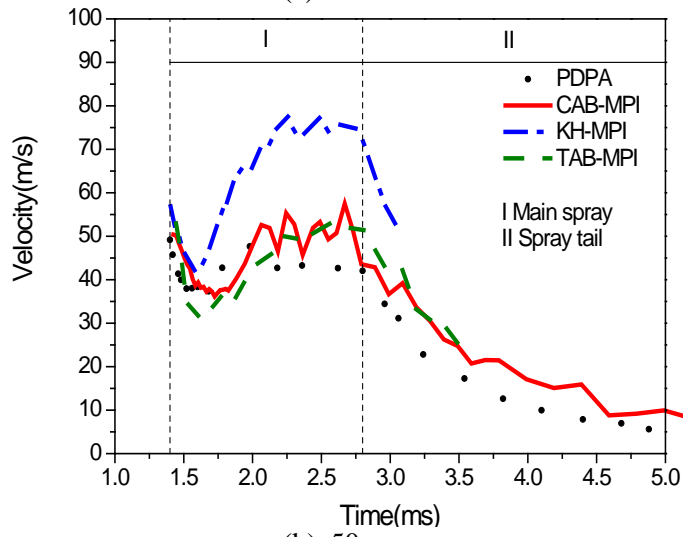
4.3.2.2 EVALUATION OF SECONDARY BREAKUP MODELS

After analyzing the main parameters, three secondary breakup models are evaluated with PDPA data and backlit images. Figs.4.14 and 4.15 present the comparison between the predicted and experimental temporal evolutions of the axial mean velocity and AMD at different distances away from the nozzle exit, respectively.

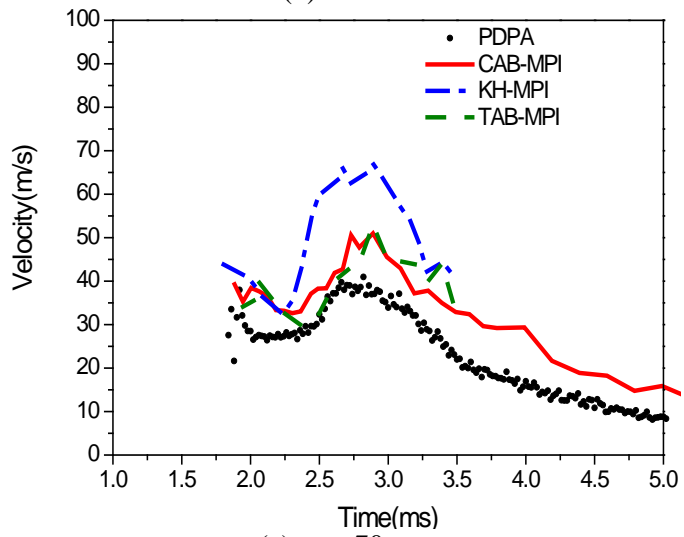
The temporal evolutions of the experimental results present similar trends at various axial distances. The case at 50mm axial distance is taken as an example to shorten the length. As described in Fig.4.3, the spray structure is artificially separated into two parts: “main spray” and “spray tail”, which are marked in the Fig.4.14b. In the main spray, the droplets in the spray front are firstly decelerated by the drag force and then subsequent droplets pass through the sample volume with less influence of drag force. With the increase of the number of these droplets, the average axial velocity restores to the high level whose mean value is relatively steady. Then, in the spray tail, the average velocity reduces dramatically to a low level. The initial droplets with high momentums to arrive at this measurement location have, in general, the largest diameters (50microns), as is evident from Fig.4.15b. Following this is a continuing breakup process towards a smaller mean droplet size, when the main spray and spray tail pass through.



(a) 32mm



(b) 50mm



(c) 70mm

Fig.4.14 Temporal evolutions of axial mean velocity at various distances downstream from the nozzle exit.

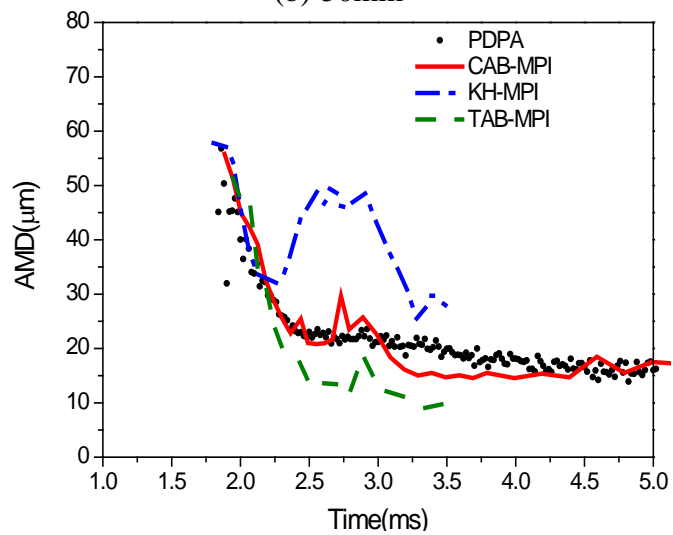
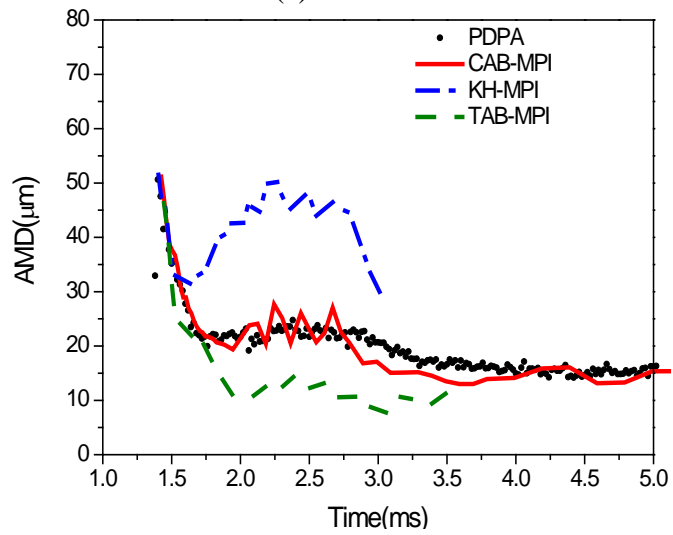
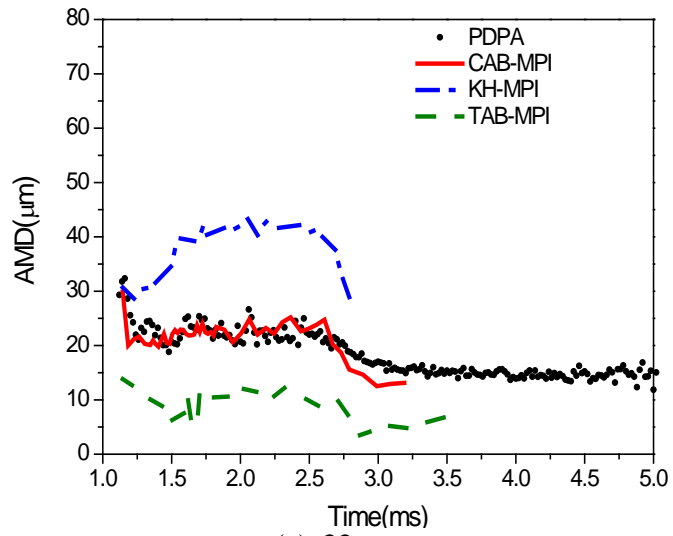


Fig.4.15 Temporal evolutions of AMD at different axial distances away from the nozzle exit.

The KH-MPI model significantly over-predicted the droplet size especially during the main spray; hence there was higher droplet axial velocity, due to the fact that larger droplets tend to maintain their moving momentum with little effect of drag force. As compared to the TAB-MPI model, the predicted droplet size and velocity evolution by using the CAB-MPI model were shown to have a better agreement with the measurement. As a result, the CAB-MPI was selected to study the DMF sprays.

However, the axial velocity was over-predicted by the CAB-MPI model especially during the spray tail, as presented in Fig. 4.14b and 4.14c. This discrepancy could be possibly explained by the sampled volume of the PDPA measurement not being perfectly aligned with the nozzle hole axis and this error increases with the distance away from the nozzle tip.

From the macroscopic view, Fig.4.16 shows the snapshots of the shadowgraph and simulation at six different instants. It can be found that the overall spray shapes are well predicted by the CAB-MPI model, while a visually sharp front can be observed in the KH-MPI model at the late stage. It should be noted that small droplets are created from two sources: one from the breakup of the parent droplets and another from new drops shed from the parent drops in the KH model [116]. Hence, as shown in Fig.4.16, the KH-MPI model shows a denser droplet distribution than the CAB-MPI model after 1.4 ms. However reversely, in the TAB-MPI model, caused by its abrupt secondary breakup, a large number of droplets in the front exchange their momentums to the air which leads to under estimation on the spray tip penetration after 1.6 ms.

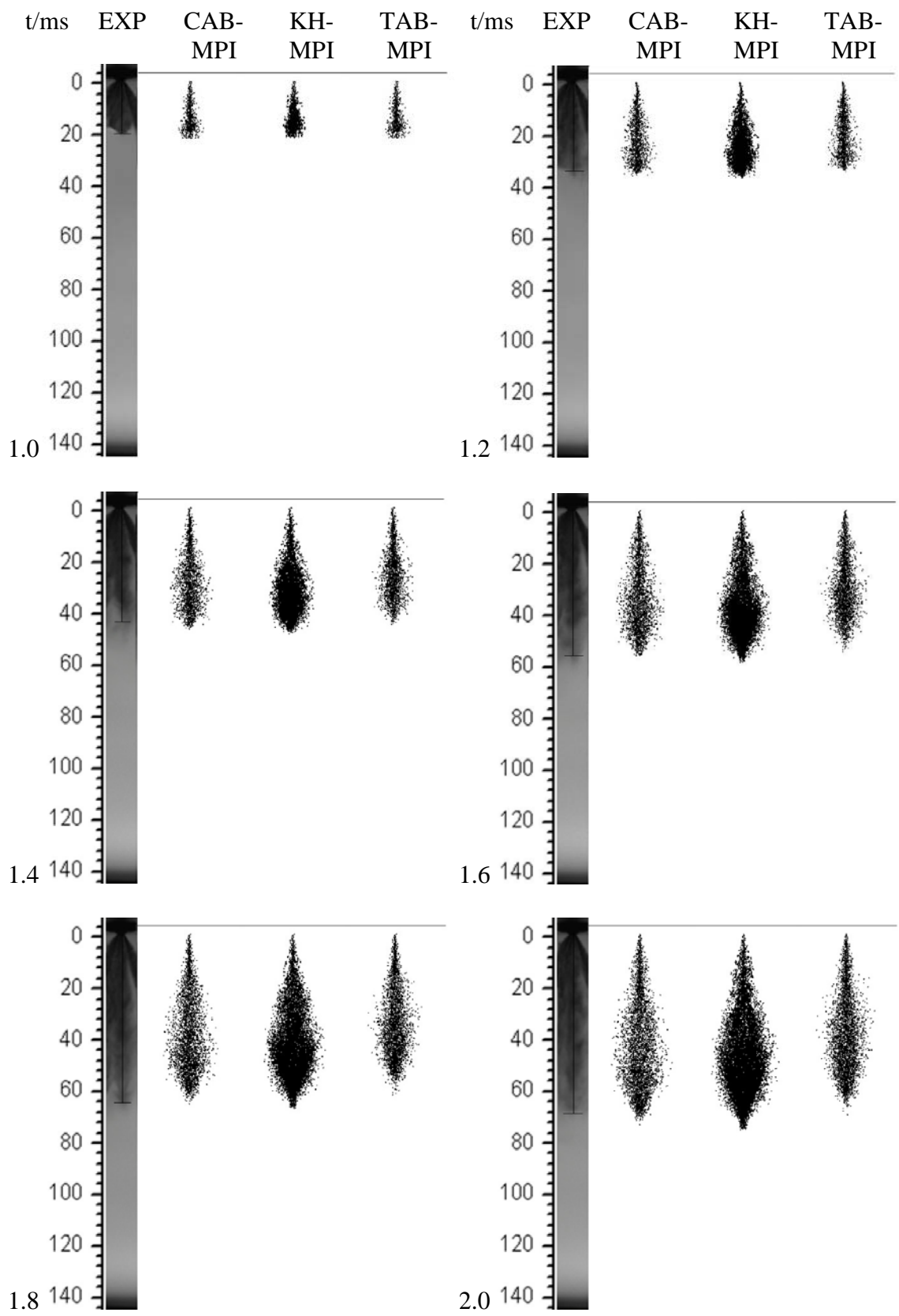


Fig.4.16 Comparisons of predicted and measured spray development

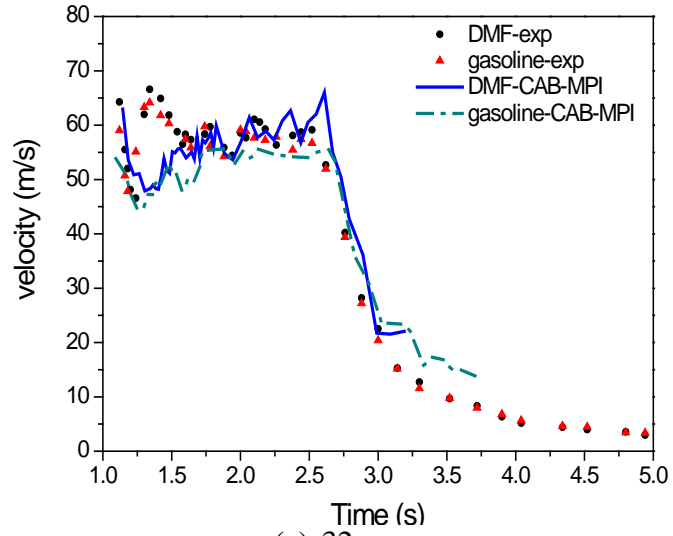
Compared to the over-prediction on its axial mean velocity and AMD by the KH-MPI and underestimation on its AMD by the TAB-MPI, the simulation results using the CAB-MPI model achieved overall good agreement with the measured results in terms of spray tip penetration, axial mean droplet velocity and AMD distribution.

4.4 Study of the DMF Spray Characteristics

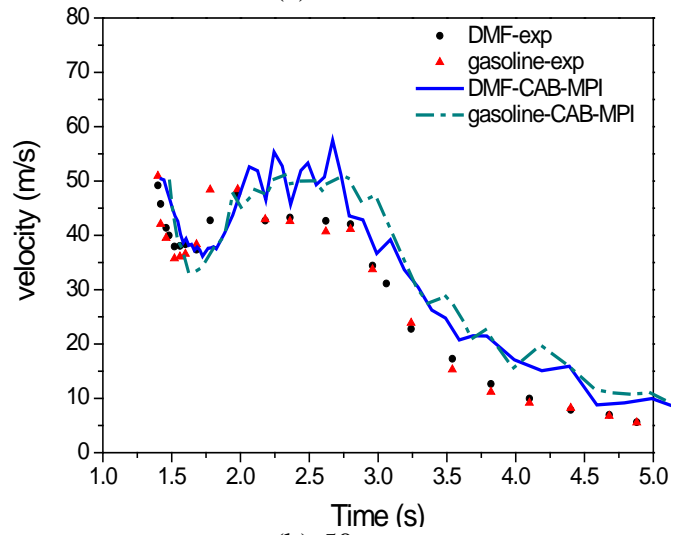
4.4.1 Effect of Fuel Properties

To better understand the spray characteristics of DMF and its application to an SI engine, the fuel spray of DMF and gasoline were investigated by experimental and computational methods in terms of spray penetration, droplet velocity and size distribution of both fuels.

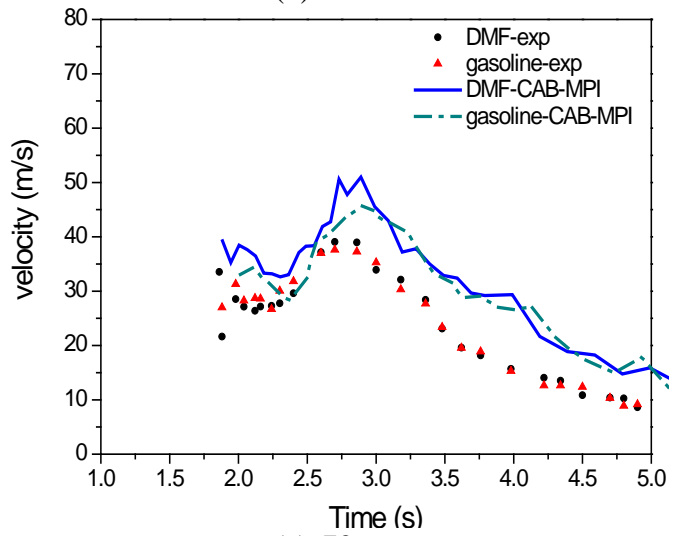
Firstly, the CAB-MPI model for gasoline was also obtained by the measurements as described in section 4.3. Figs.4.17 and 4.18 present temporal evolution of axial velocity and AMD at the axial distance of 32mm, 50mm and 70mm downstream from the nozzle tip, respectively. The PDPA measurement shows the mean droplet size of DMF spray is slightly larger than that of gasoline spray, due to its slower droplet breakup process. A similar trend of the predicted mean droplet size evolution between both DMF and gasoline sprays is observed in Fig.4.18. In general, the predicted axial velocity and mean droplet size match reasonably well with the measurement across all the measurement planes. This indicates that the CAB secondary breakup model with the MPI primary atomization model, is capable of capturing the main spray characteristics of DMF and gasoline fuels.



(a) 32mm

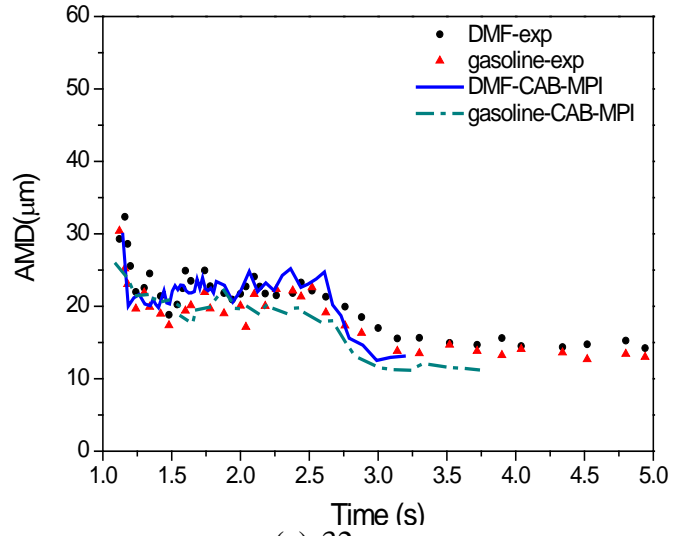


(b) 50mm

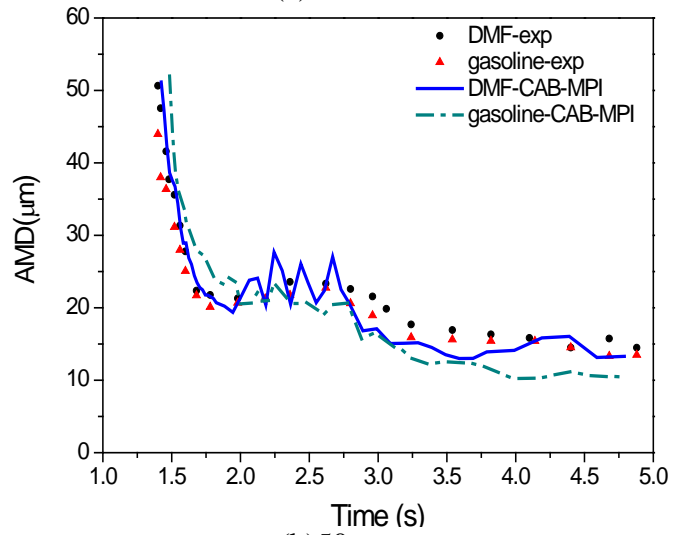


(c) 70mm

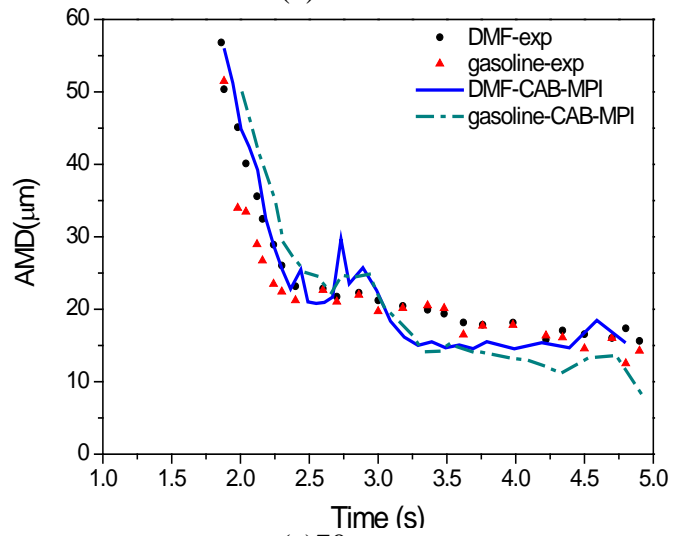
Fig.4.17 Comparison of DMF and gasoline on temporal evolution of axial mean velocity at various distances downstream from the nozzle exit.



(a) 32mm



(b) 50mm



(c) 70mm

Fig.4.18 Comparison of DMF and gasoline on temporal evolution of AMD at various distances downstream from the nozzle exit.

However it seems that the predicted AMDs of DMF are slightly smaller in the early part of Figs.4.18b and 4.18c, while in fact, they are not. It can be seen that the axial average velocity of gasoline is slightly lower than that of DMF in Fig.4.17a, which results in a short delay on its arrival time for the far field from the nozzle compared to DMF in Figs.4.18b and 4.18c. This delay makes a visual effect on the comparison of AMD evolution. Besides, there is a gap between the measured and numerical results during the early part of spray evolution for the 32 mm case in Fig.4.17a. The discrepancy of the early stage of spray evolution between the simulation and measurement can be explained by the initial sac spray associated with the injector sac volume and the transient injector needle opening effect. The sac spray is normally characterized by large droplet size and long penetration length, due to poor atomization, which is observed in Fig.4.17a. However, in the current simulation the mean injection rate is assumed simply as a square wave, without the consideration of the sac spray.

In addition, it is notable that the initial AMD of DMF is larger than that of the gasoline spray, and the mean droplet size difference decreases as AMD reaches a stable level as shown in Fig.4.18. Based on Eq.3.21, the calculated primary breakup diameter is proportional to the surface tension. Under a certain condition, higher surface tension leads to larger primary breakup diameter and lower Weber number. The surface tensions of DMF and gasoline are known to be 25.9 and 20 dyne/cm (see Table.1.2), respectively. Thus, the higher surface tension of DMF results in a larger mean droplet size to that of gasoline.

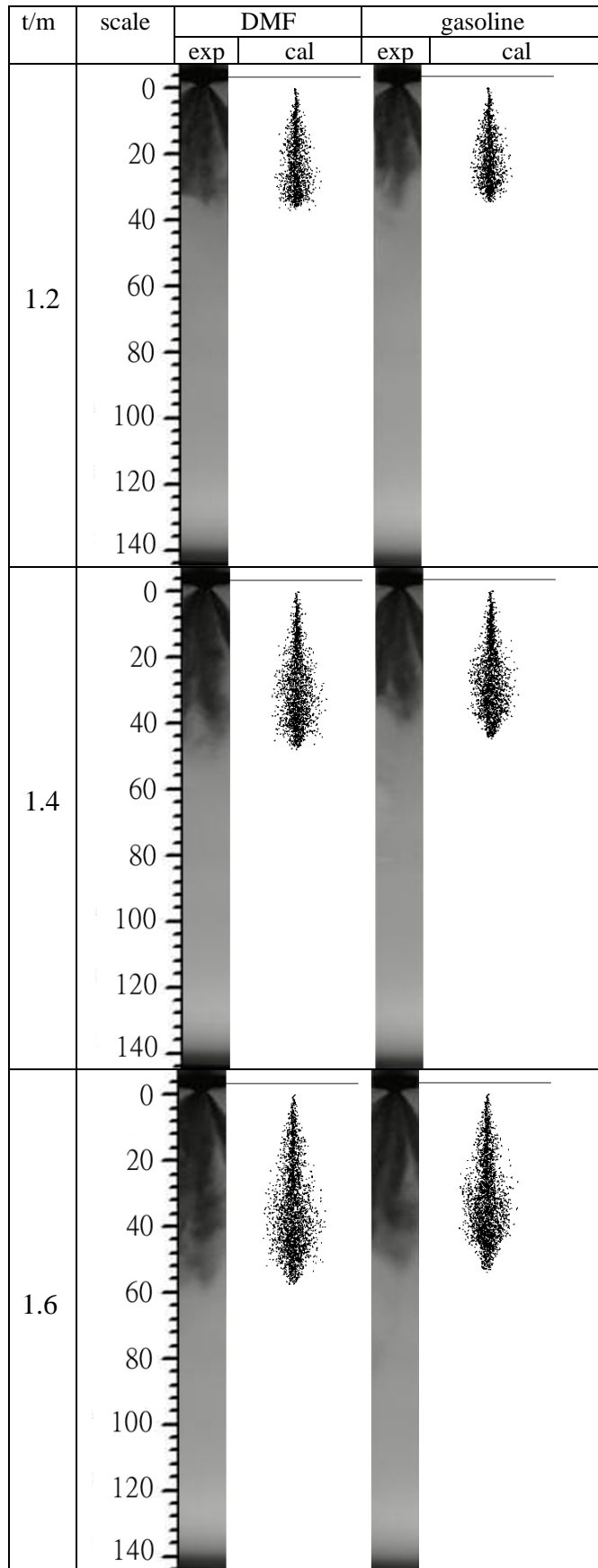


Fig.4.19 Comparisons of DMF and gasoline on spray development

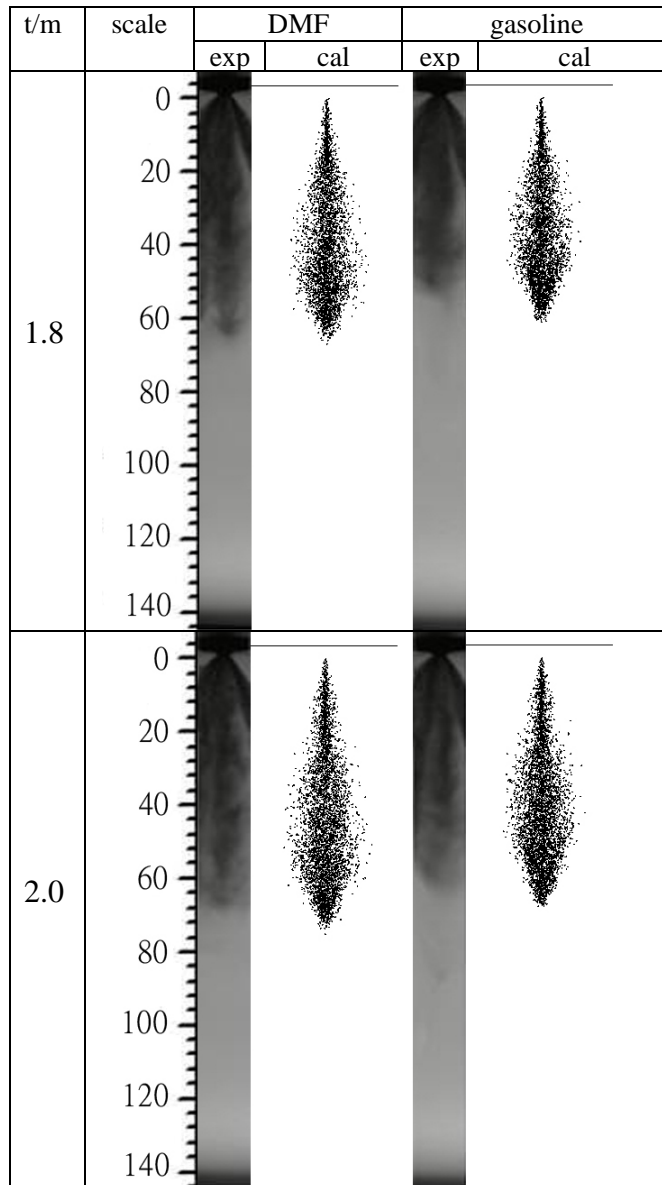


Fig.4.19 Comparisons of DMF and gasoline on spray development (cont.1)

In order to understand how the spray plume develops, Fig.4.19 presents the snapshots of the shadowgraph and simulation of both DMF and gasoline sprays. It is shown clearly that the tip penetration of DMF is slightly longer than that of gasoline, despite their similar velocities [163]. As compared with the experiment, the spray simulation is in a good consistency with the shadowgraphs in terms of the overall spray plume shapes and spray tip penetration,

although slightly over-predicted penetrations are observed at 2.0 ms for both of fuels, owing to the overestimation of axial velocity at far field as illustrated in Fig.4.17c.

4.4.2 Effects of Injection Pressure

To accelerate the vapor rate of fuel and improve the mixing quality in the real SI engine, a high injection pressure, such as 150 bar is a common option. Thus, the influence of injection pressures on DMF's spray characteristics was studied in terms of spray tip penetration and local SMD by a visualization technique and PDPA, respectively.

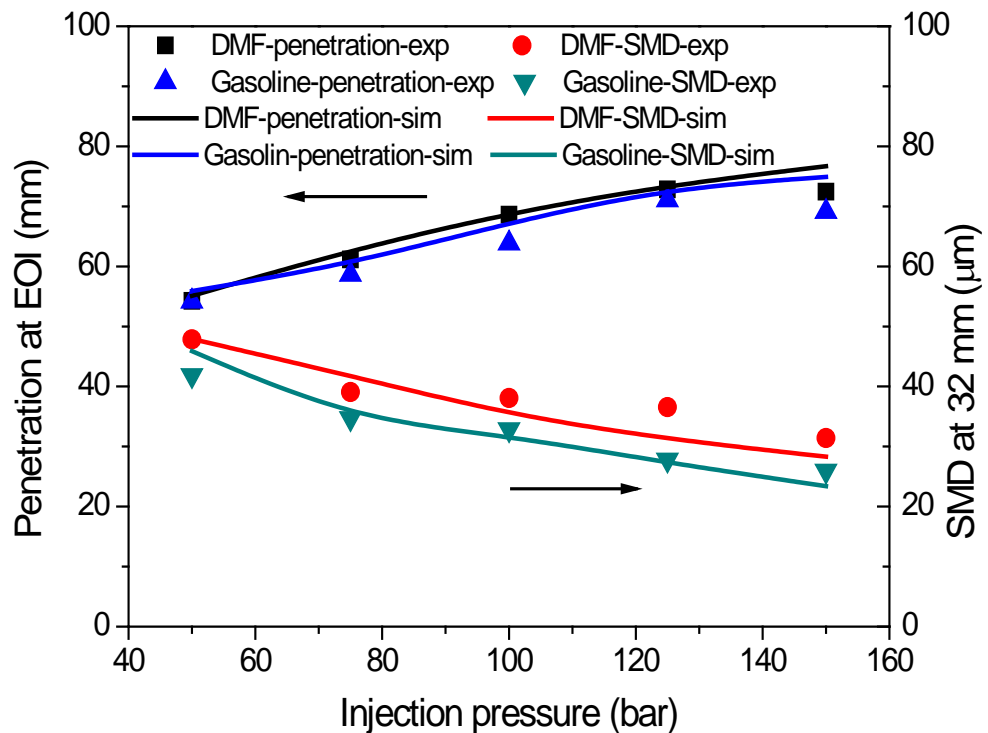


Fig. 4.20 Comparisons of spray tip penetration at EOI and local SMD at the axial distance of 32 mm downstream from the nozzle exit under various injection pressures.

The injection pressures are adjusted at 50 bar, 75 bar, 100 bar, 125 bar and 150 bar. The spray structure under various injection pressures is captured by the Shadowgraph technique. The

spray penetration at the end of injection was chosen for quantitative analysis. Firstly, as presented in Fig.4.20, the tip penetration reflects a considerable linearity with injection pressure on experimental and computational results, but it decreases slightly from 125 bar to 150 bar from visualization data. It is possible that under an injection pressure of 150 bar, vapor penetration becomes remarkable and droplet evaporation slows down the tip penetration growth. In addition, the similarity of DMF and gasoline on spray tip penetration maintains under different injection pressures.

Also the influence of injection pressure on the droplet size was studied at the same position with DMF and gasoline, as shown in Fig.4.20. The testing position was chosen on the axis, 32mm from the nozzle. In general, the higher the injection pressure is, the smaller the SMD is. In the scenarios among the chosen injection pressures, a nice linear trend can be observed. The profiles of DMF and gasoline show similar trends. However, the SMD of DMF spray decreases from almost 50 μm at an injection pressure of 50bar to approximately 30 μm at 150bar, which is generally 5 μm higher than that of gasoline at the same injection pressure. Overall predicted SMD of both fuels reproduces the experimental results. However, under an injection pressure of 50 bar, simulated SMD of gasoline is almost 4 μm higher than the measured SMD. In the case of DMF, it is notable that a considerable difference is found between experimental and predicted results at certain injection pressures. Given that the experimental results are scattered around the predicted values, the difference may result from the measurement error.

4.4.3 Effects of Ambient Pressure

Fig. 4.21 illustrates the influence of the ambient pressure on the spray tip penetration at EOI and spray cone angle of both fuels. Generally, predicted penetration at EOI and spray cone angle achieves a good agreement with those measured. From the trend of development, it can be seen from Fig. 4.21, spray tip penetrations of two fuels remarkably reduce with increasing ambient pressure; in contrast, spray cone angles increase with increasing ambient pressure. As to the penetration at EOI, it is interesting that penetration of gasoline is more sensitive to ambient pressure than that of DMF.

Specifically, penetration of gasoline decreases almost linearly as the ambient pressure increases; while after a sharp decline from 1 to 3 bar, the reduction rate of DMF penetration slows down from 3 to 6 bar. In terms of spray cone angle, a tiny difference between these two fuels can be found under individual ambient pressures. According to Eq.3.31, the spray cone angle is inversely proportional to the fuel liquid density. Under a certain condition, higher fuel liquid density leads to smaller spray cone angle. The liquid densities of DMF and gasoline are known to be 895.4 and 751 kg/m³ as listed in Table 1.2, respectively. Thus, the higher liquid density of DMF results in a smaller spray cone angle, compared to that of gasoline.

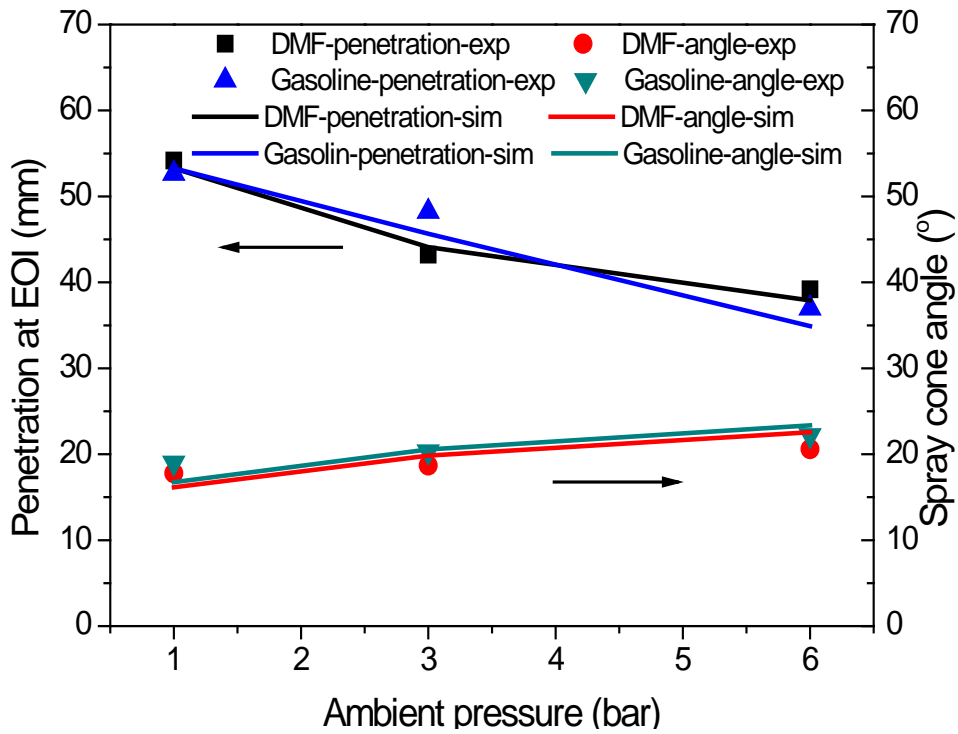


Fig.4.21 Spray tip penetration at EOI and spray cone angle under various ambient pressures

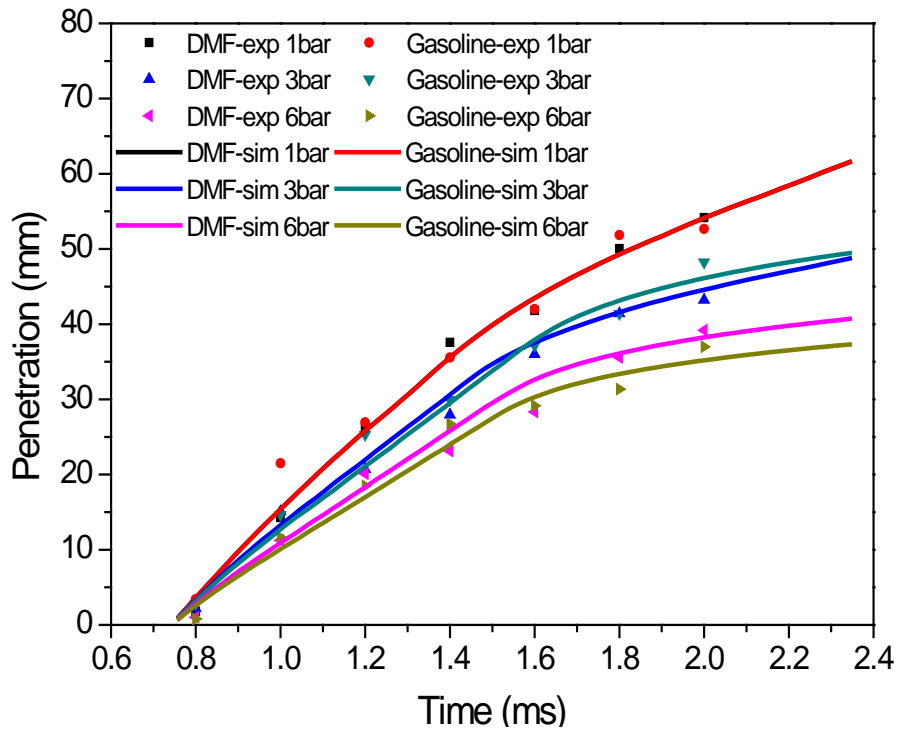
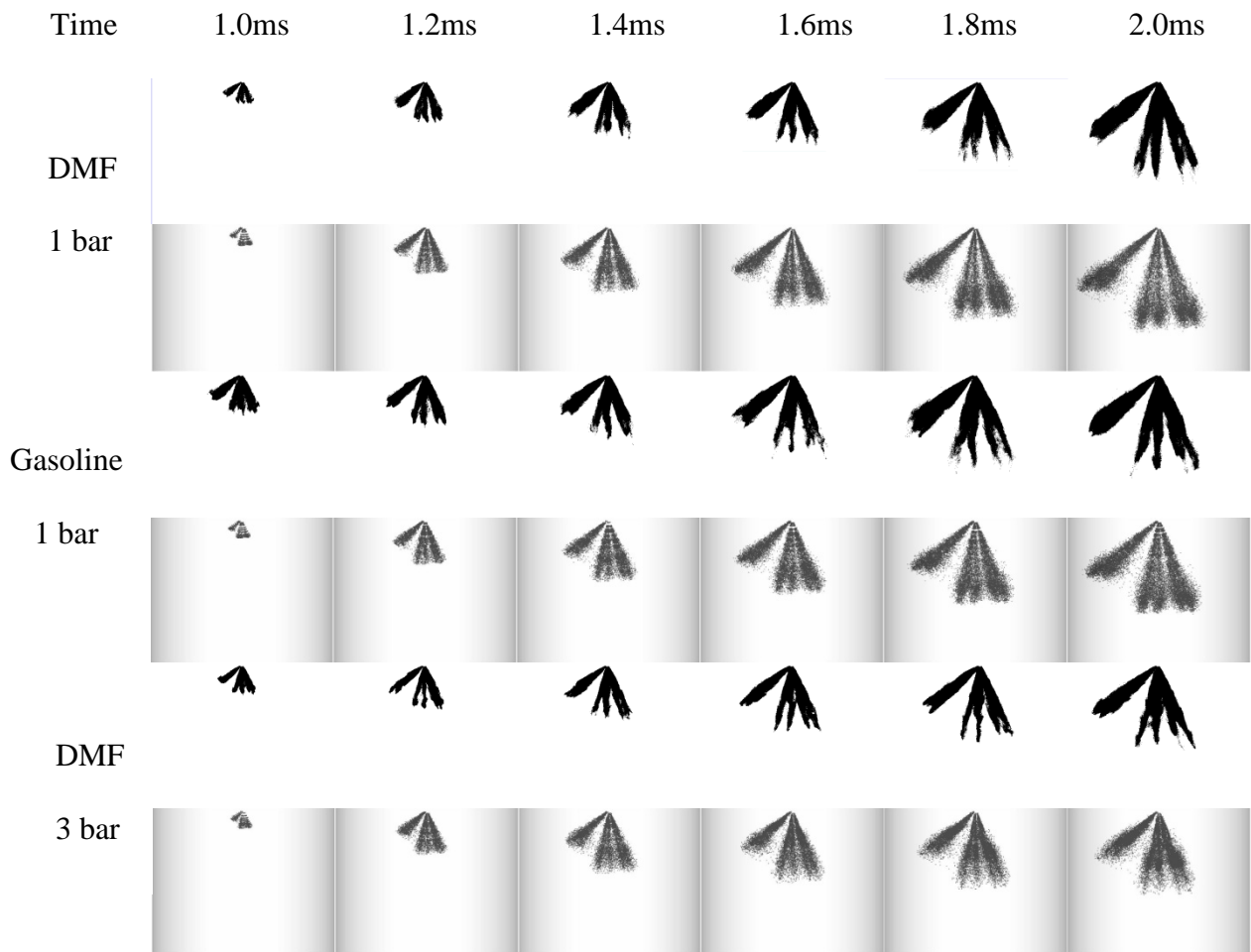
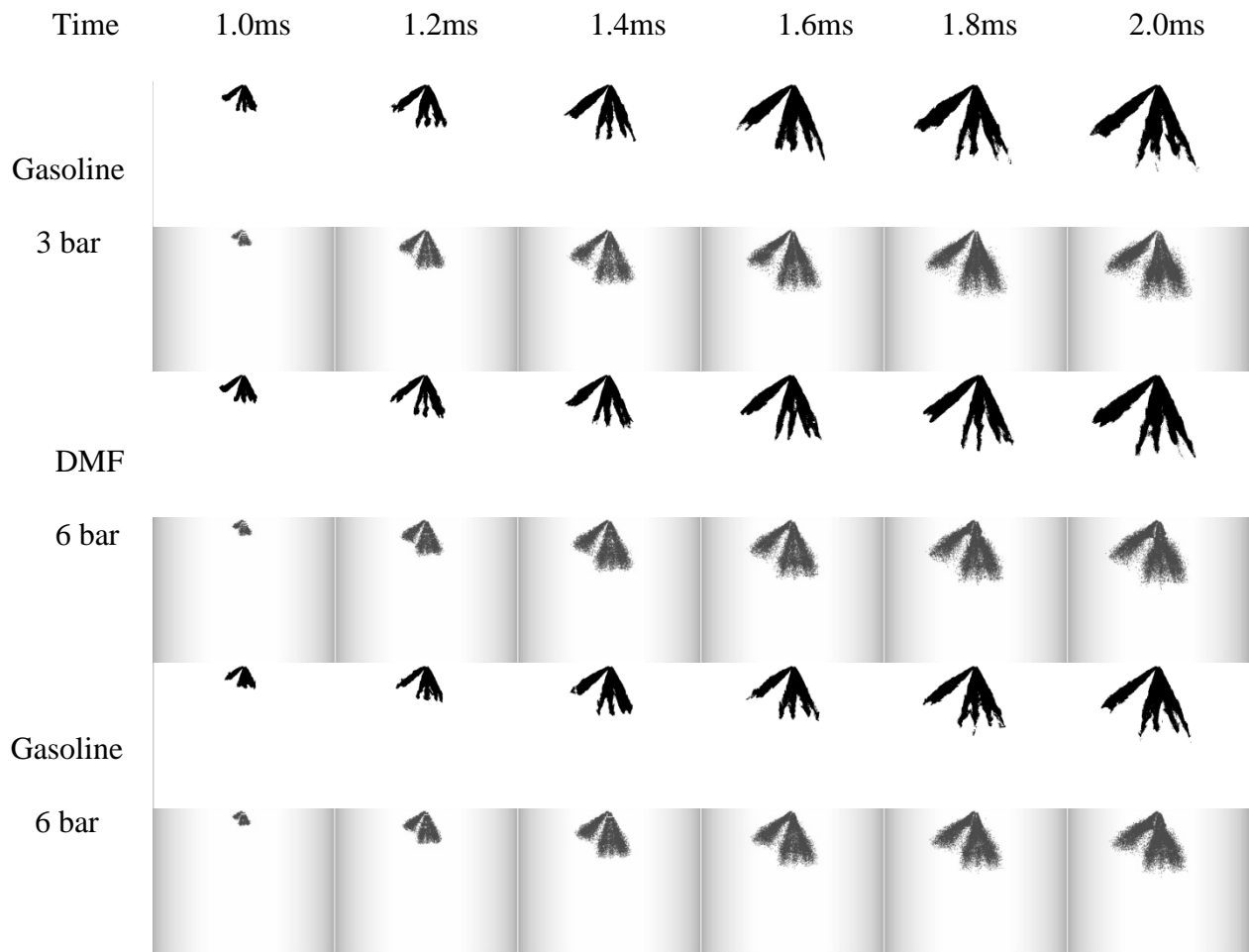


Fig.4.22 Temporal evolution of spray tip penetration under various ambient pressures

Fig.4.22 presents the temporal evolution of spray tip penetration of both fuels under ambient pressures of 1, 3 and 6 bar, respectively. Generally, the predicted profile of spray tip penetration reproduces the trend of the experimental results. From the view of individual fuel sprays, there was almost no difference in spray tip penetration between the two fuels under 1 bar; when the ambient pressure is up to 3 bar, the initial gradient of penetration of gasoline was slightly smaller than that of DMF; when the ambient pressure reaches 6 bar, the growth rate of penetration of gasoline is obviously lower than that of DMF.



4.23 Comparison of spray development under various ambient pressures



4.23 Comparison of spray development under various ambient pressures (cont.)

In order to understand how the spray multi-jet develops, Fig.4.23 presents the snapshots of the shadowgraph and simulation of both DMF and gasoline sprays under various ambient pressures of 1 bar, 3 bar and 6 bar. As compared to the experiment, the spray simulation is in consistency with the shadowgraphs in terms of the overall spray plume shape and spray tip penetration, although slightly underestimated penetrations are observed near the end of injection under an ambient pressure of 6 bar for both fuels, due to the interaction among individual jets at far field as shown in Fig.4.23.

4.5 Summary

In order to simulate the spray atomization of DMF as engine fuel, an MPI primary breakup model was implemented into KIVA and secondary breakup models including KH, TAB and CAB were evaluated. These three breakup models were validated and evaluated in the aspects of spray tip penetration, droplet diameter and droplet velocity by PDPA and backlit imaging experiments. The conclusions obtained from the simulation research, given as:

1. The spray tip penetration of DMF was well reproduced by the MPI primary breakup model, which includes a better description of the primary droplet disintegration from the intact liquid core. Compared to the over-prediction on its axial mean velocity and AMD by the KH-MPI and underestimation on its AMD by the TAB-MPI, the simulation results by using the CAB-MPI model achieved an overall good agreement with the measured results in the aspects of spray tip penetration, axial mean droplet velocity and AMD distribution.
2. The spray tip penetration is adjusted with the constants in the Hiroyasu model of $H_0=3.0$, $H_{ln}=8.0$ and $L_{c,grow}=0.75$. The spray cone angle model is adjusted with the constant of $C_\theta=0.5$ in the Naber-Siebers model.
3. Compared to gasoline, higher surface tension of DMF leads to larger primary breakup diameters and further mean diameters. The profiles of temporal evolutions of the droplet size distribution and velocity of DMF spray are similar to those of gasoline.
4. As the injection pressure increases, generally penetrations of both fuels increase and SMD reduces. At the same injection pressure, SMD of DMF spray is generally 5 μm larger than that of gasoline at the axial distance of 32mm from the nozzle exit.

5. With the increase of ambient pressure, spray tip penetrations of both fuels decrease and spray cone angles increase reversely. Generally, in terms of penetration, the decrease of DMF spray is smaller than that of gasoline; additionally, spray cone angle of DMF spray is slightly smaller than that of gasoline due to its higher liquid density.

Chapter 5 SPRAY MODEL VALIDATION IN A SINGLE CYLINDER ENGINE

5.1 Introduction

In Chapter 4, the spray model has been validated in an open air or constant volume vessel. In this proceeding chapter, the spray model will be validated in a real single cylinder engine by using a High Speed Photography (HSP) imaging technique, where two typical injection strategies, early and late injections are considered. The initial pressure and temperature are taken from the results of a 1-D WaveTM model. To provide the initial conditions for 3-D CFD simulation, a 1-D code Wave is validated with experimental results.

5.2 Experimental Set-up

The engine used in this study is a 4-valve single cylinder SI optical engine based on the configuration of a Jaguar 2.5L V6 gasoline direct injection engine (see Fig.5.1). HSP data were captured by a high speed digital camera Phantom V7.1. A view in a horizontal direction can be captured through a solid glass liner and a view in a vertical direction can be captured using a 65mm round quartz window installed in the extended piston, offering an optical access path through the combustion chamber with a 45 degree stationary mirror. This high-speed camera was synchronized with the fuel injection. After performance matching, the sample rate was set to 6006 frames per second.

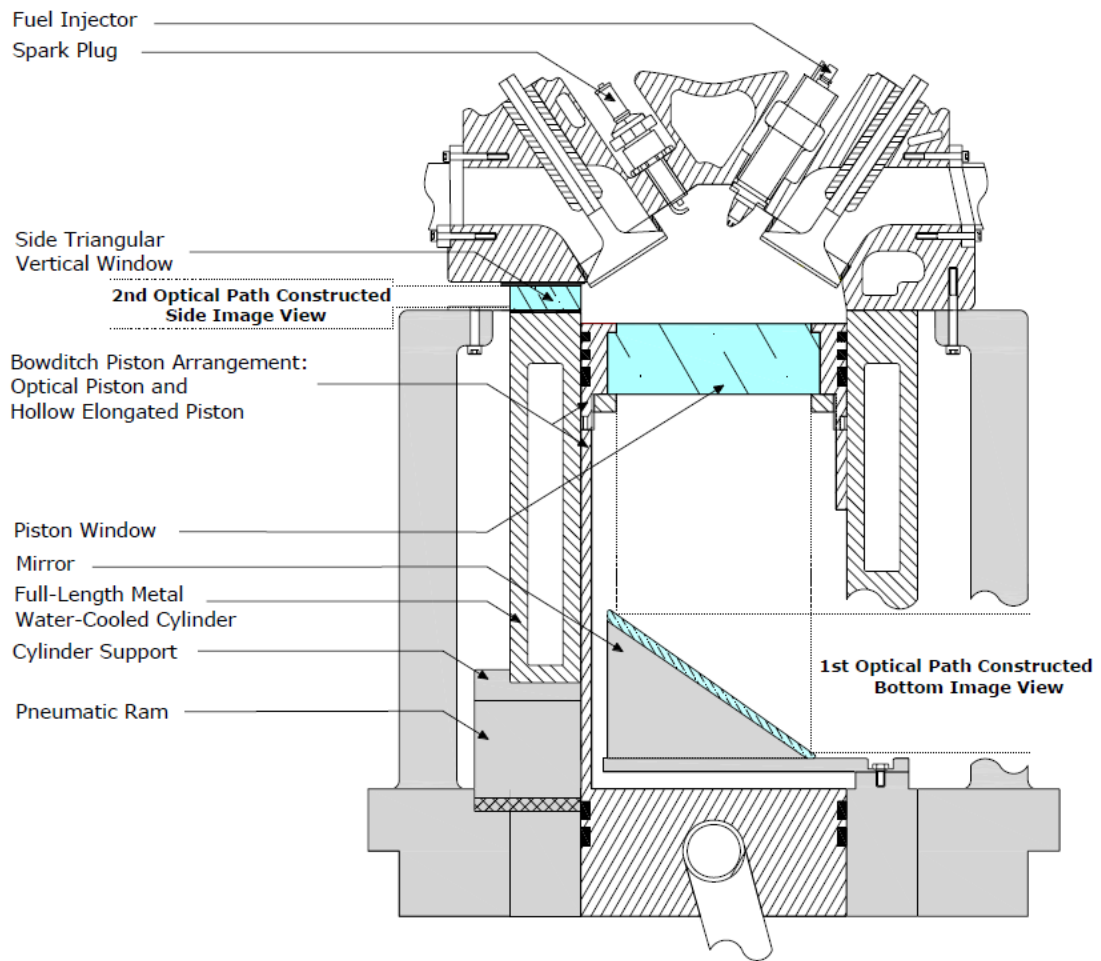


Fig.5.1 Schematic of the optical engine [170]

5.3 Model Validation

Table 5.1 shows the modeled engine specifications and injection parameters. The engine is run at wide open throttle (WOT) and 800rpm. The calculation is conducted from Exhaust Valve Opening Time (EVO) at 204 °CA Before Top Dead Centre (BTDC) (0 °CA relative to intake TDC) to 260°CA After Top Dead Centre (ATDC). The initial pressure and temperature are taken from the results of a 1-D Wave model. Given that the computation domain was a closed system under this circumstance, the initial flow field was assumed to be uniform.

Table 5.1 Engine specifications and injection parameters

Displacement	0.56L	
Bore	89.0mm	
Stroke	90.3mm	
Connecting Rod	154mm	
Compression Ratio	11.3:1	
Intake Valve Open	16°CA BTDC	
Exhaust Valve Close	37 °CA ATDC	
Injector Type	6-hole solid cone	
Injection Pressure	150 bar	
Injection Duration	1ms	
Injected Fuel Mass	11.48mg	
Start of Injection	80 °CA ATDC	250°CA ATDC

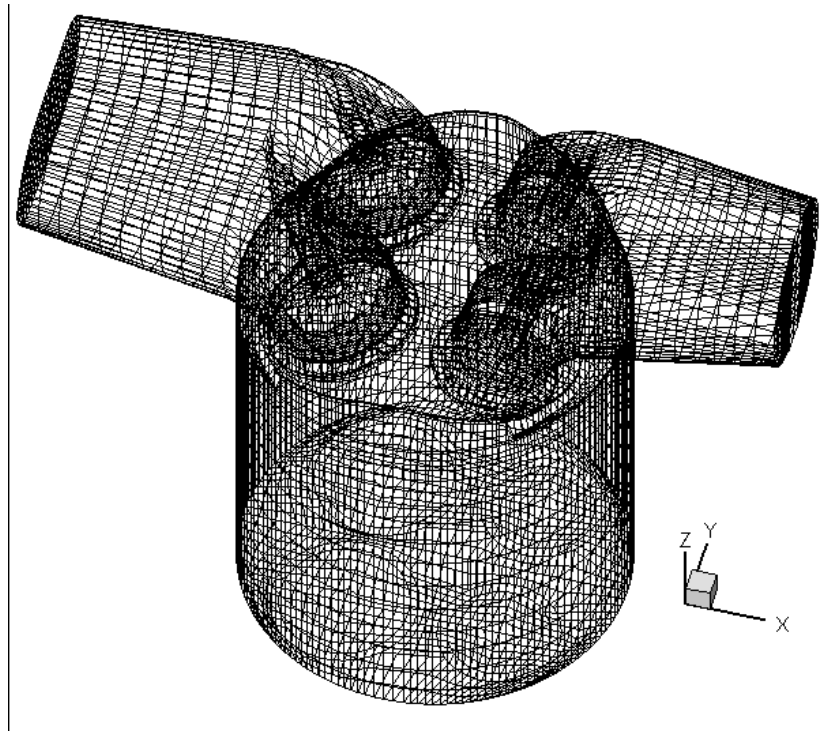


Fig.5.2 Three-dimensional mesh in the simulation of the optical engine

Fig.5.2 presents the three-dimensional mesh generated for the optical engine simulation. The total number of cells is over 50,000. Beale [184] obtained grid independent results with a

1mm cell size and the case with a 2mm cell size achieved an acceptable accuracy in the prediction of the evaporated spray [185]. In other words, the selection of a 2mm cell size was based on the balance between accuracy and time expense.

5.3.1 Numerical 1-D Single Cylinder Engine Model

As a supporting tool, a 1-D engine and gas dynamics simulation software Wave has been applied to provide the initial cylinder pressure and temperature for 3-D CFD simulation. Fig.5.3 shows a schematic view of the 1-D model established with the elements in Wave software. Based on the configuration of virtually an intake, combustion and exhaust system, the performance of a 4-valve single cylinder optical engine can be reproduced.

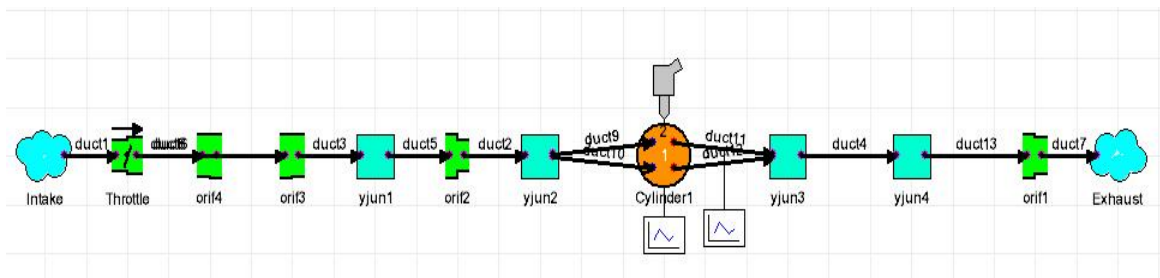


Fig.5.3 Schematic of Wave model for the single cylinder optical engine

In order to validate this 1-D engine model, a motored condition has been selected as the test case. Fig.5.4 presents the comparison of experimental and calculated in-cylinder pressure temporal evolution on the condition of a motoring engine. From the presented pressure chart, it is evident that computational values match well with the measured values and the peak pressure and pressure rise rate are predictable with the current engine model. The maximum divergence between these results is at 158°CA ATDC, corresponding approximately to 10%.

It is indicated that the discrepancy results from the simplification of the geometry in the intake and exhaust system and assumption of flow discharge coefficient.

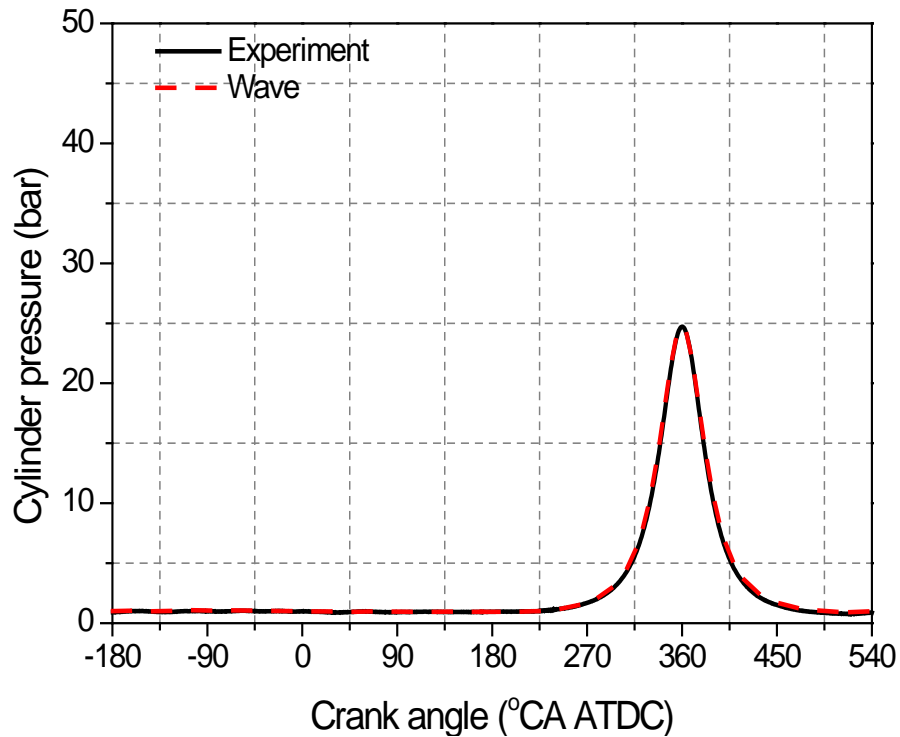
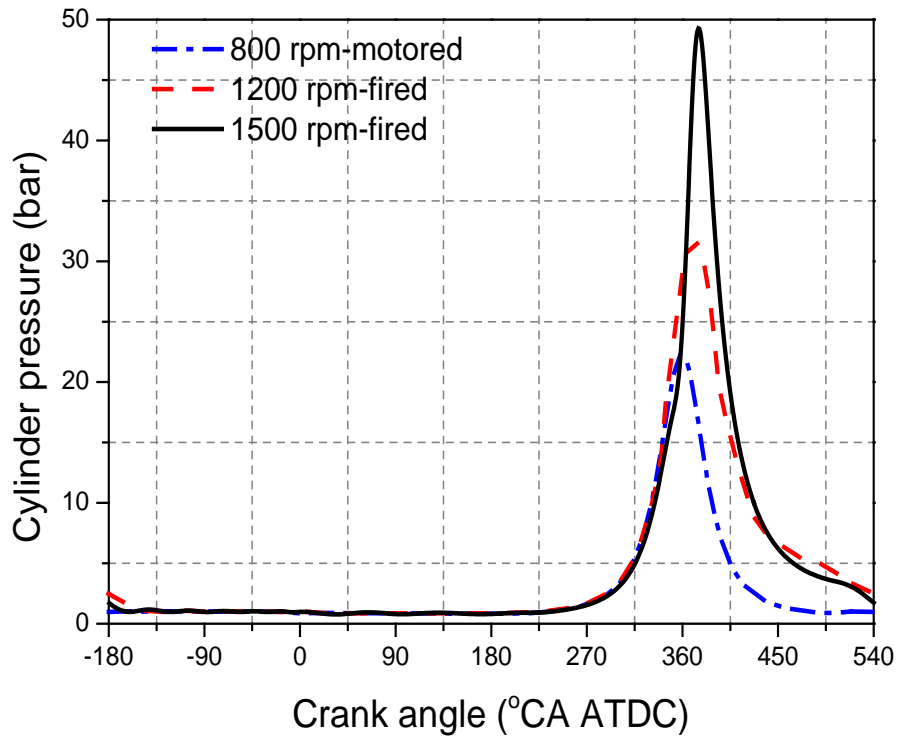
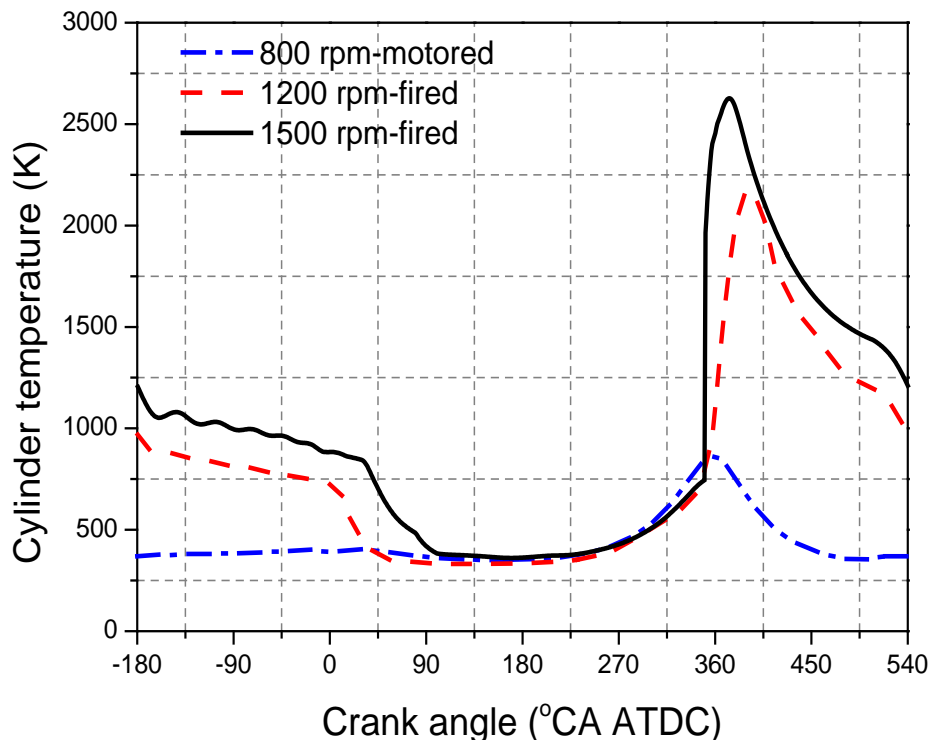


Fig.5.4 Comparison of in-cylinder experimental and simulation pressure trace in a motored condition

Fig.5.5 presents the predicted cylinder pressure and temperature against the crank angle for the subsequent validation of the spray and combustion modelling, including a motored condition at 800 rpm and fired conditions at 1200 and 1500 rpm.



(a) Pressure



(b) Temperature

Fig.5.5 Cylinder pressure and temperature histories predicted by Wave for the modeling validation

5.3.2 Validation with HSP Images from an Optical Engine

This sub-section will discuss the comparisons of High Speed Photography (HSP) images and simulation results for early and late injection events.

Firstly, the pattern of the six-hole injector is shown in Fig.5.6. As presented, there are two sets of three asymmetric holes in the injector nozzle, which is originally used for a spray-guided combustion system. Different inclination angles are used to spread fuel into individual areas of the cylinder. The symmetric plane of spray is laid parallel with the tumble plane of the engine as seen in Fig.5.6b. This style of injector layout is used for the purpose of the current HSP imaging to identify the individual sprays at the orientation of the tumble plane.

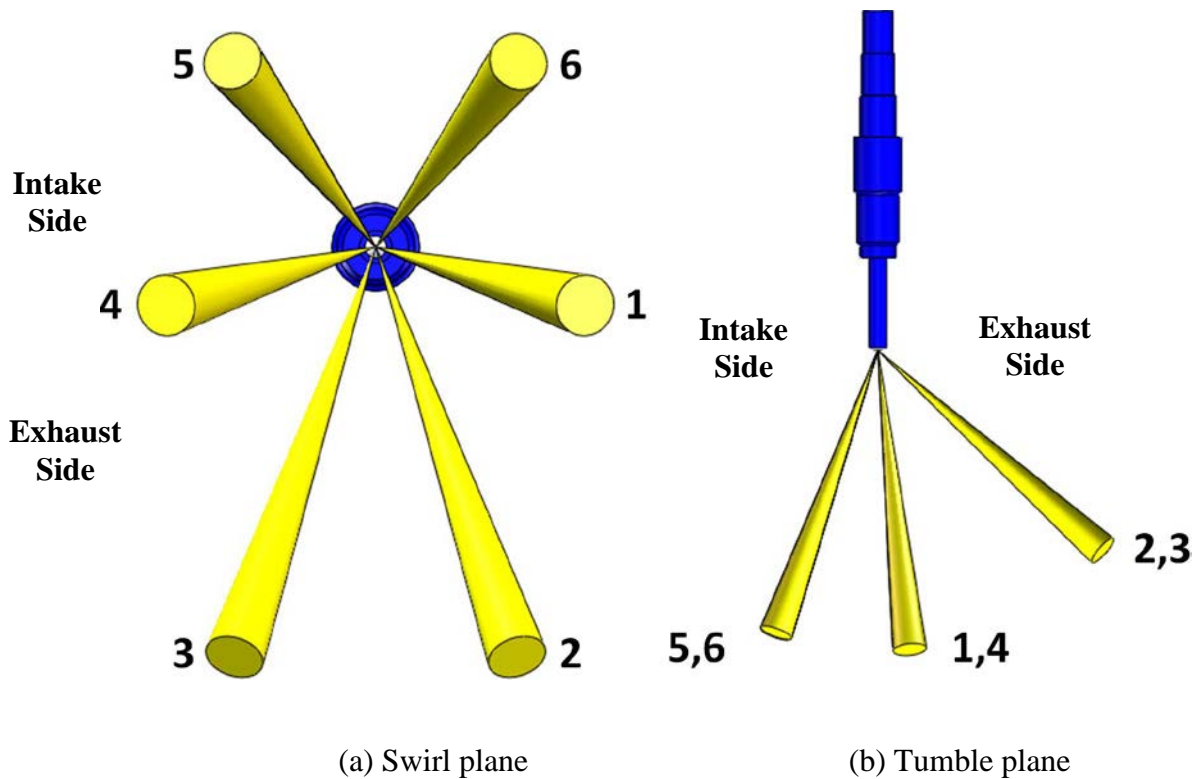


Fig.5.6 Schematic of Spray Pattern in HSP Imaging

Figs.5.7 and Fig.5.8 present the comparison of HSP images and simulation results in an early injection case with a start of injection at 80° CA ATDC from the side and bottom views, respectively. The injector is vertically installed in the cylinder head with an offset from the centre (spark plug) as seen in Fig.5.8.







°CA ATDC	HSP Image	Simulation
80.8		
81.6		
82.4		

Fig.5.7 Side view of HSP images and CFD comparisons in an early injection event


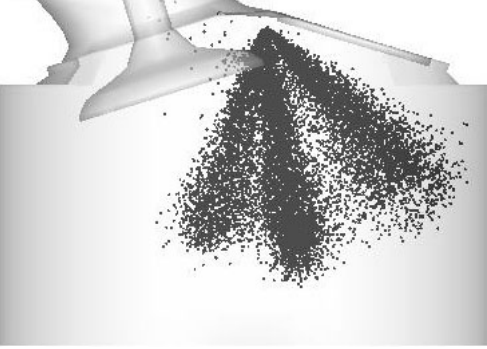

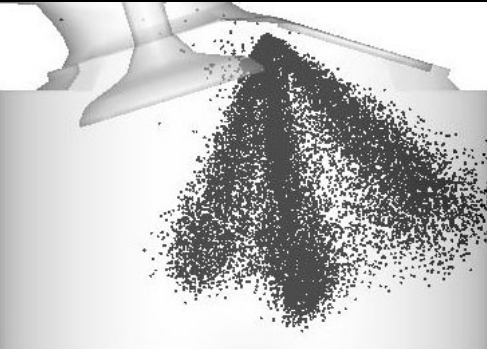

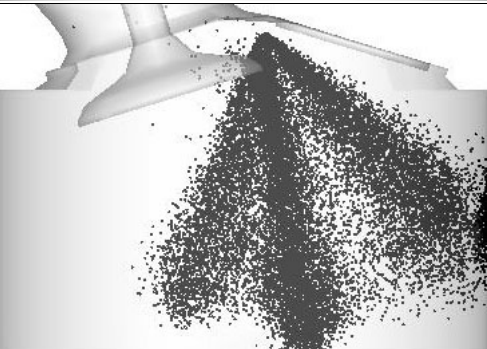
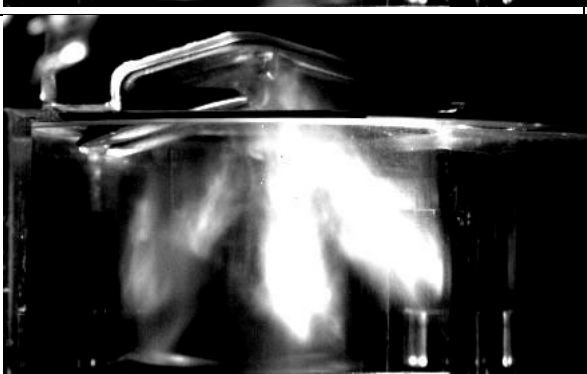
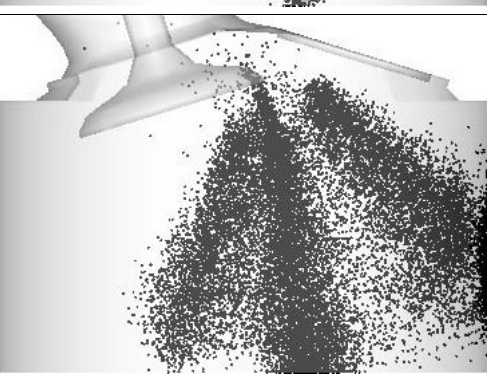
°CA ATDC	HSP Image	Simulation
83.2		
84.0		
84.8		
85.6		

Fig.5.7 Side view of HSP images and CFD comparisons in an early injection event (cont.)

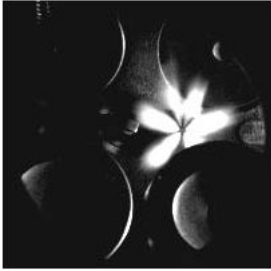
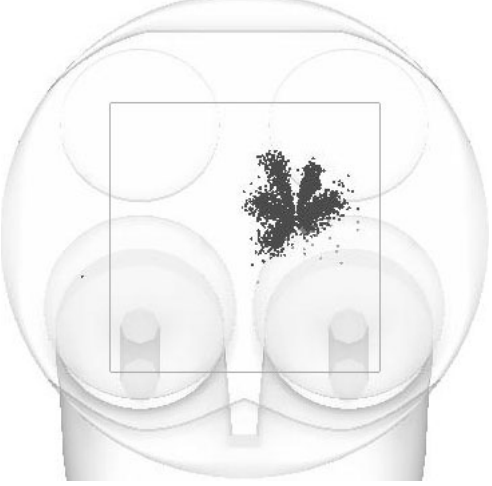
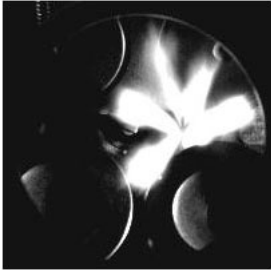
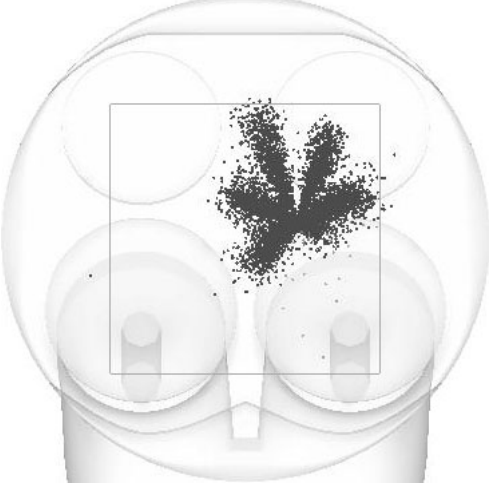
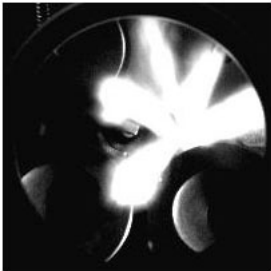
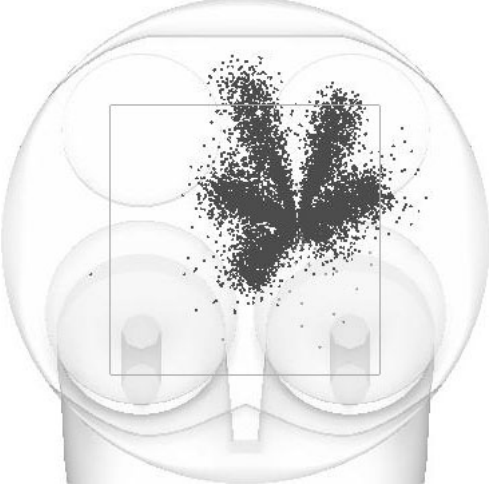
°CA ATDC	HSP Image	Simulation
80.8		
81.6		
82.4		

Fig.5.8 Bottom view of HSP images and CFD comparisons in an early injection event

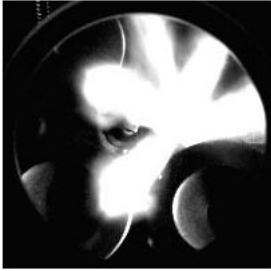

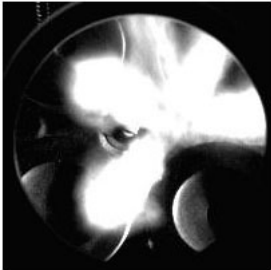
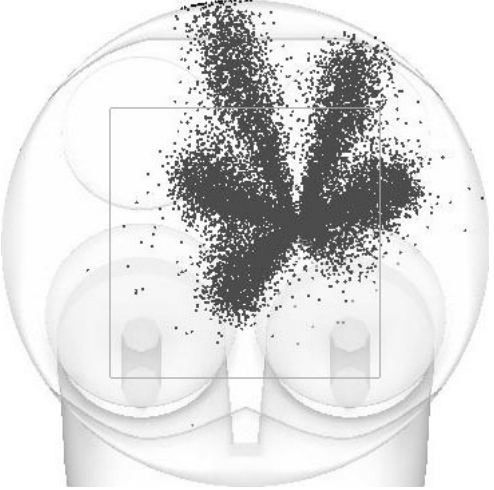
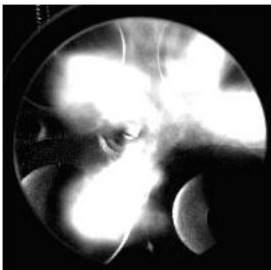
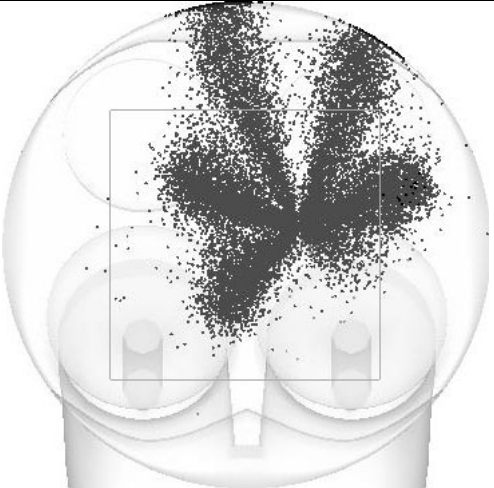
°CA ATDC	HSP Image	Simulation
83.2		
84.0		
84.8		

Fig.5.8 Bottom view of HSP images and CFD comparisons in an early injection event (cont.1)

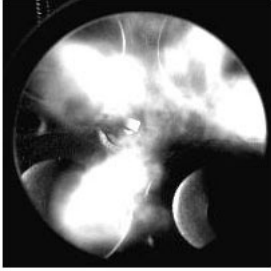
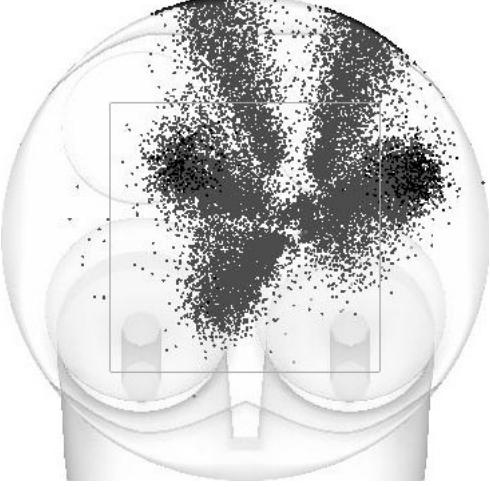
°CA ATDC	HSP Image	Simulation
85.6		

Fig.5.8 Bottom view of HSP images and CFD comparisons in an early injection event (cont.2)

From the side view of the early injection event, at the beginning of injection, almost no interaction between air flow and spray interaction occurs. The interactions become more intense near the end of injection. Finally, the predicted and measured sprays impinge on the piston surface at the same time. From the bottom view, the initial small plumes spread out and then as the piston moves downward, the plumes at the intake side penetrate deeper and the whole pattern becomes asymmetric. This trend of spray development is reproduced by the simulation results. It is notable that it shows one plume impinges on the intake valve and this impingement impedes its penetration into the cylinder, especially after the end of injection (i.e. 85.6° CA ATDC) as seen in Fig.5.7. In addition, spray impingement on the cylinder wall can be observed at 84.0 ° CA ATDC although it is impossible to observe from the HSP images due to its limited visible range limited by the piston window, as presented in Fig. 5.1. In general, the shapes and penetration of the plumes shown in the HSP images are closely predicted by the CFD simulation.

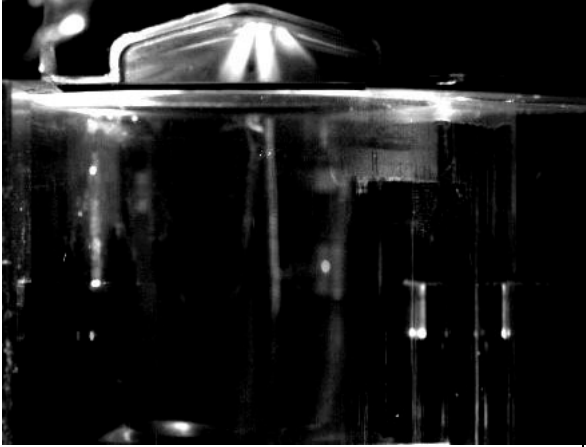
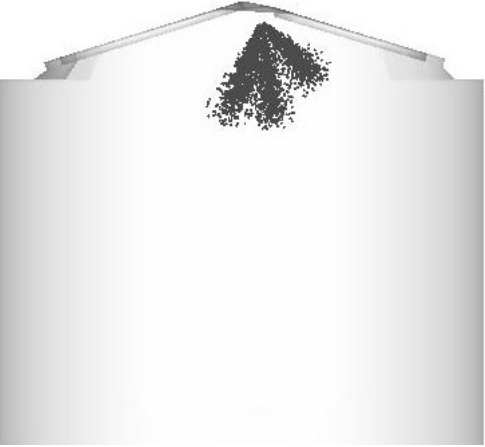
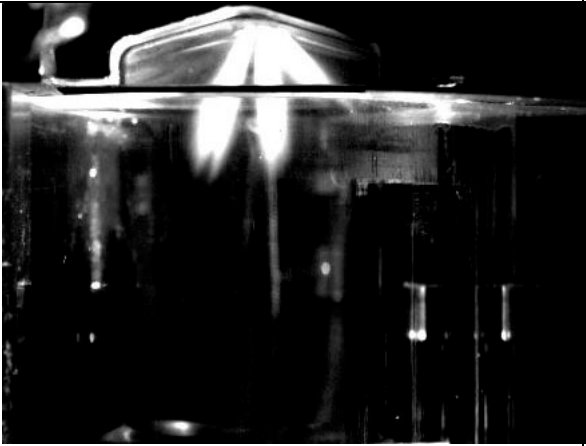
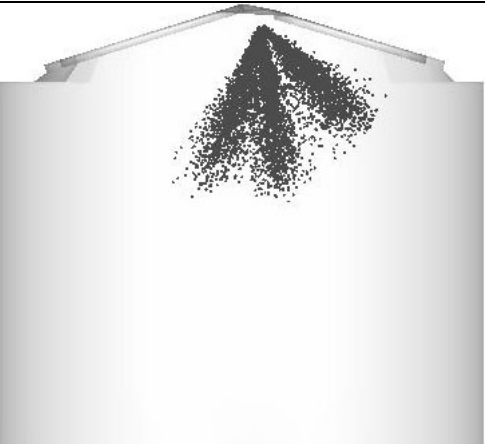

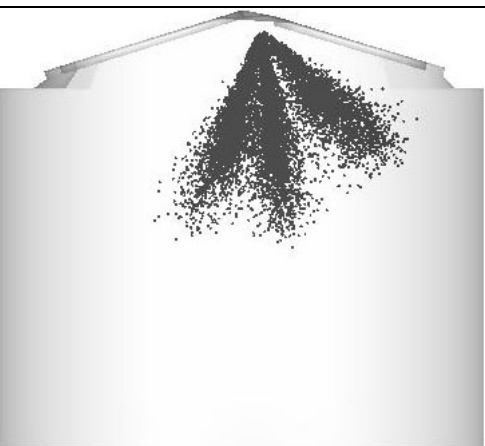
°CA ATDC	HSP Image	Simulation
250.8		
251.6		
252.4		

Fig.5.9 Side view of HSP images and CFD comparisons in a late injection event


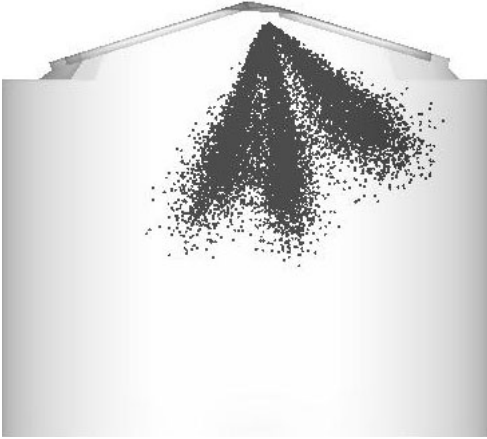

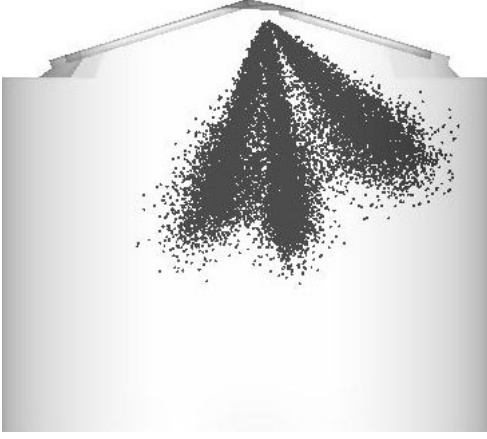


°CA ATDC	HSP Image	Simulation
253.2		
254.0		
254.8		

Fig.5.9 Side view of HSP images and CFD comparisons in a late injection event (cont.1)


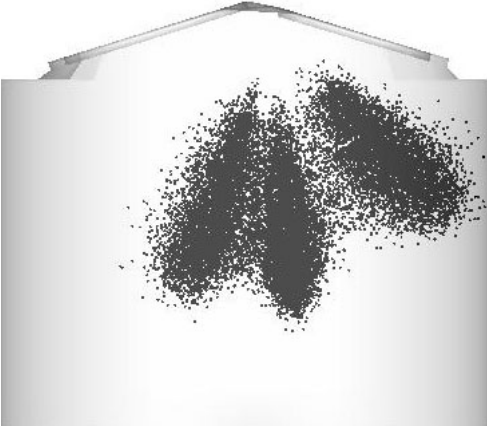
°CA ATDC	HSP Image	Simulation
255.6		

Fig.5.9 Side view of HSP images and CFD comparisons in a late injection event (cont.2)

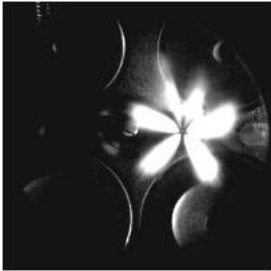
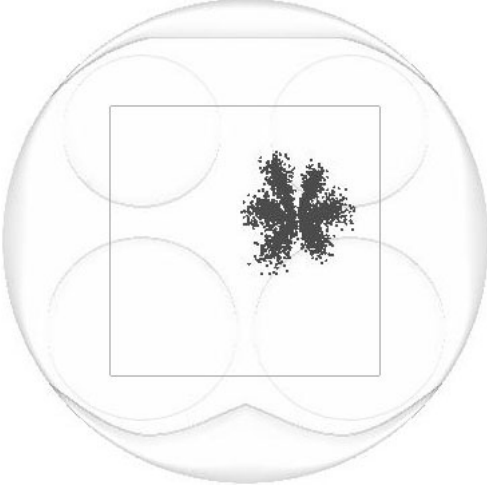
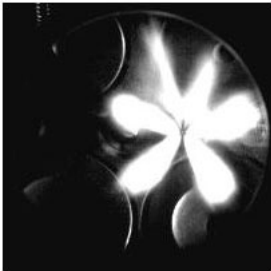
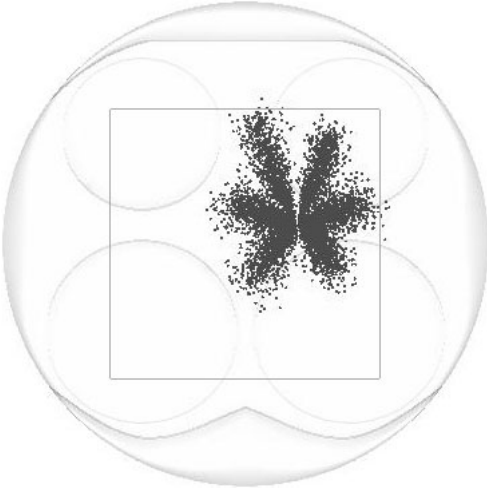
°CA ATDC	HSP	Simulation
250.8		
251.6		

Fig.5.10 Bottom view of HSP images and CFD comparisons in a late injection event

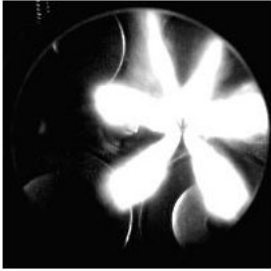
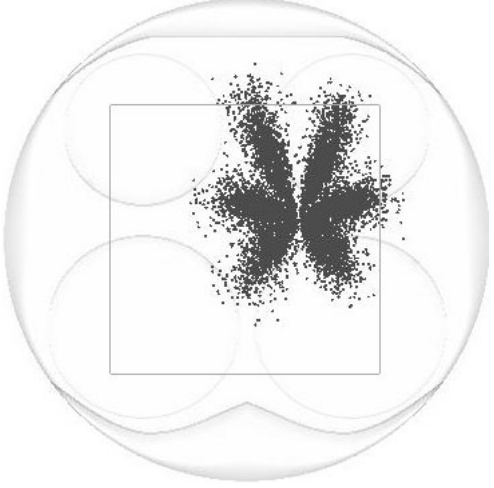
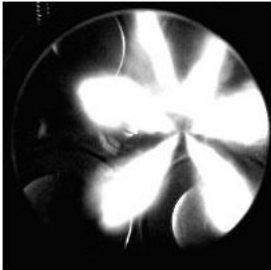
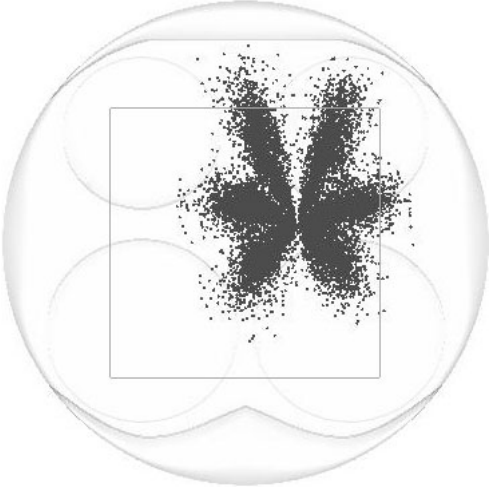
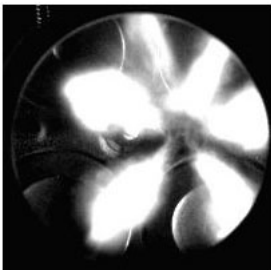
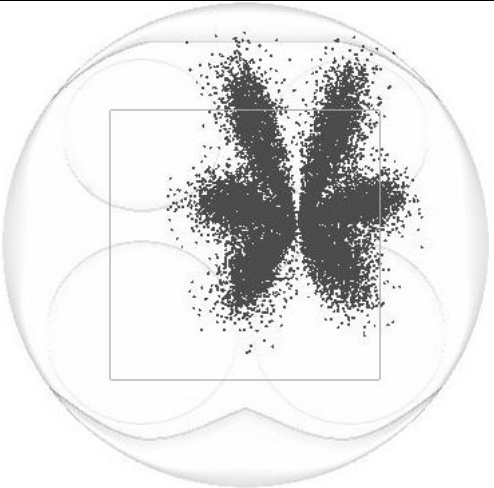
°CA ATDC	HSP	Simulation
252.4		
253.2		
254.0		

Fig.5.10 Bottom view of HSP images and CFD comparisons in a late injection event (cont.1)

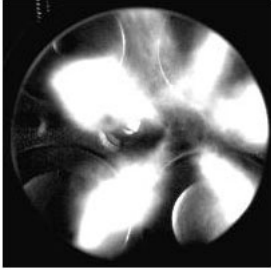
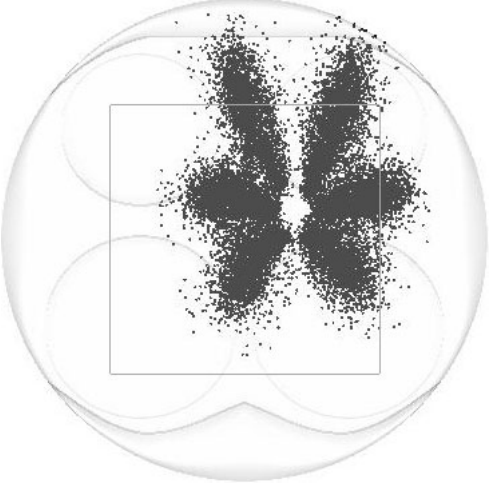
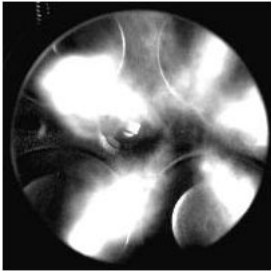
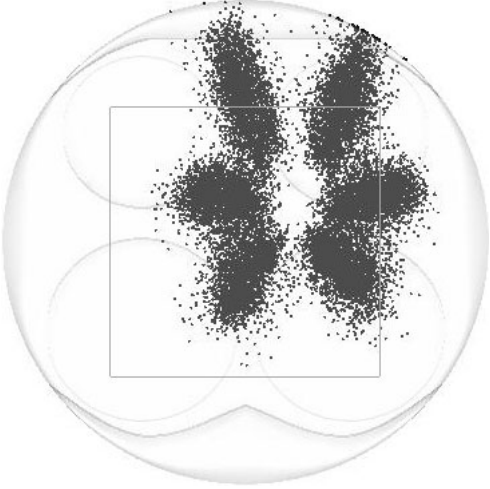
°CA ATDC	HSP	Simulation
254.8		
255.6		

Fig.5.10 Bottom view of HSP images and CFD comparisons in a late injection event (cont.2)

The comparisons in the late injection sequence are presented in Fig.5.9 and Fig.5.10. The late injection starts at 250° ATDC. Compared to the early injection events, intake and exhaust valves have been closed; there was no effect of intake flow on the spray development, and even little effect of the flow field during the late injection. Therefore, an almost symmetric growth of plumes is presented in Fig.5.10. Additionally, a higher ambient pressure shortens the penetration of plumes. The shape and penetration at the beginning of injection are well predicted. However, with the development of plumes, as calibrated in the constant volume

vessel, overestimated spray cone angle limits the deeper penetration of spray. Thus, slightly underestimated penetrations are observed near the end of injection in Fig.5.9.

Overall, the simulation accurately predicts the spray penetration and the spray impinged on the piston and intake valve in the early injection event. While in the late injection event, the overall spray cone angle is over-predicted and further penetrations of plumes are underestimated by the simulation.

5.4 Summary

Using the HSP imaging technique, the spray model was validated in a single optical engine, with initial conditions from validated 1-D engine simulation code Wave. Then comparisons of HSP images and CFD simulation were carried out in the early and late injection events. The conclusions are listed as follows:

1. In general, as with the results from the constant volume vessel, a good agreement in the aspects of global spray structure and spray penetration is achieved for the in-cylinder simulation. However CFD underestimates slightly the spray penetration in the late injection event.
2. Compared to the late injection events, a great effect of intake flow on the development of individual plumes occurs in the early injection cases. It is beneficial to optimize the interaction of intake flow and spray for the preparation of fuel-air mixture.
3. From both the HSP images and CFD simulation, the spray impinges upon the piston and the cylinder wall, contributing to the increase of HC emissions. Besides, spray

impingement on the intake valve impedes its penetration; further this will postpone the fuel evaporation process and even result in the loss of fuel mass remaining in cylinder after IVC. These are important considerations when calibrating the start of injection timing for this engine.

Chapter 6 ANALYSIS OF MIXTURE PREPARATION IN A STOICHIOMETRIC DIRECT INJECTION DMF ENGINE

6.1 Introduction

In Chapter 5, the spray model has been validated in a single optical engine; the interaction between air flow and spray, and spray impingement have also been discussed. Compared to conventional gasoline fuel, these effects on the mixing quality in the case of DMF fuel will be further analyzed and discussed with this validated engine model in this chapter. Also, the effects of engine speed and injection timing will be analyzed.

6.2 Simulation Build up

The modelled engine specifications are shown in Table 5.1 and the injection parameters are listed in Table 6.1. The engine was run at wide open throttle (WOT) and 1500rpm. The calculations were conducted from exhaust valve opening time (EVO) at 204 °CA BTDC to 340 °CA ATDC (0 °CA relative to intake TDC). All the initial and boundary conditions were chosen equally for comparative purposes. An intake pressure of 1.0 bar and an intake air temperature of 320 K were used. The initial conditions were taken from the one-dimensional engine model, as illustrated in Fig.5.5.

The injected fuel mass was calculated by the stoichiometric ratio and air trapped in the cylinder at Intake Valve Closing (IVC) time at 225°CA ATDC. The injection pressure was fixed at 150 bar. The layout of the injector was based on the thermal engine, different from that for the HSP imaging test. The symmetric plane of spray was arranged perpendicular with the tumble plane of the engine as seen in Fig.6.1.

Table 6.1 Injection parameters

Injection Pressure	150 bar	
Injection Duration	1ms	
Injected Fuel Mass	11.48mg	
Start of Injection	80 °CA ATDC	
Fuel Type	DMF	Gasoline
Injection Duration	29.4°CA	24.6°CA
Injected Fuel Mass	0.0524g	0.0372g

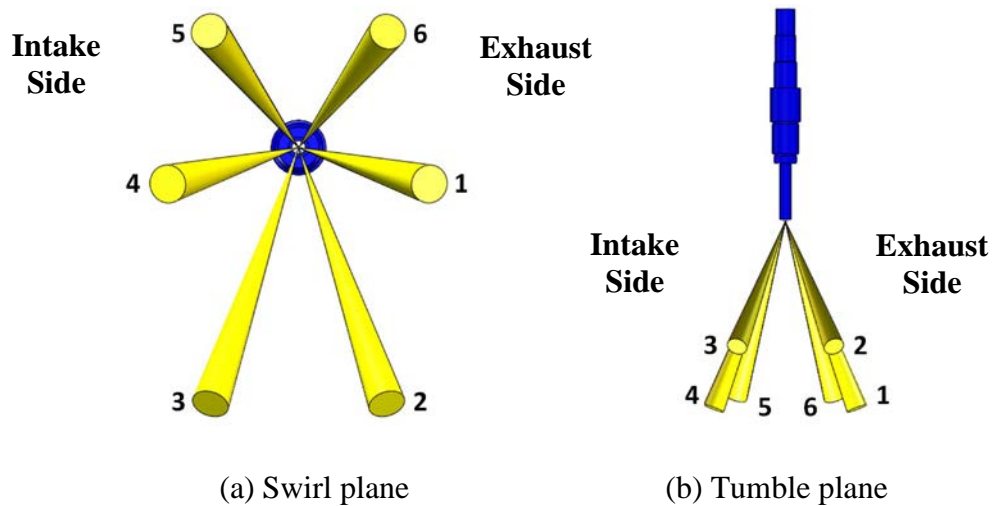


Fig.6.1 Schematic of spray pattern in the thermal engine

6.3 In-Cylinder Charge Mixing Process

6.3.1 In-Cylinder Gas Motion

Gas motion in the engine cylinder plays a crucial role in fuel-air mixing and the subsequent combustion process in the SIDI engine. Not only large-scale flow but also small-scale flow like turbulence, are important characteristics for the charge mixture. In this section, these important features of gas motion in cylinder will be analyzed.

As to the large-scale flow, intake flow jets, vortices and recirculation zones are generally the main effects on the in-cylinder mixing. During the intake stroke, the complex flow structure attributed to the intake jet is presented in Fig. 6.2. The large-scale rotation motion is stimulated by intake flow, piston movement and the interaction between the intake jet and cylinder boundary (wall and piston) as shown in Fig.6.3:

1. Interaction of intake gas streams (Jet-Jet).

The (Jet-Jet) flow structure interaction focuses in a narrow horizontal cross-section jet area and splits the cylinder into two symmetric halves. A vast amount of fresh charge can be delivered into the cylinder during this interaction.

2. Interaction of the intake jets with the cylinder wall (Jet-Wall).

The part of the intake jet flow close to the cylinder wall evolves and forms a high shear structure. And then along the cylinder wall, the fresh charge moves downwards to the piston.

3. Interaction of the intake jets with the in-cylinder bulk flow (Jet-Bulk).

In the upper part of the cylinder, the intake jet interacts with the residual in-cylinder bulk flow. Within this region, a high stratification can be expected in terms of composition, density and temperature of mixture.

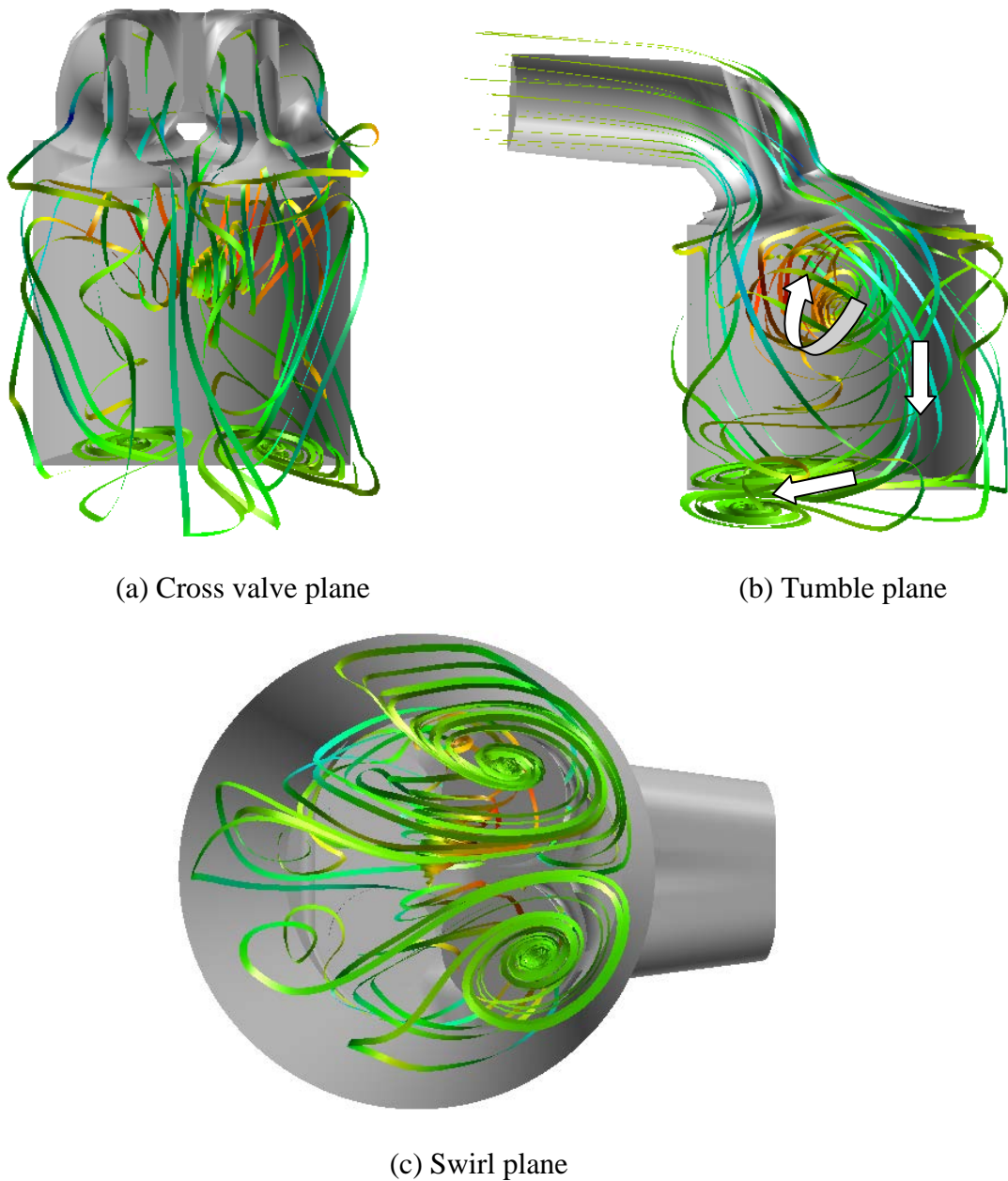


Fig.6.2 Calculated streamlines at 120° CA ATDC showing the vortex and coherent structures

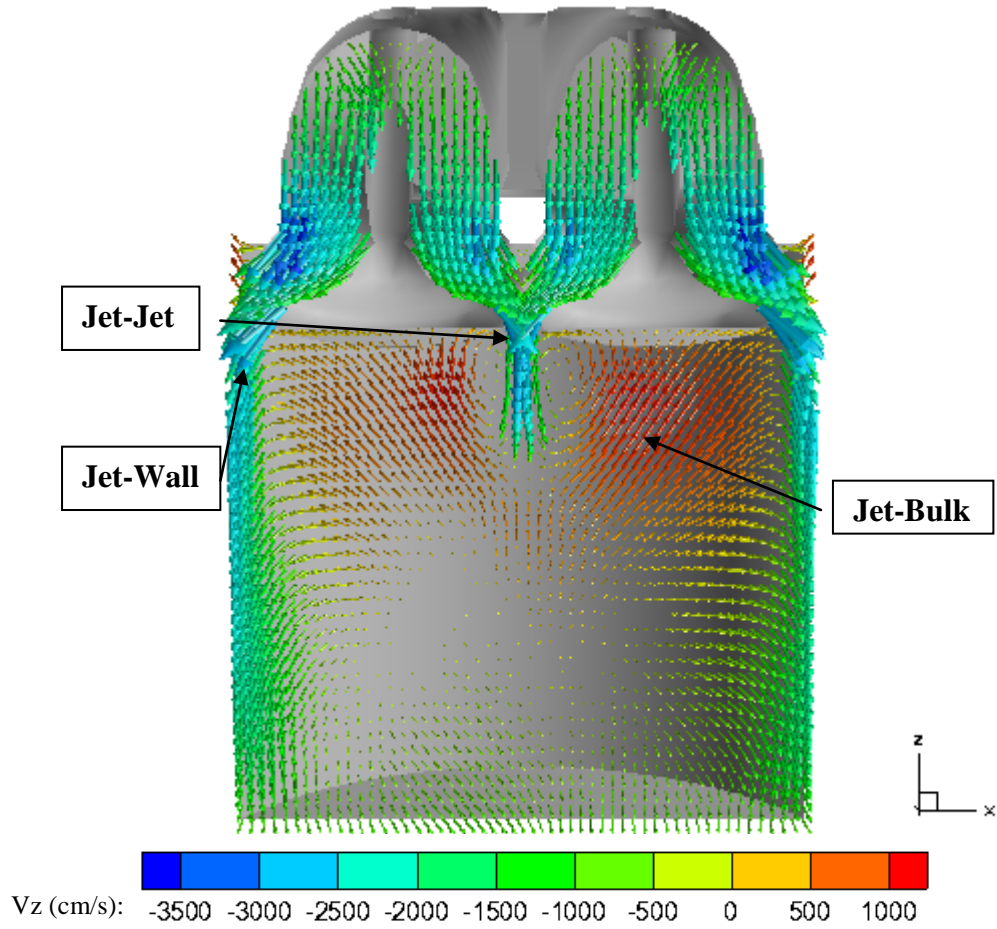


Fig.6.3 Intake flow vectors in the middle of the intake valves

In order to give a whole view of in-cylinder fluid motion, three indicators, tumble, swirl, and cross tumble ratios are commonly used to quantify the large-scale flow motion. The Swirl Ratio (SR) is defined as the total angular momentum in the z axis, normalized by the crankshaft angular speed and rotational inertia of the instantaneous mass center, and is given by:

$$SR = \frac{A_z}{I_z \omega_c} \quad (\text{Equation 6.1})$$

where A_z is the total angular momentum integrated over the cylinder. I_z is the integrated angular inertia of the fluid along the z -axis and ω_c is the angular velocity of the crankshaft.

The tumble ratio (TR_y) and cross tumble ratio (TR_x) are given similarly to the swirl ratio. The positive orientations of those ratios are illustrated in Fig. 6.4, in which the reference axes are given as the coordinate axes.

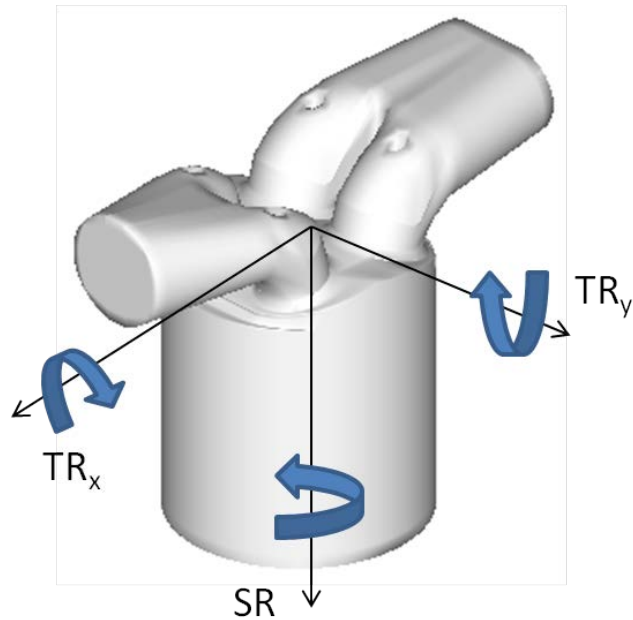


Fig. 6.4 Schematic of the swirl and tumble components

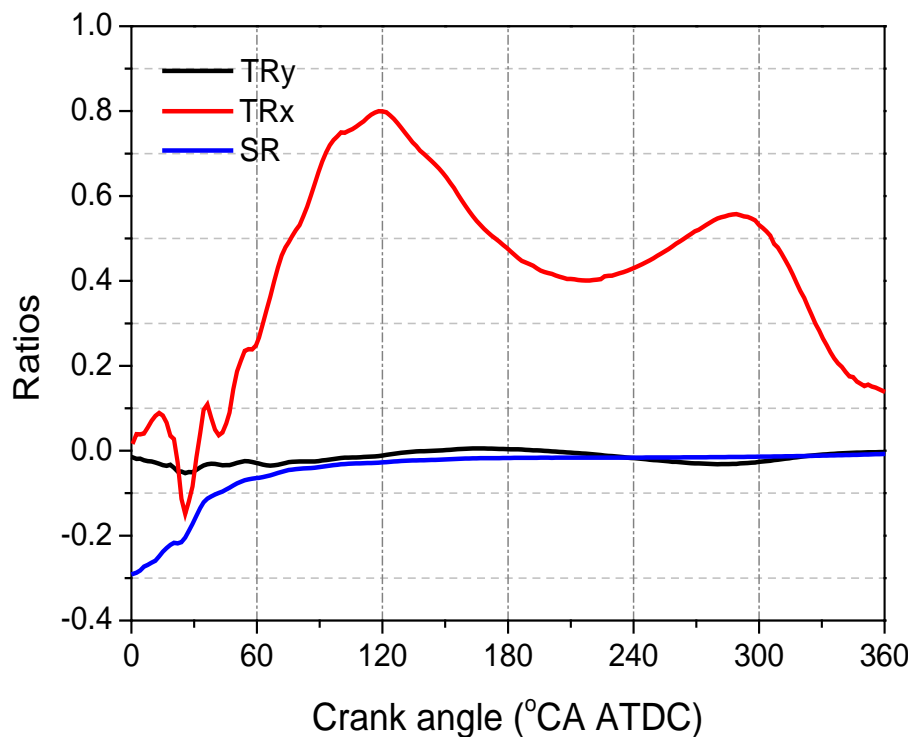


Fig. 6.5 Swirl, tumble and cross tumble ratios in intake and compression strokes

Fig.6.5 shows the evolution of the Tumble Ratio (TR_y), cross tumble ratio (TR_x) and Swirl Ratio (SR) against the crank angle. As the exhaust valve moves back, the value of the swirl ratio decreases and becomes nearly stable after 60°CA ATDC; the cross tumble ratio remains at a low level as seen in Fig.6.5. Overall, the SR and TR_x are incomparable to the TR_y due to the symmetric intake valves' layout of the engine. As Fig.6.5 illustrates, two obvious peaks can be observed in the evolution of the tumble ratio. The first peak occurs at 120°CA ATDC, with a value of 0.8, promoted by the intake jet. As the intake generated flow decays, the tumble motion is greatly affected by the piston movement, and the second peak of tumble ratio is stimulated by the maximum piston velocity in the compression process. In the late compression stroke, due to the limited space within the cylinder, the large-scale rotating flow structures are gradually compressed into small-scale ones and the angular velocity increases according to the angular momentum conservation. Due to the increase of angular velocity, the tumble ratio reaches its second peak at 290 °CA ATDC.

Except for the large-scale flow motion, the small-scale turbulent flow also is a core factor in the fuel-air mixing process. In particular, it is known that the transport rate of turbulent diffusion is several orders greater than that of molecular diffusion [42]. Two parameters, turbulence kinetic energy and turbulent kinematic viscosity are introduced to quantify the turbulence motion in the small-scale mixing process.

The evolution of turbulence kinetic energy against the crank angle is illustrated in Fig.6.6. During the intake stroke, the profile of turbulence kinetic energy is similar to that of tumble ratio. The peak of turbulence kinetic energy appears around 100°CA ATDC, just a little earlier than the timing of the first peak of tumble ratio. This indicates that intake jet flow is

the critical factor contributing to the production of turbulence energy. Specifically, an intake jet with high velocity during the process of the three interactions mentioned forms a larger velocity gradient and further produces more turbulence kinetic energy. However, as the compression process commences, intake generated flow almost has disappeared and the turbulence kinetic energy decays rapidly near IVC due to turbulent dissipation. The second inconspicuous peak of the turbulence kinetic energy, appearing after the second peak of the tumble ratio, is expected to be motivated by the compression of large-scale flow motion as seen in Fig.6.6.

The additional parameter, turbulent kinematic viscosity, is an analogical transport coefficient from the kinetic theory of gases. The turbulent kinematic viscosity is defined with a function of the turbulence kinetic energy and its dissipation rate, shown as

$$\mu_t = C_\mu \rho_g \frac{\kappa^2}{\varepsilon} \quad (\text{Equation 6.2})$$

where μ_t represents turbulent kinematic viscosity, C_μ is the model constant, ρ_g is the gas density, κ is turbulence kinetic energy and ε is its dissipation rate. Fig.6.7 presents the evolution of the turbulent kinematic viscosity. A ladder-shaped profile of the turbulent kinematic viscosity against the crank angle can be seen. The plateau stage begins right after the first peak of the tumble ratio, and then it experiences a small increase and drops after the second peak of tumble ratio. This reveals the close relationship of turbulent kinematic viscosity and large-scale flow structure, that is, during the compression process, the generation of small-scale flows from large-scale flows compensates for the decay of turbulence developed in the intake stroke, to a certain extent.

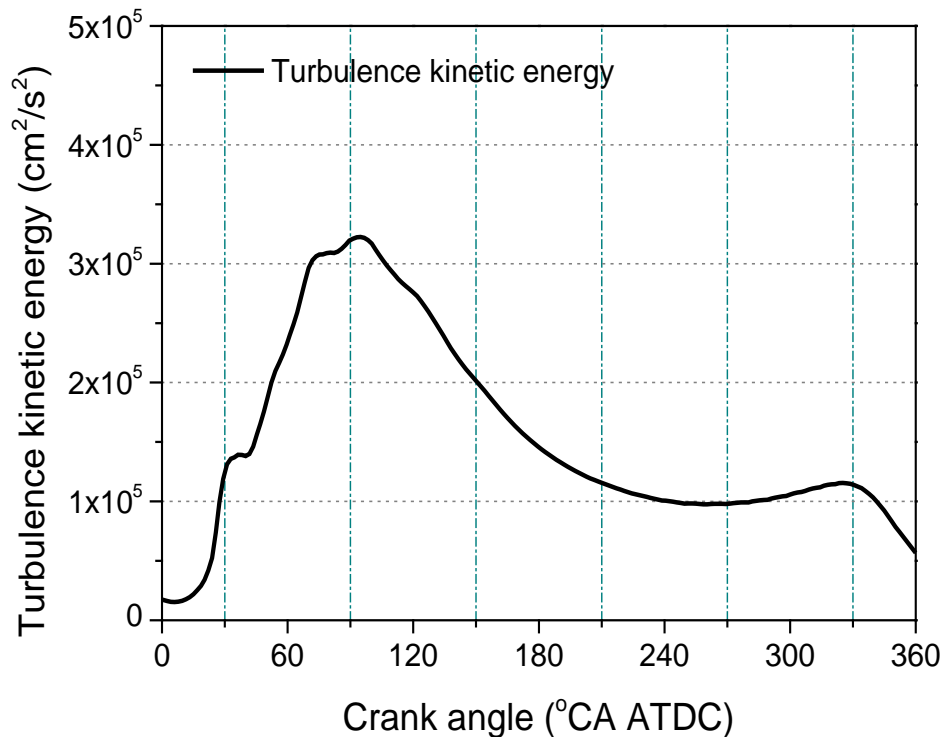


Fig. 6.6 Turbulence kinetic energy during the intake and compression strokes

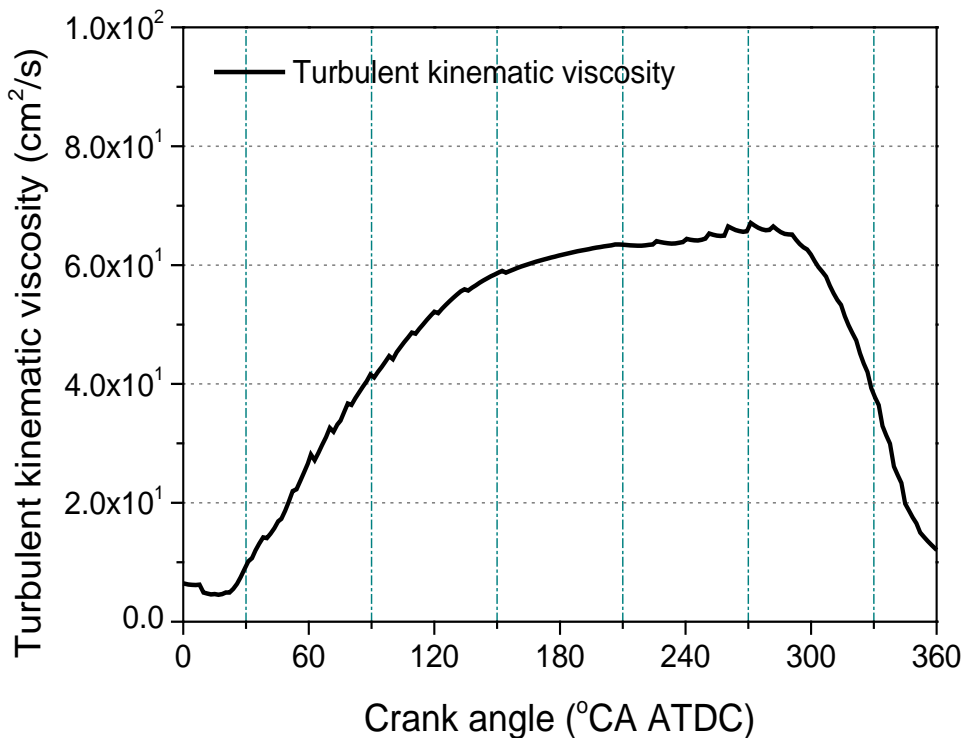


Fig. 6.7 Turbulent kinematic viscosity during the intake and compression strokes

6.3.2 Effects of Fuel Properties on the Mixing Process

Except for the tumble motion and the small-scale flow motion, the spray-gas interaction is also a major factor in the in-cylinder mixing process. Also, subsequent spray impingement and the evaporation process affect the final mixing quality. Thus, the discussion of this section will concentrate on the comparison of DMF spray and gasoline spray in the above terms.

Fig.6.8 illustrates the DMF and gasoline spray-gas interactions in the side view of the engine. Fig.6.9 presents the temporal evolutions of the liquid fuel impinged on the wall divided by the total mass of the fuel injected. As presented in Fig.6.8a, at 85°CA ATDC (5°CA after SOI), the plumes of both fuel jets disperse significantly and interact with each other downstream of the nozzle tip. Compared to gasoline spray, it is easier to identify the edge of the DMF plumes. This is in that DMF spray has a smaller spray cone angle than that of gasoline spray, as analyzed in Chapter 4. In addition, although the spray patterns are symmetrical, with the interaction of the intake jet flow, spray on the right side spreads out widely and has a longer penetration. Due to the longer penetration of DMF spray, its jet attains to the piston earlier as shown in Fig.6.8b. After EOI, a remarkable spray-wall impingement takes place and reaches the maximum around 120°CA ATDC, which equals to 5% of the total liquid fuel (seen in Fig.6.9). The fuel spray moves towards the left side of the cylinder driven by the clockwise tumble flow, as is evident from Fig.6.8; also the percentage of spray impinged on the solid surface decreases with the drop evaporation and entrainment of the clockwise vortex.

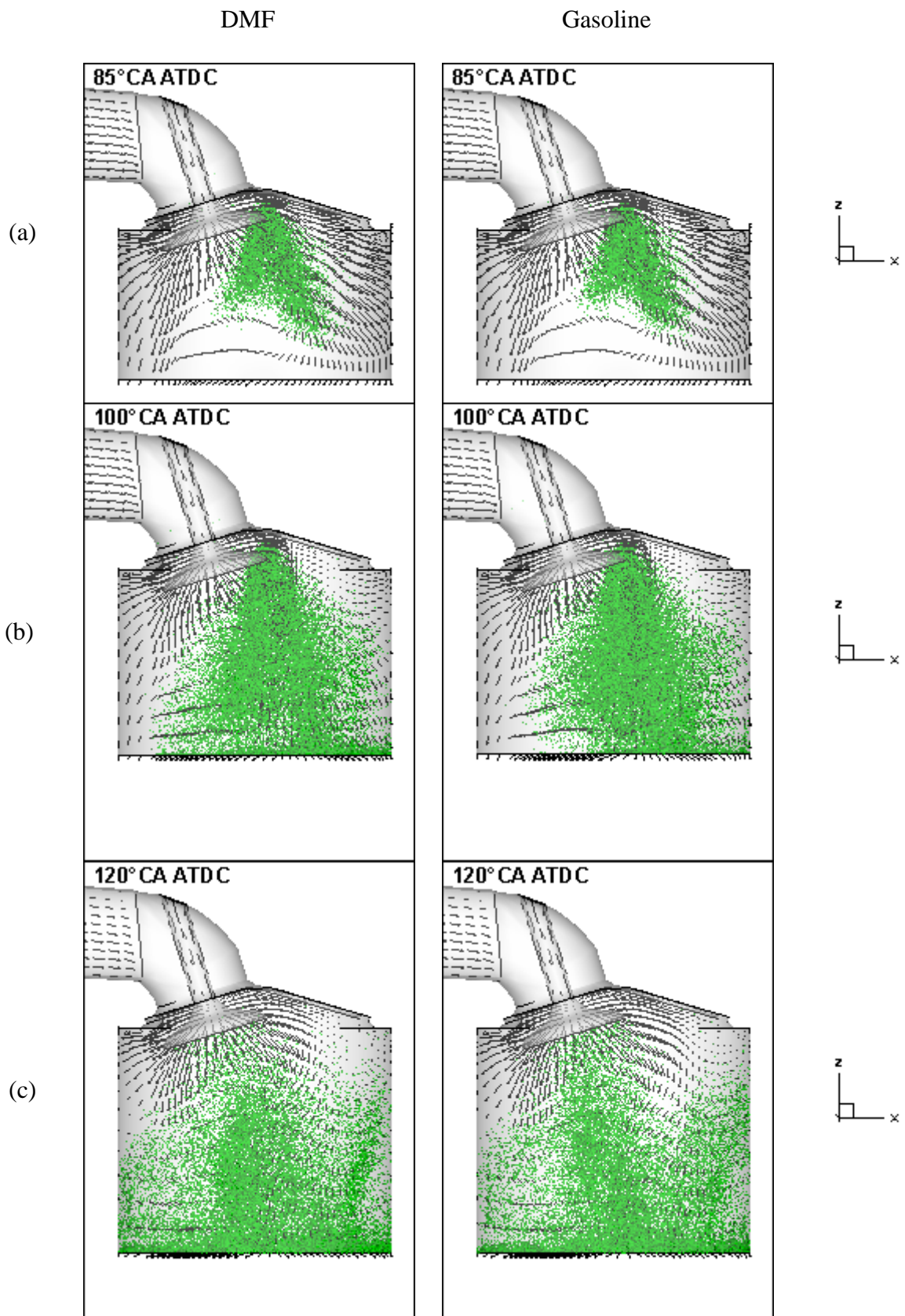


Fig.6.8. Comparison of DMF and gasoline in the spray-gas interaction

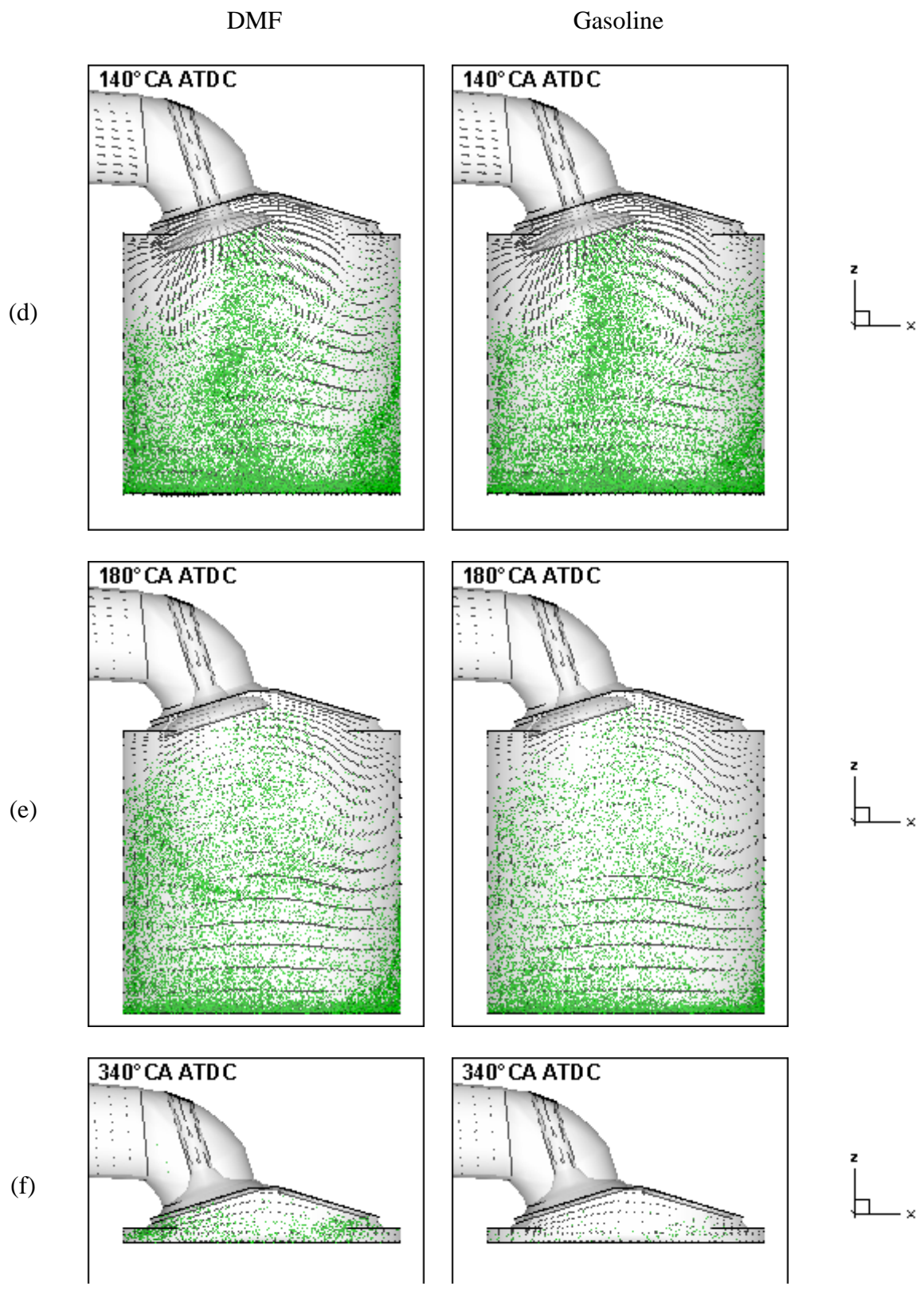
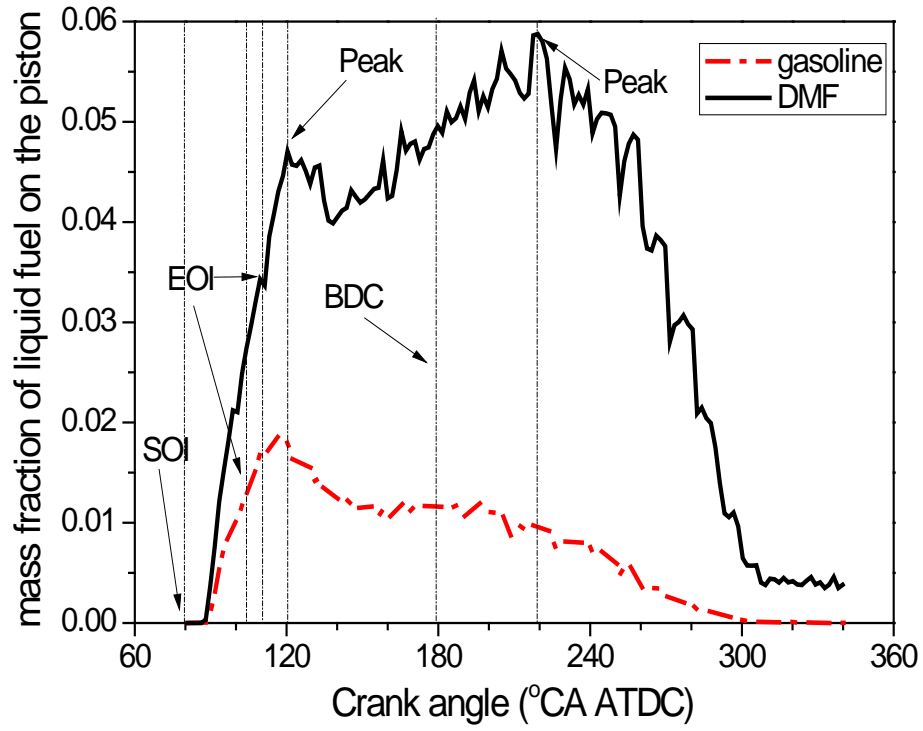
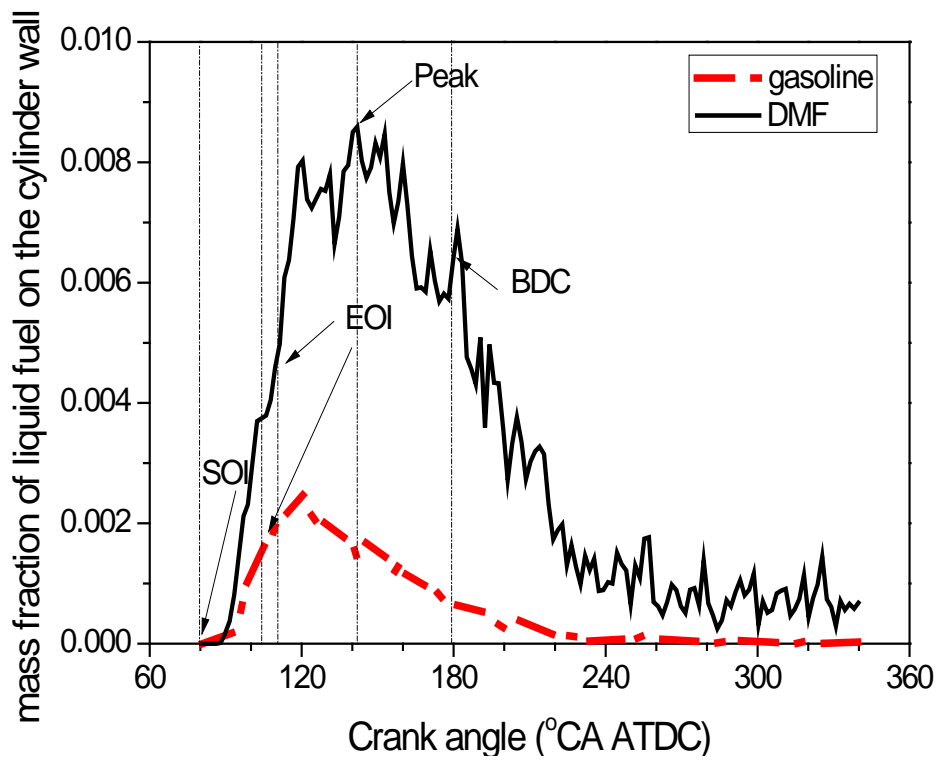


Fig.6.8. Comparison of DMF and gasoline in the spray-gas interaction (cont.1)



(a) Piston



(b) Cylinder liner

Fig.6.9. Evolutions of mass fraction of the liquid fuel impinged on the wall

At the end of compression stroke, as given in Fig.6.9, in the case of DMF, an amount of liquid DMF still remained on the piston and cylinder liner compared to almost all the droplets vanishing in the case of gasoline.

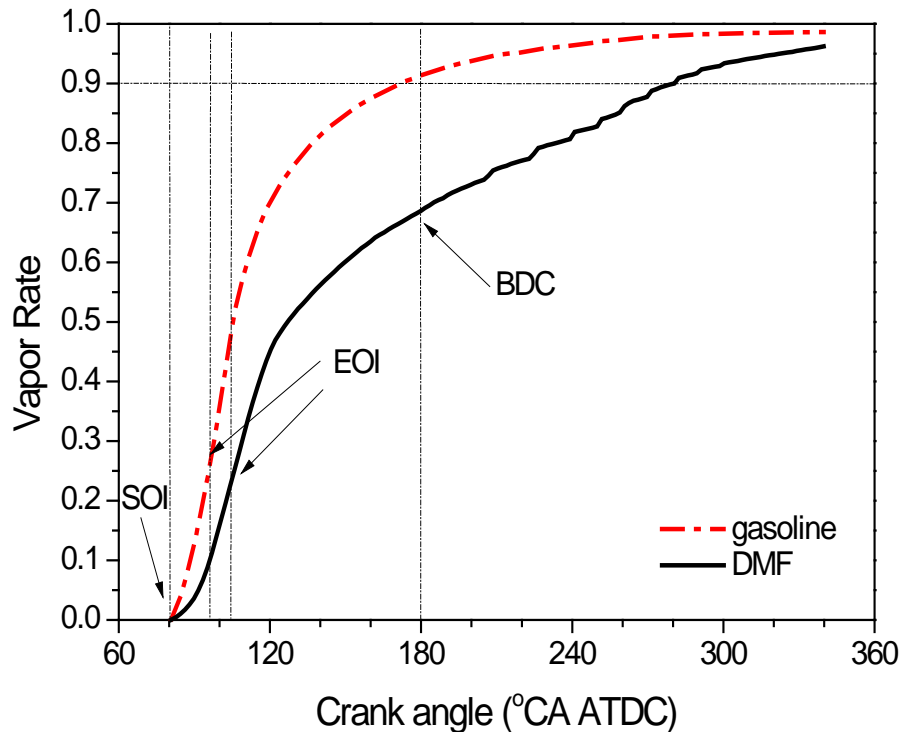


Fig.6.10. Comparison of DMF and gasoline in evaporation rate

The comparison of the global fuel evaporation rate histories for the two fuels is shown in Fig.6.10, where the fuel vapor is divided by the total injected fuel mass. Within the injection duration, due to the higher vapor pressure and smaller mean droplet size of gasoline, its vaporization rate is faster than that of DMF, as indicated by a steeper vapor rise. Then, the wall film and its evaporation become critical to the mixture formation. As illustrated, the cases of DMF and gasoline reach 90% of fuel vaporization at 171 and 281°CA ATDC, respectively. In other words, the DMF spray delays about 110°CA to attain this percentage. By 340°CA ATDC, up to 96.2% and 98.6% of fuel are vaporized for the cases of DMF and

gasoline, respectively. This implies that DMF requires more time to complete evaporation before combustion.

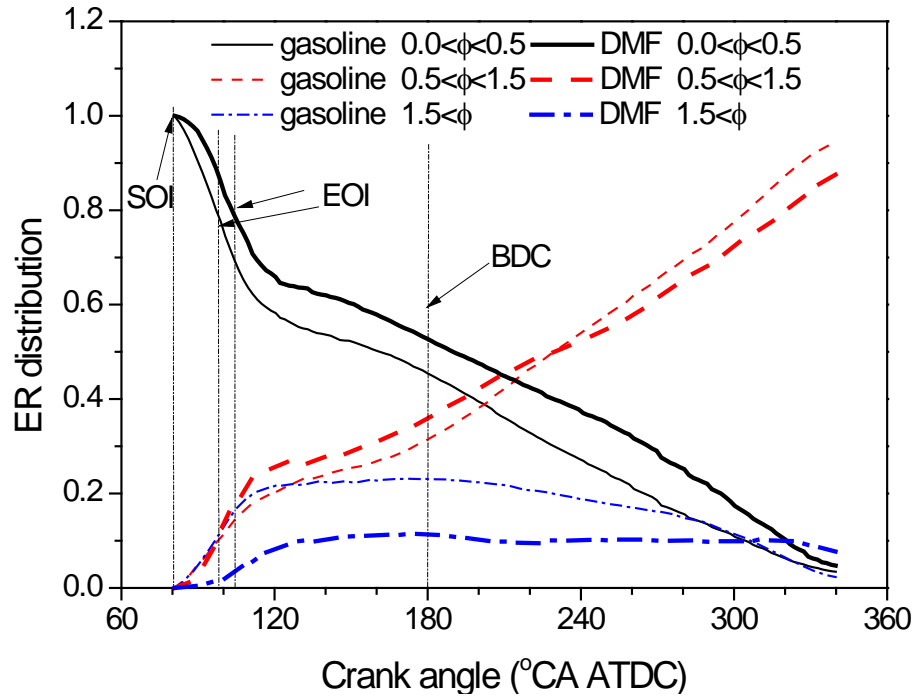


Fig.6.11. History of the percentages of three ranges of the equivalence ratio.

To quantify the quality of air/fuel mixing, the temporal evolution of the local mixture volume with various ranges of equivalence ratios (smaller than 0.5, in between 0.5 and 1.5, and larger than 1.5) are shown in Fig.6.11. The total volume in each range is divided by the transient volume of the whole cylinder. Overall, the percentage of ignitable mixture ($0.5 < \Phi < 1.5$) rises within the injection duration, whereas the percentage of extremely lean mixture ($0 < \Phi < 0.5$) presents a reverse tendency. The percentage of extra-rich mixture ($\Phi > 1.5$) grows from the start of injection to the moment when the piston and wall wetting attains the first crest value (as is evident from Fig.6.9), and then it declines slowly for gasoline and becomes steady for DMF. It is remarkable that in the case of DMF, after 220°CA ATDC , the portion of ignitable mixture rises slowly and the portion of extra-rich mixture increases slightly. At the end of the

compression stroke, the percentages of the highly rich mixture and extremely lean mixture in the case of DMF reach 7.7% and 4.7%, respectively. This is due to the fact that more liquid fuel remains on the piston and cylinder liner. Whereas gasoline is 2.3% in highly rich mixture and 3.4% in extremely lean mixture, respectively.

In order to quantify the mixing quality, Fig.6.12-6.14 present the spatial equivalence ratio ($0.5 < \Phi < 1.5$) distribution and Fig.6.15 shows the scatter plot of temperature against ER at 340°CA ATDC (near the endpoint of compression) for both fuels.

In Figs.6.12 and 6.13, from SOI to BDC, fuel-air mixing is mainly dependent on the intake jet flow and the spray-gas interaction. At the beginning of injection (85°CA ATDC), all the mixture is very lean (equivalence ratio lower than 0.5) except for a tiny area in the case of the gasoline-air mixture. The low vapor rate and relatively narrow radial dispersion of DMF spray greatly retards its mixing with air. After the EOI, more rich fuel mixture is found at the bottom of the cylinder as most of sprays impinges on the solid wall surface. Then with the tumble motion, the rich mixture moves clockwise to the cylinder liner on the intake valve side. At BDC, more than 30% of liquid DMF is under evaporation compared to the almost fully evaporated gasoline as given in Fig.6.10. Therefore, unlike the gas diffusion process of gasoline-air mixture, the DMF-air mixing concentrates on the wall film evaporation process after BDC. Overall, compared to the case of gasoline, DMF-air mixing presents a narrower area of rich fuel-air mixture in the beginning of the compression stroke and worse homogeneity at the end of the compression stroke, as presented in Fig.6.11.

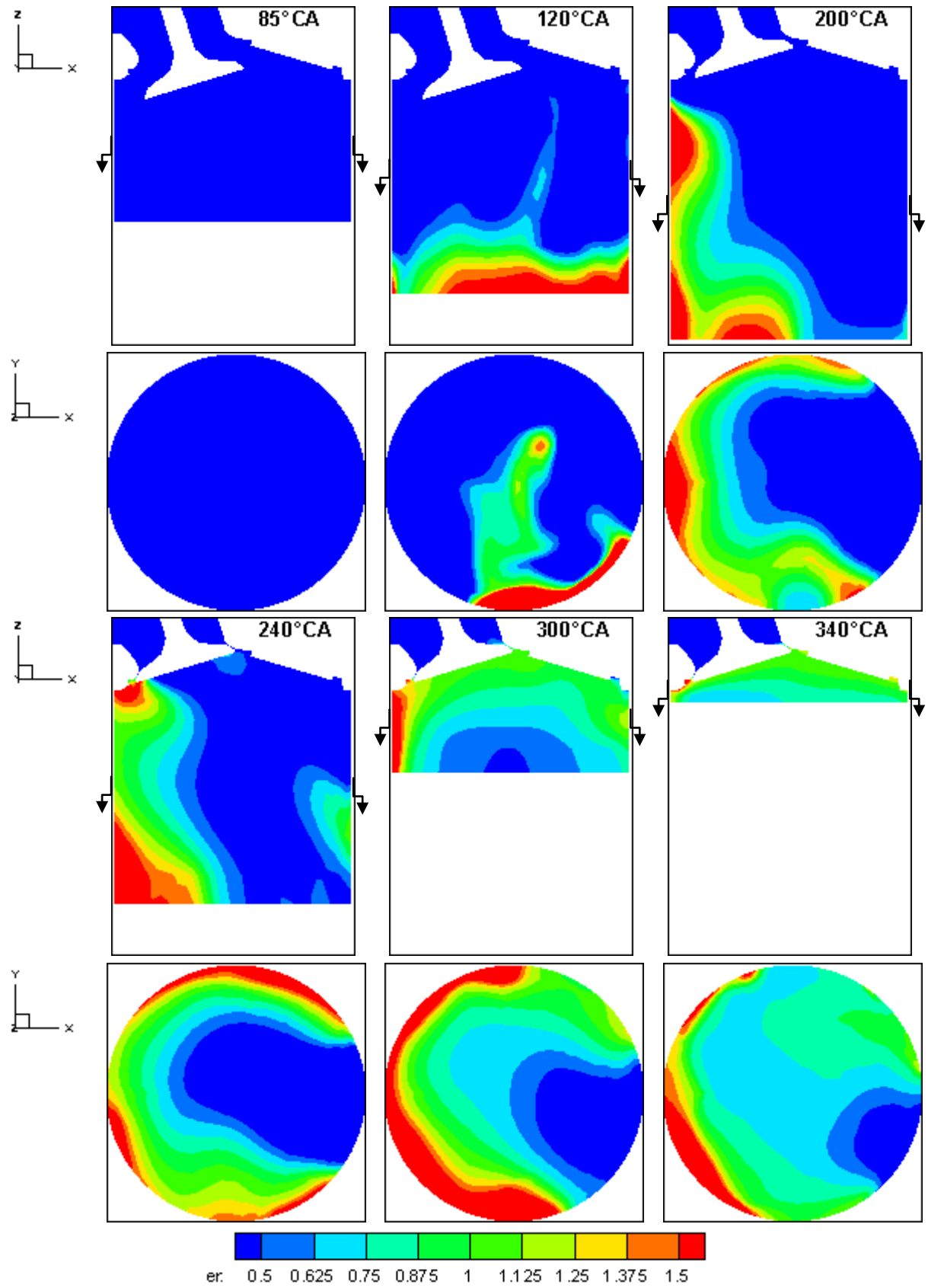


Fig.6.12. Calculated distribution of local equivalence ratio in the case of DMF.
 Top: the xz plane--tumble plane, below: the xy plane--the middle plane along the z axis.

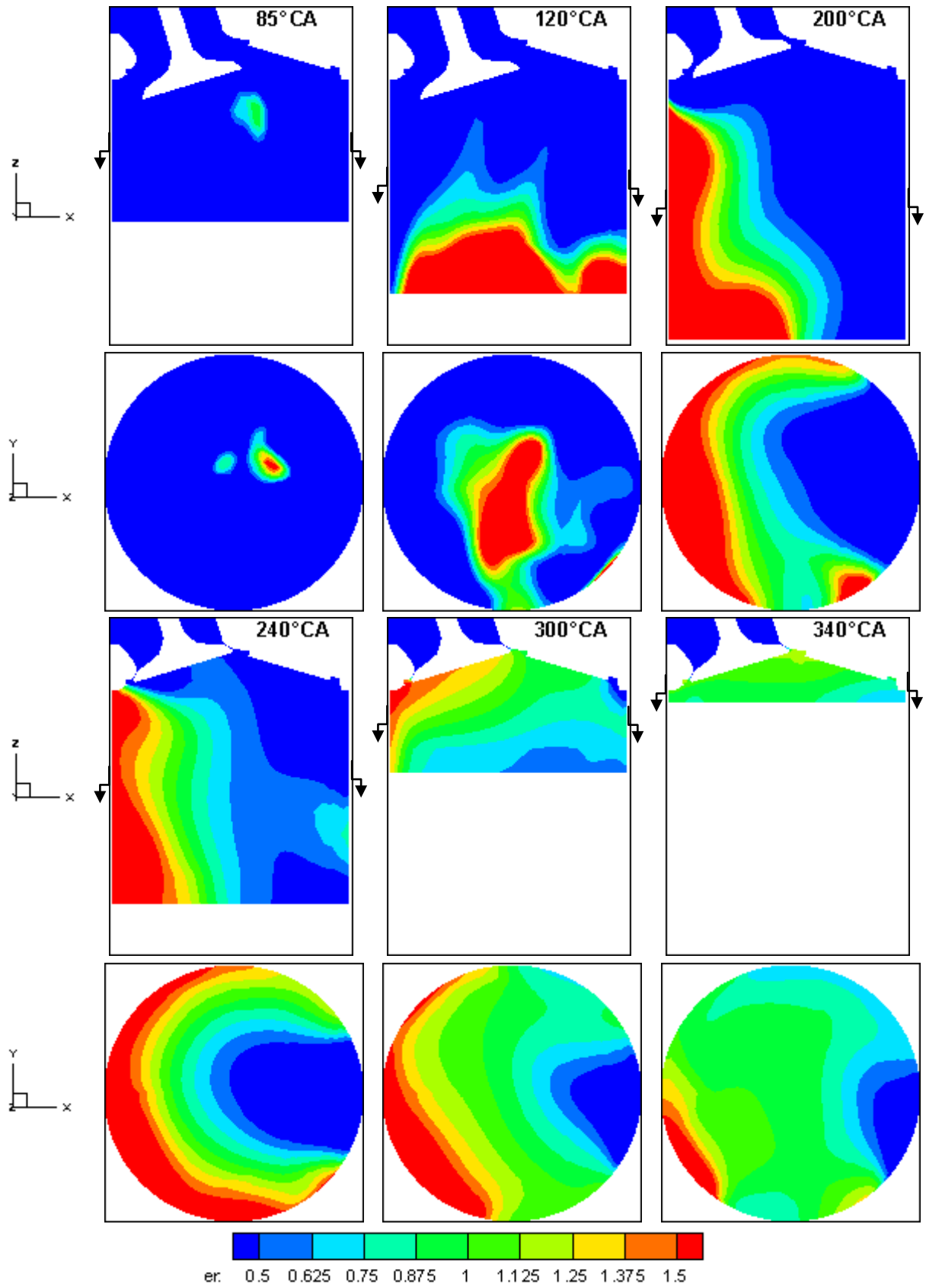


Fig.6.13. Calculated distribution of local equivalence ratio in the case of gasoline. Top: the xz plane--tumble plane, below: the xy plane--the middle plane along the z axis.

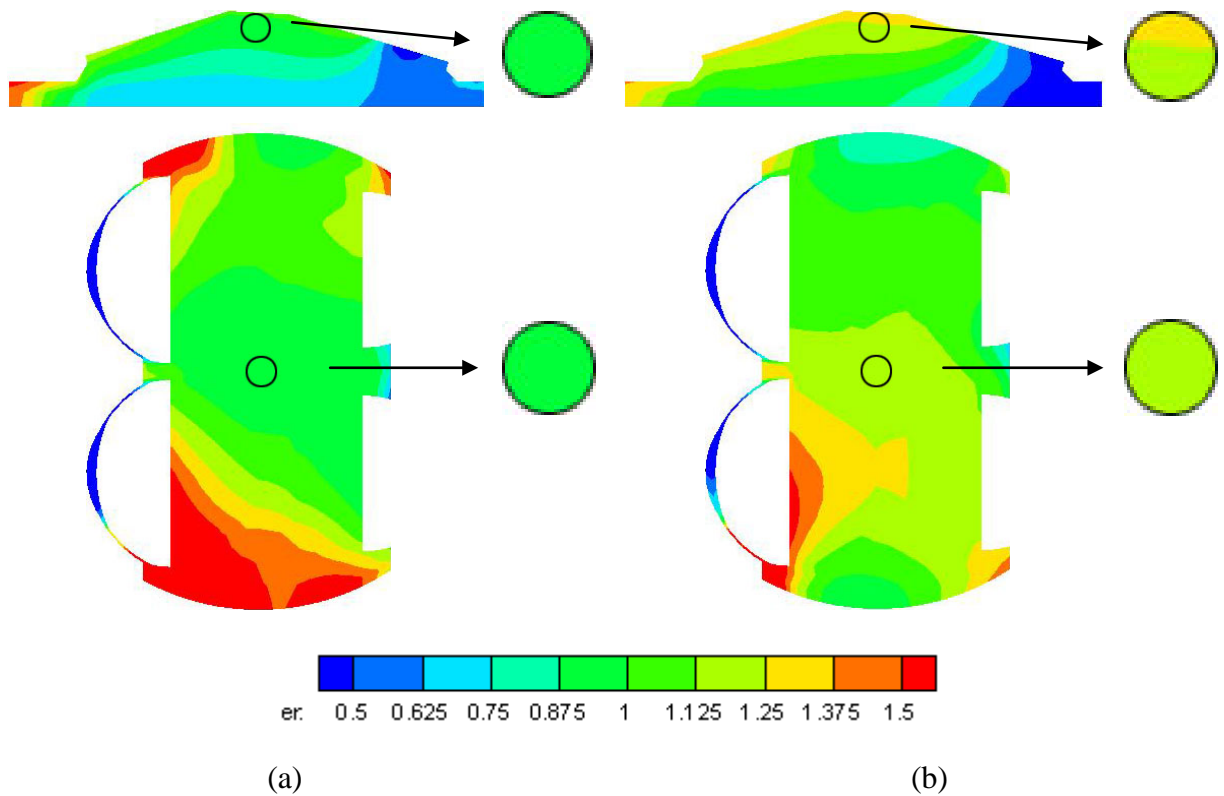


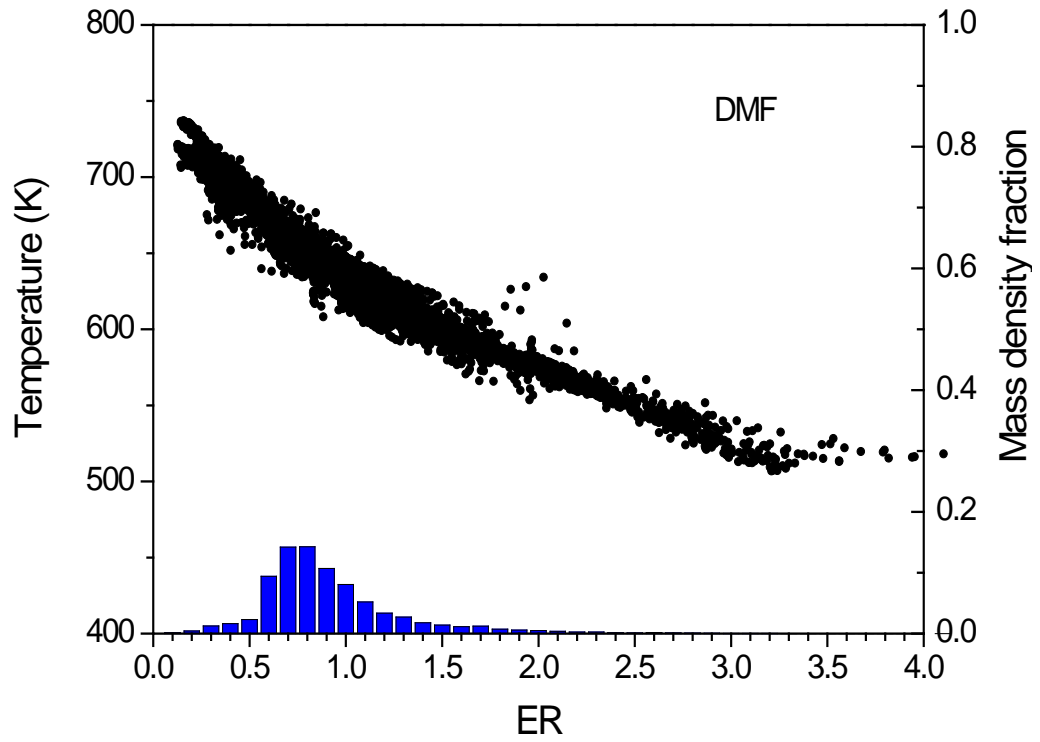
Fig.6.14. Comparison of equivalence ratio distribution near the spark plug at 340 °CA ATDC. (a-DMF, b-gasoline)

In Figs.6.12 and 6.13, at 240°CA ATDC, with the clockwise motion of swirl flow, another zone of rich mixture is found on the right-bottom corner. When approaching to the TDC (340°CA ATDC), since the tumble motion decays rapidly, some portion of extremely lean mixture remains on the right side; more extra-rich mixtures can be observed on the chamber roof and cylinder liner for the case of DMF.

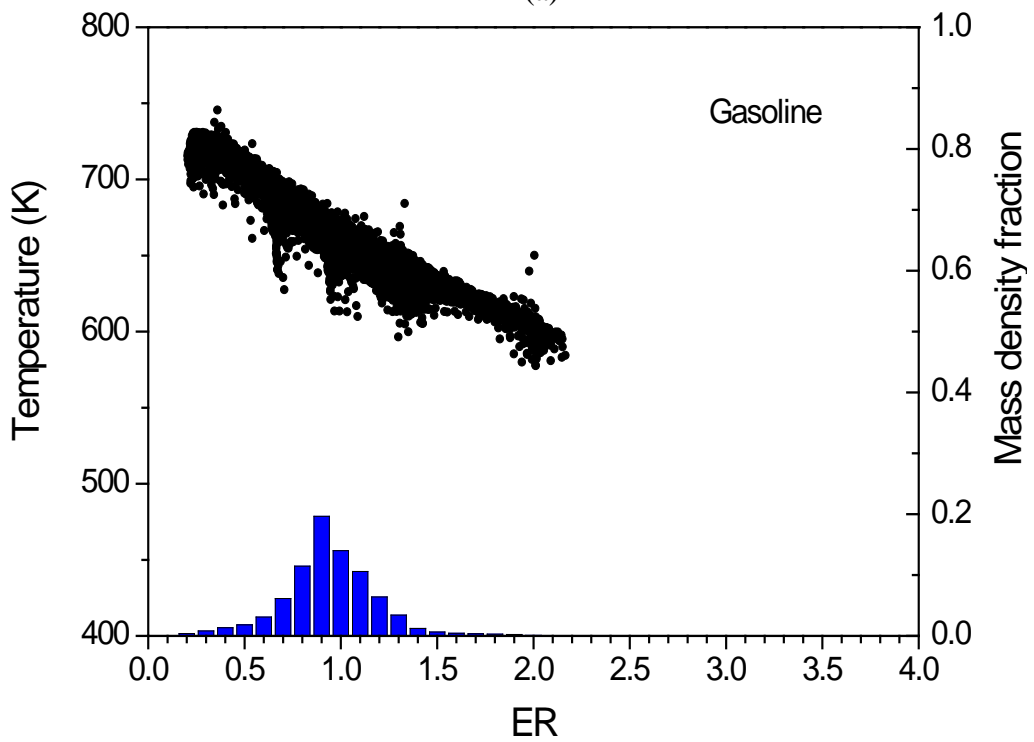
On magnifying the spark plug area at 340°CA ATDC, it is clear that the local equivalence ratio of DMF-air mixtures is in the range of 0.875 to 1; whereas for gasoline, it is in range of 1.125 to 1.25 (slightly higher than stoichiometric ratio), which corresponds to the range of equivalence ratio for maximum laminar flame speed [146]. Thus, the equivalence ratio

distribution of the gasoline case around the spark plug is more beneficial to combustion preparation, compared to the case of DMF.

Moreover, a closer examination of equivalence ratio distribution at the end of compression stroke can be given in Fig.6.15. The upper plots in Fig.6.15 show the equivalence ratio distribution against temperature at the end of compression stroke, which are represented by the scatter plots of the temperature in all the calculated cells against the transient Equivalence Ratio (ER) in the combustion chamber. Due to a large amount of liquid DMF impinged on the wall, an extra-rich mixture ($ER > 2.0$) is formed in the low-temperature area near the cylinder head and liner (as seen in Fig.6.15a). The bar charts in Fig.6.15 present the mass density distribution of equivalence ratio. It is plotted in such a way that its range from 0.1 to 4.0 is divided into 40 equal bins with intervals of 0.1 and the mass of cells related to each bin of ER is summed up and divided by the total mass within the cylinder. Hence, the taller and narrower the mass density distribution, the more uniform the air/fuel mixing in the cylinder. Compared to gasoline, a wider spread of ER distribution can be found in the case of DMF. Furthermore, for a global view of ER distribution, its mean value and standard deviation of mass density distribution are calculated. At the end of the compression stroke, the average equivalence ratio of DMF is 0.96 with a standard deviation of 0.67, whilst the overall equivalence ratio of gasoline is 0.99 with a standard deviation of 0.29. As can be seen, based on the present gasoline GDI injector and spray pattern, a more homogeneous mixture is formed in the case of gasoline than that of DMF spray. This indicates that a new spray pattern tailored for DMF spray is needed, if DMF fuel is applied in such a gasoline direct injection engine.



(a)



(b)

Fig.6.15. Scatters of temperature against ER and ER distribution in the mass density fraction of at 340°CA ATDC (a) DMF (Mean= 0.96, COV=0.67) (b) Gasoline (Mean=0.99, COV=0.29)

6.4 Evaluation of Mixing Quality

In this section, the engine was fuelled with DMF. Firstly, the effect of the injection timing was investigated under the engine speed of 1500 rpm. Then the engine speed was adjusted to high speeds of 3000 and 6000 rpm with SOI of 80°CA ATDC in order to study the performance of DMF-air mixing in the extreme conditions.

6.4.1 Effect of Injection Timing

The injection timings selected in this study are listed in Table 6.2. To fully understand the effect of injection timing on the mixing quality, the starts of injection varied from 24 °CA after EVC to 35°CA after IVC. In general, injection timings can be divided into early injection during the induction period (SOI at 60°, 80°, 100°CA, 120 °CA, 140°CA and 160°CA ATDC, respectively) and late injection after IVC (SOI at 240° CA, 250°CA and 260°CA ATDC).

Table 6.2 Injection timings and charge cooling effect on engine performance.

Case No.	1	2	3	4	5	6	7	8	9
SOI	60° CA	80° CA	100° CA	120° CA	140° CA	160° CA	240° CA	250° CA	260° CA
Temperature (K) at Intake BDC	325.8	326.2	327.2	328.5	332.5	342.0	344.9	344.9	344.9
Air Flow Rate (g/s)	22.29	22.25	22.19	22.10	21.98	21.59	21.36	21.36	21.36

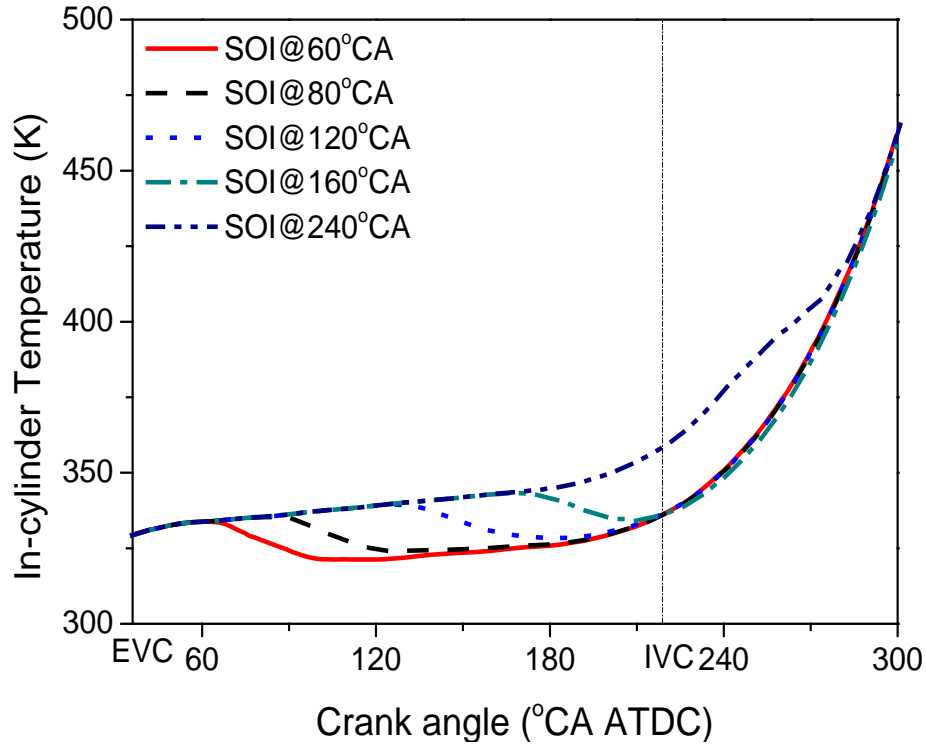
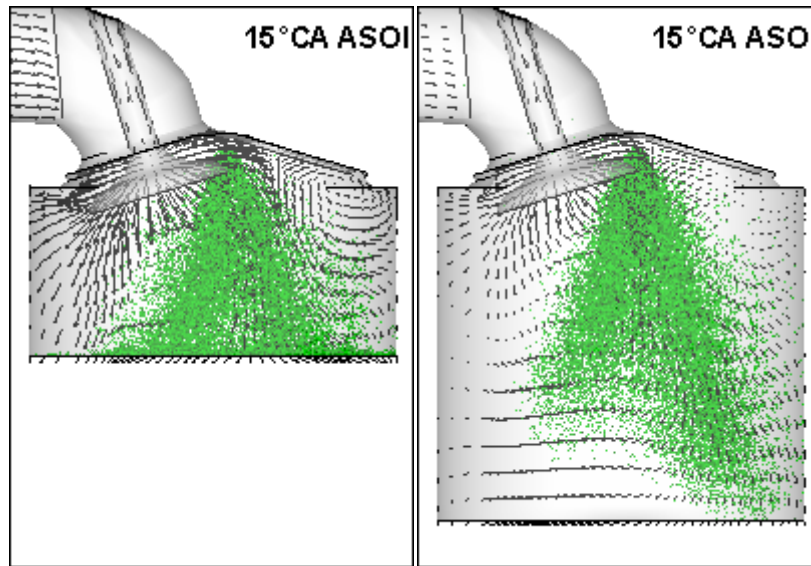


Fig.6.16 Effect of injection timing on in-cylinder charge temperature.

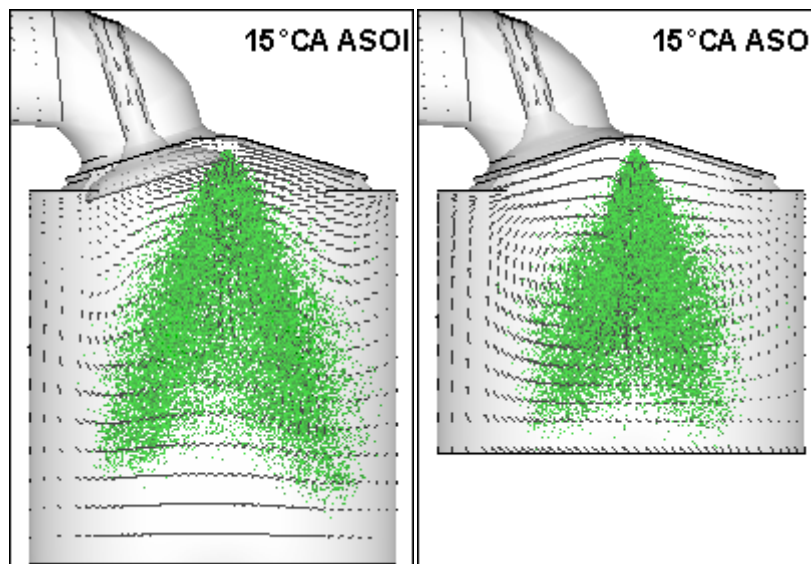
Charge cooling effect, as a unique characteristic for a direct injection engine, is a key factor for the mixture preparation. Associated with the fuel evaporation, thermal energy of surrounding gas is absorbed by droplets due to the fuel latent heat consumed. In order to investigate the effect of injection timing on the in-cylinder temperature, Fig.6.16 illustrates the comparisons of the mean in-cylinder charge temperature for all the cases studied. As can be seen in Fig.6.16, significant reductions of charge temperature occur during the intake period when the injection timing is after EVC and before IVC. The temperatures at intake BDC are summarized in Table 6.2. For the fuel injection after IVC (Case 7, 8 and 9), the temperature at intake BDC is about 6% higher than that of Case 1, as listed in Table 6.2. Additionally, reduction of charge temperature leads to the growth of intake airflow mass within the intake stroke. As shown in Table 6.2, the air flow rates in the Cases 1 to 6 (early injection) are 4.4%, 4.2%, 3.9%, 3.5%, 2.9% and 1.1% higher than that of Case 7,

respectively, whose injection timing is after IVC. It is noticeable that the charging cooling effect is relatively strong when the fuel is injected before 120°CA ATDC and decays when the injection time is further retarded.

As to the influence of in-cylinder gas motion on the spray, Fig.6.17 illustrates the spray and gas flow in the side view of the engine at 15°CA after the Start of Injection (SOI). As shown in Fig.6.17, in the extremely early injection (SOI at 60°CA ATDC), the spray impingement on the piston has already occurred, due to the small confining space of combustion chamber. In the case of SOI at 120°CA ATDC (when the tumble ratio achieves the maximum), the plume at the right side is significantly longer than the one at the left side due to its dominant interaction with strong intake generated jet flow as seen in Fig.6.17b. When the injection timing starts near BDC, the difference between the two sides tends to disappear as the flow motion weakens (see Fig.6.17c). Further, when the injection timing is adjusted after IVC (SOI at 240°CA ATDC), a clear symmetric pattern of spray can be seen in Fig.6.17d and the spray penetration is shorter than the early injection cases, caused by the higher in-cylinder temperature and pressure.



(a) SOI@60°CA ATDC (b) SOI@120°CA ATDC



(c) SOI@160°CA ATDC (d) SOI@240°CA ATDC

Fig.6.17 The spray-gas interaction at15°CA after SOI.

The computed evolutions of spray-wall impingement are presented in Fig.6.18. A great effect of injection timing can be indicated on the fuel piston impingement, owing to the in-cylinder flow motion. In the cases of early injection, a noticeable plateau stage is observed in Fig.6.18a, due to the fact that the downwards intake jet flow impedes the droplets away from

the piston surface until tumble flow decays. As SOI is retarded, the plateau stage shortens. Compared to early injection, late injection timing (SOI at 240°CA ATDC) creates more piston impingement due to the increasingly smaller space of the combustion chamber driven by the piston upwards movement. Reversely, more cylinder liner impingement exists in the case of the advanced injection timing as presented in Fig.6.18b. It is evident that the relative position between spray and the piston, when fuel injection takes place, is the dominant factor in the cylinder liner wetting.

The evolutions of fuel vaporization at various injection timings are shown in Fig.6.19. Compared to the early injection cases, the late injection case (SOI at 240°CA ATDC) has higher evaporation rate without the charge cooling effect, as demonstrated by a steeper vapor phase curve and shorter duration (~ 60°CA) to attain 90% vaporization. This is corresponding to the sharp reduction of piston impingement after short peak duration as presented in Fig.6.18a. It is also noted that in the early injection cases, significant fuel impingement slows down the vaporization rate and therefore, almost all the cases reach 90% evaporation at 290°CA ATDC, which implies that advancing the injection timing alone is unbeneficial to completion of vaporization.

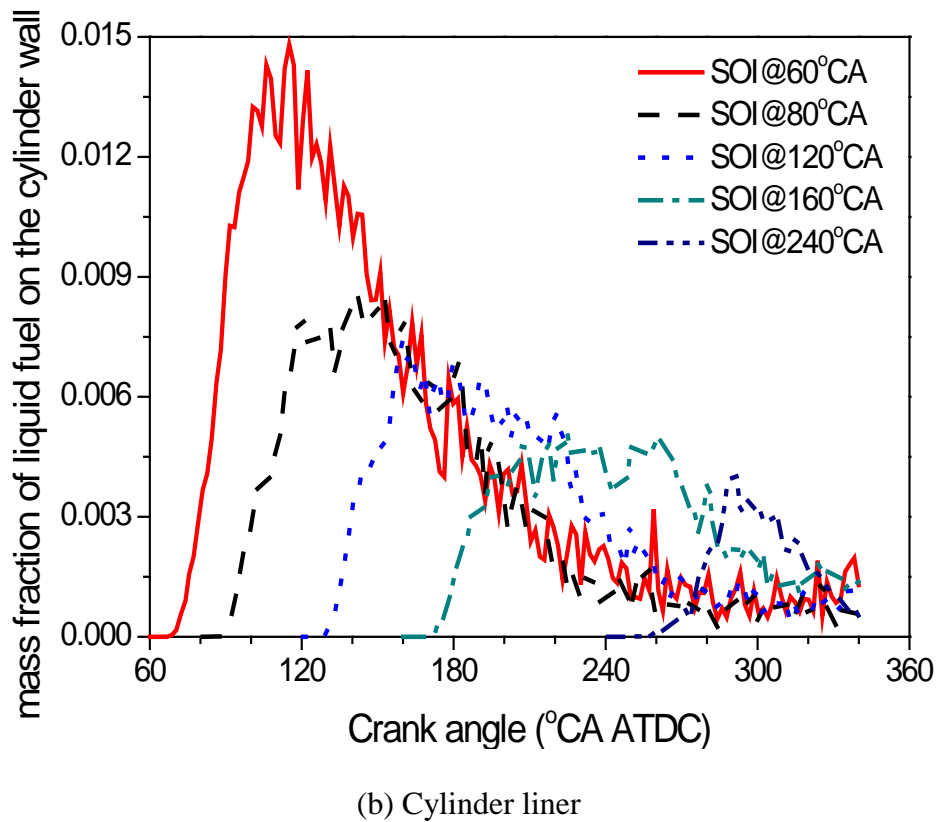
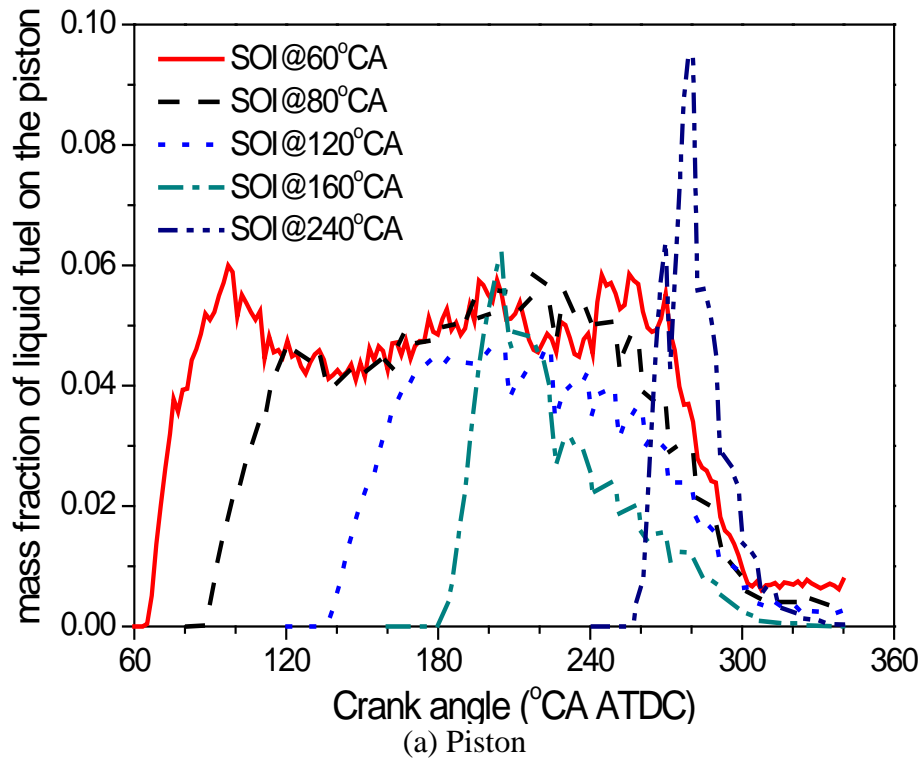


Fig.6.18 Evolutions of mass fraction of the liquid fuel impinged on the wall for the cases at various injection timings.

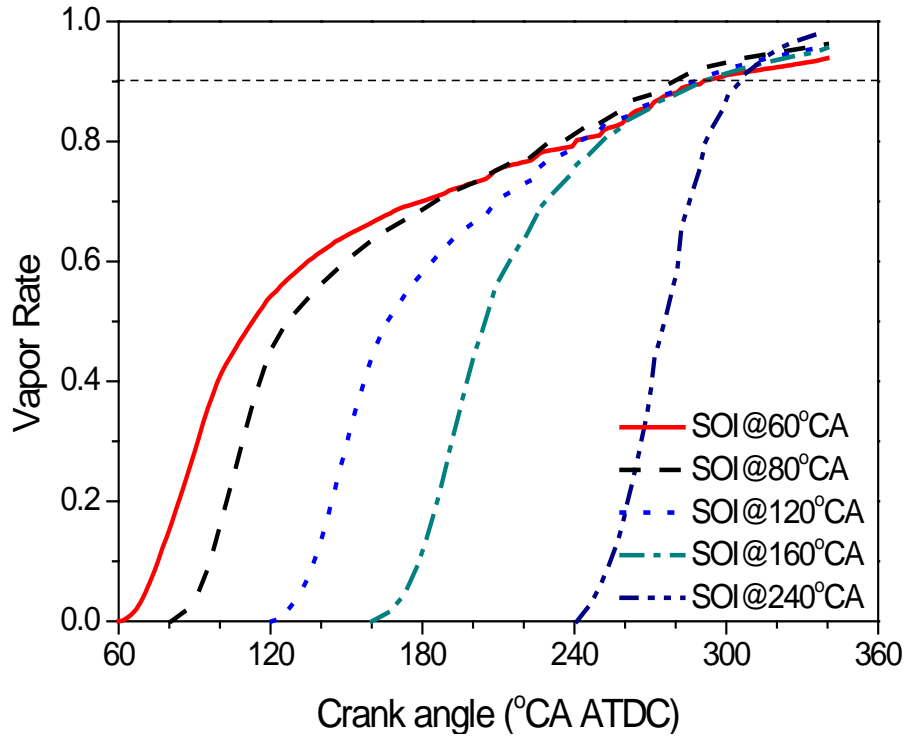


Fig.6.19 Evolutions of fuel vaporization at various injection timings at various injection timings.

To investigate the global quality of the mixture preparation, the temporal evolutions of three ranges of equivalence ratio mixture at various injection timings are presented in Fig.6.20. At the end of the compression stroke, an overall largest percentage of ignitable mixtures is observed in the case of injection at 120° ATDC, corresponding to the maximum of the tumble ratio as illustrated in Fig.6.5. In general, the case of SOI at closer timing to the maximum point of tumble ratio presents more rapid reduction of very lean mixture and growth of ignitable mixture. However, compared with the cases of SOI at 80 and 160°CA ATDC, a slightly higher percentage of ignitable mixture is formed at the end of the compression stroke for the latter case (as shown in Fig.6.20), owing to less fresh charge entrained (as listed in Table 6.2). When injection timing is further retarded after IVC (SOI at 240°CA ATDC), a dominant stratified distribution is observed, as demonstrated by least 10 % of both extremely

lean and over rich mixtures remained at the end of the compression stroke and this indicates the DMF-air mixture lacks of mixing time.

Apart from the global insights of mixing characteristics, the spatial equivalence ratio distribution was also analyzed. The scatter plot of equivalence ratio against temperature and the bar chart of mass density distribution of equivalence ratio at the end of compression stroke for the early injection and late injection cases are presented in Fig.6.21 to 6.24.

For the cases of injection during the intake period, caused by the strong interaction between spray and intake generated flow, the region of relatively lean equivalence ratio moves clockwise from the exhaust valve side (right hand side) towards the bottom; while the region of relatively rich equivalence ratio moves from the bottom to the exhaust valve side. Interestingly, attributed by the maximum tumble flow motion, compared to the other cases, an almost symmetrical distribution can be observed in Fig.6.21d when fuel is injected at 120°CA ATDC; moreover, the most homogeneous mixture is formed at the end of the compression stroke for this case, as shown in Fig.6.22. When the injection timing is further retarded, the inhomogeneity of the fuel-air mixture increases as the in-cylinder charge motion weakens as presented in Fig.6.22d and 6.22e.

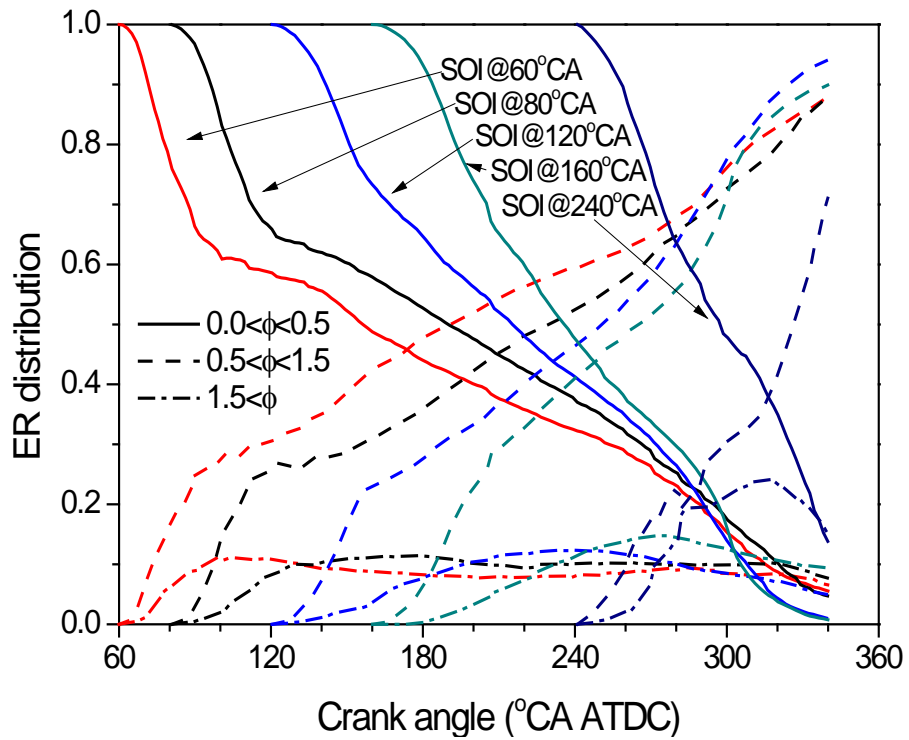


Fig.6.20 Evolutions of the percentages of three ranges of the equivalence ratio at various injection timings.

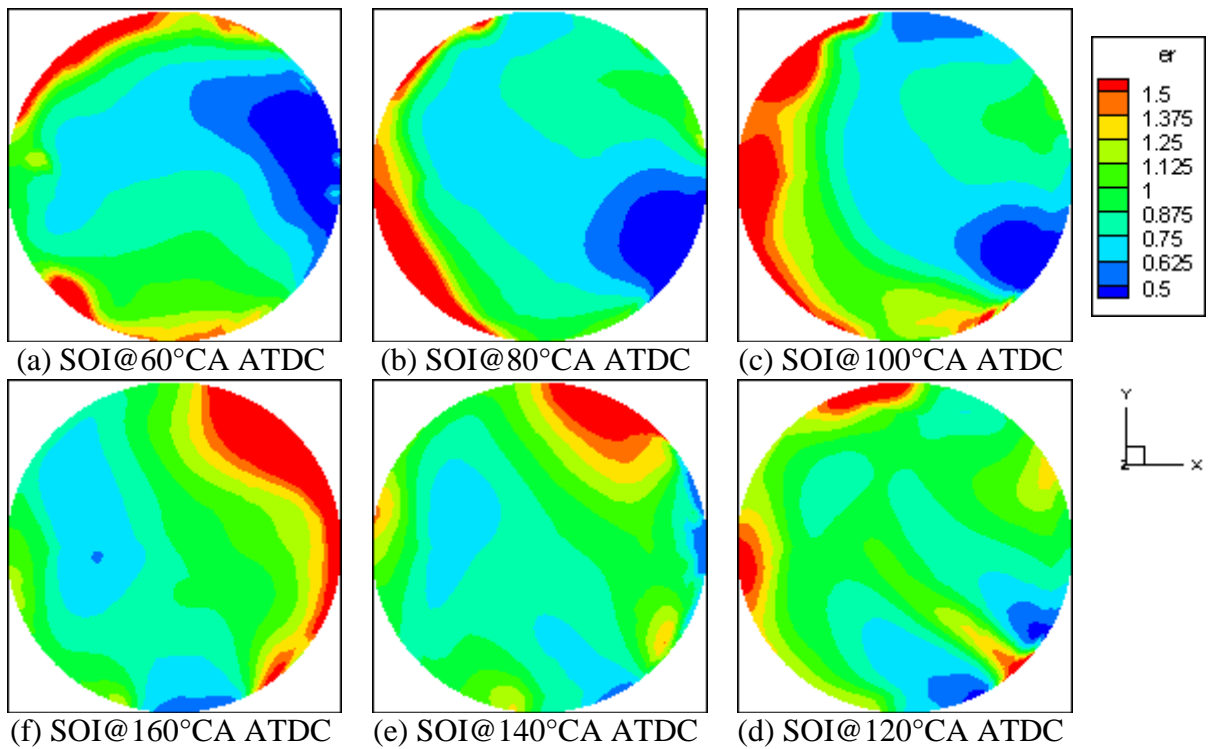


Fig.6.21 Spatial ER distribution at 340°CA ATDC of the early injection cases.

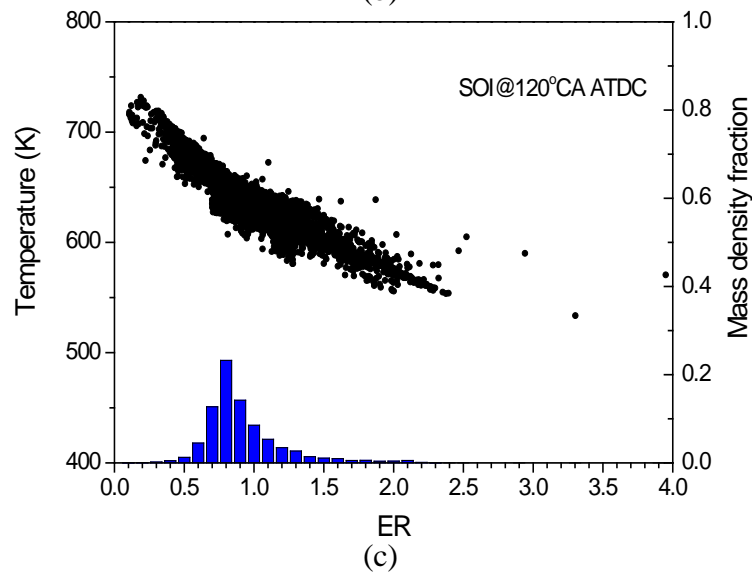
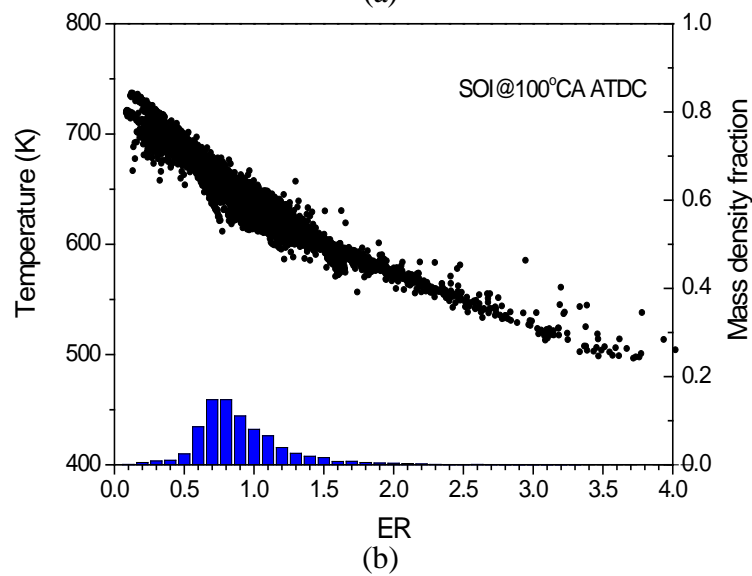
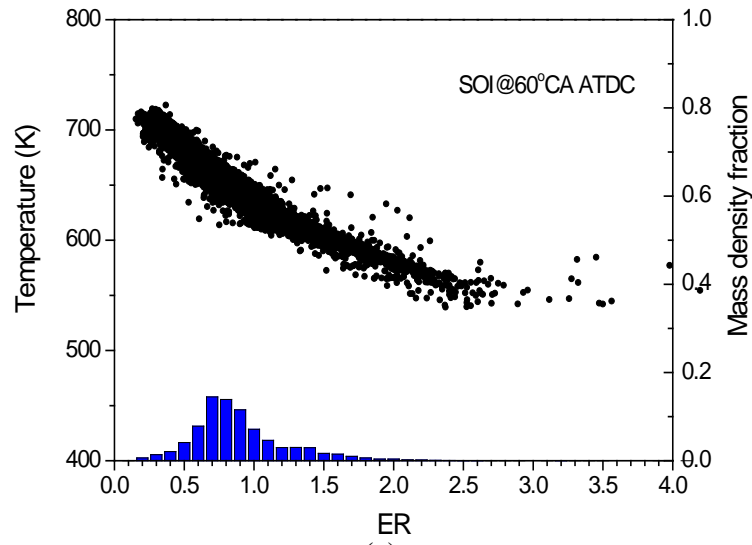


Fig.6.22 Scatters of temperature against ER and ER distribution in the mass density fraction at 340°CA ATDC of the early injection cases.

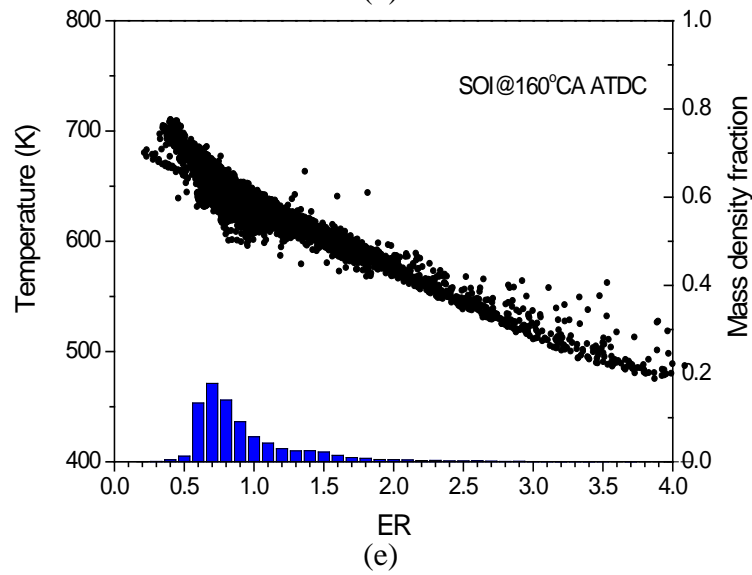
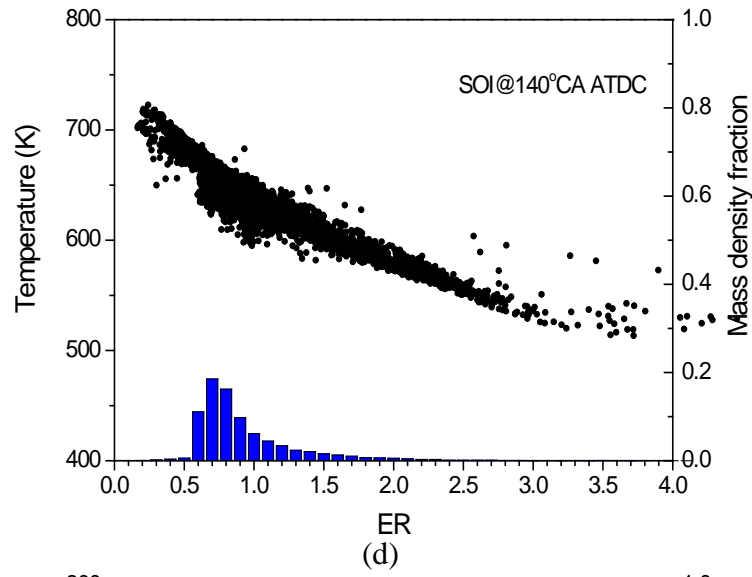


Fig.6.22 Scatters of temperature against ER and ER distribution in the mass density fraction at 340°CA ATDC of the early injection cases. (cont.)

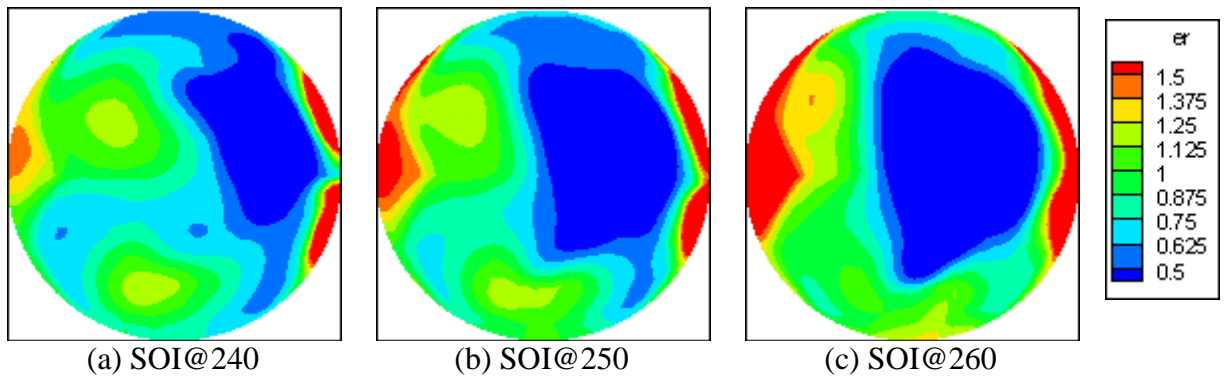


Fig.6.23 Spatial ER distribution at 340°CA ATDC of the late injection cases.

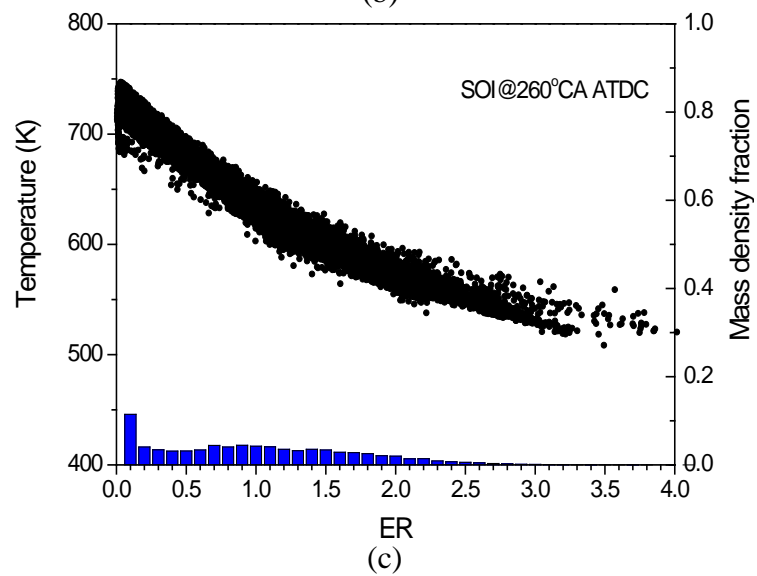
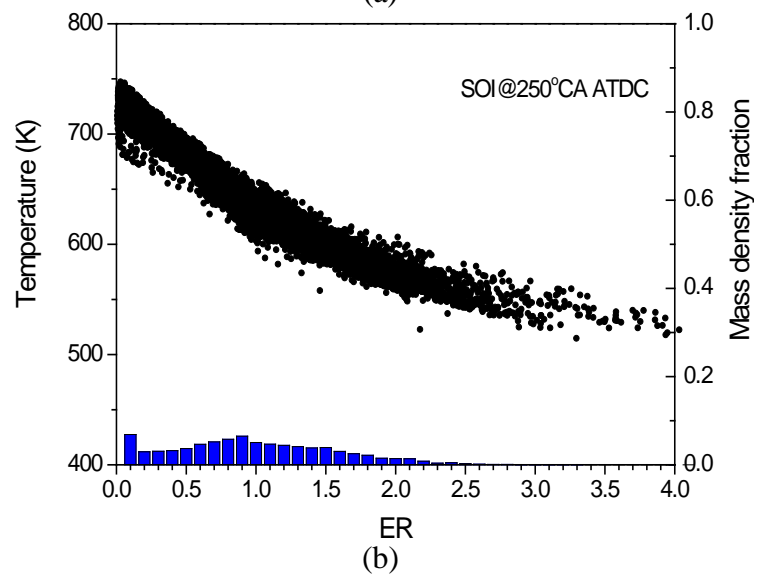
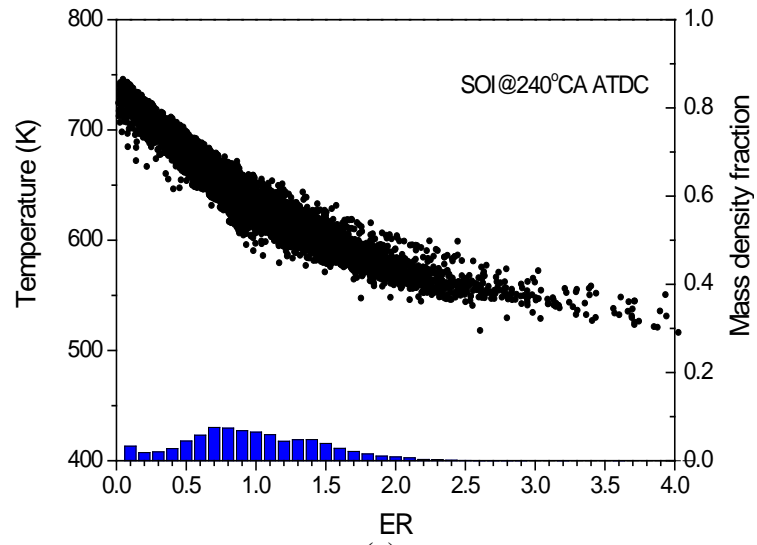


Fig.6.24 Scatters of temperature against ER and ER distribution in the mass density fraction at 340°CA ATDC of the late injection cases.

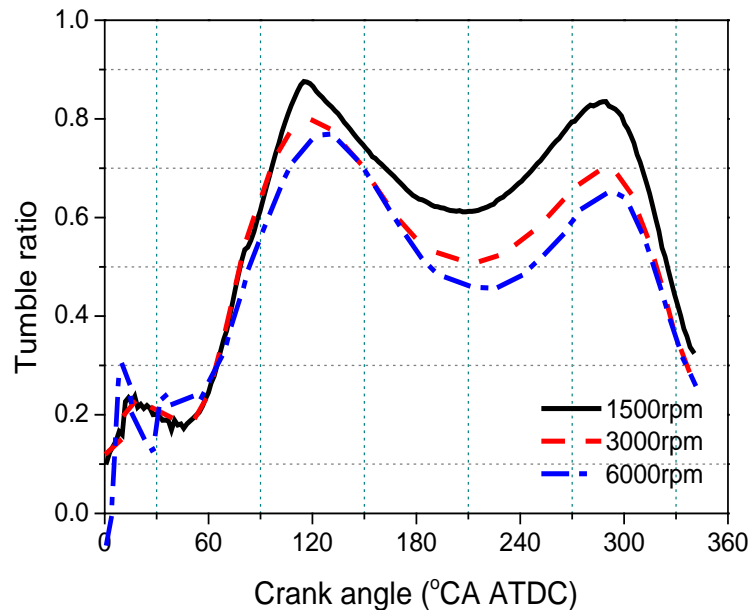
As to the cases when fuel injection takes place after IVC, without the effect of interaction between spray and intake generated flow, the location of lean mixture and rich mixture almost do not alter with the injection timing retarded. The lean mixture is concentrated at the middle right side and the rich mixture is concentrated at the two sides as shown in Fig.6.23. Compared to the cases of early injection, a more remarkable stratification of mixture characterized by a wider range of equivalence ratio distribution is found in Fig.6.24 for the late injection cases. In general, the mixture formation becomes worse with the injection timing retarded. Thus, the most stratified mixture is seen when the fuel is injected at 260°CA ATDC, where the mass density of equivalence ratio of no more than 0.1 has been already beyond 10%. It can be summarized that although over 95% evaporation of fuel has been finished, as seen in Fig.6.19, given by the weak in-cylinder flow motion and the short mixing time available, a portion of fresh charge is still short of mixing time with fuel vapor by the end of the compression stroke, as indicated in Fig.6.23 and 6.24.

6.4.2 Effect of Engine Speed

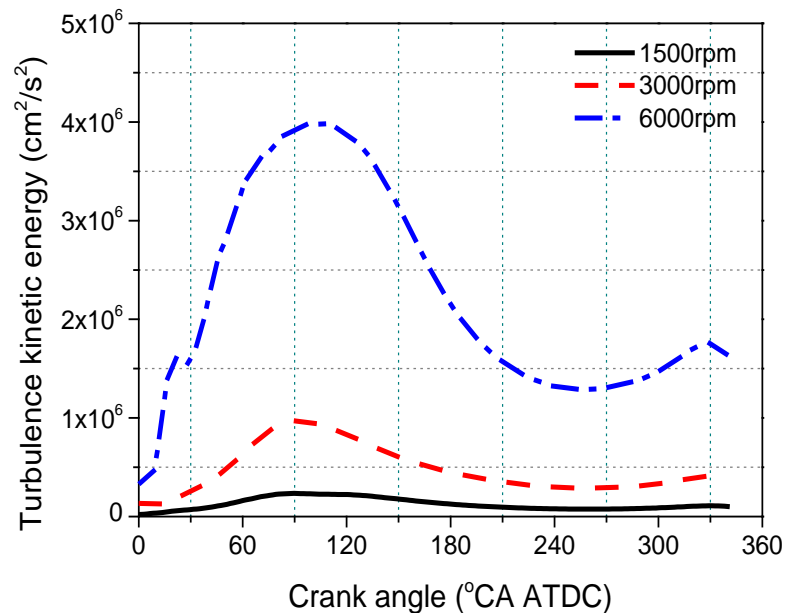
Another two engine speeds (3000 rpm and 6000 rpm) were chosen to study the characteristics of the fuel-air mixing process over a range of engine speeds. The injection parameters are listed in Table 6.3. Compared with Table 6.1, tiny differences among variable engine speeds indicate that the engine speed makes little effect on the fresh charge trapping but the injection duration is remarkably prolonged at higher speed, due to the relatively short time per cycle.

Table.6.3 Injection parameters under 3000 rpm and 6000 rpm

Speed	3000 rpm	6000 rpm
Fuel Mass Injected	0.0525g	0.0526g
Injection Duration	59.0°CA	118.3°CA
Relative Fuel/Air Ratio	Stoichiometric	



(a) Tumble ratio



(a) Turbulence kinetic energy

Fig.6.25 Evolution of tumble ratio and turbulence kinetic energy under various engine speeds

Evolutions of the tumble ratio and turbulence kinetic energy are presented in Fig.6.25. With the engine speed increases, the maximum of the tumble ratio reduces and the phasing of peaks and troughs are slightly retarded as presented in Fig.6.25a. In terms of the small-scale flow motion, a significant growth on the magnitude of turbulence kinetic energy can be observed in the high speed cases as shown in Fig.6.25b. When the engine speed increases from 1500 rpm to 3000 rpm, the maximum of the turbulence kinetic energy has doubled and further increased in the case of 6000 rpm, the value is up to four times higher than at the engine speed of 1500 rpm with the effect of the high-velocity intake jet flow.

Fig.6.26 illustrates comparisons of the interaction between spray and in-cylinder flow from the side view of engine under various engine speeds at 100°CA, 140°CA, 200°CA and 340°CA ATDC. When the engine speed increases, a greater magnitude of flow field is created due to the increase of mean piston speed and intake flow velocity. At higher speeds, a more intense interaction between spray and intake jet flow is found in Fig.6.26. The pattern of plumes is varied from mild asymmetry to severe asymmetry when the engine speed increases from 1500 rpm to 6000 rpm. Especially at the extremely high speed of 6000 rpm, the orientation of spray movement is obviously tilted towards the exhaust valve side by the strong intake generated flow as shown in Figs.6.26a and 6.26b. Compared with 3000 rpm, it is noticeable that plumes at the left side are driven towards the intake valve side by a strong clock-wise vortex in the centre of the cylinder, which is produced by the intake jet flow with the piston downwards movement as seen in Fig.6.26b.

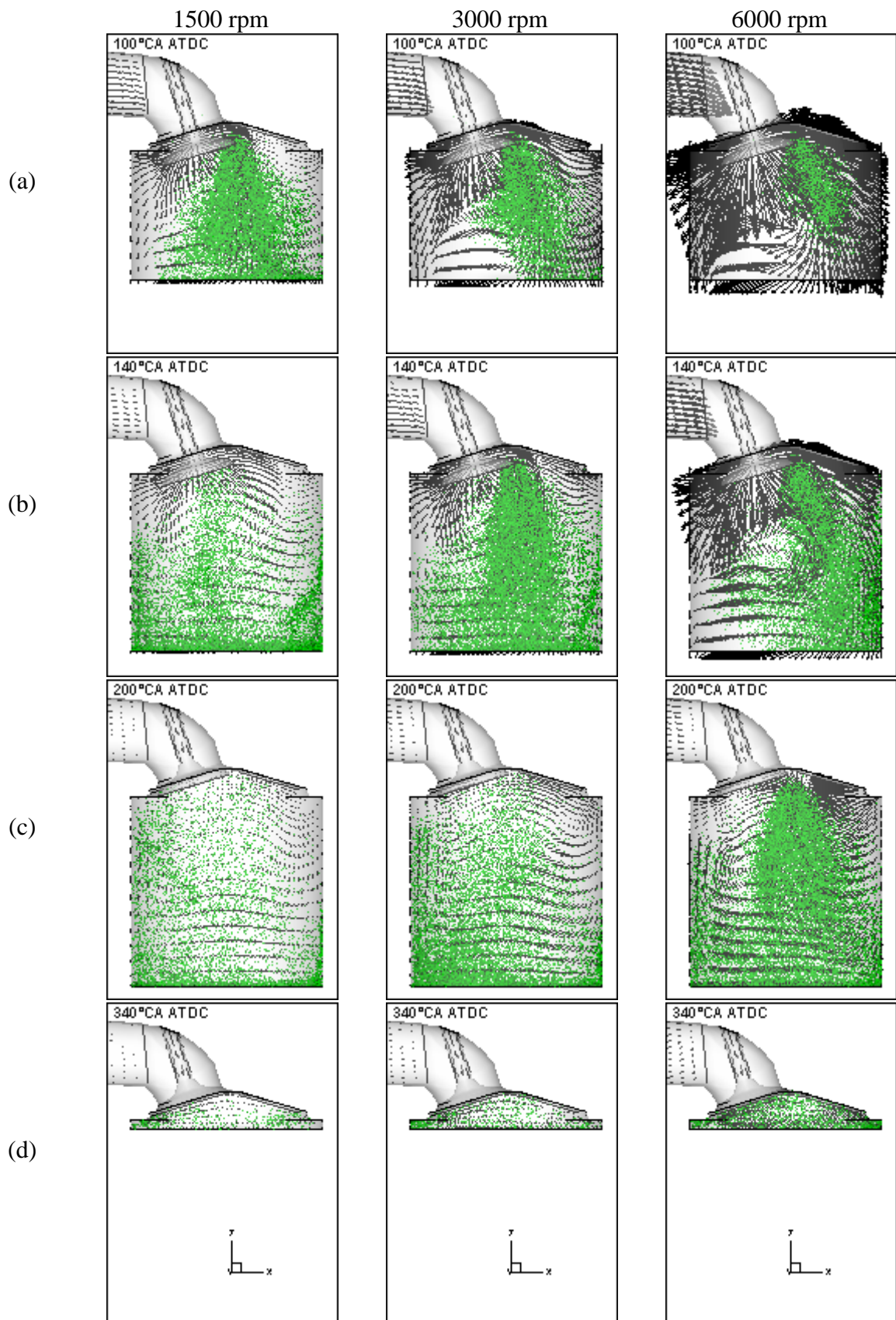
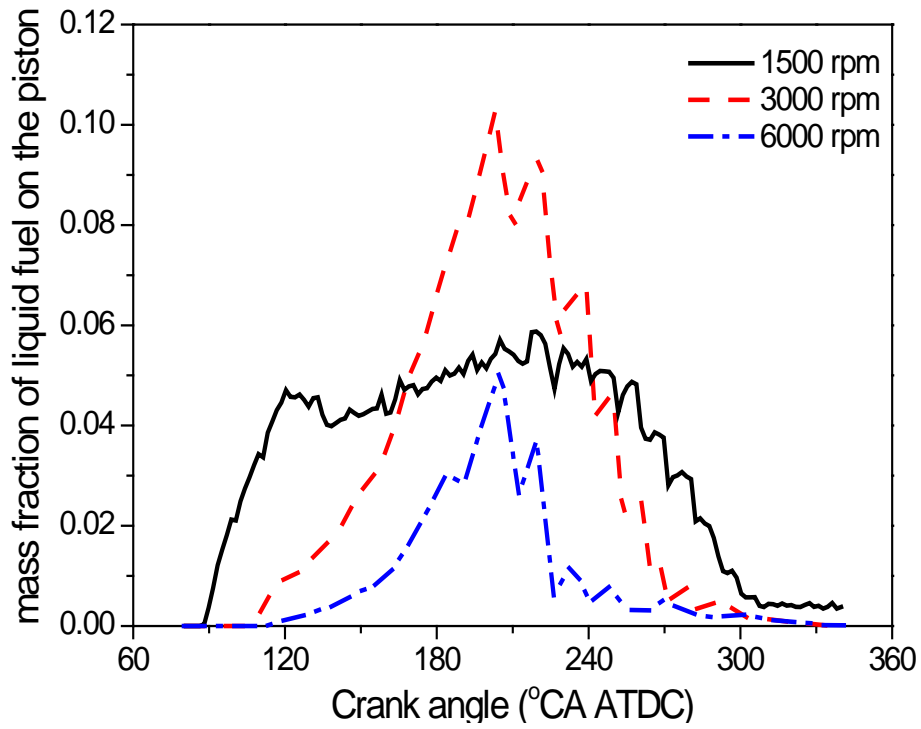


Fig.6.26 Comparisons of in-cylinder fuel and air flow under various engine speeds

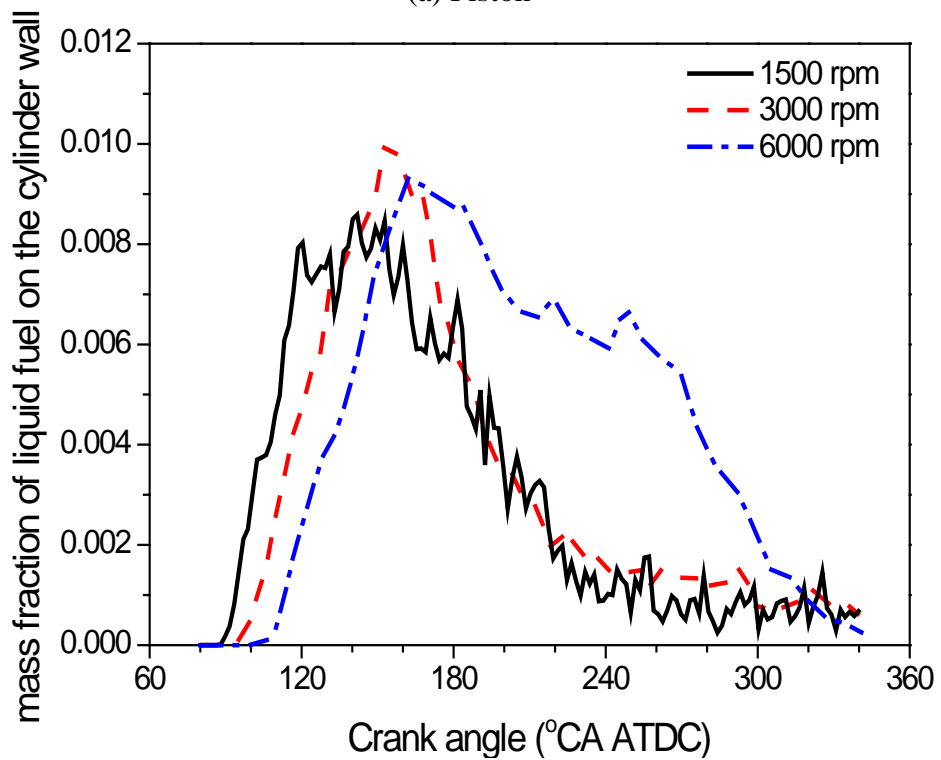
In addition, at high speeds, due to longer injection duration, the penetration is shorter than that of the case at 1500 rpm at the same crank angle as seen in Fig.6.26a; as shown in Fig.6.26d, by the end of the comparison stroke, the spray-gas interaction is greatly enhanced due to the increase of turbulence kinetic energy (see Fig.6.25b).

The evolutions of the spray-wall impingement at various engine speeds are illustrated in Fig.6.27. The in-cylinder flow motion makes a dominant effect on the spray impingement. At high speeds, the mighty turbulence kinetic energy strengthens the small-scale mixing and turbulence diffusion, and further shortens the residence time of droplets impinged on the piston surface.

More fuel impingement on the piston is created in the case of 3000 rpm than in the other two cases as shown in Fig.6.27a, driven by the downwards high-velocity intake jet flow. Unlike the case of 3000 rpm, at an engine speed of 6000 rpm, a certain amount of spray is delivered to the intake valve side by the central vortex, contributing to the reduction in the portion of spray impingement on the piston to a great extent. However, in this case, the plumes tilted to the exhaust valve side produce severe wetting in the cylinder liner by the strong intake jet flow; additionally, it can be indicated that the long injection duration prolonged the residence time of droplets on the cylinder liner as seen in Fig.6.27b.



(a) Piston



(b) Cylinder liner

Fig.6.27 Evolutions of mass fraction of the liquid fuel impinged on the wall under various engine speeds.

Fig.6.28 illustrates the global fuel vaporization histories for different engine speeds. When the engine speed increases, the initial vapor rate reduces; after BDC, the fuel evaporation is accelerated by strong turbulence diffusion. At 280°CA ATDC, 90% fuel changes into vapor in both 1500 rpm and 3000 rpm cases; whereas in the case of 6000 rpm, extra 20°CA is taken to attain this percentage as presented in Fig.6.28 due to overlong injection duration. However, the vaporization rate in the 6000 rpm case increases faster than the other two cases after 260°CA ATDC, motivated by the second increase of turbulence kinetic energy as presented in Fig.6.25 and the vaporization rate is up to 97.6% at the end of compression stroke.

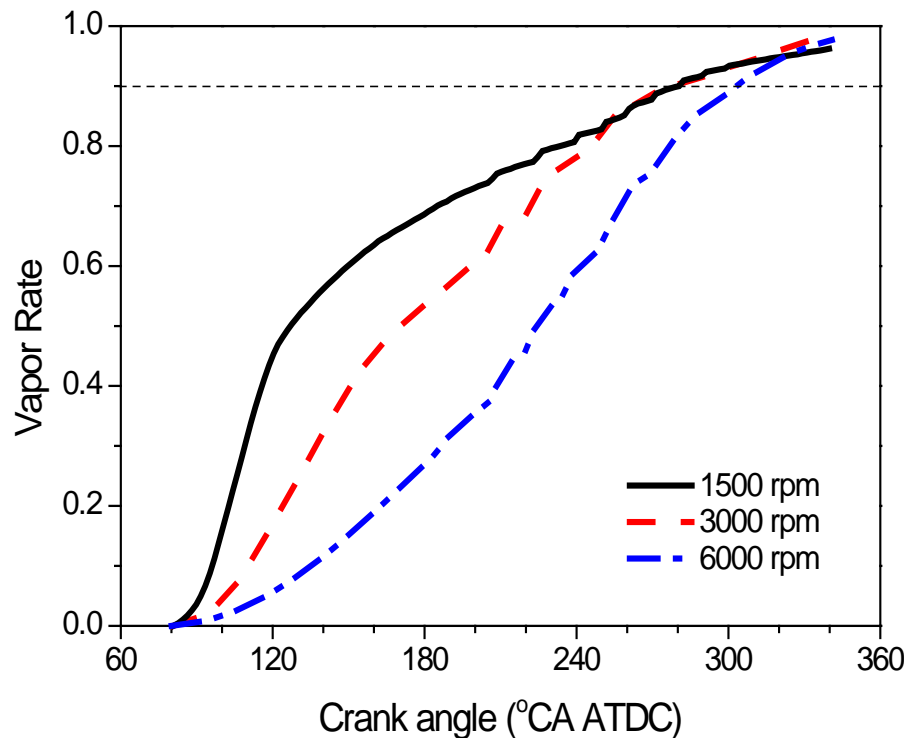


Fig.6.28 Evolution of fuel vaporization under various engine speeds.

The evolutions of average equivalence ratio distribution at different engine speeds are shown in Fig.6.29. In general, the growing/decreasing trends at high speeds are retarded due to the prolonged injection durations. Compared with the 1500 rpm case, severe piston impingement

impedes the increase of ignitable mixture after BDC for the case of 3000 rpm. Whereas at an engine speed of 6000 rpm, the end of injection is postponed to after BDC and hence, a remarkable increase of the percentage of ignitable mixture begins at 200°CA ATDC (the percentage at this crank angle is right over 20%). At the end of the compression stroke, a more stratified mixture is formed with the increase of engine speed, as demonstrated by higher percentages in both very lean mixture and over rich mixture compared to the case at 1500 rpm.

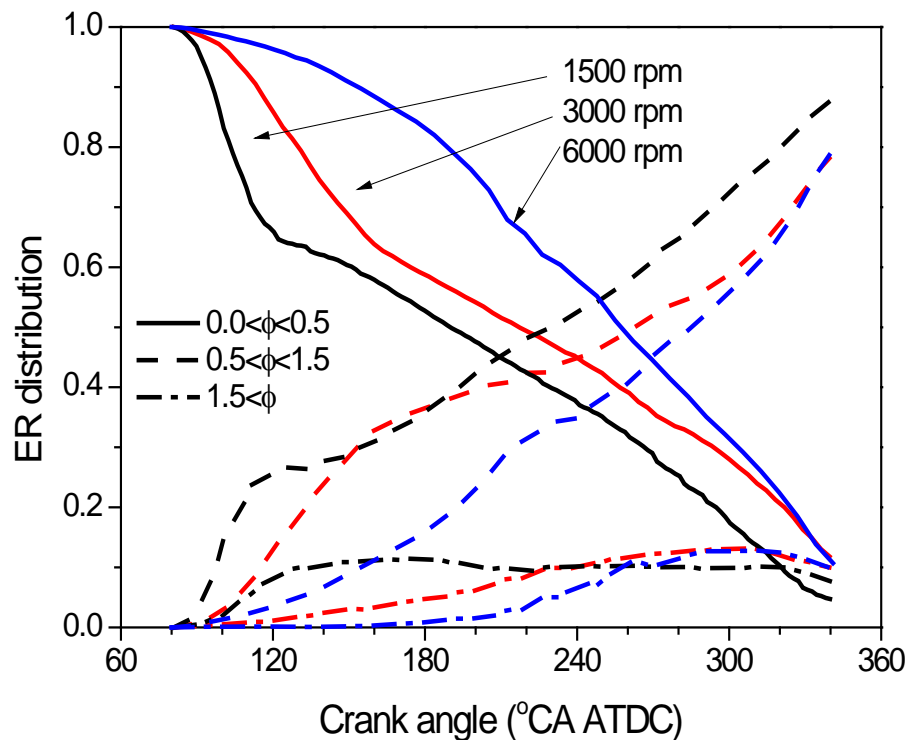


Fig.6.29 Evolution of the percentages of three ranges of the equivalence ratio under various engine speeds

Moreover, the spatial distributions of equivalence ratio at the end of the compression stroke for different engine speeds are presented in Figs.6.30 and 6.31. As shown in Fig.6.30, in all the cases, the general trend of the spatial distribution of equivalence ratio remains: the

relatively rich and very lean mixtures are concentrated at the intake and exhaust valve sides, respectively. Compared with Fig.6.15a, more mixture stratification exists at high speeds, indicated by a wider spread of equivalence ratio distribution and this is attributed by the lesser mixing time of the fuel vapor and fresh charge as shown in Fig.6.31.

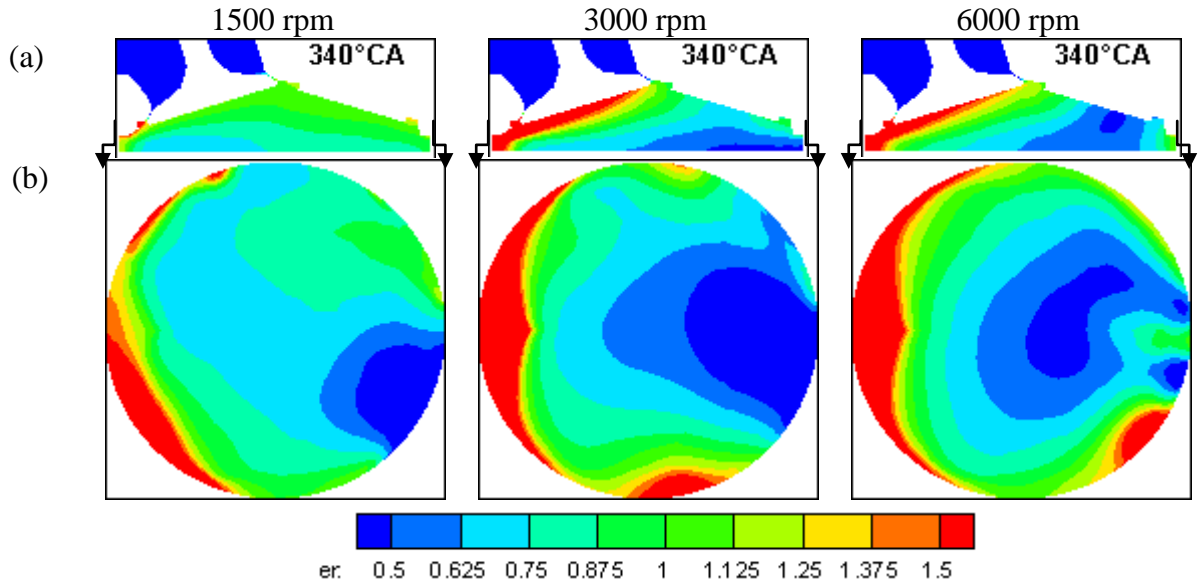
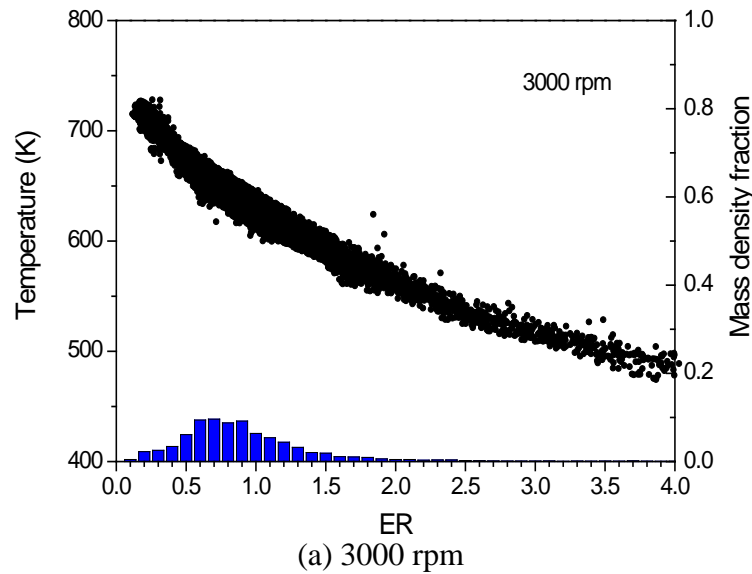


Fig.6.30 Spatial ER distribution at 340°CA ATDC under various engine speeds.



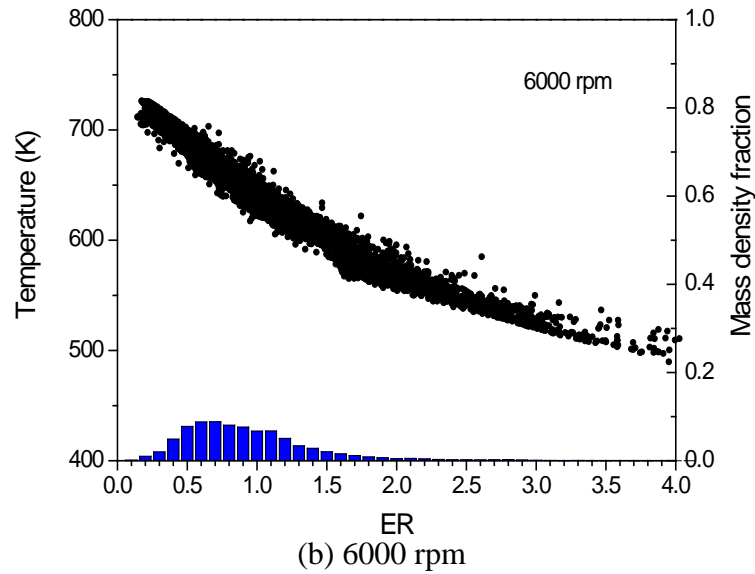


Fig.6.31 Scatters of temperature against ER and ER distribution in the mass density fraction at 340°C/CA ATDC under engine speeds of 3000 rpm and 6000 rpm.

6.5 Summary

With the validated spray model, a three-dimensional model is chosen to study the influence of fuel property, injection timing and engine speed on in-cylinder mixing. The discussion about the effect on in-cylinder fuel distribution and mixing quality in a stoichiometric DI engine can be concluded as follows:

1. Significant impingement on the piston and the cylinder liner was revealed with DMF spray in a DI engine, due to the combined effect of a slower evaporation rate, more injected fuel amount and larger mean droplet size, as compared to the case of gasoline spray. At the end of the compression stroke, the percentages of the highly rich mixture and extremely lean mixture of the case of DMF reach 7.7% and 4.7%, respectively. The average equivalence ratio in the cylinder for DMF is 0.96 whilst the overall equivalence ratio of gasoline is 0.99. In general, gasoline spray forms a more

homogeneous mixture than that of DMF spray. In addition, the mixture equivalence ratio of DMF around the spark plug is leaner than that of gasoline.

2. With the effect of charge cooling, more fresh charge can be trapped for the early injection cases. Fuel injection timing in the early intake period has a stronger effect of charge cooling. In addition, charge cooling makes a significant effect on the in-cylinder mixture preparation. When the fuel is injected in the early intake period (60°CA ATDC), the initial confined space contributes to considerable fuel impingement on the piston and cylinder wall, which slows down the subsequent vaporization process. With the effect of the strong intake generated flow, the fuel-air mixing is greatly enhanced for the case of fuel injection in the middle intake period (120°CA ATDC), so that a more homogenous fuel distribution than in the other cases is formed at the end of the compression stroke. In the late injection case (260°CA ATDC), severe fuel impingement on the piston surface, insufficient mixing time and weak gas flow motion lead to the most inhomogeneous mixture.
3. Engine speed has a strong effect on the in-cylinder gas motion. With the increase of engine speed (1500 rpm to 3000rpm, 6000 rpm), the tumble ratio reduces overall and its phasing is slightly postponed; whereas the turbulence energy is remarkably intensified by the increasing mean piston speed and intake air velocity. In the meantime, the magnified intake generated flow contributes to more spray impinged on the piston (3000 rpm) or on the cylinder liner (3000 rpm and 6000 rpm). Although the intense turbulence diffusion compensates for the negative effect of fuel impingement to a certain extent, wider spread of fuel distributions are formed at the end of the compression stroke, attributed by the lesser mixing time of fuel vapor and fresh charge at higher speeds.

Chapter 7 ANALYSIS OF SI COMBUSTION IN A STOICHIOMETRIC DI DMF ENGINE WITH CTC MODEL

7.1 Introduction

After the analysis of its mixing quality, the combustion characteristics of DMF will be investigated in this chapter. Its laminar flame characteristics were captured in a constant volume vessel by the Schlieren visualization technique. The key characteristic of laminar flame, laminar burning velocity will be determined according to the analysis of the flame growth. The laminar-kinetics time in the CTC model is derived directly from the Schlieren flame speed measurement. With regards to the turbulent-mixing time in the CTC model, the model constants are calibrated against the measured in-cylinder pressure and combustion phasing. Then the calibrated CTC model is validated with the HSP images of flame propagation. Finally, the qualitative comparison between DMF and gasoline with regards to combustion phasing, engine performance and emissions will be discussed.

7.2 Experimental Set-up and Data Analysis

7.2.1 Experimental Setup

The Schlieren imaging was done under an initial pressure of one bar and three various initial

temperatures (50°C, 75°C and 100°C). As presented in Fig.7.1, the test was carried out in a constant volume vessel, with two 100mm-diameter round windows at the light source (a 500 W xenon lamp) and image acquisition (high speed camera) sides; in order to provide a uniform temperature field, heat coils were installed on each corner of the wall of the vessel. The spark was initiated by a pair of tungsten electrodes, which were triggered by the TTL signal with a pulse width of 10 ms [167].

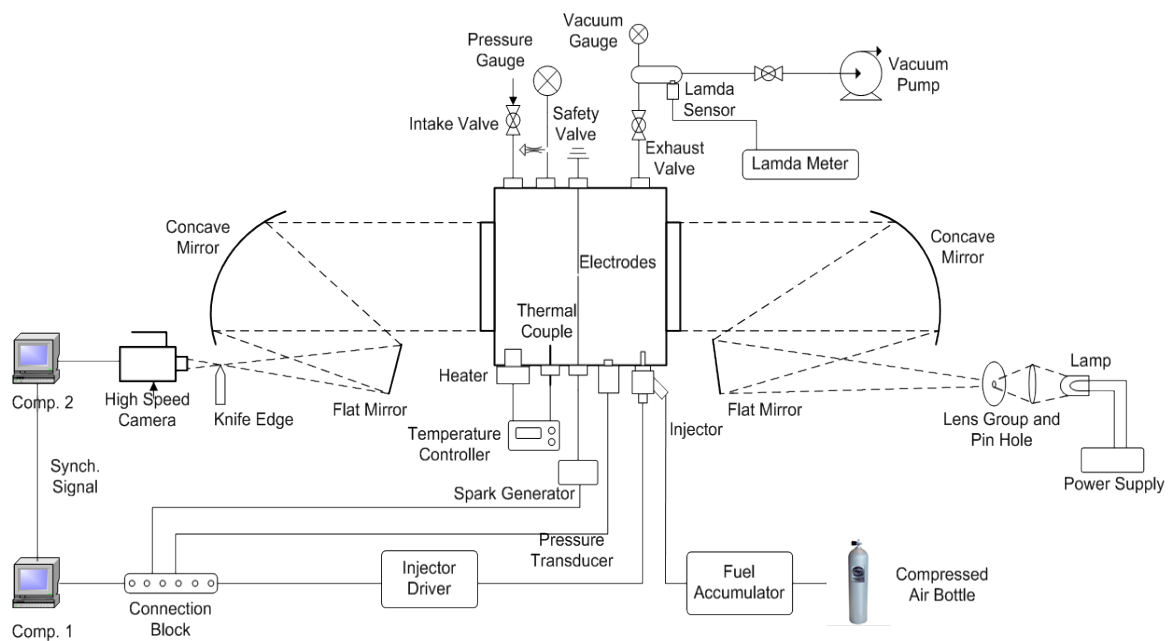


Fig.7.1. Schematic of the Schlieren system setup [167].

The lamp light was first collimated by a pin hole, and then passed through a Z-type light path and finally a spotlight used for the Schlieren visualization was generated through a knife-edge. A sample rate of 3 kHz was adjusted in the high speed camera. The fuel was injected using a multi-hole GDI injector at an injection pressure of 100 bar. The amount injected was determined by the injection duration according to the pre-calibrated data. To alleviate the

interference of the residual gas, a vacuum pump was installed to scavenge the vessel before the start of every test [167].

7.2.2 Data Processing

The image processing and the laminar burning velocity were calculated by the in-house developed MATLAB code. The flame front along the electrodes was distorted by the flame quenching and hence the vertical direction was chosen for the detection of the flame front radius (see Fig.7.2). Additionally, the measurement region with a range of 6-18mm in radius was chosen for the laminar flame analysis as presented in Fig.7.2, in order to minimize the influences of the ignition accumulation in the early stage and the pressure fluctuation reflected by the surrounding wall [186].

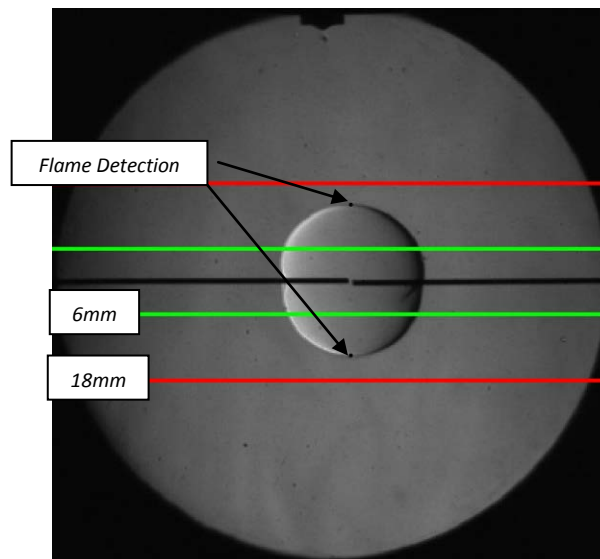


Fig.7.2. Illustration of the study range in the Schlieren image. [167]

7.2.3 Laminar Burning Velocity

Laminar burning velocity considered as the indicator of the chemical kinetics of reactions, makes a direct effect in the fuel burning rate and engine performance. This will be discussed in this subsection. The laminar burning velocity was calculated by measuring the flame growth as illustrated in Fig.7.3.

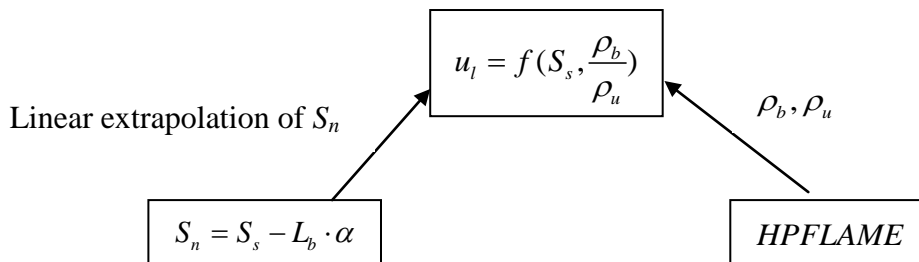


Fig.7.3 Charts of the calculation method of the laminar burning velocity.

As presented in Fig.7.3, the laminar burning velocity u_l is defined as a function of the unstretched flame speed S_s and the density ratio (ρ_b/ρ_u) of the burned and the unburned gases. The former parameter can be obtained by the linear extrapolation of the stretched flame speed S_n ; the latter can be indirectly calculated through the HPFLAME code [167]. Using the radius r_u measured from the Schlieren images, the stretched laminar flame speed S_n , can be determined by [167]:

$$S_n = \frac{dr_u}{dt} \quad \text{(Equation 7.1)}$$

Fig.7.4 presents the laminar burning velocities of the two fuels at different initial temperatures and equivalence ratios. Firstly it is clearly shown that laminar burning velocity is sensitive to the equivalence ratio. Under the identical initial temperature, the variation of the laminar flame speed in Fig.7.4 looks like a parabolic curve, which is shown as high in the middle and low on both sides; the flame speed is peaked in the range of $\phi = 1.15 \sim 1.25$, which is slightly richer than the stoichiometric ratio. This is consistent with the flame characteristics of the common hydrocarbon fuels [187]. Additionally, the influence of the initial temperature on the shape of the profile is highlighted: with the initial temperature increasing, the curvature of the profile reduces for both fuels, as presented in Fig.7.4.

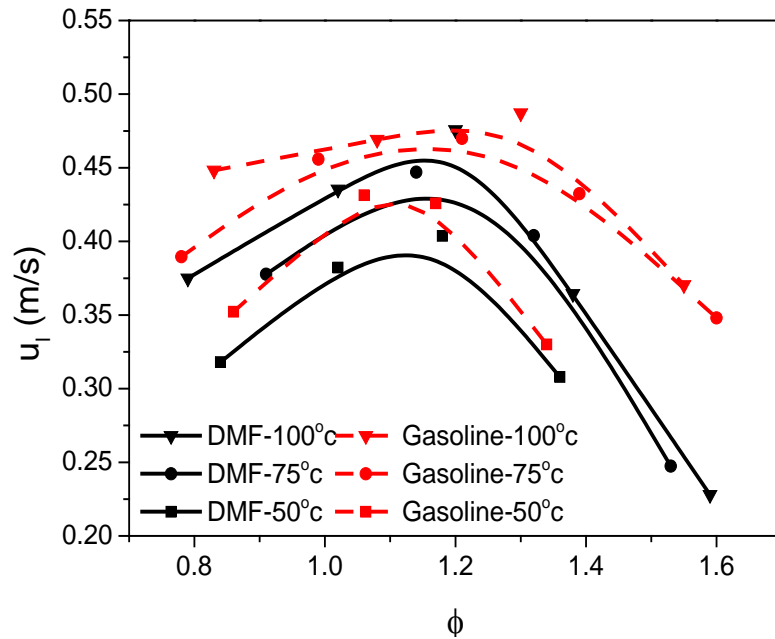


Fig.7.4 Laminar burning velocities of DMF and gasoline at different initial temperatures and equivalence ratios adopted from [167]

As compared to gasoline, the laminar burning velocity of DMF is observed to be slightly slower than that of gasoline overall. The profiles of both fuels are similar as the equivalence ratio is ranging from 0.8 to 1.2; however, in the rich region ($\phi = 1.2 \sim 1.6$), the decrease rates of

the laminar burning velocity in the DMF cases are greater than in the gasoline cases (except the case of 50°C). For instance, at 75°C the difference between the two fuel cases is about 0.05 m/s at $\phi=0.9$; whereas the difference becomes 0.125 m/s at $\phi=1.5$, five times larger than the former one.

7.3 Laminar Combustion Model Validation

In this subsection, the laminar combustion model will be calibrated based on the Schlieren data. Numerical simulation on DMF laminar flame propagation was undertaken in the constant volume cylindrical chamber with a size of 60 mm in diameter and 60 mm in depth. The spark location lies at the top centre of the cylinder. The numerical grid used for analysis is 27,000 computational cells (radial x circumferential x axial cells = 30x30x30). The cell size agrees with that in the engine simulation.

It must be emphasized that ignition is greatly mesh-dependent [188]. As subsection 7.2.2 mentioned spark energy affects the flame speed fairly during the initial period; additionally, as the flame front radius exceeds a certain size, the influence of the boundary of the chamber and pressure wave reflection become significant on the flame propagation. Thus, subsequent numerical analysis of laminar combustion characteristics of DMF will be also concentrated on the period when flame front radii are between 6-18mm.

7.3.1 Numerical Mean Stretched Flame Speed

As to the supporting data for calibration, as defined as the change rate of the flame radius in Eq.7.1, the stretched flame speed is a visual indicator of laminar flame propagation. Thus, unlike in the common 1D simulation of laminar flame propagation, the average stretched flame speed ($\overline{S_n}$) instead of the laminar flame speed is selected for the subsequent calibration of the laminar combustion model.

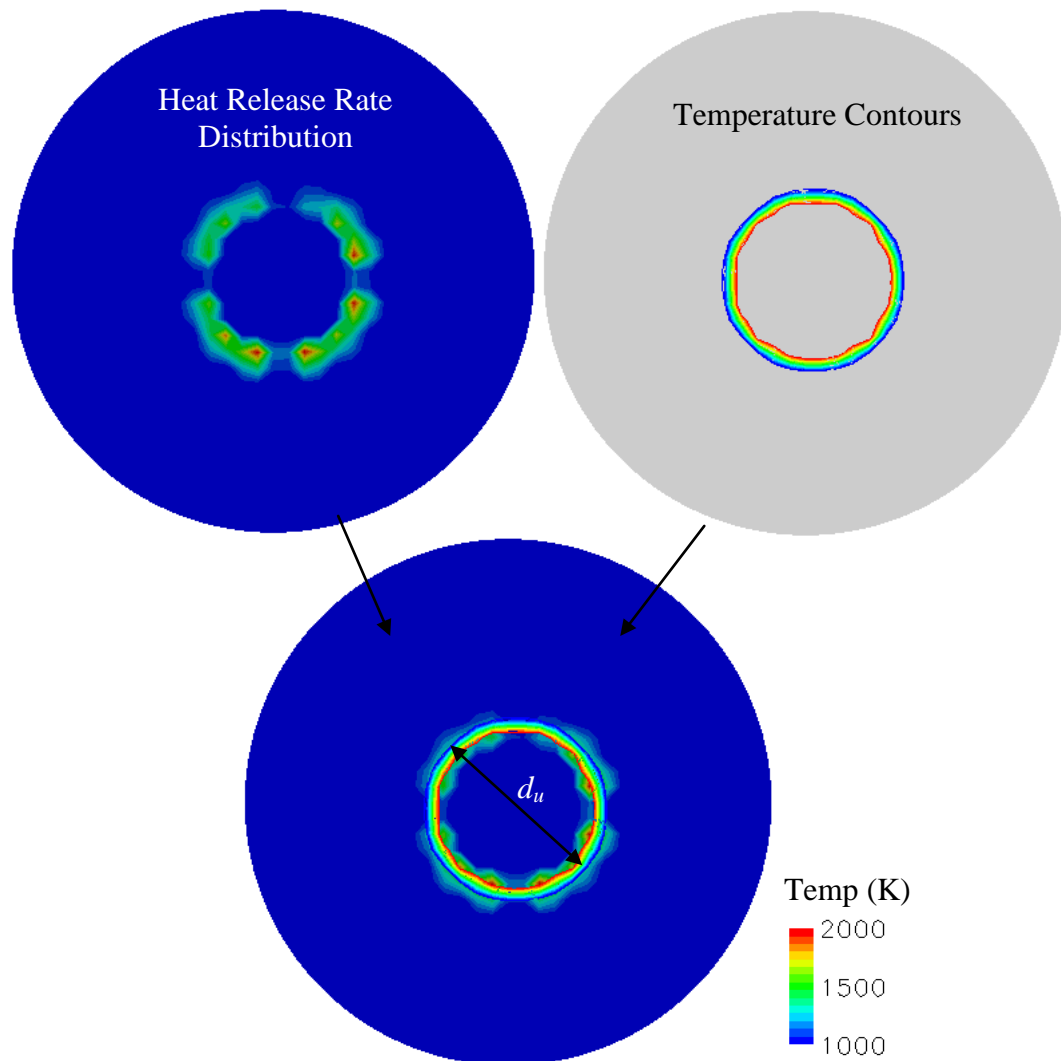


Fig.7.5 Illustration of flame front detection

As to the flame front detection, local temperature and heat release rate are introduced to identify the flame front diameter (d_u). As illustrated in Fig.7.5, in the bottom cut-away view of the central plane, the edge of flame front is detected by a local temperature higher than 1000 K within the high heat release rate region.

7.3.2 Effect of Laminar Combustion Model Parameters

In the laminar timescale, the ignition delay of DMF was measured by Sirjean et al. [189] in a shock tube and expressed by power-laws in the concentrations of fuel, oxygen and argon (diluent gas):

$$\tau_i = 1.8 \times 10^{-16} \cdot [DMF]^{0.34(\pm 0.04)} \cdot [O_2]^{-0.79(\pm 0.03)} \cdot [Ar]^{-0.37(\pm 0.05)} \cdot \exp(21000(\pm 300)[K]/T)[s]$$

(Equation 7.2)

Choosing the ignition delay as the laminar kinetic time and comparing with Eq.3.43, the values or data ranges of the laminar kinetic time parameters can be determined, that is, $A_l = 1.8 \times 10^{-16}$, $FI = 0.34(\pm 0.04)$, $OI = -0.79(\pm 0.03)$ and $E = 21000(\pm 300)$.

In addition, the correlation of dilution ratio (residual ratio) with the laminar burning velocity of DMF was obtained by Li et al. [169], and expressed as follows:

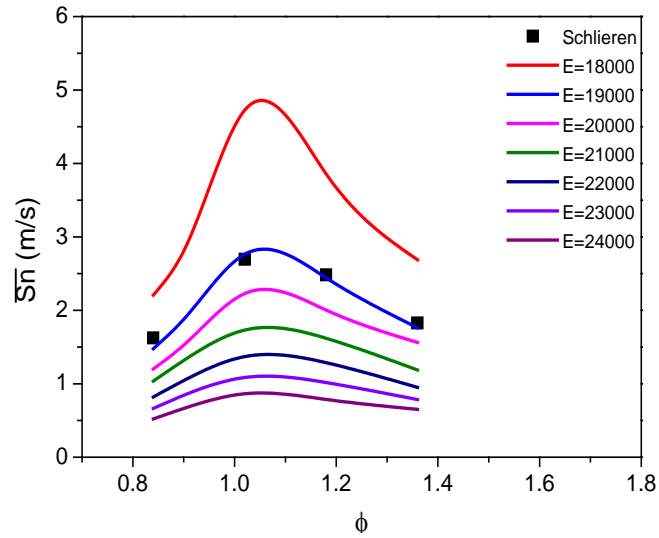
$$\frac{u_l}{u_{l,R}} = -2.63R' + 1$$

(Equation 7.3)

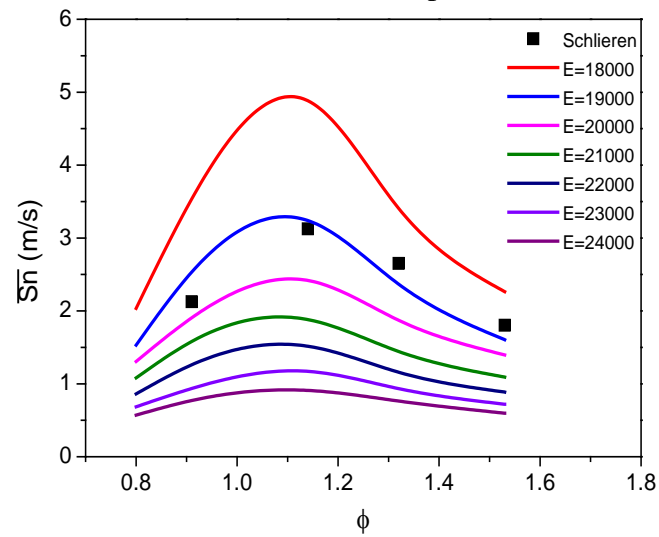
where $u_{l,R}$ refers to the laminar burning velocity with dilution. According to Eq.3.41, the parameters in the correction function of residual gas can be calculated or obtained, $R_a=1.85$ and $R_b=-2.63$.

After the approximate selection of the model constants, particular values of three primary parameters of FI , OI and E need to be determined. Fig.7.6 presents the effect of apparent activation energy E on the mean stretched flame speed at various equivalence ratio and initial temperatures with the FI and OI fixed at 0.34 and -0.79, respectively. The mean stretched flame speed is strongly dependent on E , as presented in Fig.7.6. As defined in Eq.3.43, the results reflect an exponential relationship with the activation temperature E ; when E reduces from 19000 to 18000, the overall profile increases dramatically and particularly, the maximum is almost doubled as seen in Fig.7.6a. From the view of equivalence ratio, a lower value of E leads to a steeper curve. That is, the mean stretched flame speed closing to the maximum point ($\phi=1.0\sim 1.2$) is more sensitive to apparent activation energy E compared to the lean or rich mixtures. Overall, in the case of E selected as 19000, numerical prediction achieves a better agreement with the Schlieren data.

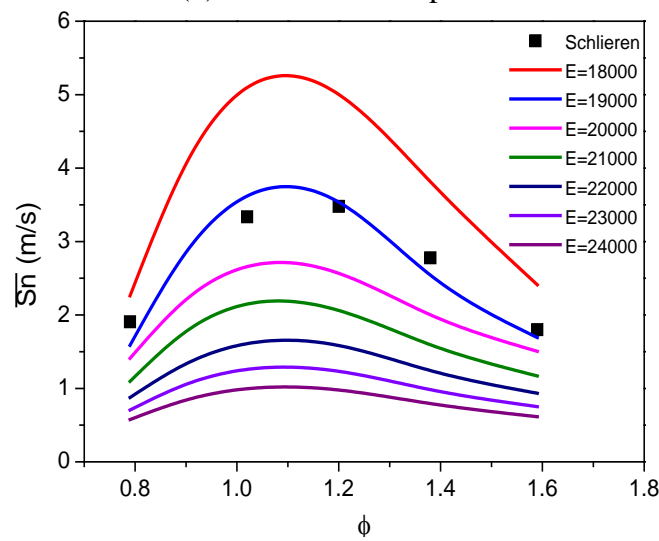
Fig.7.7 and Fig.7.8 present the sensitivities of exponential indexes of fuel and oxygen concentrations FI and OI , respectively. Under the same initial temperature and equivalence, as FI or OI enlarges, the mean stretched flame speed increases. For the lean mixture, the flame speed is more sensitive to the fuel concentration and whereas it is more sensitive to oxygen concentration for the rich mixture [187]. Compared with Fig.7.7, almost no discernible difference can be observed when $\phi=0.8$ in Fig.7.8. The optimal group of parameters are $FI=0.34$, $OI=-0.79$ and $E=19000$.



(a) 50°C initial temperature

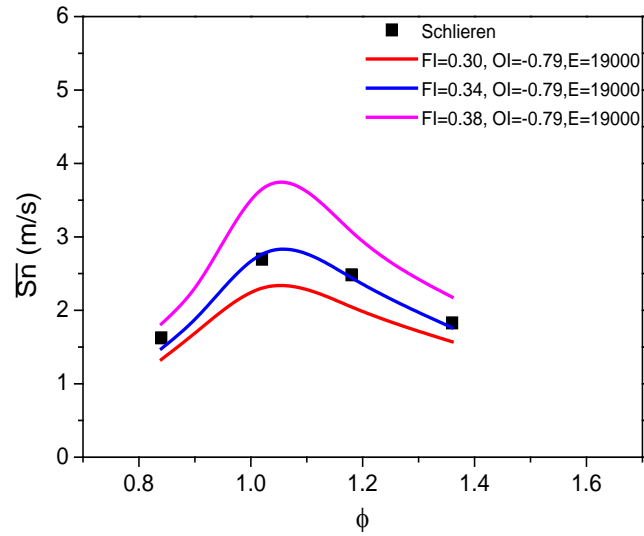


(b) 75°C initial temperature

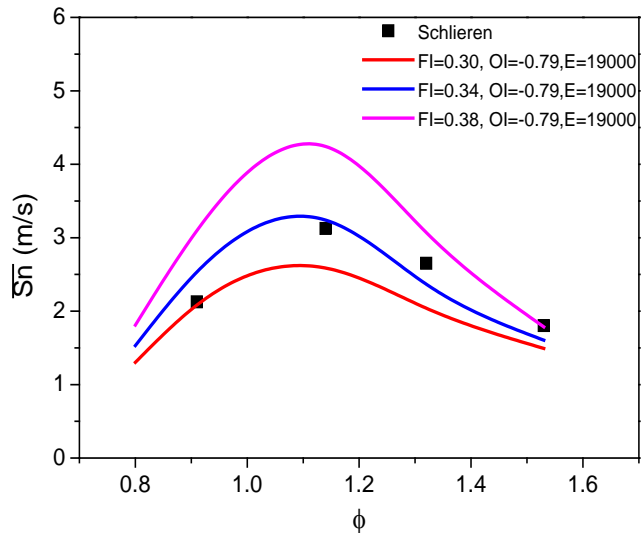


(b) 100°C initial temperature

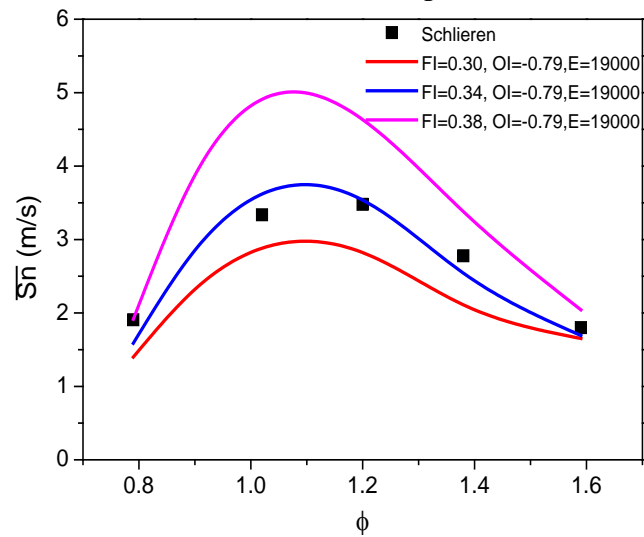
Fig.7.6. Effect of E on mean stretched flame speed at different equivalence ratios.



(a) 50°C initial temperature

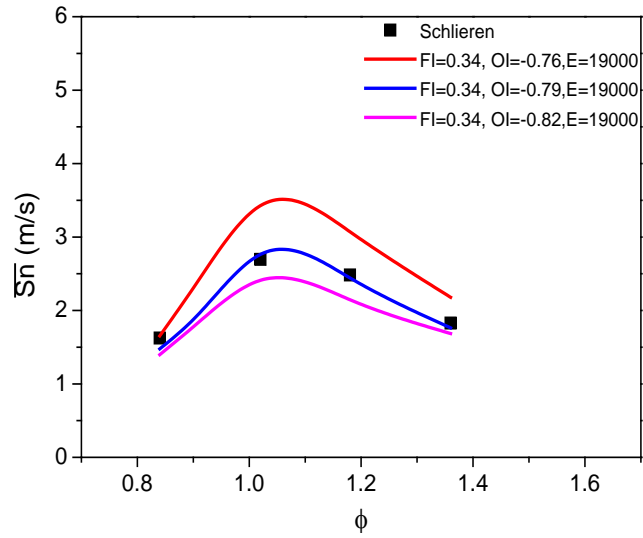


(b) 75°C initial temperature

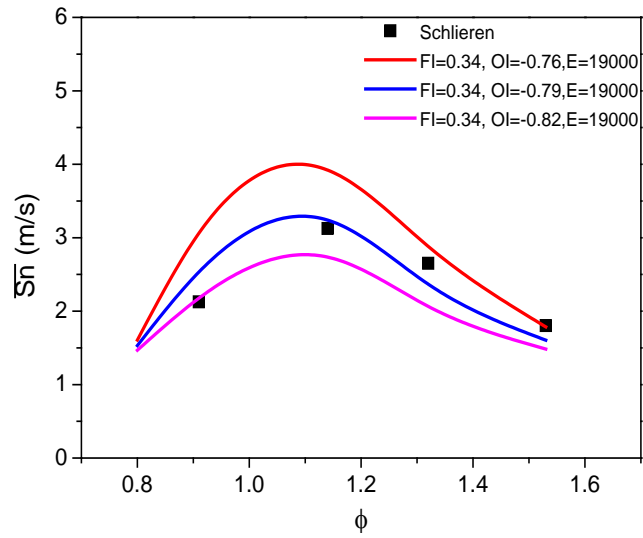


(b) 100°C initial temperature

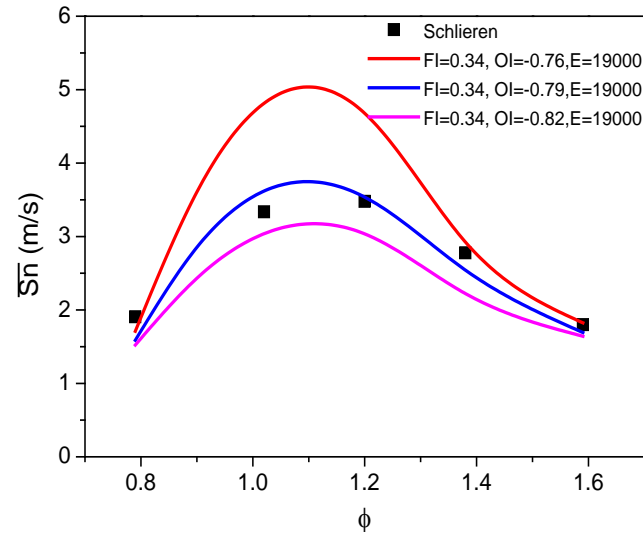
Fig.7.7. Effect of FI on mean stretched flame speed at different equivalence ratios.



(a) 50°C initial temperature



(b) 75°C initial temperature



(c) 100°C initial temperature

Fig.7.8. Effect of OI on mean stretched flame speed at different equivalence ratios.

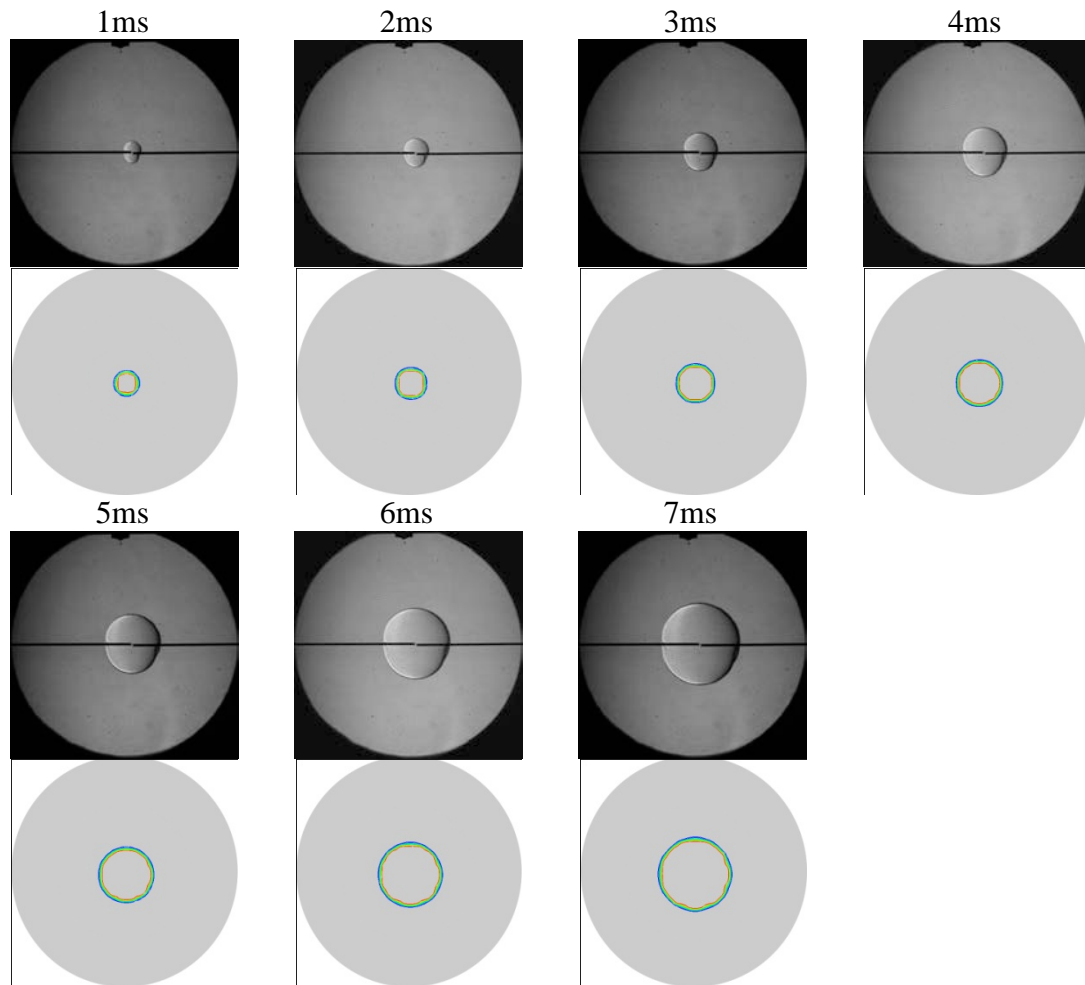


Fig.7.9 Comparisons of numerical temperature contours and Schlieren images of DMF at $\phi = 1.14$ and 75°C initial temperature.

Comparison of simulated temperature contours and Schlieren images are presented in Fig.7.9. The numerical laminar flame propagation simulated by the calibrated laminar combustion model achieves a good consistency with the Schlieren images overall. However, in the initial period (1-2ms), the numerical kernel radius is visually a bit bigger than the measured radius as shown in Fig.7.9. This discrepancy can be resulted from the distortion of the kernel by the electrodes.

7.4 Turbulent Combustion Model Validation in Premixed Charge Spark Ignition Combustion

The model validation for turbulent combustion was conducted in a stoichiometric premixed charge SI engine with the specifications listed in Table 5.1. The engine was run at a speed of 1500rpm. The calculations were conducted from IVC at 225°CA ATDC to EVO at 204 °CA BTDC. The spark timing was fixed at 344°CA ATDC. All the initial and boundary conditions were chosen equally for comparative purposes. The initial pressure and temperature were taken from the 1D engine simulation results using Wave, as presented in Fig.5.5.

7.4.1 Effect of Turbulent Combustion Model Parameters

According to Eq.3.39 and Eq.3.44, the parameters C_{m1} and C_{m2} remain to be determined in the turbulent combustion model. The parameters will be determined by analyzing the effects of C_{m1} and C_{m2} on the engine performance obtained by Zhong et al. [162] in the subsequent subsection.

The effects were carried out with 9 groups of parameters as listed in Table 7.1. The values in Case 1 were the default values of the two model constants as given in [146]. With the C_{m2} fixed at 0.06 and the values of C_{m1} ranging from 1.4 to 2.2, the first five cases were used to investigate the effect of C_{m1} . While the latter cases with Case 1 were used for the investigation of the effect of C_{m2} through adjusting the values of C_{m2} and fixing C_{m1} at 1.4.

Table 7.1 Cases of the effects of C_{m1} and C_{m2}

No. of Case	1	2	3	4	5	6	7	8	9
C_{m1}	1.4	1.6	1.8	2.0	2.2	1.4	1.4	1.4	1.4
C_{m2}	0.06	0.06	0.06	0.06	0.06	0.10	0.08	0.04	0.02

Fig.7.10 and Fig.7.11 present the influence of C_{m1} and C_{m2} on the Mass Fraction Burned (MFB) curve, respectively. As defined in [181], MFB is the instantaneous accumulated heat release normalized by the sum of the heat release within the whole combustion process. Thus, the combustion process could be classified into individual durations corresponding to percentage of the MFB.

Firstly, the combustion initial duration, as defined from the spark timing to the 10% MFB, is presented in Fig.7.10a and Fig.7.11a. With the C_{m1} increasing from 1.4 to 2.2, the phasing of 10% MFB changes from 357.1 to 362.7 °CA ATDC as illustrated in Fig.7.10a. This means the initial combustion process is remarkably extended to almost 6 °CA; while a maximum difference of 2 °CA of the phasing of 10% MFB can be observed with the variation of C_{m2} as presented in Fig.7.11. This indicates the initial duration is more sensitive to C_{m1} than C_{m2} , corresponding to the description in subsection 3.6.1 that the C_{m1} represents the effect of turbulent length scale divided by the laminar burning velocity in the initial duration. From the view of comparison between the simulation and measurement, Cases 3 and 4 achieve better agreements with the experimental results.

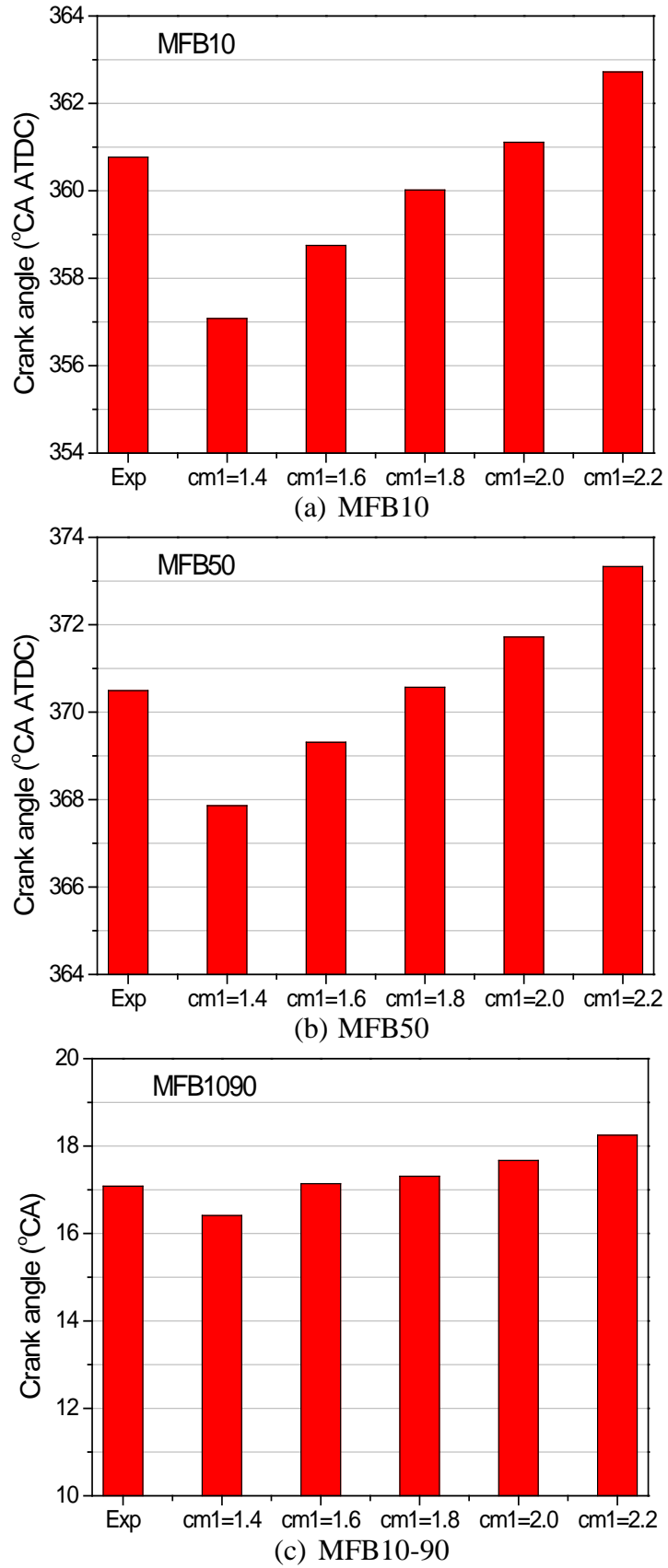


Fig.7.10 Effect of C_{m1} on the Mass Fraction Burned ($C_{m2}=0.06$)

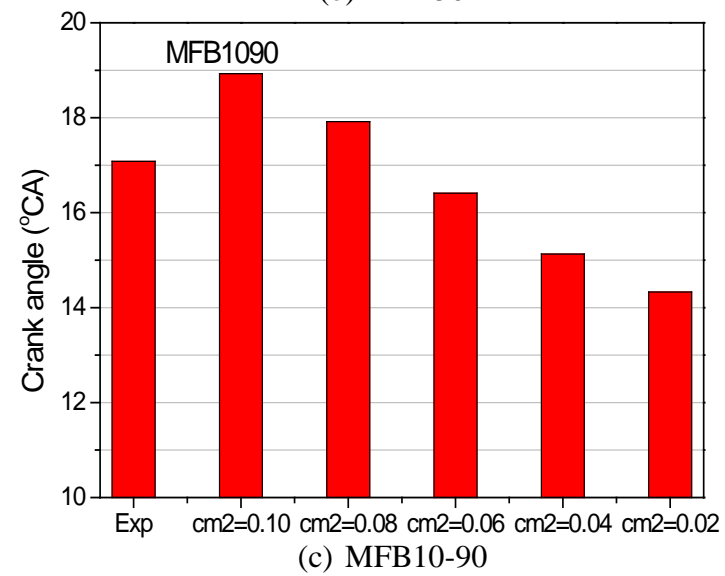
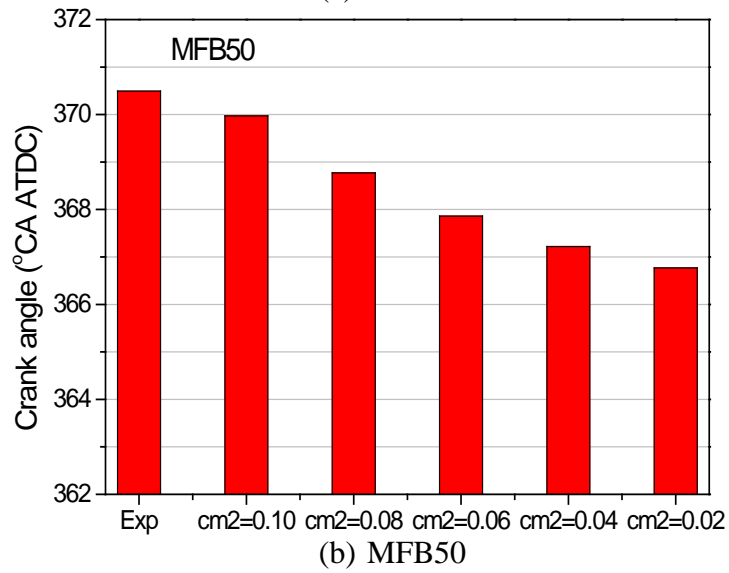
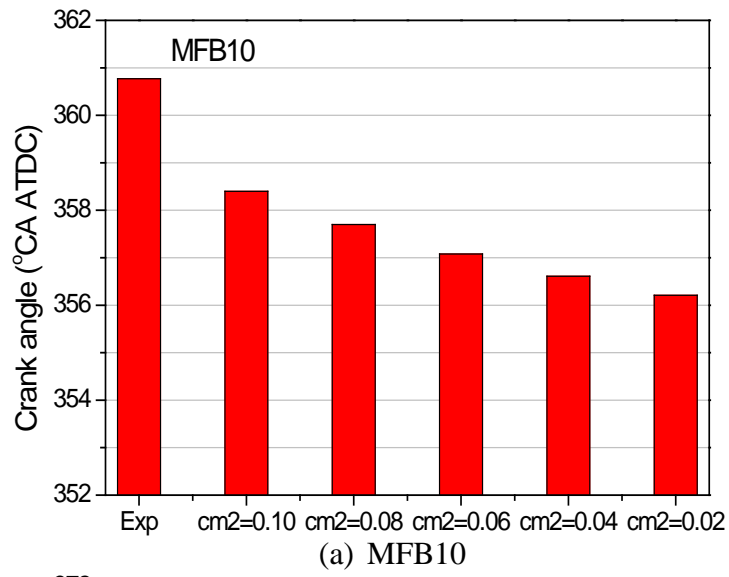


Fig.7.11 Effect of C_{m2} on the Mass Fraction Burned ($C_{m1}=1.4$)

Secondly, the combustion duration, defined by the interval of 10% MFB and 90% MFB (MFB 10-90) in the crank angle, is presented in Fig.7.10c and Fig.7.11c. Unlike the initial duration, there was a small difference of MFB 10-90 (no more than 2 °CA) in the variation of C_{m1} (see Fig.7.10c) and almost 5°CA extension of combustion duration, with the value of C_{m2} ranging from 0.02 to 0.10 (see Fig.7.11c). As expressed in Eq.3.44, C_{m2} is the ratio of turbulent mixing time to the eddy turnover time and therefore affects the whole duration of turbulent combustion. In other words, when C_{m2} increases, more time is consumed for turbulent mixing and the end of combustion is postponed. The optimal value of C_{m2} should be chosen between 0.06 and 0.08 compared with experimental combustion duration as presented in Fig.7.11c.

In addition, the whole combustion duration can be divided into two durations by the phasing of 50% MFB. As presented in Fig.7.10b and Fig.7.11b, both C_{m1} and C_{m2} affect the middle of combustion duration.

The effect of C_{m1} and C_{m2} on the temporal evolutions of in-cylinder pressure is shown in Fig.7.12 and Fig.7.13, respectively. As illustrated in Fig.7.12, with the C_{m1} varying from 1.4 to 2.2, the maximum in-cylinder pressure decreases from 6.1 MPa to 4.9 MPa and the phasing of the maximum delays approximately 5.5 °CA, which is consistent with the trend of MFB 50 as shown in Fig.7.10b. While, as C_{m2} varies from 0.02 to 0.10, the maximum in-cylinder pressure reduces from 6.6 MPa to 5.4 MPa and the phasing of the peak shifts about 5.5 °CA. This indicates C_{m1} and C_{m2} can be considered as comparative factors on the maximum in-cylinder pressure, although the combustion phase differs.

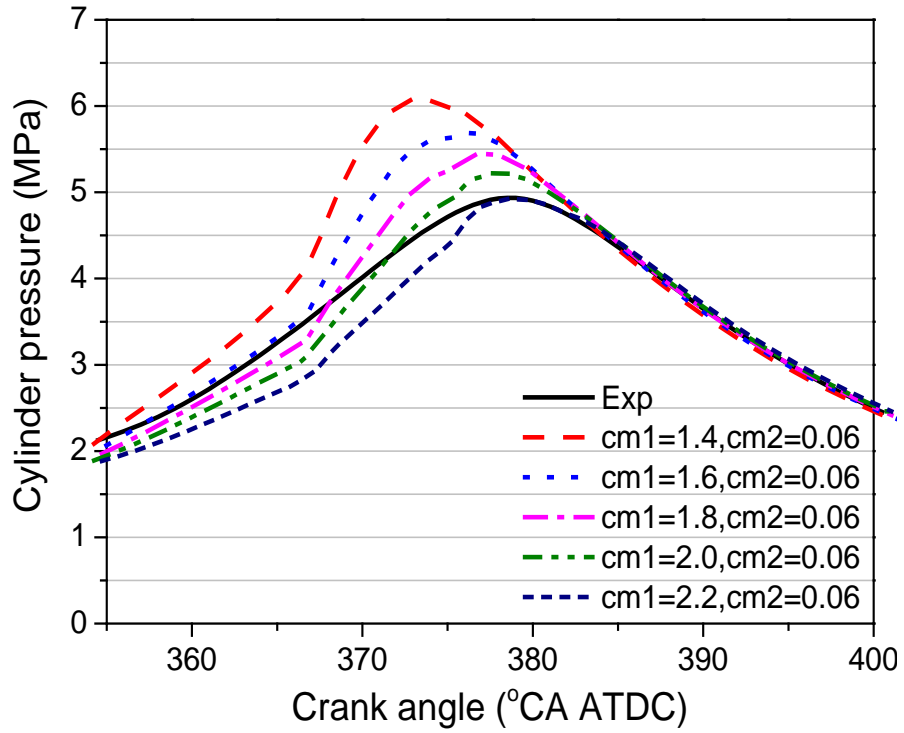


Fig.7.12 Effect of C_{m1} on the pressure trace ($C_{m2}=0.06$)

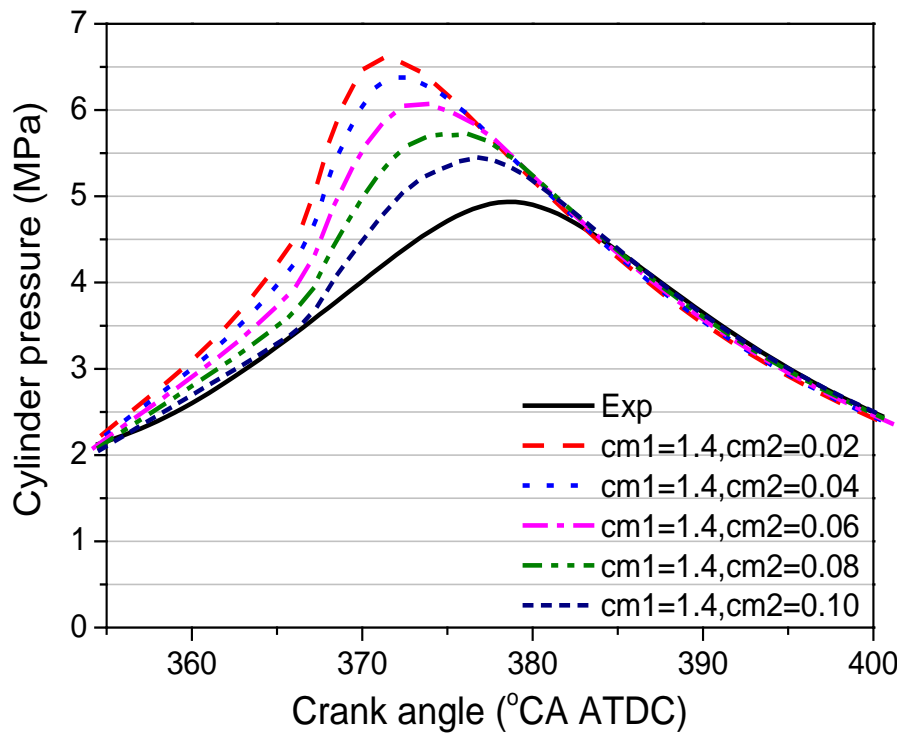
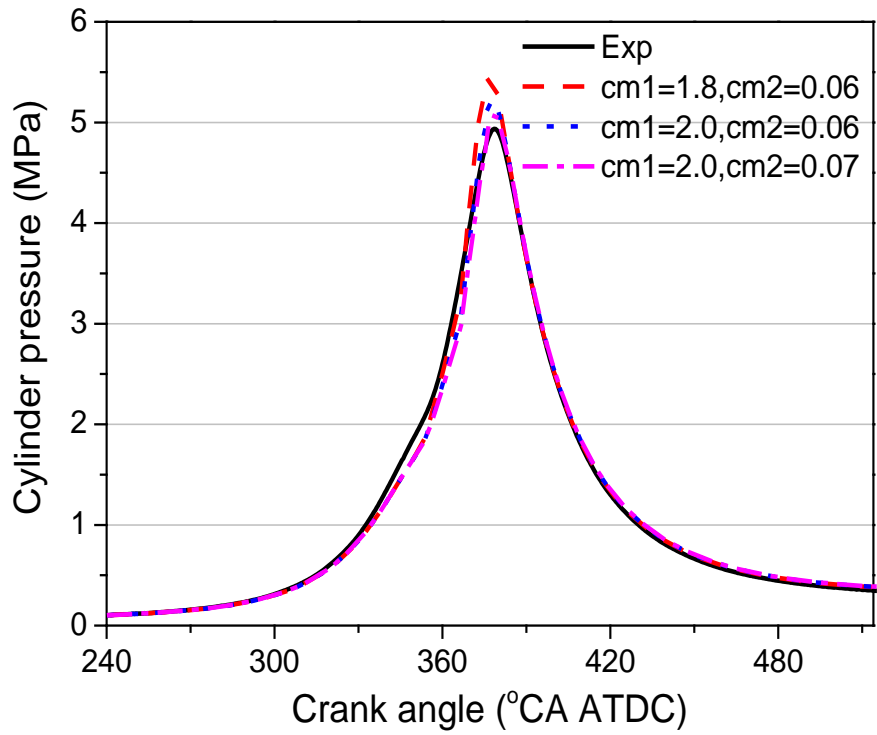
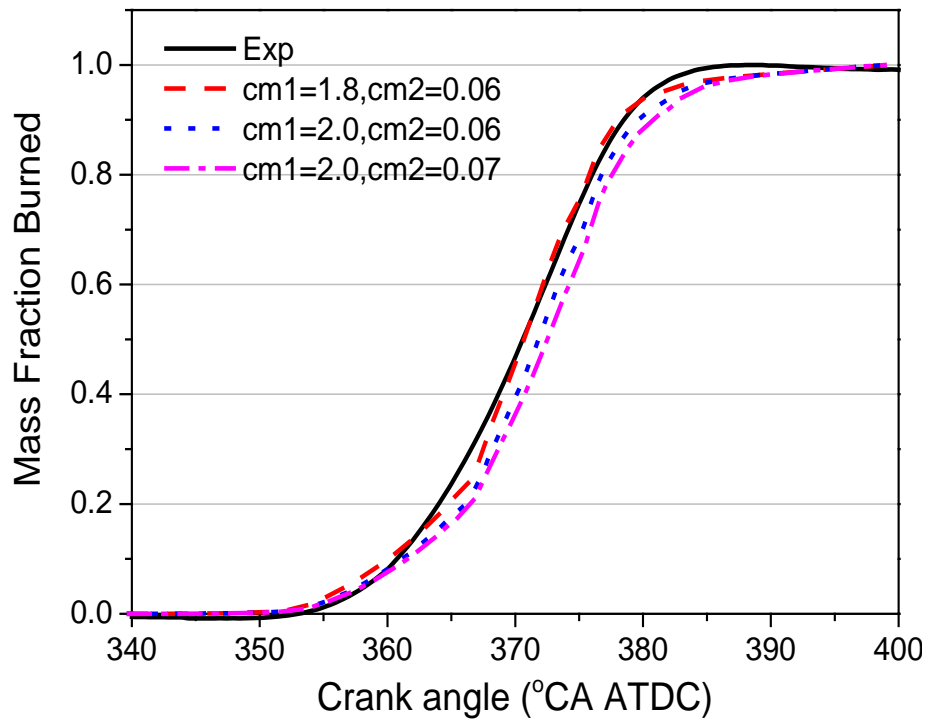


Fig.7.13 Effect of C_{m2} on the pressure trace ($C_{m1}=1.4$)



(a) Pressure trace



(b) Mass fraction burned

Fig.7.14 Comparisons of temporal evolutions of pressure and mass fraction burn predicted by the calibrated model and experimental results.

After analyzing the effects of C_{m1} and C_{m2} on the mass fraction burned and in-cylinder pressure profile, it should be summarized that the initial combustion duration can be mainly adjusted by the value of C_{m1} , whereas the whole combustion duration and the maximum in-cylinder pressure can be calibrated by the parameter of C_{m2} . Thus, two optimal cases (Case 3 and Case 4) of C_{m1} on MFB are selected as the base cases for the further calibration. Fig.7.14 presents the comparisons of the final calibrated case, Case 3, Case 4 and experimental case on the temporal evolutions of in-cylinder pressure and mass fraction burned. The final calibrated case ($C_{m1}=2.0$, $C_{m2}=0.07$) narrows the gap of the in-cylinder pressure peak between the numerical and experimental cases as seen in Fig.7.14a and its relative error is about 2.5%. Although the combustion duration is slightly extended, the initial combustion duration achieves a good consistency with that of the measurement as presented in Fig.7.14b. Thus, the final calibrated case basically reproduces the real engine performance during the combustion process.

7.5 CTC Model Validation in Direct Injection Spark Ignition

Combustion

After the calibration for chosen conditions, the CTC model will be validated for the experimental conditions with the High-Speed Photography (HSP) data in a Direct Injection Spark Ignition (DISI) optical engine. Then by using this combustion model, the comparisons of DMF and gasoline in terms of the engine performance especially during the combustion process will be carried out in this section.

7.5.1 Validation with HSP data

The combustion process of DMF in the optical engine was observed by Ma et al. [170] using an HSP technique through the piston optically accessible window. At least 40 cycles were recorded for each measuring point. The combustion propagation of the single shot images selected reflects the average temporal evolution of the flame speed. The engine was run at a speed of 1200 rpm, with a load of 5.5 bar IMEP. The spark timing was 336 °CA ATDC.

The calculations were conducted from EVO at 204 °CA BTDC to 400°CA ATDC. The initial pressure and temperature were taken from the 1D engine simulation results of Wave code, as presented in Fig.5.5.

Sequences of single cycle HSP images and numerical temperature spatial distributions in a DISI engine are presented in Fig.7.15. The numerical combustion propagation was reflected by the temperature distributions (temperature contours on a plane at $z=9.9\text{cm}$ perpendicular to the cylinder axis) and flame front was represented by the temperature iso-surfaces of 2000 K.

Although some parts of the flame in the HSP images are beyond the visible range after 373°CA ATDC, it can be still seen that the overall combustion propagation is fairly predicted by the calibrated CTC model in terms of combustion phase, flame growth and rough shape of flame boundary. It is noticeable that the numerical results reproduce the phenomenon of a faster propagation of flames towards the exhaust valves, due to the higher local temperature and the clockwise in-cylinder tumble motion, as discussed in [170].

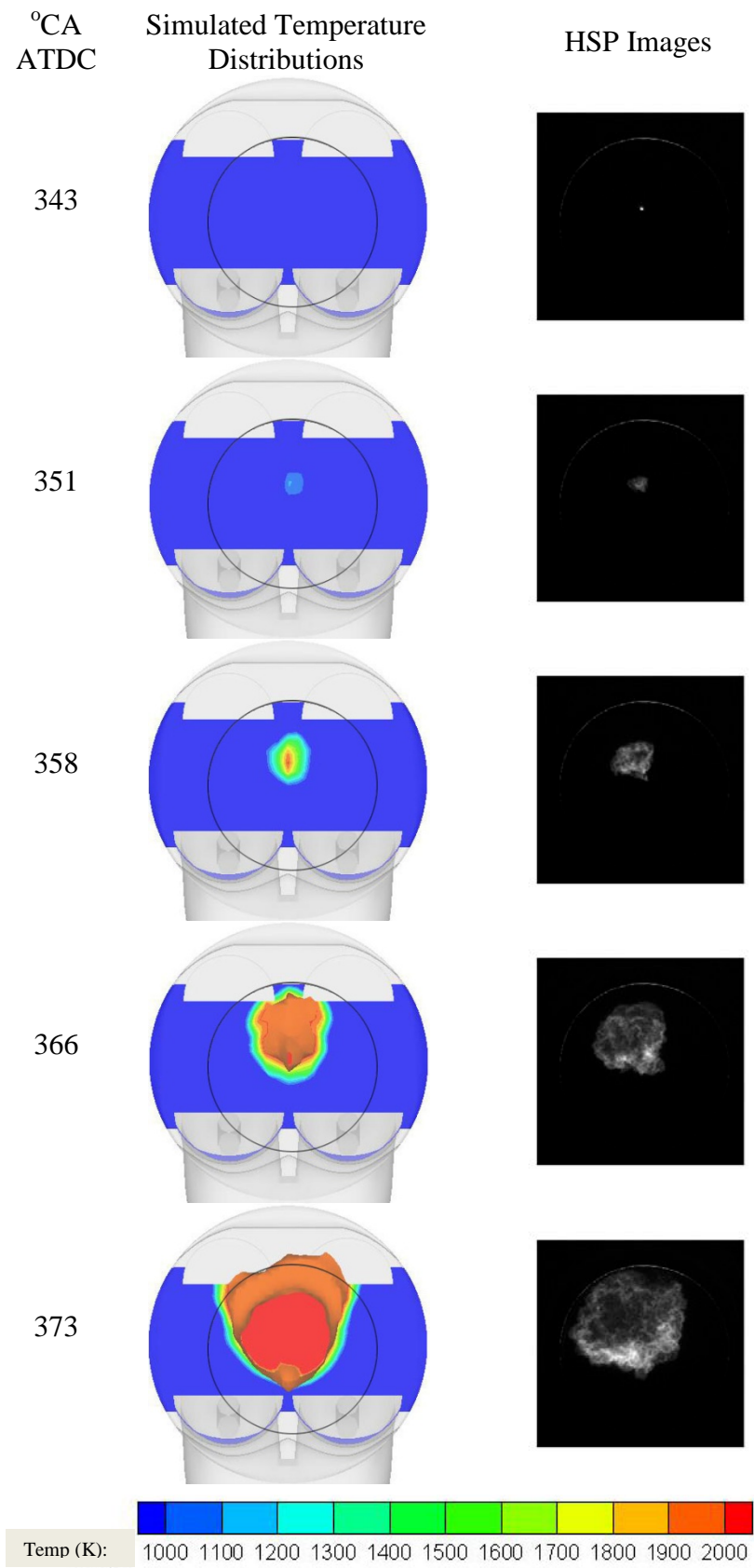


Fig.7.15 Comparisons of numerical combustion process and HSP images in a DISI engine

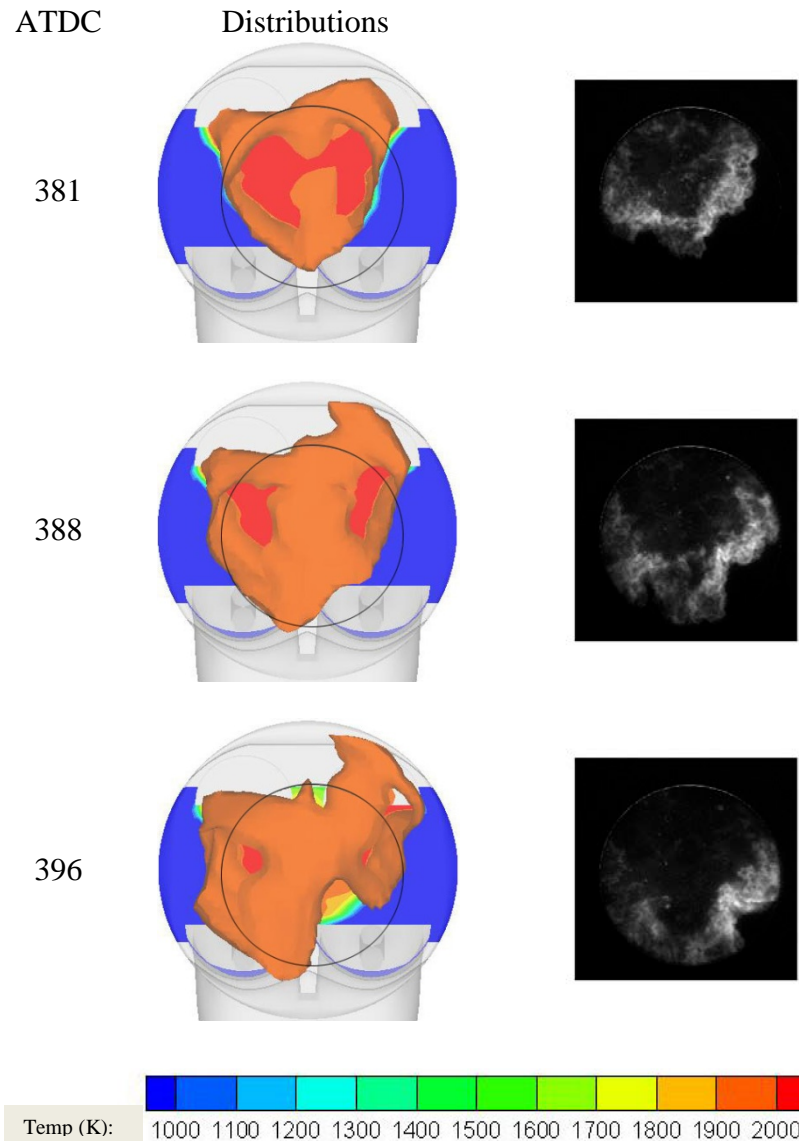


Fig.7.15 Comparisons of numerical combustion process and HSP images in a DISI engine (cont.)

In Fig.7.15, there was regular spark ignited flames' propagation from the crank angle 351° to 358° CA ATDC and after 363° CA ATDC, the flames are slightly distorted due to the clockwise swirl motion. In addition, the result indicates that a dominant turbulent combustion occurs after 373° CA ATDC by the strong wrinkling of the flames and the profiles of the wrinkles are semblable to those of the HSP images, as presented in Fig.7.15. Although a small

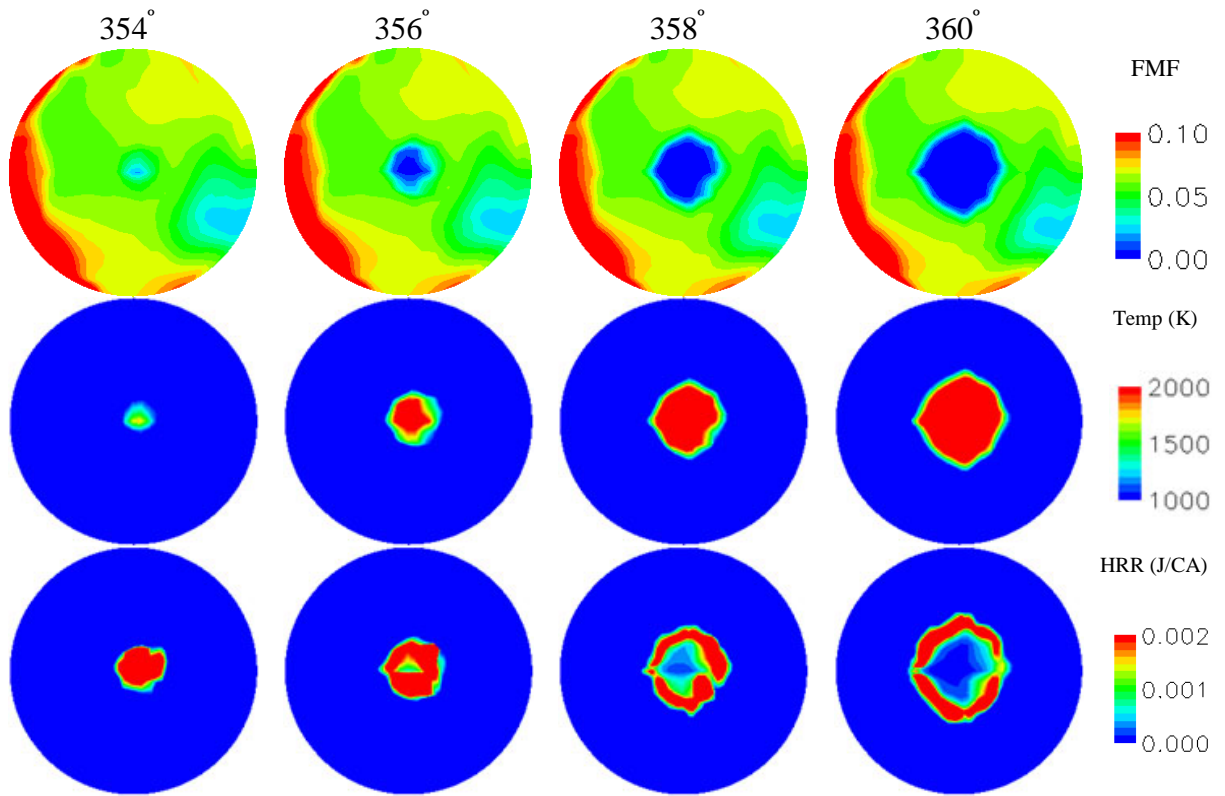
difference of flame shape exists at the beginning of combustion, this discrepancy may result from the cycle-to-cycle variation in the SI combustion process.

7.5.2 Comparisons of DMF and Gasoline on the DISI Combustion and Engine Performance

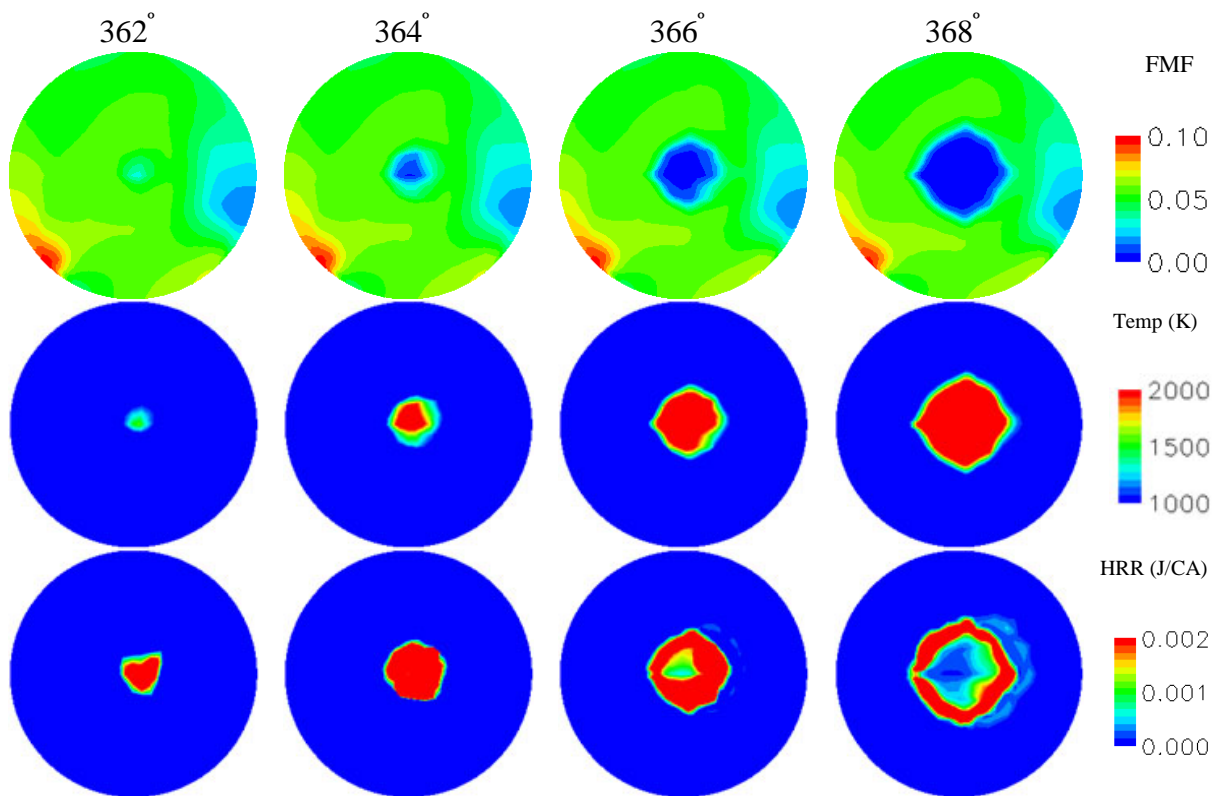
The comparisons of DMF and gasoline in the mixture preparation have been discussed in subsection 6.3.2. Now the comparisons in the subsequent combustion process will be explored in this subsection.

All the initial and boundary conditions are consistent with those described in section 6.2. The spark timing for the DMF and gasoline cases were 344° CA ATDC and 350° CA ATDC, respectively, consistent with the optimum spark timings of a thermal engine (based on the Knock-Limited Spark Advance [171]). As listed in Table 1.2, DMF has a high research octane number (DMF: 101.3, gasoline: 96.8). This indicates DMF has a higher antiknock quality and this contributes to the further advanced spark timing referred to the spark timing of gasoline.

As shown previously in Fig.6.15, compared to the case of gasoline, more stratified mixtures are formed at the end of the compression stroke in the case of DMF. Thus, in order to investigate the influence of fuel properties and fuel stratification on the combustion, the comparisons will be analyzed in terms of spatial distributions of Fuel Mass Fraction (FMF), charge temperature and heat release rate (HRR).

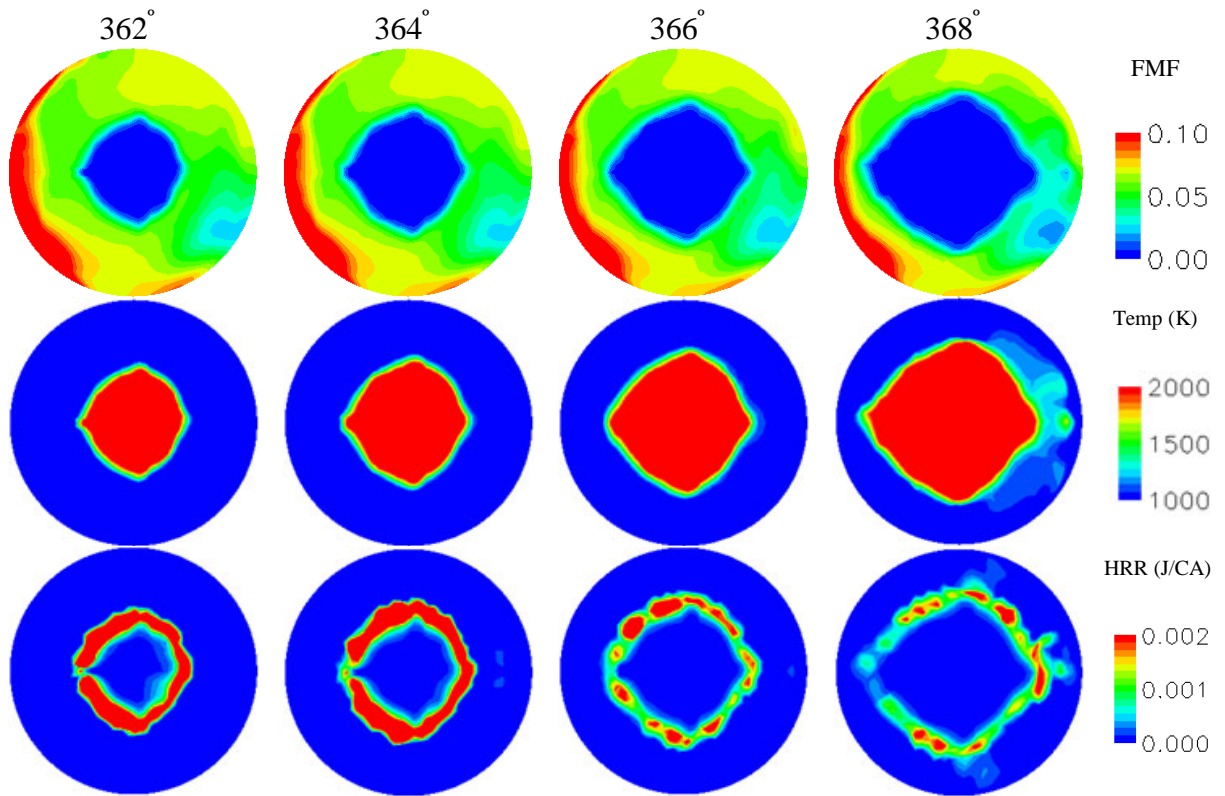


(a) DMF

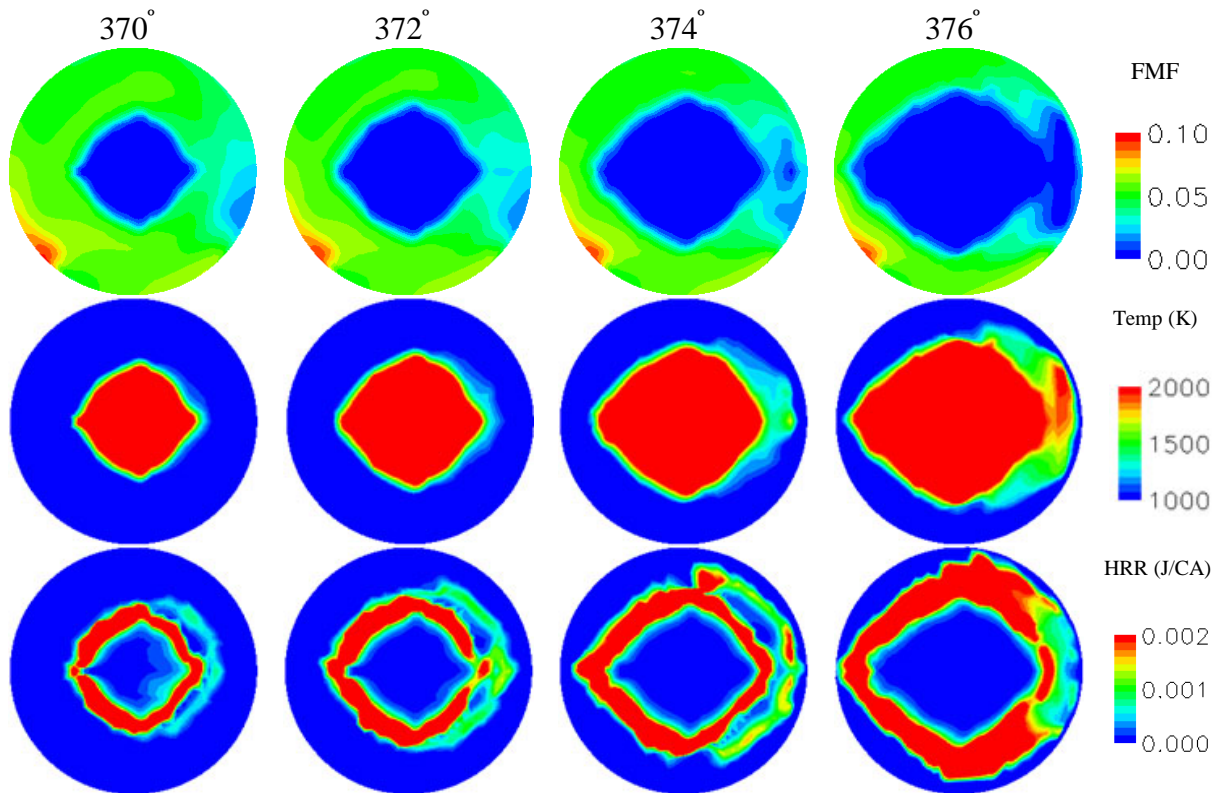


(b) Gasoline

Fig.7.16 Temporal evolution of the initial combustion duration (0-10% MFB) at $z=9.03\text{cm}$

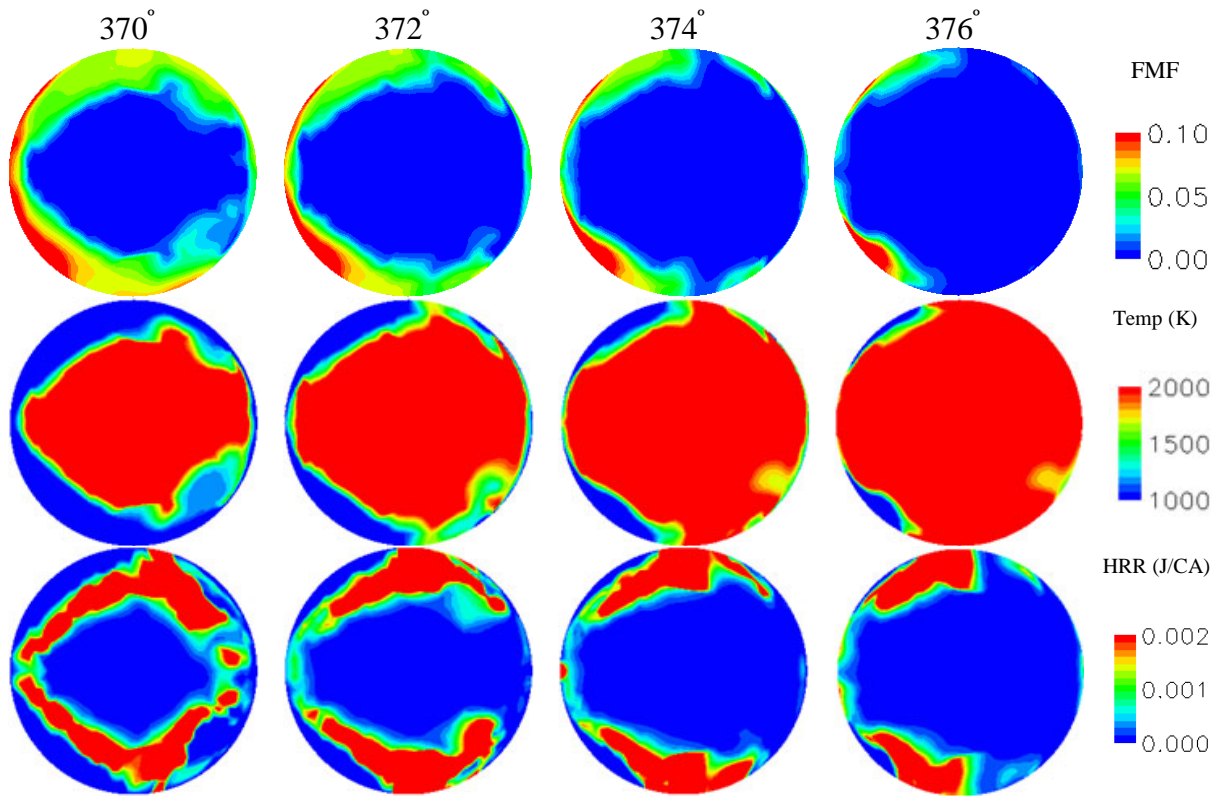


(a) DMF

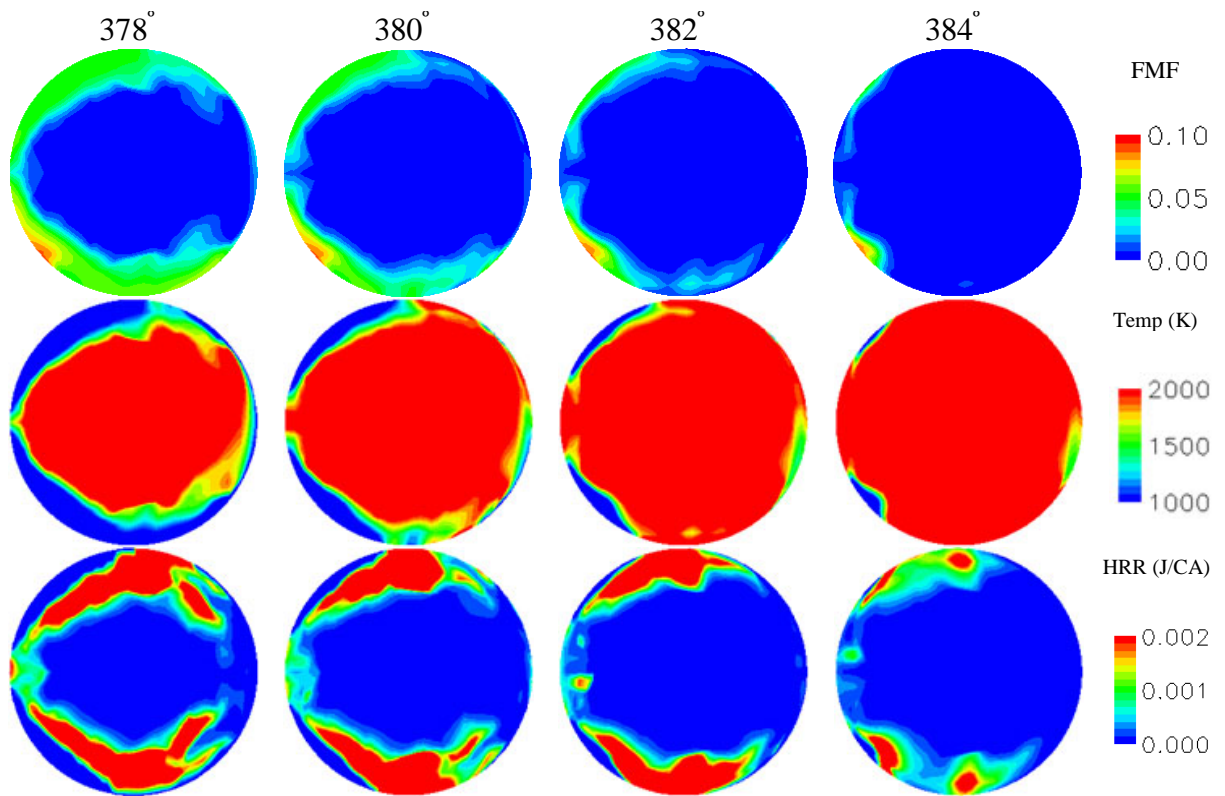


(b) Gasoline

Fig.7.17 Temporal evolution of the first half of the combustion duration (10-50% MFB) at $z=9.03\text{cm}$



(a) DMF



(b) Gasoline

Fig.7.18 Temporal evolution of the second half of the combustion duration (50-90% MFB) at $z=9.03\text{cm}$

The temporal evolutions of the initial combustion process (0-10% MFB) of the DMF and gasoline cases are given in Fig.7.16. As mentioned in subsection 3.7.1, the turbulent combustion model is activated when the local temperature exceeds 1000K. As presented in the temperature contours, the ignition site of the DMF and gasoline cases develop in the centre of the combustion chamber at 354° CA ATDC and 362° CA ATDC, respectively. Meantime, a band-shape high heat release region spreads with the flame propagation and the flame speeds of the two fuels in the initial combustion duration are similar. From the FMF contours, a lean mixture region grows with the ignition development as clearly observed; compared to gasoline, more stratification of fuel concentration can be seen in the case of DMF, corresponding to the results in the analysis of the mixture preparation as presented in Fig.6.14.

Fig.7.17 presents the comparisons of the temporal evolutions in the first half combustion of the process (10-50% MFB). Basically the similarity of the flame speeds remains in the beginning of the main combustion duration. However, in the case of gasoline, from the heat release contours, a conspicuous outer ring can be seen at the exhaust valve side. This can be explained by the direction variation of flame propagation since the flame front is distorted by reaching the pent roof or with tumble motion. In addition, from the FMF contours, except for the central spread of lean mixture, another region of lean mixture at the exhaust valve side develops when approaching to the wall.

The temporal evolutions in the latter stage of the main combustion process (50-90% MFB) are presented in Fig.7.18. The proportion of high heat release rate expands suddenly when the flame front is closing to the walls. It is known that for the cells adjacent to the walls,

turbulence time scale approaches zero and so the combined time scale switches to laminar time scale; that is, combustion flame speed changes into laminar flame speed, which results in the rapid increase of heat release. Finally, the flame decays when nearly 90% of the fuel is consumed.

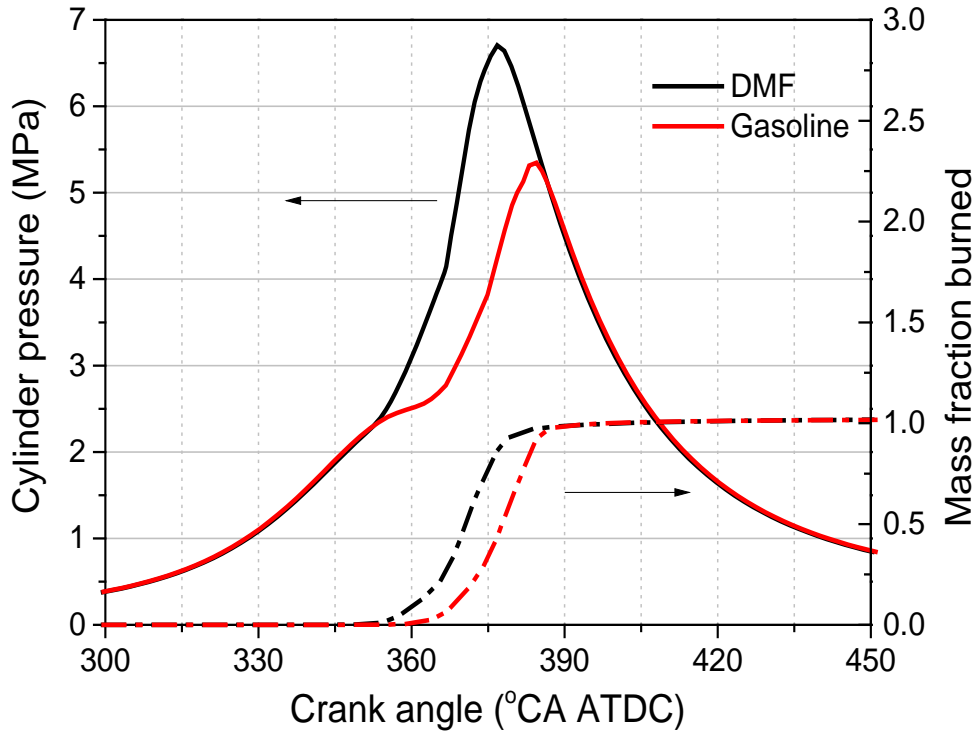


Fig.7.19 Comparisons of pressure and MFB profiles during the combustion process.

Fig.7.19 illustrates the in-cylinder pressure and MFB profiles during the combustion process. As shown in MFB profiles, the combustion phasing is obviously postponed with the retarded spark timing for the gasoline case. The advanced spark timing triggers the main combustion of DMF around TDC (361° CA ATDC as shown in Table 7.2). Since the cylinder space is at a minimum, this makes DMF more likely to produce both much higher peak pressure and maximum temperature than gasoline, contributing to its higher IMEP.

Table 7.2 Comparisons of combustion characteristics and engine performance

	DMF	Gasoline
10% MFB [$^{\circ}$ CA ATDC]	361.0	368.2
50% MFB [$^{\circ}$ CA ATDC]	370.4	377.7
90% MFB [$^{\circ}$ CA ATDC]	378.1	383.9
10-50% MFB [$^{\circ}$ CA ATDC]	9.4	9.5
50-90% MFB [$^{\circ}$ CA ATDC]	7.7	6.2
10-90% MFB [$^{\circ}$ CA ATDC]	17.1	15.7
P _{max} [MPa]	6.71	5.35
T _{max} [K]	2472	2432
IMEP [bar]	12.15	11.31
ISFC [g/kW h]	274.17	210.70
Combustion Efficiency	0.93	0.95
ISNO _x [g/kW h]	11.5	4.2

Another noticeable feature of DMF in DISI combustion is its 187% higher NO_x emissions (11.5 g/kW h), than that of gasoline (4.2 g/kW h), as presented in Table 7.2. It is known that the NO_x formation is highly related with the intensity of the combustion process. Fig.7.20 presents the predicted NO_x histories. As presented, the durations of NO_x accumulation for the two fuels are similar. However in the case of DMF, due to the advanced spark timing, the main stage of NO_x formation begins earlier, right after 360° CA ATDC and then a rapid growth occurs in the NO_x emissions within 10° CA attributed by the faster combustion and locally higher temperature around TDC.

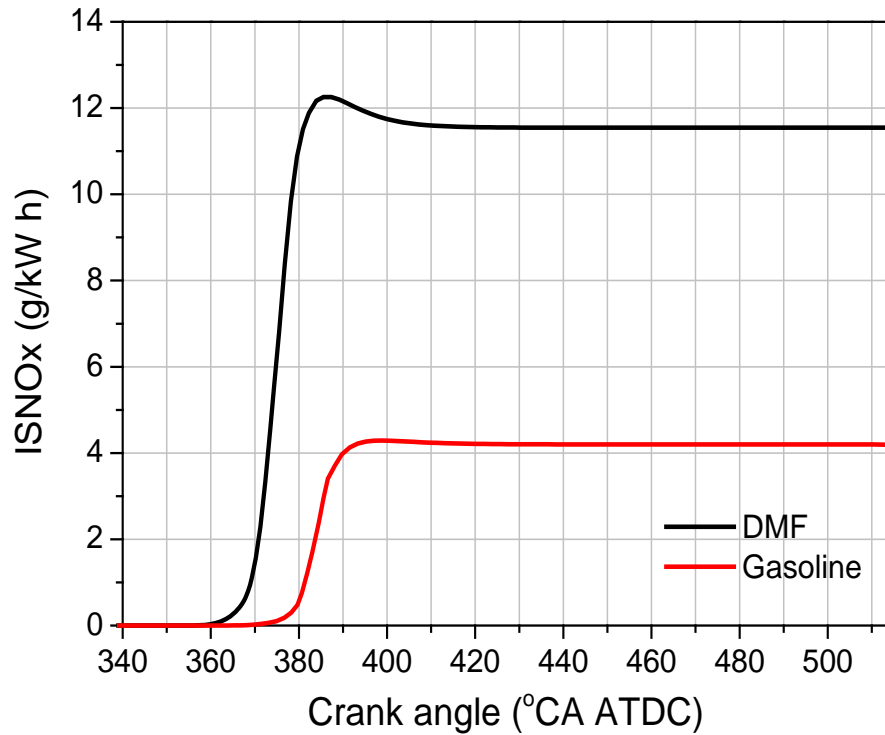


Fig.7.20 Comparisons of predicted NOx histories in the DMF and gasoline cases.

7.6 Summary

The laminar burning velocity of DMF at various initial temperatures and equivalence ratios were investigated by using the Schlieren optical method and was compared with gasoline. Next, a CTC model was calibrated against the Schlieren data and the thermal engine performance, respectively for the portions of laminar and turbulent combustion. Finally, the characteristics of DMF in DISI combustion and engine performance were validated, analyzed and compared with gasoline. The conclusions are given as below:

1. For the Schlieren test, generally the maximum of laminar burning velocity lies between the equivalence ratios of 1.15 and 1.25; the laminar burning velocity of DMF is slightly lower than that of gasoline.

2. The optimum constants in the laminar combustion model are determined as $FI= 0.34$, $OI = -0.79$ and $E = 19000$ with the comparison of mean stretched flame speed obtained by the Schlieren test; the turbulent combustion model is calibrated with the experimental combustion phase and temporal evolution of in-cylinder pressure in premixed charge SI combustion and when $C_{m1}=2.0$ and $C_{m2}=0.07$, the prediction achieves overall the best agreement with the measurement.
3. Generally, the calibrated CTC model reproduces the characteristics of the combustion phase, flame growth and profiles of flame boundary in a DISI DMF engine. Both the simulation and HSP images indicate combustion propagation is faster at the exhaust valve side and also the existence of flame distortion due to the swirl motion.
4. In DISI combustion, from the combustion phase, slightly longer combustion duration of DMF is attributed to its lower laminar burning velocity compared to that of gasoline. With respect to the engine performance, higher peak pressure, maximum temperature and higher IMEP are promoted by the advanced spark timing of the DMF case due to its good antiknocking quality; meanwhile, the higher pressure rise rate and locally higher temperature leads to 187% higher NO_x emissions than those of gasoline. In addition, strong stratification of mixture formation lowers combustion efficiency of DMF and further worsens its fuel economy, over 30% higher ISFC is produced compared to that of gasoline.

Chapter 8 CONCLUSIONS AND FUTURE WORK

In this thesis, a three-dimensional in-cylinder spray and combustion model have been exploited to simulate the DMF fuelled GDI engine. The modified and newly developed submodels include the hybrid Cascade Atomization and drop Breakup/Max Planck Institute (CAB-MPI) model and the Characteristic Time Combustion (CTC) model. In parallel, the Phase Doppler Particle Analyzer and Shadowgraph fuel spray measurement were used for validating the spray model; additionally, the combustion model was validated by the Schlieren laminar flame speed measurement, experimental in-cylinder pressure and combustion phasing and high speed photography of flame propagation.

8.1 Conclusions

Spray Characteristics of DMF in a Bomb—the investigation was focused on both macroscopic and microscopic characteristics. Compared with conventional gasoline fuel, DMF shows great similarities in the spray structure and the atomization process: similar magnitudes in the spray tip penetration length and cone angle; similar trends in the profiles of the temporal evolution of droplet size and velocity distribution. There is a marginal difference on the fuel physical properties: higher surface tension of DMF leads to damping more liquid surface instability wave, which slows down spray breakup process, hence larger droplet mean diameter.

In addition, the influence of injection pressure and ambient pressure on the spray behavior was studied. DMF and gasoline show similar trends of the spray tip penetration length and SMD and spray cone angle against the injection rail pressure and ambient pressure. However, at the same injection pressure, the magnitude of the SMD in the DMF cases is larger than that of gasoline; under the same ambient pressure, DMF has a narrower cone angle than that of gasoline due to its higher liquid density.

Spray Characteristics of DMF in a GDI Engine—both experimental and numerical results reveal the interaction between the spray jets and the in-cylinder flow such as the effect of intake flow on the spray development and spray impingement on the wall. Quantitative analysis of the mixing quality in a stoichiometric DI engine is discussed in terms of the effects of fuel properties, injection timing and engine speed using the CAB-MPI model and can be summarized as:

1. Compared with the case of gasoline, the larger droplet size of DMF slows down the evaporation processes and increases its penetration, which leads to more cylinder wall wetting. Consequently, there is a more stratified mixture in the case of DMF at the end of compression stroke (both highly rich mixture and extremely lean mixture are observed); only 96% of DMF fuel is fully evaporated; a leaner mixture exists near the spark plug.
2. With regards to the injection timing sweep, for the early injection cases, injection timing makes a dominant effect on the mixing quality due to the various extents of interactions between spray and air motion. While for the late injection cases, less fresh charge is entrained without charge cooling effect; a more stratified mixture is prepared

at the end of the compression stroke, because of their lesser mixing time between the fuel vapor and fresh charge.

3. The tumble ratio is not sensitive to engine speed. However, the turbulence energy increases significantly with engine speed; meanwhile, magnified intake flow enhances the spray inclination angle, making more spray impinged on the wall; additionally, due to prolonged injection duration, a wider spread of fuel distribution is formed at the end of compression stroke, attributed by the lesser mixing time of fuel vapor and fresh charge.

Combustion Characteristics of DMF in a GDI Engine—both chemical kinetics and fuel-air local distribution affects the combustion characteristics in a GDI engine. Compared with gasoline, DMF has a lower laminar burning velocity and to some extent, this results in longer combustion duration; in addition, a more stratified mixture seriously reduces its combustion efficiency and fuel economy (30% higher than that of gasoline). However, DMF's high research octane number enhances its antiknocking quality, making further advancing spark timing possible. Consequently, higher peak pressure, maximum temperature and higher IMEP are obtained in the case of DMF; meanwhile, the higher pressure rise rate and higher temperature leads to 187% higher NO_x emissions than those of gasoline.

8.2 Recommendations for future work

Spray Modelling

1. The spray atomization model in this study was validated in the non-evaporated sprays test. In fact, both DMF and gasoline are volatile and thus, there may be a difference of characteristics between the non-evaporated and evaporated sprays. This can be solved by using a fuel vapor detection technique such as laser induced fluorescence (LIF).
2. Given by the limitation of the PDPA technique itself, the spray characteristics in the dense region are impossible to measure, although this is critical to the validation of the primary breakup model. At present, the laser sheet drop-sizing (LSD) technique can be a practical solution, although only the SMD can be measured.
3. The cavitation-induced model adopted in this thesis oversimplifies the description of the internal nozzle flow without concerning the radical variation and the bubble formation and collapsing. A 3D numerical study can offer a further understanding of the phenomenon in the nozzle flow. Additionally, extra sub-models such as flash boiling can be implemented to involve the influence of the bubble formation and collapsing on the primary breakup.
4. The current vaporization model is a single-component model. However, DMF blending with gasoline or ethanol is one of the main objectives. The implementation of a multi-component vaporization model will be the premise for the numerical study in this direction.

Combustion Modelling

1. Since the CTC model is an empirical model, the chemical kinetics is oversimplified without any low temperature reactions. Therefore, this model is unsuitable for the prediction of the pollutant emissions such as hydrocarbon. With the development on the chemical kinetics of DMF oxidation, the combustion coupled with its reduced or detailed chemical mechanism will be a promising way for its emissions control.
2. As discussed in Chapter 6 and Chapter 7, stratification of the mixture and spray impingement on the wall are the chief problems in the case of DMF. Except for the optimization of injection timing, the current injector needs to be redesigned for DMF to reduce the chance of spray impingement. In addition, compared with gasoline, DMF has a lower volatility and its slower vaporization is not beneficial to the organization of fuel-air mixing. Increasing the tumble ratio through modifying the geometry of the intake port or the piston crown will be a practicable method to improve the mixing quality of DMF-air mixture.

References

1. Birol, F. (2010). "World energy outlook 2010". International Energy Agency.
2. http://en.wikipedia.org/wiki/European_emission_standards. 2013.
3. "Commission Regulation (EU) No 459/2012 of 29 May 2012 amending Regulation (EC) No 715/2007 of the European Parliament and of the Council and Commission Regulation (EC) No 692/2008 as regards emissions from light passenger and commercial vehicles (Euro 6) (Text with EEA relevance) ", The European Commission, Official Journal of the European Union, L 142/16, 1st June, 2012
4. https://en.wikipedia.org/wiki/Hydrogen_vehicle. 2013
5. Agarwal, A. K. (2007). "Biofuels (alcohols and biodiesel) applications as fuels for internal combustion engines". *Progress in energy and combustion science*, 33(3), 233-271.
6. IEA—International Energy Agency, 2011b. "Technology Roadmap, Biofuel for Transport". OECD/IEA, Paris. 2011
7. Wang, M. Q. (1996). "GREET 1.0-: Transportation Fuel Cycles Model: Methodology and Use". Argonne, IL: Argonne National Laboratory.
8. Wang, M. (2005). "Energy and Greenhouse Gas Impacts of Fuel Ethanol". Argonne National Lab, 23.
9. Environmental Benefits. U.S. Department of Energy - Energy Efficiency and Renewable Energy. Biomass Program.
http://www1.eere.energy.gov/biomass/printable_versions/environmental.html
10. G8, Heiligendamm Summit Declaration, 7 June 2007, p. 20;
11. IEA—International Energy Agency, 2008. *Energy Technology Perspectives* IEA, Paris. 2008.
12. Bioenergy, I. E. A. "From 1st-to 2nd-Generation BioFuel technologies." An overview of current industry and RD&D activities. IEA-OECD (2008).
13. Sims, R. E., Mabee, W., Saddler, J. N., & Taylor, M. (2010). "An overview of second generation biofuel technologies". *Bioresource Technology*, 101(6), 1570.
14. Van Rensen, S. (2011). "A biofuel conundrum". *Nature Climate Change*, 1(8), 389-390.
15. Zhao, H., Holladay, J. E., Brown, H., & Zhang, Z. C. (2007). "Metal chlorides in ionic liquid solvents convert sugars to 5-hydroxymethylfurfural". *Science*, 316(5831), 1597-1600.
16. Román-Leshkov, Y., Barrett, C. J., Liu, Z. Y., & Dumesic, J. A. (2007). "Production of dimethylfuran for liquid fuels from biomass-derived carbohydrates". *Nature*, 447(7147), 982-985.
17. Tong X, Ma Y, Li Y. "Biomass into chemicals: Conversion of sugars to furan derivatives by catalytic processes". *Applied Catalysis A: General* 2010; 385 (1–2) 1-13.
18. Binder, J. B., & Raines, R. T. (2009). "Simple chemical transformation of lignocellulosic biomass into furans for fuels and chemicals". *Journal of the American Chemical Society*, 131(5), 1979-1985.
19. Wackett, L. P. (2008). "Biomass to fuels via microbial transformations". *Current opinion in chemical biology*, 12(2), 187-193.
20. Thananathanachon, T., & Rauchfuss, T. B. (2010). "Efficient Production of the Liquid Fuel 2, 5-Dimethylfuran". *Chemie*, 122(37), 6766-6768.

21. Chidambaram, M., & Bell, A. T. (2010). "A two-step approach for the catalytic conversion of glucose to 2, 5-dimethylfuran in ionic liquids". *Green Chemistry*, 12(7), 1253-1262.
22. Dumesic, J. A., Rom, Y., & Chheda, J. N. (2009). U.S. Patent No. 7,572,925. Washington, DC: U.S. Patent and Trademark Office.
23. Kazi, F. K., Patel, A. D., Serrano-Ruiz, J. C., Dumesic, J. A., & Anex, R. P. (2011). "Techno-economic analysis of dimethylfuran (DMF) and hydroxymethylfurfural (HMF) production from pure fructose in catalytic processes". *Chemical Engineering Journal*, 169(1), 329-338.
24. Beilstein Database April 2008
25. US Department of Energy. Alternative Fuels and Advanced Vehicles Data Centre. October 2008.
26. Daniel, R., Tian, G., Xu, H., Wyszynski, M.L., Wu, X., Huang, Z., " Effect of spark timing and load on a DISI engine fuelled with 2, 5-dimethylfuran," *Fuel*, 90 (2011), pp.449–458.
27. Knovel database.
<http://www.knovel.com/web/portal/main>
28. Fuel library in KIVA-3V code
29. <http://chemed.chem.purdue.edu/genchem/topicreview/bp/ch14/property.php>
30. NREL/ TP-5400-50791. Janet Y, Earl C, McCormick R. "Utilization of renewable oxygenates as gasoline blending components". National Renewable Energy Laboratory; 2011.
31. Wang, C., Xu, H., Daniel, R., Ghafourian, A., Herreros, J. M., Shuai, S., & Ma, X. (2012). "Combustion characteristics and emissions of 2-methylfuran compared to 2, 5-dimethylfuran, gasoline and ethanol in a DISI engine". *Fuel*.
32. Rothamer, D. A., & Jennings, J. H. (2012). "Study of the knocking propensity of 2, 5-dimethylfuran–gasoline and ethanol–gasoline blends". *Fuel*.
33. <http://en.wikipedia.org/wiki/2,5-Dimethylfuran>.
34. http://en.wikipedia.org/wiki/Flash_point.
35. Arlien-Søborg, P. (1992). Solvent neurotoxicity. Informa Healthcare.
36. <https://www.avl.com/downsizing-downspeeding-gasoline>.
37. Clenci, A. C., Descombes, G., Podevin, P., & Hara, V. (2007). "Some aspects concerning the combination of downsizing with turbocharging, variable compression ratio, and variable intake valve lift". *Proceedings of the Institution of Mechanical Engineers, Part D: Journal of Automobile Engineering*, 221(10), 1287-1294.
38. http://en.wikipedia.org/wiki/Catalytic_converter
39. Pickett, L. M., "Soot Formation at Low Flame Temperature Diesel Operating Conditions", 9th International Conference "Present and Future Engines for Automobiles", San Antonio, TX, U.S.A., June, 2005
40. Kim, Y., Kim, Y., Jun, S., Lee, K. et al., "Strategies for Particle Emissions Reduction from GDI Engines," SAE Technical Paper 2013-01-1556, 2013.
41. M. Christensen., "The Effect of In-Cylinder Flow and Turbulence on HCCI Operation". SAE Paper 2002-01-2864, 2002
42. Tennekes, H., and Lumley, J.L., "A first course in turbulence", the MIT Press, Cambridge, Massachusetts, ISBN 0262200198, 1972, pp32.
43. Johansson, B., "Cycle to Cycle Variations in S.I. Engines - The Effects of Fluid Flow and Gas Composition in the Vicinity of the Spark Plug on Early Combustion," SAE Technical Paper 962084, 1996.

44. Reynolds, Osborne, 1895: "On the Dynamical Theory of Incompressible Viscous Fluids and the Determination of the Criterion." *Philosophical Transactions of the Royal Society of London. A*, v. 186, pp. 123-164.
45. Boussinesq, J. (1877), "Théorie de l'Écoulement Tourbillant", *Mem. Présentés par Divers Savants Acad. Sci. Inst. Fr.*, Vol. 23, pp. 46-50
46. Smith, A.M.O. and Cebeci, T. (1967), "Numerical solution of the turbulent boundary layer equations", Douglas aircraft division report DAC 33735.
47. Wilcox, David C. (2006). *Turbulence Modeling for CFD* (3 ed.). DCW Industries, Inc. ISBN 978-1-928729-08-2.
48. Launder, B. E.; Spalding, D. B. (1974). "The Numerical Computation of Turbulent Flows". *Computer Methods in Applied Mechanics and Engineering* 3 (2): 269–289. Bibcode:1974CMAME...3..269L..
49. Rodi, W., 1979, "Turbulence Models and their Application in Hydraulics," State of the art Paper, Presented by the IAHR-Section on Fundamentals of Division II: Exp. and Math. Fluid Dynamics.
50. Patel, V. C., Rodi, W. and Scheuerer, G. : "Turbulence Models for Near-Wall and Low-Reynolds Number Flows", *AIAA J.*, 23(1985), 1308~1319
52. Yakhot, V., Orszag, S.A., Thangam, S., Gatski, T.B. & Speziale, C.G. (1992), "Development of turbulence models for shear flows by a double expansion technique", *Physics of Fluids A*, Vol. 4, No. 7, pp1510-1520.
52. Yakhot, V. and Smith, L. M., (1992). "The Renormalization Group the epsilon-expansion and Derivation of Turbulence Models", *J. Sci. Comput.*, 7, 35.
53. Durbin, P. "Separated flow computations with the k-epsilon-v-squared model", *AIAA Journal*, 33, 659-664, 1995.
54. Laurence, D.R., Uribe J.C., Utyuzhnikov, S.V. "A Robust Formulation of the v2-f Model, Flow Turbulence and Combustion", 73, 169-185, 2004.
55. Launder, B. E., Reece, G. J. and Rodi, W. (1975), "Progress in the Development of a Reynolds-Stress Turbulent Closure.", *Journal of Fluid Mechanics*, Vol. 68(3), pp. 537-566.
56. Popovac, M., Hanjalic, K. Compound Wall Treatment for RANS Computation of Complex Turbulent Flows and Heat Transfer, *Flow Turbulence and Combustion*, 78, 177-202, 2007.
57. Launder, B. E.. "Second-Moment Closure: Present... and Future? ", *Inter. J. Heat Fluid Flow*, 10(4):282-300, 1989
58. Kolmogorov, A. N., "The local structure of turbulence in incompressible viscous fluid for very large Reynolds numbers". *Dokl. Akad. Nauk SSSR* 30, 301 (1941); also *Proc. R. Soc. A* 434, 9 (1991).
59. Rutland, C. J. (2011). "Large-eddy simulations for internal combustion engines—a review". *International Journal of Engine Research*, 12(5), 421-451.
60. Yokokawa, M., Itakura, K., Uno, A., Ishihara, T. and Kaneda, Y.. "16.4-TFlops Direct Numerical Simulation of Turbulence by a Fourier Spectral Method on the Earth Simulator", *Proceedings of the 2002 ACM/IEEE Conference on Supercomputing*, Baltimore MD (2002).
61. Reitz, R.D.. "Computer modeling of sprays, in: *Spray Technology Short Course*", Pittsburgh, PA, May 1996.
62. Herrmann, M.. Two phase flow. "CTR summer program tutorial", vol. 1. Centre for Turbul. Res., Stanford University; 2006. p. 1e122.

63. Hirt, C.W., Nichols, B.D., 1981. "Volume of fluid method for the dynamics of free boundaries". *J. Comp. Phys.* 39, 201–225.
64. Crowe, C.T., 1982. "Review—numerical methods for dilute gas-particle flows". *Trans. ASME J. Fluids Eng.*, 104 (1982), pp. 297–303
65. Dukowicz, J. K. (1980). "A particle-fluid numerical model for liquid sprays". *Journal of Computational Physics*, 35(2), 229-253.
66. Gosman, A. D., and R. J. R. Johns. "Computer analysis of fuel-air mixing in direct-injection engines". No. SAE 800091. 1980.
67. Moriyoshi, Y., Hu, X., and Takagi, M., "Experimentally Evaluated Spray Model for a Swirl-Type Injector," SAE Technical Paper 2002-01-2696, 2002.
68. Sanjosé, M., Senoner, J. M., Jaegle, F., Cuenot, B., Moreau, S., & Poinso, T. (2011). "Fuel injection model for Euler–Euler and Euler–Lagrange large-eddy simulations of an evaporating spray inside an aeronautical combustor". *International Journal of Multiphase Flow*, 37(5), 514-529.
69. Beck, J. C., & Watkins, A. P. (2003). "The droplet number moments approach to spray modelling: The development of heat and mass transfer sub-models". *International journal of heat and fluid flow*, 24(2), 242-259.
70. Suzzi, D. (2009). "Diesel nozzle flow and spray formation: coupled simulations with real engine validation".
71. de Villiers, E., Gosman, A., and Weller, H., "Large Eddy Simulation of Primary Diesel Spray Atomization," SAE Technical Paper 2004-01-0100, 2004.
72. Levich, V.G.. *Physico-Chemical Hydrodynamics*. Prentice-Hall, NY, USA, 1962.
73. Wu, P.K., Tseng, L.K., Faeth, G.M. (1992). "Primary breakup in gas/liquid mixing layers for turbulent liquids". *At Sprays* 2:295–317
74. Wu, P.K., Faeth, G.M. (1993). "Aerodynamic effects on primary breakup of turbulent liquids". *At Sprays* 3:265–289
75. Wu, P.K., Faeth, G.M. (1995). "Onset and end of drop formation along the surface of turbulent liquid jets in still gases". *Phys Fluids* 7:2915–2917
76. Wu, P.K., Miranda, R.F., Faeth, G.M. (1995). "Effects of initial flow conditions on primary breakup of nonturbulent and turbulent round liquid jets". *At Sprays* 5:175–196
77. McCarthy, M.J. and Malloy, N.A.. "Review of the stability of liquid jets and the influence of nozzle design". *Chem. Eng. J.*, Vol. 7, pp. 1–20, 1974.
78. Reitz, R.D. and Bracco, F.V.. "Mechanism of atomization of a liquid jet. *Physics of Fluids*", Vol. 25, No. 10, pp. 1730–1742, 1982.
79. Arcoumanis, C. and Gavaises, M.. "Linking nozzle flow with spray characteristics in a diesel fuel injection system". *Atomization and Sprays* 8.3 (1998) 307–347.
80. Reitz, R.D.. "Mechanisms of Atomization Processes in High-Pressure Vaporizing Sprays", *Atomization and Spray Technology*, 3:309-337, 1987.
81. O'Rourke, P.J., and Amsden, A.A., "The Tab method for numerical calculation of spray droplet breakup", SAE paper 872089, 1987.
82. Reitz, R.D. and Diwakar, R. "Structure of High-Pressure Fuel Sprays," SAE Paper 870598, SAE Transactions Vol. 96, Sect. 5, pp. 492-509, 1987.
83. Huh K.Y. and Gosman A.D. "A phenomenological model of diesel spray atomization". In *Proc. Int. Conf. Multiphase Flow*, 1991.
84. Hiroyasu, H. (2000). "Spray breakup mechanism from the hole-type nozzle and its applications". *Atomization and Sprays*, 10(3-5).
85. Hiroyasu, H. (1991). "Break-up length of a liquid jet and internal flow in a nozzle". In *Proc. 5th. ICLASS* (pp. 275-282).

86. Kim, J. H., Nishida, K., & Hiroyasu, H. (1997). "Characteristics of the internal flow in a diesel injection nozzle". *International Journal of Fluid Mechanics Research*, 24(1-3).
87. Arcoumanis, C., Gavaises, M., Flora, H., & Roth, H. (2001). "Visualisation of cavitation in diesel engine injectors". *Mécanique & industries*, 2(5), 375-381.
88. Dumouchel, C. (2008). "On the experimental investigation on primary atomization of liquid streams". *Experiments in fluids*, 45(3), 371-422.
89. Nurick, W.H., 1976. "Orifice cavitation and its effect on spray mixing". *ASME Journal of Fluids Engineering* 222, 681–687.
90. von Kuensberg Sarre, C., Kong, S., and Reitz, R., "Modeling the Effects of Injector Nozzle Geometry on Diesel Sprays," SAE Technical Paper 1999-01-0912, 1999.
91. Obermeier, F., Chaves, H., "Study of pressure fluctuations flows, separation and cavitation in the nozzle and their influence on spray formation", Proc. of the 6th Workshop of the IDEA Project, 1992.
92. Obermeier, F., "Experimental and theoretical study of the influence of unsteady high frequency flow conditions on flow separation and cavitation within a nozzle and on spray formation of fuel injectors under Diesel engine conditions", IDEA Project, Subprogram FM.1, Periodic Report No. 2, Institute für Angewandte Mechanik und Strömungsphysik der Georg August Universität, Göttingen, 1993.
93. Schneider, T., "Zur Modellierung der Zerstäubung von Flüssigkeitsfreistrahlen", Dissertation, Univ. Dortmund, 1995.
94. Kralj, C. (1996). "Numerical simulation of Diesel spray processes" (Doctoral dissertation, University of London).
95. Ruiz, F. "A Few Useful Relations for Cavitating Orifices," Proc. ICLASS-91, pp 595-602, 1991.
96. Baumgarten, C. (2006). "Mixture formation in internal combustion engines. Mixture Formation in Internal Combustion Engines", by C. Baumgarten. 2006 XVII, 294 p. 180 illus. 3-540-30835-0. Berlin: Springer, 2006., 1.
97. Arcoumanis, C., Gavaises, M., French, B., "Effect of Fuel Injection Process on the Structure of Diesel Sprays", SAE-paper 970799, 1997
98. Nishimura, A., Assanis, D.N., "A Model for Primary Diesel Fuel Atomization Based on Cavitation Bubble Collapse Energy", 8th Int. Conf. on Liquid Atomization and Spray Systems, Pasadena, pp.1249-1256, 2000.
99. Kawano, D., Goto, Y., Odaka, M., and Senda, J., "Modeling Atomization and Vaporization Processes of Flash-Boiling Spray," SAE Technical Paper 2004-01-0534, 2004.
100. Plesset, M. S., "Cavitation in Real Liquids", Amer. Elsevier Pub. (New York), p.1, (1964).
101. Reitz, R.D. and Bracco, F.V., "On the Dependence of the Spray Angle and Other Spray Parameters on Nozzle Design and Operating Conditions", SAE Paper 790494, 1979.
102. Chaves, H., Knapp, M., Kubitzek, A., Obermeier, F. and Schneider, T. "Experimental Study of Cavitation in the Nozzle Hole of Diesel Injectors Using Transparent nozzles," SAE Paper 950290, 1995.
103. Naber, J.D. and Siebers, D.L., "Effects of gas density and vaporization on penetration and dispersion of diesel sprays", SAE paper 960034; 1996.
104. Hiroyasu, H. and Arai, M. (1990). "Structures of Fuel Sprays in Diesel Engines". SAE-paper 900475.
105. Sovani, S.D., Chou, E., Sojka, P.E., Gore, J.P., Eckerle, W.A. and Crofts, J.D., 2000. "High pressure effervescent atomisation: Effect of Ambient Pressure on Spray Cone

- Angle". *Fuel*, pp 427-435.
106. Taylor, G. I. (1940). "Generation of ripples by wind blowing over a viscous fluid". *The Scientific Papers of GI Taylor*, 3, 244-254.
 107. Cheroudi, B., Chen, S.H., Bracco, F., and Onuma, Y. 1985. "On the intact core of full-cone sprays", *SAE Technical Paper Series 850126*.
 108. Liu, B, Mather, D., and Reitz, R. D., 1993, "Effects of Drop Drag and Breakup on Fuel Sprays," *SAE Technical Paper No. 930072*.
 109. Jenny, P., Roekaerts, D., & Beishuizen, N. (2012). "Modeling of turbulent dilute spray combustion". *Progress in Energy and Combustion Science*.
 110. Tanner, F.X., "Liquid Jet Atomization and Droplet Breakup Modeling of Non-Evaporating Diesel Fuel Sprays," *SAE Paper 970050*, 1997.
 111. Tanner, F.X., "A Cascade Atomization and Drop Breakup Model for the Simulation of High-Pressure Liquid Jets," *SAE Paper 2003-01-1044*, 2003.
 112. Ibrahim, E. A., Yang, H. Q., & Przekwas, A. J. (1993). "Modeling of spray droplets deformation and breakup". *Journal of Propulsion and Power*, 9(4), 651-654.
 113. Su, T. F., Patterson, M. A., Reitz, R. D., and Farrell, P. V., 1996, "Experimental and Numerical Studies of High Pressure Multiple-Injection Sprays," *SAE Technical Paper Series No. 960861*.
 114. Apte, S. V., Gorokhovski, M., & Moin, P. (2003). "LES of atomizing spray with stochastic modeling of secondary breakup". *International Journal of Multiphase Flow*, 29(9), 1503-1522.
 115. Schmehl, R. (2002). "Advanced modeling of droplet deformation and breakup for CFD analysis of mixture preparation". *Zaragoza*, 9, 11.
 116. Patterson, M.A., Reitz, R.D., "Modeling the Effects of Fuel Spray Characteristics on Diesel Engine Combustion and Emissions". *SAE Paper 980131*, 1998.
 117. Beale, J. C., and Reitz, R. D., 1999, "Modeling Spray Atomization With the Kelvin-Helmholtz/Rayleigh-Taylor Hybrid Model," *Atomization Sprays*, 9, pp. 623-650.
 118. Lee, C. S., and Park, S. W., 2002, "An Experimental and Numerical Study on Fuel Atomization Characteristics of High-Pressure Diesel Injection Sprays," *Fuel*, 81(18), pp. 2417-2423.
 119. Amsden, A.A., Ramshaw, J.D., O'Rourke, P.J., Dukowicz, J.K. (1985). *KIVA*. "A Computer Program for Two- and Three-Dimensional Fluid Flows with Chemical Reactions and Fuel Sprays". Los Alamos National Labs, Rept LA-10245-MS.
 120. Munnannur, A., & Reitz, R. D. (2007). "A new predictive model for fragmenting and on-fragmenting binary droplet collisions". *International journal of multiphase flow*, 33(8), 873-96.
 121. Qian, J., Law, C.K., 1997. "Regimes of coalescence and separation in droplet collision". *J. Fluid Mech.* 331, 59-80.
 122. O'Rourke, P.J., 1981. "Collective drop effects in vaporizing liquid sprays". Ph.D. Dissertation, Dept. Mech. Aerospace Engg., Princeton University, Princeton, NJ.
 123. Amsden, A.A., O'Rourke, P.J. and Butler, T.D. (1989). "Kiva-II: A Computer Program for Chemically Reactive Flows with Sprays". Los Alamos Report LA-11560-MS.
 124. Brazier-Smith, P.R., Jennings, S.G., Latham, J., 1972. "The interaction of falling rain drops: coalescence". *Proc. R. Soc. London, Ser. A* 326, 393-408.
 125. Tennison, P.J., Georjon, T.L., Farrell, P.V. and Reitz, R.D. (1998). "An Experimental and Numerical Study of Sprays from a Common Rail Injection System for Use in an HS-DI Diesel Engine". *SAE Paper No. 980810*.

126. Georjon, T.L., and Reitz, R.D. (1998). "A Drop Shattering Collision Model for Multi-Dimensional Spray Computations. Accepted for publication", *Atomization and Sprays*.
127. Estrade, J.P., Carentz, H., Lavergne, G., Biscos, Y., 1999. "Experimental investigation of dynamic binary collision of ethanol droplets – a model for droplet coalescence and bouncing". *Int. J. Heat Fluid Flow* 20, 486–491.
128. Post, S.L., Abraham, J., 2002. "Modeling the outcome of drop collisions in diesel sprays". *Int. J. Multiphase Flow* 28, 997-1019.
129. Ko, G.H., Ryou, H.S., 2005. "Modeling of droplet collision-induced breakup process". *Int. J. Multiphase Flow* 31, 723-738.
130. Nishad, K., Sadiki, A., and Janicka, J., "A Comprehensive Modeling and Simulation of Gasoline Direct Injection using KIVA-4 code," SAE Technical Paper 2011-01-1899, 2011.
131. Godsave, G. A. E., 1953, "Studies of the Combustion of Drops in a Fuel Spray—The Burning of Single Drops of Fuel," Fourth Symposium International on Combustion, Williams and Wilkins, Baltimore, pp. 818–830.
132. Yan, C., & Aggarwal, S. K. (2006). "A high-pressure droplet model for spray simulations". *Journal of Engineering for Gas Turbines and Power (Transactions of the ASME)*, 128(3), 482-492.
133. Ramos, J. I. (1989). "Internal combustion engine modeling" (Vol. 80). New York: Hemisphere Publishing Corporation.
134. Faeth, G. M. (1983). "Evaporation and combustion of sprays". *Progress in Energy and Combustion Science*, 9(1), 1-76.
135. Jin, J. and Borman, G., "A Model for Multicomponent Droplet Vaporization at High Ambient Pressures," SAE Technical Paper 850264, 1985.
136. Ra, Y., & Reitz, R. D. (2009). "A vaporization model for discrete multi-component fuel sprays". *International Journal of Multiphase Flow*, 35(2), 101-117.
137. Lindgren, R. and Denbratt, I., "Modeling Gasoline Spray-Wall Interactions and Comparison to Experimental Data," SAE Technical Paper 2004-01-3003, 2004.
138. Jia, M., Peng, Z., Xie, M., and Stobart, R., "Evaluation of Spray/Wall Interaction Models under the Conditions Related to Diesel HCCI Engines," SAE Int. J. Fuels Lubr. 1(1):993-1008, 2009.
139. Naber, J. and Reitz, R.D. (1988). "Modeling Engine Spray Wall Impingement". SAE Paper No. 880107.
140. Senda, D.J., Farrell, P.P.V., Kanda, T., Fujimoto, D.H., "Modeling Spray Impingement Considering Fuel Film Formation on the Wall". SAE Paper 970047, 1997.
141. Bai, C. and Gosman, A.D., "Development of Methodology for Spray Impingement Simulation". SAE Paper 950283, 1995.
142. O'Rourke, P.J. and Amsden, A.A., "A Spray/Wall Interaction Submodel for the Kiva-3 Wall Film Model". SAE Paper 2000-01-0271, 2000.
143. Haworth, D., "A Review of Turbulent Combustion Modeling for Multidimensional In-Cylinder CFD," SAE Technical Paper 2005-01-0993, 2005.
144. Spalding, D. B., 1971. "Mixing and chemical reaction in confined flames". *Proc. Combust. Institute*. 13, 649-657.
145. Abraham, J., Bracco, F.V., and Reitz, R.D., "Comparisons of computed and measured premixed charge engine combustion", *Combust. and Flame*, Vol.60, 1985, pp. 309-322.
146. Kuo, T.W., and Reitz, R.D., "Three-dimensional computations of combustion in premixed-charge and direct-injected two-stroke engines", SAE paper 920425, 1992.
147. Williams, F.A.. *Turbulent Combustion*, SIAM, Philadelphia, 1985

148. Marble, F. E. and Broadwell, J. E., "The Coherent Flame Model for Turbulent Chemical Reactions", Project Squid, Tech. Rep. TRW-9-PU, 1977
149. Peters, N., *Turbulent Combustion*; Cambridge University Press, 2000
150. Fan, L. and Reitz, R., "Development of an Ignition and Combustion Model for Spark-Ignition Engines," SAE Technical Paper 2000-01-2809, 2000.
151. Amsden, A. A., "A KIVA Program with Block-structured Mesh for Computer Geometries", Los Alamos National Lab Report, LA-12503-MS, 1993.
152. Fan, L., Li, G., Han, Z., and Reitz, R. D., "Modeling Fuel Preparation and Stratified Combustion in a Gasoline Direct Injection Engine," SAE Paper 1999-01-0175, 1999.
153. Duclos J. M. and Colin O., "Arc and Kernel Tracking Ignition Model for 3D Spark-Ignition engine calculations". Proceedings of COMODIA 2001 conference, 2001.
154. Dahms, R., Drake, M., Grover, Jr., R., Solomon, A., "Detailed Simulations of Stratified Ignition and Combustion Processes in a Spray-Guided Gasoline Engine using the SparkCIMM/G-Equation Modeling Framework," SAE Int. J. Engines 5(2):141-161, 2012.
155. Karimi, K. (2007). "Characterisation of multiple-injection diesel sprays at elevated pressures and temperatures" (Doctoral dissertation, School of Engineering, University of Brighton).
156. Kook, S., Le, M., Padala, S., and Hawkes, E., "Z-type Schlieren Setup and its Application to High-Speed Imaging of Gasoline Sprays," SAE Technical Paper 2011-01-1981, 2011.
157. Soid, S. N., & Zainal, Z. A. (2011). "Spray and combustion characterization for internal combustion engines using optical measuring techniques—A review". *Energy*, 36(2), 724-741.
158. Dantec-Dynamics, BSA Flow Software Version 4.10 Installation & User's Guide. 10th ed. 2006.
159. Zhao H, Ladommatos N., "Optical Diagnostics for in-cylinder mixture formation measurement in IC engines". *Prog Energ Combust* 1998;24:297e336.
160. Malarski, A., Schürer, B., Schmitz, I., Zigan, L., Flügel, A., & Leipertz, A. (2009). "Laser sheet droplet sizing based on two-dimensional Raman and Mie scattering". *Applied optics*, 48(10), 1853-1860.
161. Zhang, Y., Kotani, Y., Yoshida, A., and Nishida, K., "A challenge to vapor distribution measurement of multi-component evaporating fuel spray via laser absorption-scattering (LAS) technique," SAE Technical Paper 2007-01-1892, 2007.
162. Zhong, S., Daniel, R., Xu, H., Zhang, J., Turner, D. and Wyszynski, M.L., "Combustion and emissions of 2, 5-Dimethylfuran in a direct-injection spark-ignition engine," *Energy Fuels*, 24 (2010), pp. 2891–2899.
163. Tian, G., Li, H., Xu, H., Li, Y., & Satish, M. R. (2010). "Spray characteristics study of DMF using phase doppler particle analyzer. *SAE International Journal of Passenger Cars-Mechanical Systems*, 3(1), 948-958.
164. Wu, X., Daniel, R., Tian, G., Xu, H., Huang, Z. and Richardson, D., "Dual-injection: the flexible Bi-fuel concept for spark-ignition engines fuelled with various gasoline and biofuel blends," *Applied Energy*, 88 (2011), pp. 2305–2314.
165. Wu, X., Huang, Z., Wang, X., Jin, C., Tang, C. and Wei, L., "Laminar burning velocities and flame instabilities of 2, 5-dimethylfuran–air mixtures at elevated pressures," *Combust Flame*, 158 (2011), pp. 539–546.

166. Wu, X., Huang, Z., Jin, C., Wang, X., Zheng, B. and Zhang, Y., "Measurements of laminar burning velocities and markstein lengths of 2,5-dimethylfuran air diluent premixed flames", *Energy Fuels*, 23, pp. 4355–4362, 2009.
167. Tian, G., Daniel, R., Li, H., Xu, H., Shuai, S. and Richards, P., "Laminar burning velocities of 2, 5-Dimethylfuran compared with ethanol and gasoline", *Energy Fuels*, 24 (2010), pp. 3898–3905.
168. Wu, X., Huang, Z., Yuan, T., Zhang, K. and Wei, L., "Identification of the combustion intermediates in a low-pressure premixed laminar DMF/oxygen/argon flame with tunable synchrotron photo ionization", *Combust Flame*, 156 (2009), pp. 1365–1376.
169. Li, Q., Fu, J., Wu, X., Tang, C. and Huang, Z., "Laminar flame speeds of DMF-iso-octane-air-N₂/CO₂ mixtures". *Energy Fuels* 2012;26(2):917–9925.
170. Ma, X., Jiang, C., Xu, H., and Richardson, S., "In-Cylinder Optical Study on Combustion of DMF and DMF Fuel Blends," SAE Technical Paper 2012-01-1235, 2012.
171. Wang, C., Xu, H., Daniel, R., Ghafourian, A., Herreros, J. M., Shuai, S., & Ma, X. (2012). "Combustion characteristics and emissions of 2-methylfuran compared to 2, 5-dimethylfuran, gasoline and ethanol in a DISI engine". *Fuel*.
172. Amsden, A.A., "KIVA-3V, release 2, improvements to KIVA-3V", Los Alamos National Laboratory Report No. LA-UR-99-915, 1999.
173. Amsden, A.A., "KIVA-3V: A block-structured KIVA program for engines with vertical or canted valves", Los Alamos National Laboratory Report No. LA-13313-MS, 1997.
174. Amsden, A.A., "KIVA-3: A KIVA Program with blocked-structured mesh for complex geometries", Los Alamos National Laboratory Report No. LA-12503-MS, 1993.
175. Han, Z., and Reitz, R.D., "Turbulence modelling of internal combustion engines using RNG κ - ϵ model", *Combustion Science and Technology*, Vol.106, 1995, pp. 267.
176. Papageorgakis, G., and Assanis, D.N., "Optimising gaseous fuel-air mixing in direct injection engines using an RNG based κ - ϵ model", SAE paper 980135, 1998.
177. Han, Z., and Reitz, R.D., "A temperature wall function formulation for variable density turbulent flows with application to engine convection heat transfer modelling", *International Journal of heat and mass transfer*, Vol. 40, 1997, pp. 613-625.
178. Lefebvre, A. H. (1989). *Atomization and sprays* (Vol. 1040, No. 2756). CRC Press LLC.
179. Kong S.C., Han Z., and Reitz, R.D. "The Development and Application of a Diesel Ignition and Combustion Model for Multidimensional Engine Simulation", SAE paper 950278, 1995.
180. Bowman, C.T., "Kinetics of pollutant formation and destruction in combustion", *Prog. Energy Combust. Sci.*, Vol.1, 1975, pp. 33-45.
181. Heywood, J.B., "Internal combustion engine fundamentals", McGraw-Hill Book Company, ISBN 0-07-100499-8, 1988, pp. 574.
182. Gupta S, Poola R, Sekar R. Injection parameter effects on diesel spray characteristics. SAE paper 2000-01-2787; 2000
183. Epilog for itapeERC -- supplemental input file to kiva3v-library. <http://homepages.cae.wisc.edu/~hessel/manualsAndEpilogues/epilogItapeERC.txt>
184. Beale, J.C., and Reitz, R.D., "Modeling Spray Atomization with the Kelvin-Helmholtz/Reyleigh-Taylor Hybrid Model", *Atomization and Spray*, Vol.9, pp.623-650, 1999.
185. Juneja, H., Ra, Y., and Reitz, R.D., "Optimization of Injection Rate Shape Using Active Control of Fuel Injection," SAE Paper 2004-01-0530, 2004.
186. Bradley, D., Hicks, R.A., Lawes, M., Sheppard, C.G.W. and Woolley, R. , "The Measurement of Laminar Burning Velocities and Markstein Numbers for Iso-octane–Air

- and Iso-octane–n-Heptane–Air Mixtures at Elevated Temperatures and Pressures in an Explosion Bomb". *Combustion and Flame*, 1998. 115: p. 126–144.
187. Westbrook, C.K. and Dryer, F.L., "Simplified Reaction Mechanisms for the Oxidation of Hydrocarbon Fuels in Flames". *Combustion Science and Technology*, 27:31–43, 1981.
188. KIVA 4 itape5 input definition site
<http://homepages.cae.wisc.edu/~hessel/manualsAndEpilogues/kiva4itape5inputs/xignl1zigt1.html>
189. Sirjean, B., Fournet, R., Glaude, P.A., Frederique, B.L., Wang, W. and Oehlschlaeger, M.A., "A Shock Tube and Chemical Kinetic Modeling Study of the Oxidation of 2,5-Dimethylfuran", *J. Phys. Chem. A*, 2013, 117 (7), pp 1371–1392.